Directed Motion of Colloidal Particles via Chemical Reactions: Osmotic Propulsion
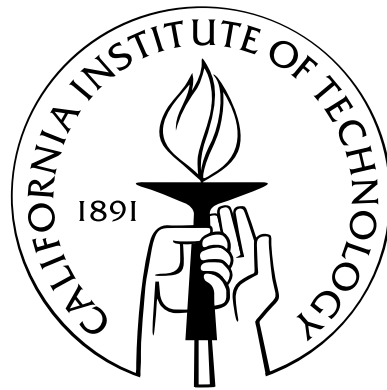
Thesis by

Ubaldo M. Córdova-Figueroa

In Partial Fulfillment of the Requirements

for the Degree of

Doctor of Philosophy

California Institute of Technology

Pasadena, California

2008

(Defended May 21, 2008)

Acknowledgements

During my time as an undergraduate student of chemical engineering in the University of Puerto Rico, Mayagüez Campus, I found myself with the monumental question of what I wanted to do with the rest of my life. It didn't take me long to realize that I wanted to continue on with my studies with an unfaltering desire to come back to my country and share with others all of my learned experiences. After 5 years of hard work, I have achieved what I set out to accomplish since the inception of my career in higher education. My journey, at times, was slow and confusing, but still full of important personal milestones that have made a lasting impact in my life. I learned to appreciate and understand the true power of education. This mission has come to fruition, not only because of my personal strengths, but also because of the collective support of many people that have motivated me to succeed in spite of constant difficulties. I want to take this moment to wholeheartedly thank everyone that has helped me throughout this process.

I appreciate all the help and advice I received from my advisor John F. Brady. From his frequent emails to all the interesting conversations we had in his office, where we would tackle and discuss all the problems presented in my thesis. I hope I can retain from him much of his abilities and strengths, and continue a strong friendship throughout my career in Academia.

I would also like to thank my committee — Julie Kornfield, Zhen-Gang Wang, Todd

I want to thank my family who instilled in me the values and skills I hold a strong belief for and practice to this day. It is because of you that I am where I am.

To God, because even when I questioned all of your mysteries, you never deserted me.

Abstract

Recent experiments showing reaction-driven propulsion at nanoscales have appeared as a possible mechanism for the transport of particles that may help us to not only understand chemo-mechanical transduction in biological systems, but also to create novel artificial motors that mimic living organisms and which can be harnessed to perform desired tasks. Reaction-driven propulsion consists of the generation of a localized potential gradient by an on-board surface chemical reaction. In this study, we propose and investigate a model for self-propulsion of a colloidal particle — the osmotic motor — immersed in a dispersion of "bath" particles. The non-equilibrium concentration of bath particles induced by a surface chemical reaction creates an osmotic pressure imbalance on the motor causing it to move. The departure of the bath particle concentration distribution from equilibrium is governed by the Damköhler number Da — the ratio of the speed of reaction to that of diffusion — which is employed to calculate the driving force on the motor, and from which the self-induced osmotic velocity is determined via application of Stokes drag law. To illustrate the significant physics in osmotic propulsion, a first-order surface reaction on a portion of the motor's surface is assumed, for the most part, in this work. The implications of these features for different bath particle concentrations and motor sizes are discussed. Furthermore, we investigate the role played by the distribution of reactions on the motor's surface. Different responses are expected depending on the amount of reactive surface in the limiting

behaviors of the reaction speed. Lastly, we consider a motor with constant production of particles on a hemisphere as a model that resembles actin-based motility of biological cells and organelles.

This research demonstrates that such an osmotic motor is possible and addresses such questions as: How fast can the motor move? How large of a force can it generate? What is the efficiency of such an osmotic motor? All motor behaviors discussed in this work are shown, after appropriate scaling, to be in good agreement with Brownian dynamics simulations.

Contents

List of Figures

xiv

Chapter 1

Introduction

1.1 Introduction

What is a machine? And why do we need them? The scientific definition of a "machine" is any device that transmits or modifies energy. In common usage, the meaning is restricted to devices that have rigid moving parts that perform, or assist in performing some work (see Concise Oxford Dictionary), although animals, including humans, and plants can also be considered machines; even though they are a product of evolution rather than of design. Machines usually require some energy source ("input"), and always achieve some sort of work ("output"). A machine has a design and it is constructed following some processes. It also uses power and it operates according to information built into it when it is fabricated. Some machines are even used to construct or to replicate other machines.

There is no doubt that machines are an integral part of our daily lives. For centuries we have conquered the "human-scale" world by fabricating large machines (e.g., cars, computers, house appliances, telephones) that have facilitated global communication, transportation, and scientific advances, just to name a few. However, in the past decades we have paid considerable attention to the endless possibilities that the nano and molecular world have to offer. On December 29, 1959, physicist Richard Feynman in his famous lecture "There's Plenty of Room at the Bottom" considered the possibility of direct manipulation of individual atoms as a more powerful form of synthetic chemistry than used at the time. Feynman suggested that it should be possible, in principle, to do chemical synthesis by mechanical manipulation, and he presented the possibility of building a tiny, swallowable surgical robot by developing a set of one-quarter-scale manipulator hands slaved to the operator's hands to build one-quarter scale machine tools analogous to those found in any machine shop. This set of small tools would then be used by the small hands to build and operate ten

sets of one-sixteenth-scale hands and tools, and so forth, culminating in perhaps a billion tiny factories to achieve massively parallel operations. As the sizes got smaller, they would have to redesign some tools because the relative strength of various forces would change. Gravity would become less important, while Brownian motion, surface tension, Van der Waals interactions, etc., would become more important. Feynman's lecture at that moment in history was partly responsible for the beginning of a collective dialogue that explored the potential of manipulating the molecular world.

Since then, scientists and engineers have sought nanotechnology as an alternative medium to solve many current problems in medicine (i.e., blood diseases, cancer, drug delivery), air and water pollution, sensors to detect molecules or particles, and to make devices smaller to conserve space, energy, materials, and money. But perhaps the most important challenge that nanotechnology faces is the creation of useful work by an object in a world dominated by randomness and uncertainty. Directed motion or propulsion is a difficult challenge that must be overcome in order to make many of these devices "come to life".

Nanoscale machines already exist in the form of functional molecular components in living cells — such as molecules of protein or ribonucleic acid, aggregates of molecules, and organelles — in enormous variety and sophistication. In fact, some cells include molecular machines that seem similar to familiar human-scale machines; for example, a rotary motor fixed in the membrane of a bacterium turns a shaft and superficially resembles an electric motor. Enzymes such as myosin, kinesin, dynein, and their relatives are linear motors, which convert the energy of adenosine triphosphate (ATP) hydrolysis into mechanical work along polymer substrates. Motion derives from a mechano-chemical cycle during which the motor protein binds to successive sites along the substrate in a manner used by the motor to move. Some of these molecular motor proteins and their application in biological processes

and nanotechnology have been studied by Vale and Milligan (2000) and Feringa (2007).

The remarkable solutions that nature has found to control molecular motion has served as an inspiration for researchers to conceptualize, design, and build entirely molecular machines — an assembly of a distinct number of molecular components that are designed to perform machinelike movements as a result of an appropriate external stimulation (Browne and Feringa 2007). These molecular machines can be operated using photons or electrons supplied by photochemically and electrochemically driven reactions that are commonly found in biological cells and can be easily mimicked artificially. Recent efforts in both molecular biology and nanofabrication technology established the potential for building functional nanoelectromechanical systems that are powered by biological motors and chemical energy sources (Montemagno and Bachand 1999). Li and Tan (2002) proposed a single deoxyribonucleic acid (DNA) molecular nanomotor. Vicario et al. (2006) designed a synthetic, light-driven molecular motor that is embedded in a liquid-crystal film that exceeds the size of the motor molecule by a factor of 10,000. The changes in the shape of the motor during the rotary steps cause a rotational reorganization of the liquid-crystal film and its surface relief, which ultimately causes the rotation of microscale particles on the film. Morin et al. (2006) described the synthesis of a nanocar that bears a light-powered molecular motor in its central portion for an eventual paddlewheel-like propulsion action along a substrate surface for motion of the vehicles. Numerous other molecular machines have been proposed, however, major challenges in their development remain, such as directional movement along specified trajectories.

Microfabrication has developed as an extraordinarily successful technology for manufacturing small, electronically functional devices. The development of these so-called micro-electromechanical systems (MEMS) is proceeding rapidly, but the functions of the machines

are still elementary (Hassan 2006; Ko 2007). Many interesting problems and technical challenges are common in the fabrication of nanodevices with moving parts (Jeng et al. 2007). A crucial one is friction and sticking. Small devices have large ratios of surface to volume and surface effects, such as electrostatics and wetting, which become much more important for them than for large devices. This critical fact could potentially hinder the fabrication of MEMS to operate under realistic environments where surface interactions could damage the structure and function of these devices.

Perhaps the greatest promise for nanotechnology lies in the potential of biotechnological advances (Mulhall 2002). At present, biotechnology refers to the use of living organisms or nature-inspired devices to modify human health and the human environment. However, its definition has been stretched to address other fields such as agriculture and waste treatment. Prospective nano-level manipulation of DNA offers the opportunity to radically expand the horizons of genomic medicine and immunology. Tissue-based biosensors may unobtrusively be able to monitor and regulate site-specific medicine delivery or regulate physiological processes (Edelberg et al. 2002). Nanosystems might serve as highly sensitive detectors of toxic substances or be used by inspectors to detect traces of biological or chemical weapons (Sanders et al. 2001). In a similar way, many challenges in the implementation and operation of biotechnological devices continue to be unanswered, specifically the inevitable question of how to operate these devices without its dependence on external inputs.

Can autonomous, self-controlled, self-replicated, and multi-tasking nanomotors be created? There are numerous limitations for small-scale objects to overcome. At this length scale, Brownian forces usually dominate over other forces (e.g. gravity, interparticle forces) and inertial terms are relatively unimportant (low Reynolds number). Thus, any effort to steer a purposeful course would be hindered by the relentless collisions of surrounding

molecules. Navigators at the nanoscale would have to self-regulate constantly to correct a path deviated by erratic motions or circumstances. This is a fundamental problem that makes sophisticated tasks that require the detection of specific targets complicated. An interesting feature at low Reynolds number is that whatever these objects are doing at the moment is entirely determined by the forces that are exerted on the object at that moment, and not by any previous forces (time independent). Swimming for a device at this scale could be achieved by deforming its body. For propulsion, the device must break any symmetric motions in order to take advantage of its surrounding environment. If the environment is constantly evolving, the device must be able to change its mechanism for motion.

By today's standards, expensive and large external equipment is required to operate nanodevices. Imagine a nanomotor injected into your body fighting cancer cells, and its operation depends on another machine that is of the size of a room! This illustration is not far from reality, which makes it impossible, in some conditions, to achieve all-in-one devices that could operate in multitasking environments autonomously and at high efficiency. Another issue is the source of energy for these devices. How is the energy to be supplied to nanomachines? And, by which method? One important advantage of nanomachines is that the individual units require only a tiny amount of energy to operate. In spite of all these limitations, some progress has been made in the last few years. New and creative ideas from multiple research groups, some of which are addressed below, have surfaced to overcome these issues in order to move towards the goal of creating autonomous nanodevices.

Self-movement can be found in many systems and in different physical conditions. Studies of autonomous motors under isothermal conditions may help us to not only understand

chemomechanical transduction in biological systems, but also to create novel artificial motors that mimic living organisms. Scientists and engineers have paid attention to the latest advances in biology to understand, fundamentally, what drives microorganisms and other biological machines. Genetic engineering is already processing down this path. All motor organs or organelles in living systems work through the dissipation of chemical energy under almost isothermal and nonequilibrium conditions. It is hard for nanoscience to compete with the flagella biological motor in bacteria like *Escherichia coli* — an assembly of proteins embedded in cell membranes that decompose ATP for energy, and, through whip-like rotary motion, provide motility to bacteria in a liquid. A flagellum is a propulsive organelle that includes a reversible rotary motor embedded in the cell wall and a filament that extends into the external medium. These microorganisms could potentially be used to power microfluidic devices. A new type of propulsion inspired by the motility mechanism of bacteria with peritrichous flagellation, such as *Escherichia coli*, *Salmonella typhimurium*, and *Serratia marcescens* was constructed by Behkam and Sitti (2007). The flagella of these bacteria are randomly distributed over the cell surface and each flagellar motor rotates independently of the others. Hydrodynamic interactions among flagella cause them to coalesce and bundle behind the cell during swimming. The work by Behkam and Sitti (2007) intends to exploit the potential of flagellar motion for microrobot propulsion.

The design and construction of nanoengines that convert stored chemical energy into motion has become an important discovery by nanotechnology, especially those that can operate autonomously (Ozin et al. 2005). Although biomolecular motors (Soong et al. 2000) and phoretic mechanisms (Anderson 1989) have been the focus of research as a means for powering nanodevices, many of the proposed techniques and theoretical models rely on external forcing or signaling, which adds complexity, not to mention the macro-scale

size required for some driving mechanisms. In simple terms, phoretic transport describes the motion of a particle when an external field (e.g., concentration, temperature, electromagnetic) is applied. The resultant particle velocity is proportional to the field gradient. Consider a colloidal particle placed in a solution in which the concentration of some solute is not uniform. The particle may spontaneously migrate towards regions of higher or lower concentrations as a result of physical interactions between the solute molecules and the surface of the particle (Anderson 1989). Derjaguin et al. (1993) and Dukhin and Derjaguin (1974) first called this transport diffusiophoresis; a mechanism that has been applied for the formation of surface coatings (Dukhin et al. 1982). The actual action that induces motion occurs in an interfacial region separating the particle and the fluid. The dynamics of interfacial layers are related to the length scale in consideration and the state of matter in each of the phases. It can be shown that the velocity and stresses are continuous on the length scale of the thickness of the interfacial region, but appear discontinuous on the scale of the size of the particle. Similar phenomena occurs at fluid/fluid interfaces where now a flow is induced by surface tension gradients — the so-called Marangoni effect (Velarde et al. 2003). Evidently, a gradient such as concentration and surface tension is sufficient for particle motion. While external fields have been used to sort and separate particles based on their response, this type of transport does not afford the flexibility of moving objects autonomously.

Autonomous motion not only occurs in nature, but also in man-made settings at different scales and by different mechanisms. Schmid et al. (2000) observed that shortly after deposition of Sn in Cu (111), two-dimensional crystal islands proceed to move spontaneously along the surface in a systematic fashion. Self-propulsion of camphor crystals placed on an air/water interface occurs by the preferential dissolution of camphor from one side of the

crystal; dissolution creates a surface tension gradient which induces crystal island motion (Nakata et al. 2002). Ismagilov et al. (2002) described the behavior of small hemicylindrical plates with a small area of platinum on one surface that floats at the interface of an aqueous solution of hydrogen peroxide. These plates move under the impulse of bubbles generated by the platinum-catalyzed decomposition of hydrogen peroxide. Liquid pumping by chemically tunable nanoscopic propellers designed with molecular-scale blades was realized by molecular dynamics simulations, demonstrating a novel method for the selective pumping of hydrophobic and hydrophilic liquids, an important application for the potential design and assembly of molecular pumps and motile devices (Wang and Kral 2007). Effective designs of small scale swimming robots have come from a variety of sources. One of the first swimming microrobots was introduced by Fukuda et al. (1994). This microrobot has a pair of fins with undulatory motion. Another propulsion method, theorized by Sendoh et al. (1999), uses an external magnetic field to rotate a small screw in liquid, attractive for medical surgery and catheter purposes.

The idea that anisotropic forces can be created on a small object by an on-board chemical motor that recognizes the use of thermal fluctuations and changes in chemical equilibrium increases the possibility of discovering whole new classes of entirely synthetic nanomachines. Recently, Paxton et al. (2004) and Howse et al. (2007) demonstrated that it is possible to power the motion of nanoscale objects by using surface catalytic reactions — so-called catalytic nanomotors. In the Paxton et al. (2004) experiments, a nanorod with one end made of platinum and the other end of gold was immersed in a hydrogen peroxide solution and autonomous motion was observed. In an independent work, Howse et al. (2007) constructed a polystyrene microsphere with one side coated with platinum. Similarly, autonomous motion was observed when the microsphere was placed into a hydrogen peroxide solution. A

number of mechanisms have been suggested for nanomotor propulsion (Paxton et al. 2006; Howse et al. 2007), including: bubble propulsion (as observed in Ismagilov et al. (2002) experiments), diffusiophoresis, electrophoresis, surface-tension gradients, etc., all of which rely on the establishment of a gradient to provide the driving force for motion. Although both researchers (Paxton et al. 2004; Howse et al. 2007) have stated that their mechanisms for propulsion, if compared, are different, this clearly shows that the potential and diversity of reaction-driven motility remains unexplored.

Creation of such a gradient requires an on-board power source — chemical energy. But, How exactly does a local chemical reaction generate motion? Or, what is the simplest motor one can envision? What mechanism would it use for propulsion? How fast could it move? How large of a force could it generate? Golestanian et al. (2005) proposed a simple model for the reaction-driven propulsion of a small device based on an asymmetric distribution of reaction products and motivated by the experiments of the catalytic nanorod. Their propulsion mechanism is based on the thin-interfacial limit expressions for phoretic motion (Anderson 1989). Another model for autonomous propulsion was proposed by Ruckner and Kapral (2007) for the self-propelled motion of a chemically powered nanodimer comprised of two linked spheres, one of which has equal interactions with A and B solvent species but catalyzes the reaction $A \rightarrow B$. The other sphere is not chemically active but interacts differently with the two species. The nonuniform solvent interactions with the nanodimer causes an asymmetric distribution of solvent species that the nanodimer utilizes for propulsion. Both the motor and the solvent were described at the particle level using hybrid mesoscopic-molecular dynamics scheme. These two models do not cover some of the questions raised above which are important issues for the motor's behavior. However, this suggests that a fundamental or unifying description to what is observed experimentally is

needed.

In this thesis we propose a very simple mechanism: osmotic propulsion. It is well known that when a semi-permeable membrane separates a fluid that contains colloidal particles, a fluid flow is produced from the side of low particle concentration to the side of high particle concentration. The flow may be stopped, or even reversed, by applying external pressure on the side of higher concentration. The pressure that stops the flow is called the osmotic pressure. Particle movement is determined by fluctuations of thermal collisions with nearby fluid molecules. Whenever a wall blocks a particle's motion, it will transfer momentum to it and, therefore, generate a pressure on it. If we now stop holding the membrane, the osmotic pressure difference between the two sides of the system will push the membrane until thermodynamic equilibrium is reached. Therefore, the process of collisions with a moving wall is a mechanism by which the microscopic kinetic energy of the (Brownian) particles is transformed into macroscopic mechanical work. Experimentally, Nardi et al. (1999) demonstrated that osmotic permeation of solvent across a spherical semipermeable membrane in a concentration gradient can lead to a pumping action: solvent is pumped from the low to the high concentration side of the sphere. Autonomous motion can be achieved by a chemical reaction at a particle's surface generating a local imbalance in the osmotic pressure of the surrounding medium.

As shown in the experiments of Paxton et al. (2004) and Howse et al. (2007), the possibility of extracting mechanical work from Brownian motion using surface chemical reactions delivers a new propulsion mechanism for colloidal particles suspended in a continuous phase. Colloidal particles tend to move freely and randomly, but if the structure in the vicinity of the particle is disturbed, for example, as a result of a surface chemical reaction, some average directional movement can be obtained, which is often needed for nanotechnological

devices in operations that require net displacement. Similar osmotic motion occurs in the problem of multicomponent diffusion (Batchelor 1983), where a gradient in concentration of one species can drive the flux of another. Batchelor showed that in a multicomponent suspension of colloidal particles accompanied by spatial gradients of concentration as a consequence of Brownian motion (thermal fluctuations), the mean flux down a small concentration gradient due to diffusion is identical, as if each of the particles is acted on by a steady applied force (thermodynamic force) that represents a departure from an isotropic equilibrium state. Similarly, depletion flocculation occurs when small particles (e.g., polymers, salts) are excluded from a zone separating two nearly touching colloidal particles and the imbalanced osmotic pressure of the small particles causes an entropic attractive force (Asakura and Oosawa 1954). But now consider a concentration distribution of colloidal particles that is created locally by a surface chemical reaction on another particle. The resulting imbalanced osmotic force will induce autonomous motion — an osmotic motor. This is a simple means by which random entropic motion can be harnessed by a surface chemical reaction to create directed motion.

The author's work presented in this thesis has focused on developing theoretical models for osmotic propulsion by studying possibly the simplest scenario: a suspension of hard-spheres consisting of an osmotic motor particle of radius a creating local asymmetric concentration disturbances to a surrounding dispersion of "bath" particles of radii b via a nonuniform surface chemical reaction. In this work we describe a simple model for self-propulsion that takes into consideration the on-board properties of the motor and its ability to harness the surrounding medium to create a net driving force. This device, or motor, illustrates in simple terms the conversion of chemical/free energy into useful work. Our mechanism shares the idea of concentration gradient driving the motion but appears to be different

from, and it is not restricted to a thin-interfacial limit, as in the work by Golestanian et al. (2005).

The rest of the thesis is organized as follows. In Chapter 2 (published previously, Córdova-Figueroa and Brady 2008) we present a simple model for self-propulsion of a colloidal particle — the osmotic motor — immersed in a dispersion of "bath" particles. The non-equilibrium concentration of bath particles induced by a surface chemical reaction creates an osmotic pressure imbalance on the motor causing it to move. We explicitly consider the mass balance associated with the chemical reaction at the motor surface by having reactants, R, go to products, P, via $R \rightarrow sP$, where "s" is the stoichiometry of the reaction. The ratio of the speed of reaction to that of diffusion governs the bath particle distribution, which is employed to calculate the driving force on the motor, and from which the self-induced osmotic velocity is determined. We show that what determines the magnitude and sign of the osmotic force is the combination $(1 - sD_R/D_P)$, where D_R and D_P are the diffusivities of the reactants and products, respectively. For slow reactions, the self-propulsion is proportional to the reaction velocity. When surface reaction dominates over diffusion the osmotic velocity cannot exceed the diffusive speed of the bath particles. Implications of these features for different bath particle volume fractions and motor sizes are discussed. Theoretical predictions are compared with Brownian dynamics simulations based on the algorithms presented by Foss and Brady (2000) for sheared colloidal dispersions and by Carpen and Brady (2005) for active particle-tracking microrheology.

In Chapter 3 we give a formal statistical mechanical model for self-propulsion of the osmotic motor. The pair-level Smoluchoswki equation for the distribution of bath particles surrounding the osmotic motor subject to a nonuniform first-order surface chemical reaction on half motor is derived in the absence of hydrodynamic interactions and rotary Brownian

motion. From this, we solve for the pair-distribution function $g(\boldsymbol{r})$ — the probability of finding a bath particle relative to the osmotic motor. The departure of the bath particle concentration distribution from equilibrium is governed by the Damköhler number Da: the ratio of the speed of reaction to that of diffusion. We describe two possible scenarios for the osmotic motor: One, in which the motor is held fixed by an external force (e.g., optical tweezers) and a second case where the motor is free to translate. The computed microstructure about the motor is employed to calculate the net driving force on the motor, from which the self-induced "osmotic" velocity is determined via application of Stokes drag law. The motor velocity has to be found self-consistenly as it influences the concentration distribution and thus the driving force. No mention of such a self-regulation has appeared in prior work. The ratio of the motor velocity U to that of diffusion, $D/(a + b)$, is known as the Péclet number Pe, which is a function of the Damköhler number, the product $\beta = \phi_b(1+a/b)^2$ (ϕ_b is the bath particle volume fraction and a/b is the size ratio of motor to bath particle), and the bath particle concentration gradient generated at contact. The product β corresponds to the number of bath particles within a bath particle radius of the motor surface. Increasing Da drives the suspension away from equilibrium, and thus generates a gradient in bath particle concentration, which is utilized by the motor. For small Da, when Brownian motion dominates over reaction, the motor velocity is proportional to the speed of reaction and becomes independent of the bath particle concentration and the particle's size in the limit of high β. For finite Da but high β, the motor velocity saturates, resulting in $U \sim D/(a + b)$ — the relative diffusive speed. In the limit of high Da and β, when reaction and advection dominate over diffusion, it is observed that the gradient in bath particle concentration driving propulsion decays to zero as the motor velocity increases. As a consequence, the motor velocity diverges and becomes dependent of bath particle

concentration and size ratio in this limit. The behavior of the motor for arbitrary bath particle volume fractions and motor sizes are discussed.

In addition to the theory, we performed a Brownian dynamics simulation (Foss and Brady 2000; Carpen and Brady 2005), which allows us to test the theoretical framework and understand at a particle-level description the mechanism of osmotic propulsion. The surface reaction is emulated by using a reaction probability P_s defined as the probability in which a bath particle that collides with the reactive surface has reacted. By analogy with previous work on microrheology, we propose methods to scale up the theory to account for more concentrated suspensions. Finally, a simple formula for the energy conversion efficiency from free chemical energy to mechanical work is derived.

In Chapter 4 we extend and examine our theoretical framework for propulsion of the osmotic motor immersed in a dispersion of bath particles to other distributions of reactive sites (in Chapter 3 all calculations were performed solely to half-reactive motors). In this work, hydrodynamic interactions between particles and rotary Brownian diffusion are also neglected. Also, we assume that bath particles only interact with the motor thus behaving as an ideal gas. These assumptions enable us to have a simple model system to allow a clear analysis towards the understanding of many features unique to osmotic motors with different distributions of reactive sites. This also permits an easy introduction to optimizing self-propulsion. Our main goals are to understand the behavior of the motor for other reaction distributions and to provide a guide for optimizing the design of osmotic motors, which could be broadened to other types of transport mechanisms. We consider the size of the reactive site at the motor's surface to be determined by the polar angle θ_s — the angle that locates the transition from reactive to passive surface and is measured from the front of the motor. The distribution of bath particles relative to the osmotic motor is employed to

calculate the osmotic force on the motor, from which the motor velocity is determined via application of Stokes drag law. The motor behavior is controlled by the Damköhler number Da, the product β, and the angle θ_s. Once again we consider two possible scenarios for the motor: one consisting of a motor held fixed and another one where the motor is free to diffuse. We investigate the net osmotic force created by the fixed motor and its dependence on the angle θ_s. We compute the optimal angle θ_s necessary to obtain maximum osmotic force as a function of the Damköhler number. For the free motor scenario, the velocity of the motor for various θ_s and its implications for different bath particle concentrations and motor sizes are discussed. The behavior of the free motor is maximized by finding the optimal angle θ_s needed to create maximum velocity according to the Damköhler number and the properties of the suspension. Our theoretical results are compared to Brownian dynamics simulations based on the method described in Chapter 3 and modified to consider other distributions of reaction.

In Chapter 5 we propose a model for self-propulsion of an osmotic motor creating a constant flux of product particles j_0 on a hemisphere. The net driving force is investigated in the limits of slow and fast product particle flux (relative to the diffusive flux of bath particles) for different bath particle concentrations and motor to bath particle size ratios. In addition, we develop a Brownian dynamics simulation (Foss and Brady 2000; Carpen and Brady 2005) that emulates the creation of particles at the motor's surface applying a simple algorithm that considers stochastic variations to the constant flux via a Poisson distribution as the simulation time progresses. A relationship between the particle level interpretation of the flux and the macroscopic quantity that is the Damköhler number was derived enabling us to compare the simulation results with the theory. We also propose ideas for a problem that consists of a reversible reaction on a portion of the motor. This

type of reaction unifies the recent work done considering a first-order surface reaction and the constant flux proposed in Chapter 5.

Finally, Chapter 6 offers some general conclusions and directions for future research.

Before continuing, the author wishes to make one point. The chapters that follow were written as individual papers and are thus entirely self-contained. The reader may, therefore, read them in whichever order desired. Neverthless, note that there is a certain amount of repetition in the introductory sections and in the theoretical framework of each chapter.

1.2 Bibliography

J. L. Anderson. Colloid transport by interfacial forces. *Annu. Rev. Fluid Mech.*, 21:61–99, 1989.

S. Asakura and F. Oosawa. On interaction between two bodies immersed in a solution of macromolecules. *J. Chem. Phys.*, 22(7):1255–1256, 1954.

G. K. Batchelor. Diffusion in a dilute polydisperse system of interaction spheres. *J. Fluid Mech.*, 131:155–175, 1983.

B. Behkam and M. Sitti. Bacterial flagella-based propulsion and on/off motion control of microscale objects. *Appl. Phys. Lett.*, 90(2), 2007.

W. R. Behkam and B. L. Sitti. Making molecular machines work. *Nature Nanotech.*, 1: 25–35, 2006.

I. C. Carpen and J. F. Brady. Microrheology of colloidal dispersions by Brownian dynamics simulations. *J. Rheol.*, 49(6):1483–1502, 2005.

U. M. Córdova-Figueroa and J. F. Brady. Osmotic Propulsion: The Osmotic Motor. *Phys. Rev. Lett.*, 100(15):158303–158307, 2008.

B. V. Derjaguin, S. S. Dukhin, and A. A. Korotkova. Diffusiophoresis in electrolyte-solutions and its role in the mechanism of the formation of films caoutchouc latexes by the ionic deposition method. *Prog. Surf. Sci.*, 43(1–4):153–158, 1993.

S. S. Dukhin and B. V. Derjaguin. *Electrokinetic Phenomena.* J. Willey and Sons, 1974.

S. S. Dukhin, Z. R. Ulberg, G. L. Dvornichenko, and B. V. Derjaguin. Diffusiophoresis in

electrolyte solutions and its application to the formation of surface coatings. *Russ. Chem. Bull.*, 31(8):1535–1544, 1982.

J. M. Edelberg, J. T. Jacobson, D. S. Gidseg, L. L. Tang, and D. J. Christini. Enhanced myocyte-based biosensing of the blood-borne signals regulating chronotropy. *J. Appl. Physiol.*, 92(2):581–585, 2002.

B. L. Feringa. The art of building small: From molecular switches to molecular motors. *J. Org. Chem.*, 72(18):6635–6652, 2007.

D. R. Foss and J. F. Brady. Brownian Dynamics simulation of hard-sphere colloidal dispersions. *J. Rheol.*, 44(3):629–651, 2000.

T. Fukuda, A. Kawamoto, F. Arai, and H. Matsuura. Mechanism and swimming experiment of micro mobile robot in water. *Proc. IEEE Robotics and Automation Conf.*, 814–819, 1994.

R. Golestanian, T. B. Liverpool, and A. Ajdari. Propulsion of a molecular machine by asymmetric distribution of reaction products. *Phys. Rev. Lett.*, 94(22), 2005.

I. Hassan. Thermal-fluid MEMS devices: A decade of progress and challenges ahead. *J. Heat Trans-T. ASME*, 128(11):1221–1233, 2006.

J. R. Howse, R. A. L. Jones, A. J. Ryan, T. Gough, R. Vafabakhsh, and R. Golestanian. Self-motile colloidal particles: From directed propulsion to random walk. *Phys. Rev. Lett.*, 99(4), 2007.

R. F. Ismagilov, A. Schwartz, N. Bowden, and G. M. Whitesides. Autonomous movement and self-assembly. *Angew. Chem. Int. Ed.*, 41(4):652, 2002.

Shuen-Lin Jeng, Jye-Chyi Lu, and Kaibo Wang. A review of reliability research on nan-
   otechnology. *IEEE T. Reliab.*, 56(3):401–410, 2007.

W. H. Ko. Trends and frontiers of MEMS. *Sens. Actuators, A*, 136(1):62–67, 2007.

J. W. J. Li and W. H. Tan. A single DNA molecule nanomotor. *Nano Lett.*, 2(4):315–318,
   2002.

C. Montemagno and G. Bachand. Constructing nanomechanical devices powered by
   biomolecular motors. *Nanotechnology*, 10(3):225–231, 1999.

J. F. Morin, Y. Shirai, and J. M. Tour. En route to a motorized nanocar. *Org. Lett*, 8(8):
   1713–1716, 2006.

D. Mulhall. *Our Molecular Future: How Nanotechnology, Robotics, Genetics, and Artificial
   Intelligence Will Change Our World.* Prometheus Books, 2002.

S. Nakata, Y. Doi, and Y. Hayashima. Intermittent motion of a camphene disk at the center
   of a cell. *J. Phys. Chem. B.*, 106(44):11681–11684, 2002.

J Nardi, R Bruinsma, and E Sackman. Vesicles as osmotic motors. *Phys. Rev. Lett.*, 82
   (25):5168–5171, 1999.

G. A. Ozin, I. Manners, S. Fournier-Bidoz, and A. Arsenault. Dream nanomachines. *Adv.
   Mater.*, 17(24):3011–3018, 2005.

W. F. Paxton, S. Sundararajan, T. E. Mallouk, and A. Sen. Chemical locomotion. *Angew.
   Chem. Int. Ed.*, 45(33):5420–5429, 2006.

W. F. Paxton, K. C. Kistler, C. C. Olmeda, A. Sen, S. K. St. Angelo, Y. Y. Cao, T.

E. Mallouk, P. E. Lammert, and V. H. Crespi. Catalytic nanomotors: Autonomous movement of striped nanorods. *J. Am. Chem. Soc.*, 126(41):13424–13431, 2004.

G. Ruckner and R. Kapral. Chemically powered nanodimers. *Phys. Rev. Lett.*, 98(15), 2007.

C. A. Sanders, M. Rodriguez, and E. Greenbaum. Stand-off tissue-based biosensors for the detection of chemical warfare agents using photosynthetic fluorescence induction. *Biosens. Bioelectron.*, 16(7-8):439–446, 2001.

A. K. Schmid, N. C. Bartelt, and R. Q. Hwang. Alloying at surfaces by the migration of reactive two-dimensional islands. *Science*, 290(5496):1561–1564, 2000.

M. Sendoh, N. Ajiro, K. Ishiyama, M. Inoue, K. I. Arai, T. Hayase, and J. Akedo. Effect of machine shape on swimming properties of the spiral-type magnetic micro-machine. *IEEE Trans. Magn.*, 35(5, Part 2):3688–3690, 1999.

R. K. Soong, G. D. Bachand, H. P. Neves, A. G. Olkhovets, H. G. Craighead, and C. D. Montemagno. Powering an inorganic nanodevice with a biomolecular motor. *Science*, 290(5496):1555–1558, 2000.

R. D. Vale and R. A. Milligan. The way things move: Looking under the hood of molecular motor proteins. *Science*, 288(5463):88–95, 2000.

M. G. Velarde and R. K. Zeytourian. *Interfacial Phenomena and the Marangoni Effect.* Springer, 2003.

J. Vicario, M. Walko, A. Meetsma, and B. L. Feringa. Fine tuning of the rotary motion by structural modification in light-driven unidirectional molecular motors. *J. Amer. Chem. Soc.*, 128(15):5127–5135, 2006.

B. Wang and P. Kral. Chemically tunable nanoscale propellers of liquids. *Phys. Rev. Lett.*, 98(26), 2007.

Chapter 2

Simple model of osmotic propulsion

2.1 Abstract

A model for self-propulsion of a colloidal particle — the osmotic motor — immersed in a dispersion of "bath" particles is presented. The non-equilibrium concentration of bath particles induced by a surface chemical reaction creates an osmotic pressure imbalance on the motor causing it to move to regions of lower concentration. The ratio of the speed of reaction to that of diffusion governs the bath particle distribution which is employed to calculate the driving force on the motor, and from which the self-induced osmotic velocity is determined. For slow reactions, the self-propulsion is proportional to the reaction velocity. When surface reaction dominates over diffusion the osmotic velocity cannot exceed the diffusive speed of the bath particles. Implications of these features for different bath particle volume fractions and motor sizes are discussed. Theoretical predictions are compared with Brownian dynamics simulations.

2.2 Osmotic propulsion: the osmotic motor

The design of nanoengines that convert stored chemical energy into motion is a key challenge of nanotechnology, especially for engines that can operate autonomously (Ozin et al. 2005). Although biomolecular motors (Soong et al. 2000) and phoretic mechanisms (Anderson 1989) have been the focus of intense research as a means for powering nanodevices, many of the proposed techniques rely on external forcing or signaling, which adds complexity, not to mention the macro-scale size required for some driving mechanisms. Recently, Paxton et al. (2004) demonstrated that it is possible to power the motion of nanoscale objects by using surface catalytic reactions — so-called catalytic nanomotors.

A number of mechanisms have been suggested for nanomotor propulsion (Paxton et al.

2006; Howse et al. 2007), including: bubble propulsion, diffusiophoresis, electrophoresis, surface-tension gradients, etc., all of which rely on the establishment of a gradient to provide the driving force for motion. Creation of such a gradient requires an on-board power source — chemical energy. But exactly how does a local chemical reaction generate motion? Or asked differently, what is the simplest motor one can envision? What mechanism would it use for propulsion? How fast can it move? How large of a force can it generate?

Here we propose a very simple mechanism: osmotic propulsion. When a semipermeable membrane separates a fluid containing colloidal particles, a flow is induced from the low to the high particle concentration side. The pressure that stops the flow is the osmotic pressure. If the membrane is released, the osmotic pressure difference between the two sides will cause it to move until equilibrium is established. In this way the microscopic kinetic energy of the (Brownian) particles is transformed into macroscopic mechanical motion and work.

But one does not need a membrane. A colloidal particle in solution moves randomly, but if the distribution of other colloidal particles in its vicinity is perturbed, some average directional movement can be obtained. Such is the case in multicomponent diffusion where a gradient in concentration of one species drives the flux of another (Bird et al. 1960; Batchelor 1983). Similarly, depletion flocculation occurs when small particles (e.g., polymers) are excluded from a zone separating two nearly touching colloidal particles and the imbalanced osmotic pressure of the small particles causes an entropic attractive force (Asakura and Oosawa 1954). Consider now a nonuniform concentration distribution of colloidal particles created locally by a surface chemical reaction on another (larger) particle. The resulting imbalanced osmotic force will induce autonomous motion — an osmotic motor. This is a simple means by which random entropic motion can be harnessed by a chemical reaction

to create directed motion. Just how large a force can be generated and how fast an object can move is the subject of this chapter.

Consider a single spherical motor particle of size a immersed in a fluid and surrounded by a sea of spherical "bath" particles of size b. Both the motor and bath particles are large compared to the solvent molecules so that their behavior can be described by the equations of colloidal dynamics (Russel et al. 1989). The suspension of bath particles generates an osmotic pressure $\Pi = n_b kT$, where kT is the thermal energy and n_b is the number density of bath particles. (For simplicity, the bath particles are modeled as an ideal gas.) The bath particles exert an entropic or osmotic force on the motor, which is the integral of the osmotic pressure over the surface of the motor: $\boldsymbol{F}^{osm} = -kT \int \boldsymbol{n} \, n_b(\boldsymbol{x}) dS$, where $\boldsymbol{n}$ is the outer normal to the surface located at the sum of the radii of the motor and the bath particles.

At equilibrium the bath particle concentration is uniform and the net osmotic force is zero. However, if there is a nonuniform concentration of bath particles, either caused by an externally imposed concentration gradient or by the motor itself via a chemical reaction on its surface, there will be a net osmotic force on the motor. This force must be balanced by an externally imposed force (via, eg., optical tweezers) to hold the motor fixed, or by the hydrodynamic Stokes drag force from the solvent $\boldsymbol{F}^{hyd} = -6\pi\eta a \boldsymbol{U}$, where η is the viscosity of the solvent and $\boldsymbol{U}$ is the motor velocity. (A formal statistical mechanical derivation is discussed in Chapter 3 which follows the work on single particle motion in colloidal dispersions and microrheology (Squires and Brady 2005; Khair and Brady 2006)) An externally imposed concentration gradient gives rise to diffusiophoresis (Anderson 1989), whereas a surface chemical reaction alters the local concentration of bath particles and results in *autonomous* motion — namely, the osmotic motor.

Reaction-driven propulsion was discussed recently by Golestanian et al. (2005) and Howse et al. (2007). Their propulsive mechanism is based on the thin-interfacial-limit expressions for phoretic motion (Anderson 1989). Our mechanism shares the idea of a concentration gradient driving the motion but appears to be different, and is not restricted to a thin-interfacial limit, e.g., not limited to large motors. Furthermore, these authors did not discuss the conservation of mass (or volume) associated with the chemical reaction, nor did they identify the maximum velocity obtainable by a motor, two issues that are important for the motor's behavior.

To compute the osmotic force, the concentration distribution of bath particles about the motor is needed. The bath particles are divided into reactants, labeled R, and products P. On the reactive portion of the motor surface: $R \rightarrow sP$, where for each reactant particle "s" product particles are produced; s can take any value greater than or equal to zero. Conservation of mass requires that $m_R = s\, m_P$, where m_R is the mass of the reactant particle and m_P that of the products. For spherical particles of the same density conservation of mass is equivalent to conservation of volume and therefore $b_R = s^{1/3} b_P$, where b_R and b_P are the radii of the reactants and products, respectively. The rate of consumption of R on the reactive surface is r_R, and the production of P is $r_P = -sr_R$.

We first consider a fixed motor. Since the reaction only takes place at the motor surface, the reactants and products diffuse in the surrounding fluid with translational diffusivities D_R and D_P, respectively, and their concentrations satisfy Laplace's equation. For the reactant: $\nabla^2 n_R = 0$, subject to the imposed concentration far from the motor, n_R^∞, and the flux to the motor is balanced by the reaction on the motor surface: $\boldsymbol{n} \cdot \nabla n_R = r_R(a + b_R)/D_R$. All lengths have been nondimensionalized by the sum of the motor and reactant radii: $a + b_R$. The products satisfy a similar equation with the subscript R replaced by

P. However, the osmotic force is proportional to the *total* concentration of bath particles $n_b = n_R + n_P$, which satisfies $\nabla^2 n_b = 0$, subject to $n_b^\infty = n_R^\infty + n_P^\infty$, and at the motor surface $\boldsymbol{n} \cdot \nabla n_b = r_R(a + b_R)/D_R \times (1 - sD_R/D_P)$. Defining the scaled concentration differences: $\bar{n}'_R = (n_R - n_R^\infty)/n_R^\infty$ and $\bar{n}'_b = (n_b - n_b^\infty)/n_R^\infty(1 - sD_R/D_P)$ it is easy to see that $\bar{n}'_R$ and $\bar{n}'_b$ satisfy the same Laplace equation and boundary conditions. Thus, only the reactant concentration profile is needed to completely solve the problem for all stoichiometries and diffusivity ratios. The osmotic force is

$$\boldsymbol{F}^{osm} = -n_R^\infty kT(a + b_R)^2 \left(1 - s\frac{D_R}{D_P}\right) \int_{r=1} \boldsymbol{n} \; \bar{n}'_b(\boldsymbol{x})d\Omega, \qquad (2.1)$$

where $d\Omega = dS/(a + b_R)^2$ is the solid angle[1].

The stoichiometry/diffusivity factor, $(1 - sD_R/D_P)$, tells how many products are produced per reactant, s, and how fast the products diffusive relative to the reactants, D_R/D_P. And it is this combination that governs the behavior. If we had simply $R \to P$ (or $s = 1$) and the product had the same diffusivity as the reactant, the net osmotic force would be identically zero, as it must be. However, if the reactants and products have different diffusivities, say because the reaction changes the "shape" of the particle, or perhaps its interactions with the solvent (hydrophilic/hydrophobic), then even if only one product is produced for each reactant there will still be a net osmotic force on the motor. The *sign* of the force will depend on which diffuses faster. And similar arguments apply for $s \neq 1$.

As a first analysis consider a first-order reaction with rate constant κ (units of velocity), i.e., $r_R = \kappa n_R$. The reactant concentration profile is governed by the ratio of the speed of reaction to that of diffusion — the Damköhler number $Da = \kappa(a + b)/D$. We have dropped

---

[1]Technically, for spherical reactants and products of different radii, the integral should be over the "contact" surfaces at $a + b_R$ and at $a + b_P$. However, this introduces a negligible error, especially in the large motor limit $a \gg b_{R,P}$.

the subscript R for the reactant and will simply refer to the reactant as a bath particle. The boundary condition at the motor surface now becomes: $\boldsymbol{n} \cdot \nabla \bar{n}' = Da(\bar{n}' + 1)h(\boldsymbol{n})$. The distribution of reaction on the surface is determined by the dimensionless function $h(\boldsymbol{n})$, which we take to be 1 on the reactive half and 0 on the passive half. Since the detailed stoichiometry/diffusivity appears as a scale factor in the net osmotic force (2.1), we discuss below the case when $sD_R/D_P \to 0$, which would occur if the products are much more diffusive than the reactants or when the reactant is consumed ($s = 0$) by the motor[2].

   The concentration distribution of bath particles can be found analytically by separation of variables, and Figure 2.1 shows the nondimensional osmotic force (expressed as a Stokes velocity) as a function of Da. The open symbols in the figure are the results of conventional hard-sphere Brownian dynamics (BD) simulations (Foss and Brady 2000; Carpen and Brady 2005), modified to allow for surface reaction. As the theory predicts, the scaled osmotic force is independent of the size ratio of motor to bath particles, a/b, the bulk concentration of the bath particles expressed as their volume fraction, $\phi_b = n_b^\infty b^3 \, 4\pi/3$, and from the time step Δt used in the simulations. Bath particles are consumed on the reactive side decreasing their local concentration near the motor. Thus, there are more collisions with bath particles on the passive side, resulting in an imbalanced osmotic pressure and a force on the motor in the direction of the decreasing bath particle concentration. For slow reactions, the osmotic force is linear in Da: $F^{osm} \sim n_R^\infty kT(a + b)^2(1 - sD_R/D_P)Da = n_R^\infty(a + b)^3(1 - sD_R/D_P)6\pi\eta b\kappa$, where we have used the Stokes-Einstein-Sutherland expression for the bath particle diffusivity $D = kT/6\pi\eta b$. This has a simple physical interpretation: each bath particle reacting with the motor strikes the motor with speed κ and thus hydrodynamic

---

[2]Actual consumption of reactants may indeed occur if the reactant particles irreversible adsorb on the motor's surface or are absorbed in the interior of the motor. In either case, the motor's size would change over time and this effect would need to be included in the analysis.

force $6\pi\eta b\kappa$ and there are $n_R^\infty (a+b)^3$ colliding bath particles. The stoichiometry/diffusivity factor, $(1 - sD_R/D_P)$, then gives the net osmotic force. At the other extreme of high Da, or fast reaction, the concentration on the reactive half is zero as the reaction is now diffusion limited. The osmotic force saturates and simply scales as the jump in concentration from the passive $(n_R \approx n_R^\infty)$ to reactive $(n_R = 0)$ side times the area: $F^{osm} \sim n_R^\infty kT(a+b)^2(1 - sD_R/D_P)$. The transition from reaction to diffusion controlled occurs, appropriately, at a Damköhler number of unity.

It is instructive to ask what is the magnitude of the force that must be exerted on the motor to keep it fixed? The maximum force occurs in the large Damköhler number limit for large motors $(a \gg b)$. For a motor of $a = 1\,\mu$m with a 0.1 molar bath particle concentration, the osmotic force is of order $0.2\,\mu$N, an easily measurable force. In fact, it is rather large, as optical tweezers typically exert nano-Newton forces and biological motors exert pico-Newton forces. Indeed, if the motor were released it would travel with a speed of order $10\,$m/s! This surprising and aphysical result is resolved by noting that the motor cannot travel any faster than the bath particles can diffuse — that is, no faster than their diffusive velocity $v_{bath} \sim D/(a+b)$. If the motor were to move faster than this velocity, the bath particles could not keep up, and the motor would loose the propulsive force that caused it to move in the first place.

The resolution of this paradox is to recognize that, in a frame of reference traveling with the free motor, there will be an advective flux of bath particles towards the motor that will alter the concentration distribution about the motor and consequently, the propulsive osmotic force. The strength of the advective flux compared to the diffusive motion is given by a Péclet number $Pe = U(a+b)/D$, where U is the as yet *unknown* free motor velocity. And now there will be Péclet numbers for both the reactants, $Pe_R = U(a+b_R)/D_R$,
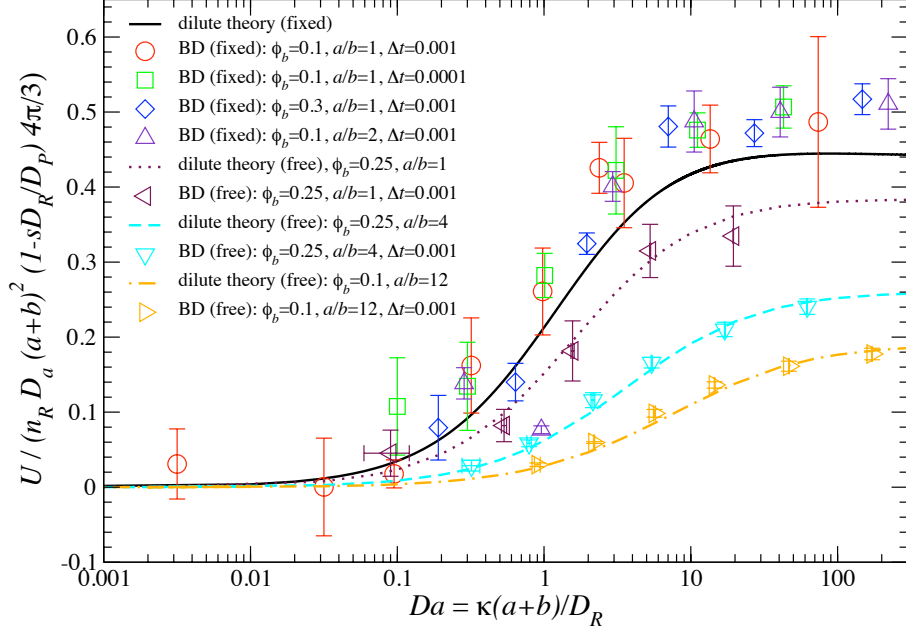
Figure 2.1: The scaled osmotic velocity for a motor with a first-order reaction on half of its surface plotted against Da for various values of $\phi_b(1 + a/b)^2$. Here, $D_a = kT/6\pi\eta a$ is the Stokes-Einstein-Sutherland "diffusivity" of the motor (see Eq. (2.2)). The theoretical predictions (curves) are compared with BD simulations (symbols). The solid curve corresponds to the fixed motor shown for comparison.

and products, $Pe_P = U(a + b_P)/D_P$, and they differ by the diffusivity ratio. The scaled reactant concentration distribution now satisfies the advection-diffusion equation: $\nabla^2 \bar{n}'_R = -Pe_R \partial \bar{n}'_R / \partial z$, where the direction of motion is taken to be the z-direction. The products also satisfy the same equation with R replaced by P. The *total* concentration $\bar{n}'_b$ does not satisfy the same equation as the reactants, unless $Pe_R = Pe_P$, which will be true in the small and large Péclet number limits. The osmotic force is still scaled as before, however, and the unknown velocity is found from balancing the Stokes drag on the motor with the osmotic force:

$$\boldsymbol{U} = -\frac{kT}{6\pi\eta a} n_R^\infty (a + b)^2 \left(1 - s\frac{D_R}{D_P}\right) \int \boldsymbol{n}\, \bar{n}'_b(\boldsymbol{x}) d\Omega, \qquad (2.2)$$

where the total concentration $\bar{n}'_b(\boldsymbol{x})$ now depends on the Damköhler and Péclet numbers. Note that the motor velocity, and thus the Péclet numbers, are unknown and must be
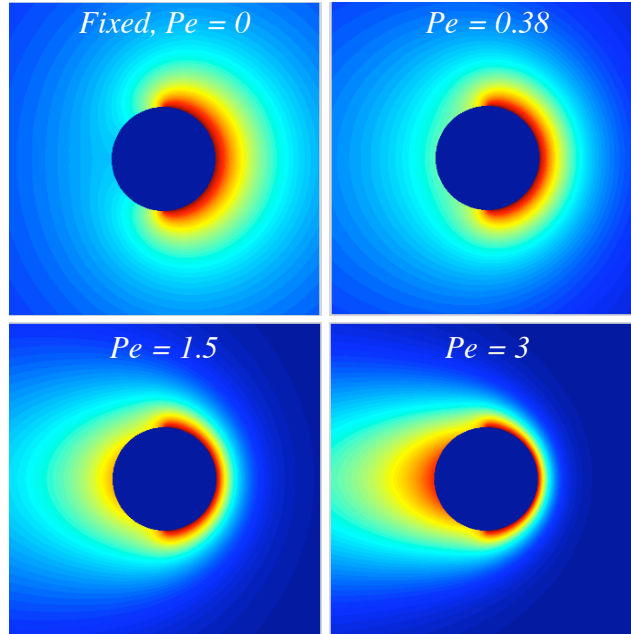
Figure 2.2: Density profiles in the symmetry plane of the osmotic motor at $Da = 100$. The four panels correspond to the four curves (from top to bottom) in Figure 2.1. Red is low bath particle concentration and blue the uniform level far from the motor. The right half of the motor is reactive and its motion is from left to right.

determined self-consistently along with the coupled concentration distributions $\bar{n}_b'$ and $\bar{n}_R'$ from the advection-diffusion equations. This is somewhat involved, and here we discuss the limiting case of $sD_R/D_P \to 0$ for which the product distribution drops out and the bath particle concentration is the same as that of the reactants.

Figure 2.1 shows the predictions for the free motor velocity as a function of Da from the analytical solution. In contrast to the fixed motor case (the solid line), the speed of the motor now *does* depend on a/b and on ϕ_b (even though the bath particles form an ideal gas). As before, the open symbols correspond to BD simulations for the same conditions of volume fraction and size ratio as in the theory and show excellent agreement. The curves correspond to increasing the product $\phi_b(1 + a/b)^2$, which follows directly from (2.2) and corresponds to the number of bath particles within a bath particle radius of the motor surface.

Figure 2.2 shows density plots of the bath particle concentration near the motor at $Da = 100$, but for different values of $\phi_b(1 + a/b)^2$, corresponding to each of the four curves in figure 2.1. Also shown on the plots are the resulting Péclet numbers corresponding to the motor velocities. As the Péclet number increases the advection of the bath particles past the motor distorts the bath particle concentration, shrinking the bath-particle-depleted region in front of the motor and leaving a trailing "wake" of reduced bath particle concentration. At even modest motor velocities (modest Pe) most of the rear of the motor has a very low bath particle concentration, which reduces the osmotic force and thus limits the speed of the motor. This self-regulation results in a maximum motor velocity of order the diffusion velocity of the bath particles $U_{max} \sim v_{bath} \sim D/(a + b)$. For a 1-$\mu$m-sized motor and nanometer-sized bath particles the maximum motor velocity is now of order 10 μm/s, a much more reasonable velocity, and one that is in fair agreement with the motivating experiments of Paxton et al. (2004).

The results in Figure 2.1 show that the fixed motor is the limit as $\phi_b(1 + a/b)^2 \rightarrow 0$ ($Pe = 0$) of the free motor, corresponding to an infinitely dilute suspension of bath particles. This is as it should be, because whether the motor is fixed or free is just a change of reference frame. For a fixed motor there will be an advective flux at infinity to supply reactive bath particles to the motor. This also implies that the motor will induce a fluid flow to supply the bath particles and can be used as a pump — a novel microfluidic pump (and mixer).

In this analysis we neglected rotary Brownian motion[3] and hydrodynamic interactions between particles. Hydrodynamics would quantitatively (not qualitatively) affect the motor speed and can be included via the well-known low-Reynolds number hydrodynamic mobility expressions (Russel et al. 1989) for the bath particle diffusivity and the advective velocity.

---

[3]For our analysis to hold, the time scale for rotary Brownian motion of the motor, $1/D_R = 8\pi\eta a^3/kT$, must be long compared to that for the establishment of the bath particle concentration, a^2/D, i.e., $b/a \ll 1$.

Also, the entropic Brownian force on the motor contains an additional term that is the integral of the spatial variation of the relative hydrodynamic mobility (see Khair and Brady (2006) for the analogous microrheology problem).

Clearly, neither the motor nor the bath particles need be spherical, nor must the bath particles form an ideal gas. And a variety of behaviors is possible depending on the nature of the chemical reaction at the motor surface, the number of motors present, etc. Rotary motion is also possible by having reactive patches strategically located about the motor surface (Paxton et al. 2005).

Osmotic propulsion provides a simple means to convert chemical energy into mechanical motion and work, and can impact the design and operation of nanodevices, with applications in directed self-assembly of materials, thermal management of micro- and nanoprocessors, and the operation of chemical and biological sensors. Studies of autonomous motors may also help to understand chemomechanical transduction observed in biological systems (Theriot 2000) and to create novel artificial motors that mimic living organisms and which can be harnessed to perform desired tasks.

2.3   Bibliography

J. L. Anderson. Colloid transport by interfacial forces. *Annu. Rev. Fluid Mech.*, 21:61–99, 1989.

S. Asakura and F. Oosawa. On interaction between two bodies immersed in a solution of macromolecules. *J. Chem. Phys.*, 22(7):1255–1256, 1954.

G. K. Batchelor. Diffusion in a dilute polydisperse system of interaction spheres. *J. Fluid Mech.*, 131:155–175, 1983.

R. B. Bird, W. E. Stewart, and E. N. Lightfoot. *Transport Phenomena.* John Wiley and Sons, 1960.

I. C. Carpen and J. F. Brady. Microrheology of colloidal dispersions by Brownian dynamics simulations. *J. Rheol.*, 49(6):1483–1502, 2005.

D. R. Foss and J. F. Brady. Brownian Dynamics simulation of hard-sphere colloidal dispersions. *J. Rheol.*, 44(3):629–651, 2000.

R. Golestanian, T. B. Liverpool, and A. Ajdari. Propulsion of a molecular machine by asymmetric distribution of reaction products. *Phys. Rev. Lett.*, 94(22), 2005.

J. R. Howse, R. A. L. Jones, A. J. Ryan, T. Gough, R. Vafabakhsh, and R. Golestanian. Self-motile colloidal particles: From directed propulsion to random walk. *Phys. Rev. Lett.*, 99(4), 2007.

A. S. Khair and J. F. Brady. Single particle motion in colloidal dispersions: a simple model for active and nonlinear microrheology. *J. Fluid Mech.*, 557:73–117, 2006.

G. A. Ozin, I. Manners, S. Fournier-Bidoz, and A. Arsenault. Dream nanomachines. *Adv. Mater.*, 17(24):3011–3018, 2005.

W. F. Paxton, S. Sundararajan, T. E. Mallouk, and A. Sen. Chemical locomotion. *Angew. Chem. Int. Ed.*, 45(33):5420–5429, 2006.

W. F. Paxton, A. Sen, and T. E. Mallouk. Motility of catalytic nanoparticles through self-generated forces. *Chem. Eur. J.*, 11(22):6462–6470, 2005.

W. F. Paxton, K. C. Kistler, C. C. Olmeda, A. Sen, S. K. St. Angelo, Y. Y. Cao, T. E. Mallouk, P. E. Lammert, and V. H. Crespi. Catalytic nanomotors: Autonomous movement of striped nanorods. *J. Am. Chem. Soc.*, 126(41):13424–13431, 2004.

W. B. Russel, D. A. Saville, and W. R. Schowalter. *Colloidal Dispersions.* Cambridge University Press, 1989.

R. K. Soong, G. D. Bachand, H. P. Neves, A. G. Olkhovets, H. G. Craighead, and C. D. Montemagno. Powering an inorganic nanodevice with a biomolecular motor. *Science*, 290(5496):1555–1558, 2000.

T. M. Squires and J. F. Brady. A simple paradigm for active and nonlinear microrheology. *Phys. Fluids*, 17(7), 2005.

J. A. Theriot. The polymerization motor. *Traffic*, 1(1):19–28, 2000.

Chapter 3

Directed motion of colloidal particles by chemical reaction: derivation, maximum force/speed, fluctuations, efficiency

3.1 Introduction

The emerging era of molecular engineering has had a great impact for the design and development of nanotechnology. Nanomachines, individually or assembled into complex architectures, may be useful for monitoring and interacting with harmful microorganisms in fluids, transporting medicine in the human body, conducting operations in cells, moving cargo around microfluidic chips, managing light beams, agitating liquids close to electrode surfaces, and searching for and destroying toxic organic molecules in polluted water streams (Ozin et al. 2005). Overall, a nanorobot's dimensions are comparable to those of biological cells and organelles. In this regime, also known as the Stokes regime, inertia of the system is negligible and motion is mainly dominated by diffusion. A consequence of the lack of inertia is that symmetric motions cannot achieve propulsion and therefore a fundamental problem arises as to how to move nanomachines in order to perform useful tasks. Recently, the research community has paid considerable attention to biomolecular motors as a possible option to power nanodevices (Soong et al. 2000; Montemagno and Bachand 1999). As an example, Morin et al. (2006) described the synthesis of a nanocar that bears a light-powered molecular motor in its central portion for an eventual paddlewheel-like propulsion action along a substrate surface for motion of the vehicles. But still, many of these techniques are subject to external forcing or signaling, which adds complexity to the problem. The design of nanoengines that can convert stored chemical energy into motion has become one of the challenges of nanotechnology, especially for motors that can act autonomously.

Studies of autonomous motors under isothermal conditions may help us to not only understand chemo-mechanical transduction in biological systems, but also to create novel artificial motors that mimic living organisms. Motor organs or organelles in living sys-

tems work through the dissipation of chemical energy under almost isothermal conditions (Yoshikawa and Noguchi 1999). Although scientists have recognized that it is hard to design better motors than those found in nature, ideas have been taken from biological systems, such as flagellated microorganisms that could be used to power microfluidic devices.

Autonomous motion not only occurs in nature, but also in man-made settings at different scales. A variety of recent experiments have shown surprising autonomous and directed behaviors that come into play without external inputs (e.g., forces). All of which have in common the self-creation of a gradient. Schmid et al. (2000) observed that shortly after deposition of Sn in Cu (111), two-dimensional crystal islands proceed to move spontaneously by free energy gradients along the surface in a systematic fashion. Self-propulsion of camphor crystals placed on an air/water interface occurs by preferential dissolution of camphor from one side of the crystals; dissolution creates a surface tension gradient which induces motion (Nakata et al. 2002). Ismagilov et al. (2002) described the behavior of small hemicylindrical plates with a small area of platinum on one surface that float at the interface of an aqueous solution of hydrogen peroxide. These plates move under the impulse of bubbles generated by the platinum-catalyzed decomposition of hydrogen peroxide. Mano and Heller (2005) showed that a carbon fiber is propelled rapidly at the water–O_2 interface when built with a terminal glucose oxidizing microanode and an O_2 reducing microanode. The flow of current through the fiber is accompanied by the transport of ions, which due to their speed at the interface, where the viscous drag is small, carries the fiber at ~ 1 cm/s. In order to move nanorods in the Stokes regime using on-board or off-board energy-rich chemical fuels, large forces will have to be applied to the nanorods because of the opposing large viscous drag.

An important breakthrough in reaction-driven motility of artificial systems was achieved

by Paxton et al. (2004). They showed that it is possible to power the motion of nanoscale and microscale objects by using catalytic reactions — so-called catalytic nanomotors. It was observed that rod-shaped nanoparticles prepared with Au and Pt segments move autonomously in aqueous hydrogen peroxide solutions by catalyzing the formation of oxygen at the Pt surface. The motion of the nanoparticles occurred in the direction opposite to those in Ismagilov et al. (2002), towards the Pt end of the rod. A number of mechanisms have been suggested for nanomotor propulsion (Paxton et al. 2006), including: bubble propulsion, diffusiophoresis, electrophoresis, surface-tension gradients, etc., all of which rely on the establishment of a gradient to provide the driving force for motion. The catalytic nanomotor experiments were expanded by showing that an external magnetic field could enable guided motion of gold/nickel/platinum nanorods in an aqueous solution of hydrogen peroxide, whereby, mobility of the nanorod is directed by the magnetic lines of force acting on the ferromagnetic nickel segment of the nanorod (Kline et al. 2005). These experiments provide an important insight of how chemical reactions could be used to operate devices and to pump fluids at nanoscales.

Following the above motivating experiments on autonomous motion, we propose a very simple mechanism for directed motion of colloidal particles: osmotic propulsion. It is well known that when a semi-permeable membrane separates a fluid that contains colloidal particles, a fluid flow is produced from the side of low particle concentration to the side of high particle concentration. The colloidal particle's movement is determined by fluctuations of thermal collisions with nearby fluid molecules. The generated fluid flow may be stopped, or even reversed, by applying external pressure on the side of higher concentration. The pressure that stops the flow is called the osmotic pressure. Whenever a wall blocks a particle's motion, it will transfer momentum to it and, therefore, generate a pressure on

it. If we now stop holding the membrane, the osmotic pressure difference between the two sides of the system will push the membrane until thermodynamic equilibrium is re-established. Therefore, the process of collisions with a moving wall is a mechanism by which the microscopic kinetic energy of the (Brownian) particles is transformed into macroscopic mechanical work. This simple principle was demonstrated experimentally by Nardi et al. (1999) in their work on osmotic permeation of solvent across a spherical semipermeable membrane in a concentration gradient leading to a pumping action: solvent is pumped from the low to the high concentration side of the sphere. Osmotic action is the basis of survival and reproduction of biological cells and a mechanism which could be used for propulsion. However, one does not need a membrane. Autonomous motion can be achieved, instead, by a reaction at a particle surface generating a local imbalance in the osmotic pressure of the surrounding medium.

The possibility of extracting mechanical work from Brownian motion using surface reactions delivers a new propulsion mechanism for colloidal particles suspended in a continuum phase. Colloidal particles tend to move freely and randomly, but if the concentration of surrounding species in the vicinity of the particle is disturbed, for example, as a result of a surface chemical reaction, some average directional movement can be obtained, which is often needed for nanotechnological devices in operations that require net displacement. Similar osmotic motion occurs in the problem of multicomponent diffusion (Batchelor 1983), where a gradient in concentration of one species can drive the flux of another. Batchelor showed that in multicomponent suspensions of colloidal particles accompanied by spatial gradients in particle concentration, as a consequence of Brownian motion (thermal fluctuations), the mean flux down a small concentration gradient due to diffusion is identical as if each of the particles is acted on by a steady applied force (thermodynamic force) that

represents a departure from an equilibrium state with an isotropic environment. Similarly, depletion flocculation occurs when small particles (e.g., polymers, salts) are excluded from a zone separating two nearly touching colloidal particles and the imbalanced osmotic pressure of the small particles causes an entropic attractive force (Asakura and Oosawa 1954).

But now consider a concentration distribution of colloidal particles that is created locally by a surface chemical reaction on another particle. The resulting imbalanced osmotic force will induce autonomous motion — an osmotic motor. This is a simple means by which random entropic motion can be harnessed by a chemical reaction to create directed motion.

In this work, a simple theoretical model for osmotic propulsion of a colloidal particle — the osmotic motor — immersed in a dispersion of "bath" particles is presented. We specify half the motor surface to be reactive in which reactants in the suspension are transformed into products by an irreversible first-order reaction. The non-equilibrium concentration of bath particles induced by the surface chemical reaction creates an "osmotic pressure" imbalance on the motor causing it to move to regions of lower bath particle concentration. This model is simple enough to permit a clear study and to admit analytical and numerical analysis that may provide a general picture of how particles could obtain directionality in stochastic environments commonly found in bio- and technological arrangements. This will be done for hard-spheres, where the particle evolution equation is derived from statistical mechanical principles in the absence of hydrodynamic interactions and rotational diffusive motion following the work on single particle motion in colloidal dispersions and microrheology (Squires and Brady 2005; Khair and Brady 2006). A physical statement of the driving force of the motor is presented in Section 3.2. The considered non-uniform surface reaction balances the particle flux to the pair-level Smoluchowski equation in order to characterize the particle interactions. Theoretically, the problem is simplified in order to determine the

pair-distribution function $g(\boldsymbol{r})$, which relates to the probability of finding bath particles as a function of the position of the motor experiencing net osmotic force. The departure of the bath particle concentration from equilibrium is governed by the Damköhler number Da: the ratio of the speed of reaction to that of diffusion. The density distribution of bath particles about the motor is employed to calculate the driving force on the motor, from which the self-induced osmotic velocity is determined via application of Stokes drag law. We shall describe two possible scenarios for the osmotic motor: one, in which the motor is held fixed by an external force (no motion) and a second case, where the motor is free to translate. The theoretical framework will be described in detail in Section 3.3. The steady-state pair-distribution function $g(\boldsymbol{r})$ for slow and fast reactions as well for arbitrary Damköhler numbers is solved. The implications of these features for different bath particle concentrations and motor sizes are discussed. We compare the fixed and free motor scenarios and show their implications on the local microstructure.

In addition to the theory, we propose in Section 3.4 the study of the osmotic motor behavior using Brownian dynamics (BD) simulations, which are particle-level simulations, where the dispersion is treated as a collection of spheres in a Newtonian fluid. The algorithm for simulating Brownian particles is well established and has been investigated and expanded by various researchers. Recently, Carpen and Brady (2005) investigated the forced motion of a particle through a colloidal suspension, which is affected by both the viscous drag and the force resulting from the microstructure deformation. Magan et al. (2003) used BD simulations to investigate the influence of the surface reaction rate on the development of size dispersion of interfacial nanostructures that form by irreversible deposition of non-interacting particles onto surfaces with randomly distributed nucleation sites. It has also been used for calculating the steady-state bimolecular rate constants of diffusion-influenced

reactions (Northrup et al. 1984; Allison et al. 1990). These studies were relevant in order to suggest a simple algorithm that emulates the irreversible first-order reaction on the motor's surface. We describe the two possible scenarios for the motor as well. We calculate the driving force on the motor, and, in the case of the free motor, the osmotic velocity. BD simulations provide a means of checking and extending our theoretical analyses and allow us to design and analyze experimental systems in which different effects can be cleanly separated. Theoretical predictions are compared with BD simulation and reported in Section 3.5.

In Section 3.6 we suggest how the dilute results can be scaled up to higher concentrations. We examine in Section 3.7 the force fluctuations resulting from random collisions between the motor and bath particles and its behavior as the speed of reaction, the bath particle concentration, and particle size are changed. In Section 3.8 we propose a formula to determine the energy conversion efficiency of chemical energy (supplied by the reactants) into motion via the dissipation of mechanical energy. Lastly, some concluding remarks are presented in Section 3.9.

3.2 Derivation of the osmotic force

Consider a suspension of N spherical Brownian particles: one particle is the osmotic motor of radius a, and the other $N - 1$ "bath" particles of radii b surround the motor in an incompressible Newtonian fluid of density ρ and viscosity η (see Figure 3.1). Both the motor and bath particles are taken to be large compared to the solvent molecules so that their behavior can be described by the familiar equations of colloidal dynamics (Russel et al. 1989), but small enough to be affected by the thermal fluctuations of the solvent and are thus Brownian. The Reynolds number $Re = \rho U a / \eta$ (with U a typical velocity scale),
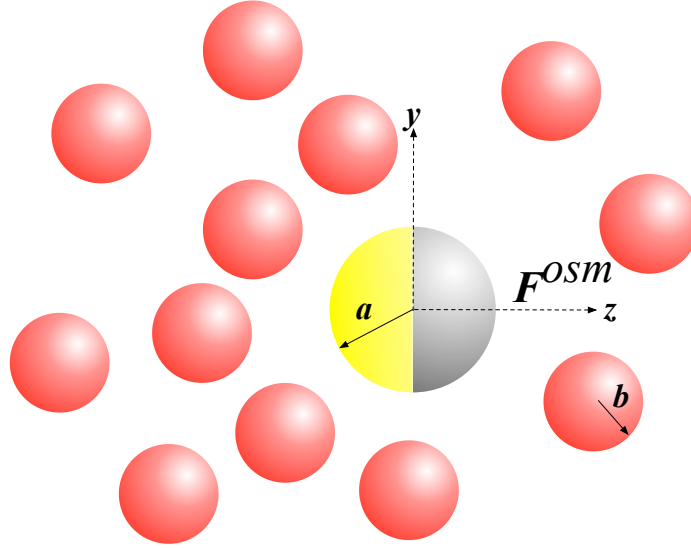
Figure 3.1: Model system for osmotic propulsion. A motor particle of radius a with a first-order reaction on half its surface (located in the z-axis) surrounded by bath particles of radii b induces an osmotic force $\boldsymbol{F}^{osm}$ that points towards low bath particle concentration regions. Particle interactions are modeled with a hard-sphere potential.

that describes the fluid inertia is small, thus enabling the use of the Stokes equations. The suspension of bath particles generates an osmotic pressure in the system $\Pi = n_b kT$, where kT is the thermal energy and n_b is the number density of bath particles. Our goal is to develop a theory that models the microstructural evolution of the suspension that is driven out of equilibrium by a chemical reaction on the motor surface.

Because asymmetric deformations of the suspension microstructure are of primary importance to obtain a "driving" force, we must solve for the distribution of bath particles surrounding the osmotic motor. Our point of departure is the N-particle Smoluchowski equation governing the spatio-temporal evolution of the N-particle probability density function $P_N(\boldsymbol{x}_N, t)$ for finding the N particles at position $\boldsymbol{x}_N$ in the fluid:

$$\frac{\partial P_N}{\partial t} + \sum_{i=1}^{N} \nabla_i \cdot \boldsymbol{j}_i = 0, \tag{3.1}$$

where $\boldsymbol{j}_i$ is the probability flux of particle i and the sum is over all the particles in the

suspension. The motion of an individual particle is governed by a balance among hydrodynamic, Brownian, and interparticle forces. Thus, the probability flux carried by particle i is given by

$$\boldsymbol{j}_i = \boldsymbol{U}_i P_N - \sum_{j=1}^{N} \boldsymbol{D}_{ij} P_N \cdot \boldsymbol{\nabla}_j (\log P_N + V_N/kT), \qquad (3.2)$$

where $\boldsymbol{U}_i$ is the velocity of particle i, $\boldsymbol{D}_{ij}$ is the relative Brownian diffusivity tensor, and V_N is the N-particle interaction potential, which is assumed to be central. There is no uniform flow at infinity in the "laboratory" frame. For simplicity, we neglect hydrodynamic interactions and rotary Brownian motion. To model the interactions among the particles, it is assumed that V_N is a hard-sphere potential so that the colloidal particles do not interact until their hard-sphere radii touch. The hard-sphere potential generates a force that prevents the hard-sphere radii, a and b of the motor and bath particles, respectively, from overlapping. The instantaneous thermal or Brownian force on the motor due to random collisions with solvent molecules is given by $\boldsymbol{F}^B = -kT\nabla \log P_N$. This expression for the instantaneous Brownian force is exact for all bath particle volume fractions, $\phi_b = 4\pi b^3 n_b/3$. At equilibrium the absence of any external (e.g., optical tweezers) or self-induced (e.g., swimming bacteria, catalytic nanomotor) forces implies that $\boldsymbol{U}_i = 0$ for each particle and the probability distribution is independent of time. This results in a balance between the interparticle potential and thermal forces, which is solved by the well-known Boltzmann distribution function $P_N^{eq} \sim \exp(-V_N/kT)$. Application of an external force or gradient, or a reaction-induced force, will cause relative motion among the particles in the suspension, drive the system away from equilibrium, and P_N away from the Boltzmann distribution P_N^{eq}.

To proceed analytically, it is necessary to restrict the analysis to the limit where bath

particles do not interact with each other and therefore behave as an ideal gas. Thus, only the motor interacts with the bath particles. We proceed by integrating Eq. (3.1) over the configurational degrees of freedom of $N - 2$ bath particles, neglecting interactions between bath particles. The neglect of such higher-order couplings could also be interpreted as our theory is restricted to low bath particle volume fractions, $\phi_b \ll 1$, for which only one bath particle interacts with the motor. Similarly, averaging the balance between the instantaneous Brownian and the hard-sphere force over the positions of the $N - 2$ bath particles and integrating by parts, results in an exact formula for the "osmotic" force on the motor due to collisions with bath particles,

$$\boldsymbol{F}^{osm} = -n_b kT \oint_{r=a+b} \boldsymbol{n} g(\boldsymbol{r}) \ dS. \tag{3.3}$$

In (3.3) the integral is over the surface of contact between the osmotic motor and bath particles, $r = a + b$, and $\boldsymbol{n}$ is the normal pointing out of the motor particle. The pair-distribution function $g(\boldsymbol{r})$ defined as $n_b^2 g(\boldsymbol{r}) = ((N - 2)!)^{-1} \int P_N(\boldsymbol{r}_N, t) d\boldsymbol{r}_3...d\boldsymbol{r}_N$ is the probability density for finding a bath particle at $\boldsymbol{r}$ relative to the motor. The interested reader can find a detailed derivation of the above equations in Squires and Brady (2005).

Eq. (3.3) is nothing more than the osmotic pressure Π sensed by the motor times the surface area available for collisions between the motor and bath particles. In the absence of any disturbance to the surrounding medium, no structural deformation is present; thus, $g(\boldsymbol{r})$ is isotropic and the integral in (3.3) is zero, resulting in no net osmotic force. However, if there is a non-uniform concentration of bath particles, either caused by an externally imposed concentration gradient or by the motor itself via a chemical reaction on its surface, there will be a net osmotic force on the motor. This osmotic force must be balanced by an

externally imposed force $\boldsymbol{F}^{ext}$ (via, e.g., optical tweezers, magnets) to hold the motor fixed, or by the hydrodynamic Stokes drag force $\boldsymbol{F}^{hyd} = -6\pi\eta a\boldsymbol{U}$. A similar observation was pointed out by Batchelor (1983) in the problem of multicomponent diffusion. The approach here produces precisely the result for the flux of one species due to a concentration gradient of another species as derived by Batchelor (1983) when hydrodynamics interactions are neglected. The surface integral of $g(\boldsymbol{r})$ at contact in Eq. (3.3) represents the local concentration of bath particles. And independently of what mechanism or input is responsible for producing a variation, a nonuniform distribution can drive the motor. An externally imposed concentration gradient gives rise to what is known as diffusiophoresis (Anderson 1989), whereas a surface chemical reaction alters the local concentration of bath particles and results in *autonomous* motion — namely, the osmotic motor.

3.3 Microstructural deformation by chemical reaction

In order to compute the osmotic force, we need to determine the pair-distribution function $g(\boldsymbol{r})$ about the motor. The bath particles are divided into reactants, labeled R, and products P. We consider one half the motor surface to be reactive (as illustrated in Figure 3.1) such that the reactant bath particles undergo an irreversible first-order reaction of products according to:

$$R \rightarrow sP, \tag{3.4}$$

where for each reactant particle "s" product particles are produced; s can take on any value greater than or equal to zero. For example, if two reactants are joined to form a product, then $s = 1/2$, while if two products are produced for each reactant, $s = 2$, and so forth. Conservation of mass requires than $m_R = sm_P$, where m_R is the mass of the

reactant particle and m_P that of the products. For spherical particles of the same density conservation of mass is equivalent to conservation of volume and therefore $b_R = s^{1/3}b_P$, where b_R and b_P are the radii of the reactants and products, respectively. The rate of consumption of R on the reactive surface is $\mathcal{R}_R$ and the production of P is $\mathcal{R}_P = -s\mathcal{R}_R$.

In this problem, changes in $g(\boldsymbol{r})$ are produced by the reaction on the reactive half of the motor, not by any external field or force. We have assumed that the pair-distribution function $g(\boldsymbol{r})$ is conserved and time-independent, which needs to be examined in light of the chemical reaction. This reaction occurs on the surface and not in the space available to $g(\boldsymbol{r})$; the reaction does not occur in the fluid phase.

The assumptions made allow a simple and clear analysis that captures and illustrates many of the significant physics important in osmotic propulsion. We proceed to formulate a physically motivated derivation of the microstructural deformation equation from which we intend to examine two scenarios for the osmotic motor: one, in which the motor is held fixed by an external force F^{ext} and another, where it is free to move.

3.3.1 Fixed motor

We first consider the fixed motor scenario as it is easiest to describe. Since the reaction only takes place at the motor surface (heterogenous reaction), the reactants and products diffuse in the fluid surrounding the motor with relative translational diffusivities D_R and D_P and number densities n_R and n_P, respectively. (In this case, the motor does not move, thus the relative diffusivities are just the diffusivities of the reactants and products.) In a frame fixed on the osmotic motor, each reactant and product particle moves diffusively.

Therefore, the probability flux for the reactant is

$$\boldsymbol{j}_R = -D_R \nabla g_R. \tag{3.5}$$

Conservation of reactant particles at steady state requires that $\nabla \cdot \boldsymbol{j}_R = 0$. The probability of finding a reactant particle relative to the motor, g_R, satisfies a pair-level diffusion equation

$$\nabla^2 g_R = 0. \tag{3.6}$$

To fully determine the pair-distribution function g_R, Eq. (3.6) must be accompanied by appropriate boundary conditions. The reactant microstructure is undisturbed far from the osmotic motor particle, giving

$$g_R \sim 1 \text{ as } r \to \infty. \tag{3.7}$$

Collisions at the motor/reactant boundary give rise to the heterogeneous reaction, mathematically stated as

$$\boldsymbol{n} \cdot \nabla g_R = \frac{\mathcal{R}_R \, h(\boldsymbol{n})}{n_R D_R} \text{ at } r = a + b_R. \tag{3.8}$$

The products satisfy a similar equation with the subscript R replaced by P. However, the osmotic force in (3.3) is proportional to the total probability density of bath particles $g = (n_R g_R + n_P g_P)/n_T$, where $n_T = n_R + n_P$ is the total number density of bath particles, which satisfies

$$\nabla^2 g = 0, \tag{3.9}$$

$$g \sim 1 \text{ as } r \to \infty, \tag{3.10}$$

$$\boldsymbol{n} \cdot \nabla g = \frac{\mathcal{R}_R \, h(\boldsymbol{n})}{n_R D_R} \frac{n_R}{n_T} \left(1 - s \frac{D_R}{D_P} \right) \text{ at } r = a + b_R. \tag{3.11}$$

The distribution of reactions on the surface is determined by the dimensionless function $h(\boldsymbol{n})$, which we take to be 1 on the reactive half and 0 on the passive half. The model can be easily extended for particles with different reactive surfaces (different forms for $h(\boldsymbol{n})$ see Chapter 4). The nonuniform reaction causes an anisotropic environment of reactant particles around the motor. The surface reaction rate is modeled as a first-order reaction: $\mathcal{R}_R = \kappa n_R g_R$, where κ is the speed of reaction. Defining the microstructural deformation functions $f_R = g_R - 1$ and $f = (g-1)/(n_R/n_T(1 - sD_R/D_P))$ that represents the deviation from equilibrium for the reactant and the bath particle distributions, respectively, and all lengths nondimensionalized by the sum of the motor and reactant radii: $a + b_R$, it is easy to see that f_R and f satisfy the same Laplace's equation and boundary conditions. For the total probability density of bath particles,

$$\nabla^2 f = 0, \tag{3.12}$$

$$f \sim 0 \text{ as } r \to \infty, \tag{3.13}$$

$$\boldsymbol{n} \cdot \nabla f = Da \, h(\boldsymbol{n}) \, (1 + f_R) \text{ at } r = 1, \tag{3.14}$$

which also describes the reactant distribution if f is substituted by f_R. We have defined a Damköhler number

$$Da = \frac{\kappa \, (a + b_R)}{D_R}, \tag{3.15}$$

that describes the ratio of the speed of reaction κ to Brownian motion, $D_R/(a + b_R)$. In general, increasing Damköhler number corresponds to driving the system away from equilibrium. Thus one need only to determine the reactant probability density to completely

solve the problem. The net osmotic force (3.3) becomes

$$
\begin{aligned}
\boldsymbol{F}^{osm} &= -n_R kT \oint_{r=a+b_R} \boldsymbol{n} g_R(\boldsymbol{r}) dS - n_P kT \oint_{r=a+b_P} \boldsymbol{n} g_P(\boldsymbol{r}) dS \\
&= -n_R kT(a+b_R)^2 \left(1 - s\frac{D_R}{D_P}\right) \oint_{r=1} \boldsymbol{n} f(\boldsymbol{r})\ d\Omega, \tag{3.16}
\end{aligned}
$$

where $d\Omega$ is the solid angle of integration and the total microstructural deformation function f depends on the Damköhler number. For spherical reactants and products of different radii, the integral should be over the "contact" surface at $a + b_R$ and at $a + b_P$. However, this introduces a negligible error, especially in the limit $a \gg b_{R,P}$. The net osmotic force is proportional to the thermal energy, kT, times the area of contact, $(a+b)^2$, times the jump in concentration of the reactant across the motor, $n_R \int \boldsymbol{n} f(\boldsymbol{r}) d\Omega$, times the stoichiometric/diffusivity factor $(1 - sD_R/D_P)$, which tells how many product particles are produced per reactant, s, and how fast the products diffuse relative to the reactants, D_R/D_P. Thus, the osmotic force is larger for relatively large motor particles and scales as $F^{osm} \sim n_R k_B T a^2 (1 - sD_R/D_P)$. For bath particles that are much larger than the motor, the available free space of self-propulsion is reduced, and consequently the entropic force of the bath particles is reduced. When bath particle collisions with the motor are uniform around the surface, as in the case of an inert or an uniformly reactive particle, the motor/bath boundary gives rise to the no-flux condition from the impenetrability of the motor particle and the Neumann boundary condition, respectively. In both cases, the microstructural deformation function $f(\boldsymbol{r})$ is symmetric and uniform everywhere, and thus the osmotic force (3.16) reduces to zero.

The correctness of the factor $(1 - sD_R/D_P)$ can be appreciated by considering some special cases. If we had simple $R \rightarrow P$ (or $s = 1$) and the product had the same dif-

fusivity as the reactant, the net osmotic force would be zero. This would correspond, if you will, to simply changing the "color" of the reactant which cannot produce any net force. However, if the reactants and products have different diffusivities, say because the reaction changes the "shape" of the particle, or perhaps its interaction with the solvent (hydrophilic/hydrophobic), then even if only one product is produced for each reactant there will still be a net osmotic force on the motor. The *sign* of the force will depend on which diffuses faster. As another example, suppose that $s = 2$, but the products and reactants have the same diffusivity. There will be now a net increase of bath particles on the reactive side and the osmotic force will be to the left in Figure 3.1 rather than to the right. If we restrict ourselves to strictly hard-sphere particles of the same density, then $D_R/D_P = b_P/b_R = s^{-1/3}$ from conservation of mass, and thus the stoichiometric/diffusivity factor becomes $(1 - sD_R/D_P) = (1 - s^{2/3})$. Since one needs only to solve (3.14) in any situation, all cases can be treated at the same time and the precise details of stoichiometry and diffusivity, an be addressed later in the final scaling factor, $(1 - sD_R/D_P)$, for the net osmotic force. And, of course, Eq. (3.16) correctly gives zero osmotic force in the absence of any reactive particles: $n_R = 0$.

3.3.2 Free motor

A second scenario is investigated that corresponds to a motor free to diffusive with a diffusivity D_a and to advect at velocity $\boldsymbol{U}$ due to the reaction-driven osmotic force. No external forces ($\boldsymbol{F}^{ext} = 0$) or imposed particle gradients act on the motor. In a frame fixed on the osmotic motor, which translates at velocity $\boldsymbol{U}$, each reactant and product particle is advected with velocity $-\boldsymbol{U}$ and moves diffusively. For dilute reactant particles the probability

flux has diffusive and "advective" terms,

$$\boldsymbol{j}_R = -\boldsymbol{U}g_R - D_R\nabla g_R, \tag{3.17}$$

where D_R is now the sum of the osmotic motor diffusivity and the reactant particles. Then, conservation of reactant particles at steady-state requires that $\nabla \cdot \boldsymbol{j}_R = 0$. The microstructural deformation function $f_R(\boldsymbol{r})$ satisfies a pair-level Smoluchowski or advection-diffusion equation made dimensionless by scaling lengths with the contact distance $a + b_R$ and the velocity with the yet unknown motor velocity U, which we must finally determine. Thus,

$$\nabla^2 f_R = -Pe_R\hat{\boldsymbol{z}} \cdot \nabla f_R, \tag{3.18}$$

and we have taken the motion to be along the z-axis ($\hat{\boldsymbol{z}}$ is a unit vector in the z-direction). Far from the motor, the reactant microstructure is undisturbed, giving $f_R \sim 0$. At contact, the boundary condition becomes

$$\boldsymbol{n} \cdot \nabla f_R = (Da\ h(\boldsymbol{n}) - Pe_R\ \boldsymbol{n} \cdot \hat{\boldsymbol{z}})\,(1 + f_R)\,. \tag{3.19}$$

Again, the products satisfy a similar equation with the subscript R replaced by P. The above expression reflects the competition between motion due to self-propulsion of the motor in driving the environment away from equilibrium and Brownian motion attempting to restore the disturbed microstructure. The Péclet numbers Pe_R and Pe_P, which appear from the scaling, may be considered as a ratio of the motor velocity U to the relative Brownian velocity $D_{R,P}/(a + b_R)$. The scaled total microstructural deformation function

$f(\boldsymbol{r})$ now satisfies

$$\nabla^2 f = -\left(\frac{Pe_R - Pe_P}{1 - s\frac{D_R}{D_P}}\right)\hat{\boldsymbol{z}}\cdot\nabla f_R - Pe_P\,\hat{\boldsymbol{z}}\cdot\nabla f. \qquad (3.20)$$

The nondimensional versions of the boundary conditions become: $f \sim 0$ as $r \to \infty$, and

$$\boldsymbol{n}\cdot\nabla f + Pe_P\,\boldsymbol{n}\cdot\hat{\boldsymbol{z}}\left(f + \frac{1}{\frac{n_R}{n_T}\left(1 - s\frac{D_R}{D_P}\right)}\right) =$$
$$\left(Dah(\boldsymbol{n}) - \left(\frac{Pe_R - Pe_P}{1 - s\frac{D_R}{D_P}}\right)\boldsymbol{n}\cdot\hat{\boldsymbol{z}}\right)(1 + f_R)\ \ \text{at}\ \ r = 1. \qquad (3.21)$$

Note that equations (4.10) and (4.12) diverges in the special case $sD_R/D_P \equiv 1$, for which there is no osmotic force. The osmotic force is still scaled as before, however, and the unknown velocity is found from balancing the hydrodynamic Stokes drag force $\boldsymbol{F}^{hyd}$ on the motor with the osmotic force. The osmotic velocity of the motor is

$$\boldsymbol{U} = -\frac{kT}{6\pi\eta a}n_R(a+b)^2\left(1 - s\frac{D_R}{D_P}\right)\oint_{r=1}\boldsymbol{n}f(\boldsymbol{r}; Da, Pe_R, Pe_P)\,d\Omega, \qquad (3.22)$$

where the microstructural deformation function f now depends on the Damköhler and Péclet numbers. Note that the motor velocity, and thus the Péclet numbers, are unknown and must be found self-consistently along with the microstructural deformation functions f and f_R from the advection-diffusion equations.

Since now the reactant and the total microstructural deformations are coupled, two simultaneous equations need to be solved to compute the osmotic force and thus the motor velocity. Therefore, the detailed stoichiometry/diffusivity is not just a scale factor as in the osmotic force for the fixed motor case. This is somewhat involved and is taken up in the

proposed work, so we discuss below the case in which the reactants are "consumed" upon reaction. This corresponds to $sD_R/D_P \to 0$, which would occur if the products are much more diffusive than the reactants or when the reactant is indeed consumed ($s = 0$) by the motor. Thus, the product distribution drops out and the total microstructural deformation function is the same as the reactants. Actual consumption of reactants may indeed occur if the reactant particles irreversibly adsorb on the motor's surface or are absorbed into the interior of the motor. In either case, the motor's size would change over time and this effect would need to be included in the analysis. We have not done so here. The reader should note that this is just the language we choose to discuss the basic physics of the osmotic propulsion. The reader may wish to think instead of two specific cases: i) $2R \to P$, in which two reactant particles are joined to form a single product particle, corresponding to $s = 1/2$ and scale factor $(1 - sD_R/D_P) = (1 - (1/2)^{1/3}) > 0$. There will now be a net depletion of bath particles on the reactive side and a propulsive force to the right as sketched in Figure 3.1. ii) $R \to 2P$, in which one reactant is split into two product particles, with corresponding scale factor $(1 - sD_R/D_P) = (1 - (2)^{1/3}) < 0$. Now there are more bath particles on the reactive side, leading to a propulsive force to the left in Figure 3.1. With this understanding in mind, we shall discuss the physics of the problem as if the reactant was consumed, $s = 0$.

From (4.9) the implicit equation for the Péclet number is

$$Pe = -\frac{kT}{6\pi\eta a}\frac{(a+b)^3}{D}n_b \oint_{r=1} n_z f(\boldsymbol{r}; Da, Pe)\, d\Omega = \phi_b\left(1 + \frac{a}{b}\right)^2 \mathcal{F}(Da, Pe), \qquad (3.23)$$

where $\mathcal{F}(Da, Pe) = -\frac{3}{4\pi}\int_{r=1} n_z f(\boldsymbol{r})d\Omega$ is a nondimensional function of the Damköhler and Péclet numbers, and must be solved in order to get a final expression for the motor

velocity. Note that in this and what follows we have dropped the subscript R for the reactant and will simply refer to the reactant as a bath particle. The Péclet number is not an independent parameter, but rather is set by the Damköhler number, the bath particle volume fraction ϕ_b, and the size ratio a/b. The term $\phi_b(a+b)^2$ in Eq. (3.23) is defined to be a new parameter β, such that β and Da determine the motor behavior. The product β corresponds to the number of bath particles within a bath particle radius of the motor surface: $\beta \sim n_b(a+b)^2 b$. Clearly, at $Pe = 0$ (or $\beta \to 0$) the free motor problem becomes the fixed motor, giving identical microstructural deformation for non-equilibrium conditions. Therefore, for the fixed motor $\mathcal{F}(Da)$ is a function of the Damkóhler number only. The fixed motor corresponds to an infinitely dilute suspension of bath particles. Whether the motor is fixed or free to move is just a change of reference frame. For a fixed motor there will be an advective flux at infinity to supply reactive particles to the motor.

The problem of osmotic propulsion consists of determining the microstructural deformation function ($f = g - 1$) and then the dimensionless function $\mathcal{F}$, which can also be interpreted as the dimensionless self-generated concentration gradient, for different physical parameters relevant to the motor and the suspension characteristics. In addition to the discussed theory, we extend this study by using Brownian dynamics simulations, which allow us to build a different method to check our proposed theoretical framework and expand it to more complex systems.

3.4   Osmotic propulsion by Brownian dynamics simulations

The Brownian dynamics method is well established and has been investigated and expanded by various researchers. Brownian dynamics (BD) simulations can be described as a simplified version of Stokesian dynamics (Brady and Bossis 1988) that simulate colloidal

particles in the absence of hydrodynamic interactions. BD was used for the study of the rheology of sheared colloidal dispersions by Foss and Brady (2000) and recently by Carpen and Brady (2005) to investigate active particle-tracking microrheology in a colloidal dispersion. A further description of BD and relevant references are given in Allen and Tildesley (1989). Here, we present a simulation method similar to that used for passive microrheology measurements, but modified to consider a reaction on the surface of one particle of the suspension designated the osmotic motor. We shall see below that the BD method provides an insightful physical interpretation of surface reactions and a particle-level description of osmotic propulsion.

The system of N particles that we address in BD is exactly the one presented theoretically in Section 3.2: a colloidal dispersion of hard-spheres consisting of the osmotic motor of radius a surrounded by bath particles of radii b immersed in an incompressible Newtonian fluid of viscosity η and density ρ (see Figure 3.1). In the colloidal dispersion there is a clear separation of time and length scales between the particles and the fluid molecules, therefore, the fluid can be treated as a continuum. No hydrodynamic interactions nor rotary Brownian motion were included in the simulations. Our main goal is to provide a simulation method that describes the dispersion microstructure about the osmotic motor configuration subject to the self-created osmotic force. We assume that the osmotic motor has a first-order reaction on half its surface that consumes bath particles ($s = 0$). (BD simulations can also be extended to motors with different distributions of reactive surface, but, as stated earlier, our intention in this work is to illustrate the general and fundamental observations in osmotic propulsion. The later will be discussed in Chapter 4.) Consumption of bath particles on one side of the motor, which is responsible for creating the imbalance in osmotic pressure, must be simulated. The macroscopic balance at motor-bath contact is incorporated into

BD simulations by considering a reaction probability P_s — the probability with which a bath particle that collides with the reactive surface is consumed. A similar approach was taken to investigate the influence of surface reaction rate on the development of size dispersion of interfacial nanostructures (Magan et al. 2003). Other approaches for stochastic modeling of reaction-diffusion problems are discussed in Erban and Chapman (2007). The two theoretical scenarios for the osmotic motor (fixed and free) discussed in Section 3.3 are also considered in the simulations. From this, we examine the time-averaged osmotic force created by the fixed motor and the time-averaged velocity of the free motor.

3.4.1 Simulation method

A detailed derivation of the simulation method has appeared in the literature (Ermak and McCammon 1978; Fixman 1978), so we shall proceed quickly. The BD method is used to describe the motion of the individual particles governed by the Langevin equation:

$$m_i \cdot \frac{d\boldsymbol{U}_i}{dt} = \boldsymbol{F}_i^H + \boldsymbol{F}_i^P + \boldsymbol{F}_i^B, \qquad (3.24)$$

where m_i is the mass of particle i, $\boldsymbol{U}_i$ is the ith particle translational velocity vector, and the force vectors $\boldsymbol{F}_i$ represent: (i) the hydrodynamic forces $\boldsymbol{F}_i^H$ exerted on particle i due to their motion relative to the fluid, (ii) the deterministic nonhydrodynamic forces $\boldsymbol{F}_i^P$, which may be either interparticle or external (e.g., hard-sphere, optical tweezer, magnetic, etc), and (iii) the stochastic forces $\boldsymbol{F}_i^B$ that give rise to Brownian motion ($i = 1$ refers to the motor and $i = 2, ..., N$ the bath particles, respectively). For colloidal systems, inertia is neglegible compared to viscous forces (small Reynolds number), and Eq. (3.24) reduces to

$$0 = \boldsymbol{F}_i^H + \boldsymbol{F}_i^P + \boldsymbol{F}_i^B. \qquad (3.25)$$

Since we are studying a system of particles with no hydrodynamics interactions, the hydro-dynamic force $\boldsymbol{F}_i^H$ only consists of the Stokes drag on an isolated particle given simply by $\boldsymbol{F}_i^H = -6\pi\eta a_i \boldsymbol{U}_i$. The stochastic or Brownian force $\boldsymbol{F}_i^B$ results from the thermal fluctuations in the fluid and is characterized by

$$\overline{\boldsymbol{F}_i^B} = 0 \tag{3.26}$$

and

$$\overline{\boldsymbol{F}_i^B(0)\boldsymbol{F}_i^B(t)} = 2kT(6\pi\eta a_i)\boldsymbol{I}\delta(t). \tag{3.27}$$

The overbars in Eq. (3.26) and (3.27) denote an ensemble average over the thermal fluctuations in the fluid, where $6\pi\eta a_i \boldsymbol{I}$ is the hydrodynamic resistance tensor in the absence of hydrodynamic interactions, $\boldsymbol{I}$ is the unit isotropic tensor and $\delta(t)$ is the delta function. The amplitude of the correlation between Brownian forces at time 0 and at time t results from the fluctuation-dissipation theorem for the N-body system. The deterministic or non hydrodynamic force $\boldsymbol{F}_i^P$ is simply the sum of any external forces $\boldsymbol{F}_i^{ext}$ and the interparticle hard-sphere force $\boldsymbol{F}_i^{HS}$. No external forces act on the bath particles, thus $\boldsymbol{F}_{2,...,N}^{ext} = 0$.

The particle evolution equation is obtained by integration of Eq. (3.24) over a time step Δt that is small compared to the time over which the configuration changes. The evolution equation for the particle positions with an error of $o(\Delta t)$ is given by

$$\Delta\boldsymbol{X}_i = \Delta\boldsymbol{X}_i^{HS} + \boldsymbol{F}_i^{ext}\Delta t + \boldsymbol{X}_i^B(\Delta t), \tag{3.28}$$

where $\boldsymbol{X}_i^B$ is characterized by

$$\overline{\boldsymbol{X}_i^B} = 0 \tag{3.29}$$

and

$$\overline{\boldsymbol{X}_i^B(\Delta t)\boldsymbol{X}_i^B(\Delta t)} = 2\left(\frac{b}{a_i}\right)\boldsymbol{I}\Delta t. \tag{3.30}$$

In Eq. (3.28), $\Delta\boldsymbol{X}_i$ is the change in particle position during the time step Δt, $\boldsymbol{X}_i^B(\Delta t)$ is a random displacement due to Brownian motion, and $\Delta\boldsymbol{X}_i^{HS}$ is a hard-sphere displacement. Here, length has been nondimensionalized by the characteristic bath particle size b, time by the diffusive time scale $b^2/D_b = 6\pi\eta b^3/kT$, and the external and interparticle forces by kT/b.

For each Δt, all particle configurations are updated first by adding the displacements due to the Brownian forces, $\boldsymbol{X}_i^B(\Delta t)$, and second by an iterative method which corrects collisions by applying the hard-sphere force/displacement $\Delta\boldsymbol{X}_i^{HS}$. This hard-sphere collision scheme is based on the "potential-free" algorithm of Heyes and Melrose (1993) in which the overlap between pairs of particles is corrected by moving the particles properly distributed amounts along the line of center back into contact. This algorithm is "potential free" in that it does not require a specific declaration of a pair potential, although it implements the hard-sphere potential which is infinite if the particles are overlapping and zero otherwise. The algorithm displaces bath particles overlapping with the motor along their lines of centers according to

$$\Delta\boldsymbol{X}_{2,\ldots,N}^{HS} = \frac{a}{a+b}(\Delta r - a - b)H(a + b - \Delta r), \tag{3.31}$$

where Δr is the interparticle separation after the Brownian displacements. The Heaviside step function is included to ensure that the displacement is only for the overlapped particles. The factor $\frac{a}{a+b}$ is chosen to return the particles back to contact. The collisions are considered to be elastic, thus the sum of interparticle forces at contact is zero. Therefore, the hard-

sphere displacement for the osmotic motor $\Delta \boldsymbol{X}_1^{HS}$ is given by

$$\Delta \boldsymbol{X}_1^{HS} = -\frac{b}{a} \Delta \boldsymbol{X}_{2,\dots,N}^{HS}. \tag{3.32}$$

In order to proceed analytically in the theory, it was assumed that bath particles do not collide with each other and so behave as an ideal gas. A direct comparison can be made with the dilute theory neglecting collisions between bath particles. This is easily simulated in BD by imposing

$$\Delta \boldsymbol{X}_{2,\dots,N}^{HS} = \frac{1}{2}(\Delta r - 2b)H(2b - \Delta r) = 0 \tag{3.33}$$

for collisions between bath particles. Thus bath particles only collide with the motor. Although, we also consider simulations relaxing the ideal gas assumption (Eq. (3.33) is not zero) enabling us to provide ideas on how to scale up the theory to higher bath particle concentrations. This topic will be addressed in Section 3.6. The hard-sphere collision scheme checks for bath particle overlaps with the motor one bath particle at a time. Therefore, the resulting hard-sphere displacement for the motor could cause new overlaps with surrounding bath particles. The algorithm resolves this issue by checking again for overlaps and correcting the position of the particles until none are found. Then, a new simulation time step Δt is taken.

The above simulation method is used to examine the dispersion dynamics surrounding the osmotic motor held fixed by an external force and the case when it is free to move. In the fixed motor case, a constant external force $\boldsymbol{F}^{ext}$ is applied on the motor to keep it fixed at a given configuration, meaning that its displacement $\Delta \boldsymbol{X}_1$ must be zero. Hard-sphere collisions between particles fall into two categories: collisions between bath particles and collisions between a bath particle and the osmotic motor. The first collision type is the

same as before: one has the option to treat the bath particles as an ideal gas or not. The second collision type needs to take into account the fact that since the motor is fixed, it is the bath particle that needs to be displaced the entire amount back to contact position. It is then straightforward to calculate the time-averaged osmotic force exerted on the fixed motor, giving

$$\boldsymbol{F}^{osm} = \boldsymbol{F}^{ext} = -\frac{kT}{b}\frac{\langle \Delta \boldsymbol{X}^{HS} \rangle}{\Delta t}, \tag{3.34}$$

where the average $\langle \cdot \rangle$ is defined as the average over a time period. Note that in this equation and what follows we have dropped the subscript 1 for the motor.

In the free motor case, no external forces are applied on the motor; thus, $\boldsymbol{F}^{ext} = 0$ and the hard-sphere force is balanced by the hydrodynamic force. The time-averaged motor velocity is given by

$$\boldsymbol{U} = \frac{D_b}{b}\frac{\langle \Delta \boldsymbol{X} \rangle}{\Delta t} = \frac{D_b}{b}\left(\frac{\langle \Delta \boldsymbol{X}^{B} \rangle}{\Delta t} + \frac{\langle \Delta \boldsymbol{X}^{HS} \rangle}{\Delta t}\right). \tag{3.35}$$

Noting that the average Brownian displacement is zero, $\langle \Delta \boldsymbol{X}^{B} \rangle = 0$, one obtains

$$\boldsymbol{U} = \frac{D_b}{b}\frac{\langle \Delta \boldsymbol{X}^{HS} \rangle}{\Delta t}. \tag{3.36}$$

The Peclét number, $Pe = U(a + b)/D$, is calculated from the resulting time-averaged velocity.

We performed conventional hard-sphere BD simulations where if a bath particle collides with the motor on the passive half, it simply gives the motor a hard-sphere kick, while if it collides on the reactive half, it has a probability P_s to undergo reaction. A random number between 0 and 1 is chosen and compared with the reaction probability P_s (0 no

reaction, 1 complete reaction). If no reaction occurs, then the bath particle collides with the motor just as it does on the nonreactive half. If the bath particle reacts, then it is simply removed from the system. We examined the cases when hard-sphere kicks of bath particles occur before or after reaction, however, both gave the same results. Overtime, all bath particles will be consumed by the motor, so to achieve a steady state (for which the theory has been developed), each time a bath particle reacts a new bath particle is inserted at random somewhere within the unit cell. In this way the bath particle concentration remains uniform over time and mimics an infinite system. The unit cell was chosen large enough (typically 500 to 5,000 bath particles) so that periodic effects are minimized. For large control volumes, the random bath particle insertion should not significantly affect the time-averaged measurements.

In the simulations, the motor is included in the definition of the volume fraction, and therefore there is a $O(1/N)$ error in determining ϕ_b. However, the number of bath particles N in the box was chosen by making sure that the volume fraction of the motor is small, $\phi_a = (a/b)^3 \phi_b / N \ll 1$, therefore, this deviation is not significant. All runs were started from a random hard-sphere configuration by allowing the system to equilibrate for volume fractions below the hard sphere phase boundary $\phi_b \approx 0.494$ (Fasolo and Sollich 2003), even though the bath particles form an ideal gas. The simulation run for very dilute solutions ($\phi_b \ll 1$) has to be longer than those for concentrated solutions. A longer duration allows for more bath particles to collide with the osmotic motor in a regime where bath particles are far from each other. Systems were allowed to reach a steady state before averaging began. We varied the number density of bath particles by a factor of 10, the ratio of motor to bath size by a factor of 12 and the time step in the simulations by three orders of magnitude in order to examine the fixed motor force and the free motor velocity. While the

BD simulations should correspond to the analytical model, note that the force imparted to the motor comes directly from the hard-sphere collisions with the bath particles, not from any integration of the concentration distribution over the surface as in (3.16). Multiple runs were performed in order to determine the statistical variation in properties.

As mentioned previously, the irreversible first-order reaction on half motor is introduced in BD simulations by the reaction probability P_s, which relates to the number of reacted (or consumed) bath particles. One of the central issues in this problem is the relation between the reaction probability P_s and the speed of reaction κ. This problem is resolved by examining the probability of finding Brownian particles in the proximity of a boundary. Lamm and Schulten (1983) derived a solution for the particle density distribution for the cases of an imperfect reactive (where not every collision leads to reaction), reflecting, and absorbing boundary in the presence of an external force. They also proposed some very useful one-dimensional Brownian algorithms for generating the displacement of particles near reactive and reflecting boundaries based on the exact probability distribution for diffusion near such surfaces. In fact, it was extended by Lamm (1984) to treat three-dimensional spherically symmetric diffusion cases. From these investigations, an optimized BD method was constructed, which considers issues near boundaries and was used for calculating the steady-state bimolecular rate constants of diffusion-influenced reactions (Northrup et al. 1984) with an efficiency never achieved with primitive methods. As Northrup et al. (1984) noted, a survival probability ω is computed from the ratio of the distribution for the case of an imperfect reactive boundary and the distribution for the case of a reflecting surface. Thus the reaction (non-survival) probability P_s is given by $1 - \omega$,

$$P_s = 1 - \left(\frac{1 - \left(Da - \frac{Pe}{2}\right)\sqrt{\pi \Delta t} \exp\left(\left(Da - \frac{Pe}{2}\right)^2 \Delta t\right) \mathrm{erfc}\left(\left(Da - \frac{Pe}{2}\right)\sqrt{\Delta t}\right)}{1 + \frac{Pe}{2}\sqrt{\pi \Delta t} \exp\left(\frac{Pe^2}{4}\Delta t\right) \mathrm{erfc}\left(-\frac{Pe}{2}\Delta t\right)} \right). \qquad (3.37)$$

We made Eq. (3.37) dimensionless by scaling time with the relative diffusive time $(a+b)^2/D$. For more details on the reaction probability derivation we refer to Lamm and Schulten (1983) and Northrup et al. (1986). The reaction probability P_s approaches unity in the case of diffusion-limited consumption, or very fast reactions. On the other hand, in the limit of $P_s \ll 1$ (slow reactions) the whole process is controlled by the reaction. In this work, the formula for P_s (3.37) could be used to find the corresponding Damköhler number Da required to compare simulation results with the theoretical solutions.

Here we propose a simpler formula for the reaction probability P_s that approximates Eq. (3.37) and satisfies the limiting cases for slow and fast reactions. To construct this formula, first we examine all mechanisms acting on the motor and their corresponding characteristic velocities as stated in the boundary condition at contact: $D\partial g/\partial r = (\kappa h(\boldsymbol{n}) - U)g$. On the right-hand side we combined the two non-Brownian processes, reaction and advection, into one. Note the speed of reaction κ is limited by the relative advection velocity U. The non-Brownian part has effective velocity $\kappa - U$ and balances Brownian motion (left-hand side). The characteristic Brownian velocity is given by $U^B \sim \Delta X^B/\Delta t \sim \sqrt{D\Delta t}/\Delta t$, where we have considered the Brownian process broken in discrete steps. Consider the ratio of the non-Brownian part with effective velocity $\kappa - U$ to the Brownian velocity U^B, which is given by $(\kappa - U)\sqrt{\Delta t/D}$. After scaling time by the relative diffusive time scale $(a+b)^2/D$, the ratio results in $(Da - Pe)\sqrt{\Delta t}$, which approximates to the relevant parameter $(Da - Pe/2)\sqrt{\Delta t}$ observed in (3.37). We construct the reaction probability P_s by a rational function made up of this parameter:

$$P_s \sim \frac{(Da - Pe)\sqrt{\Delta t}}{1 + (Da - Pe)\sqrt{\Delta t}}. \tag{3.38}$$

Even though Eq. (3.38) is simple in comparison with (3.37), it allows us to get the
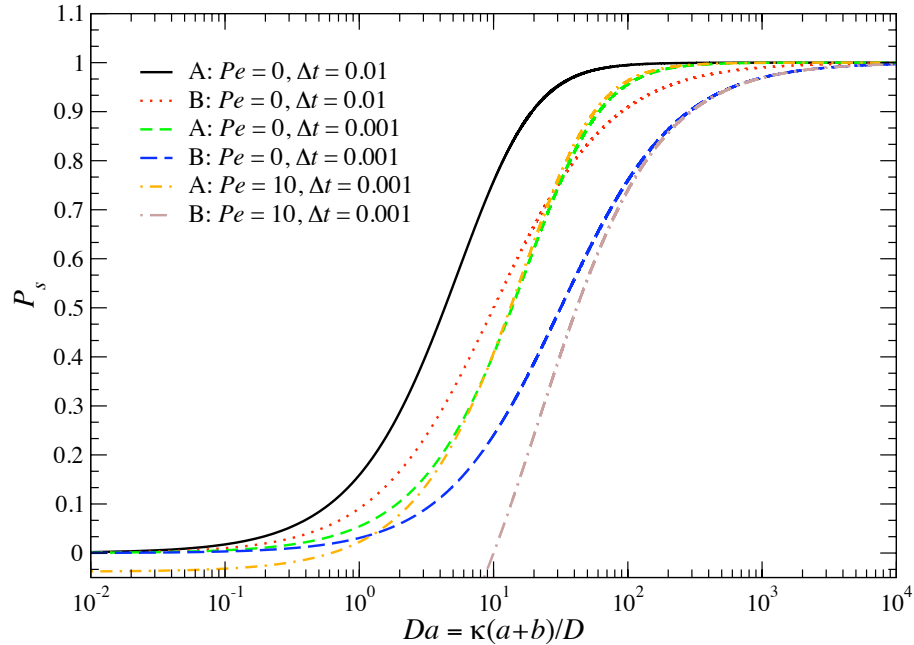
Figure 3.2: The reaction probability P_s as a function of Da for various Pe and Δt (scaled by the relative diffusive time $(a+b)^2/D$). Label A is Eq. (3.37) and label B is Eq. (3.38).

Damköhler number. The resulting Peclét number must be calculated from multiple simulation runs to properly obtain an average Da, and the resulting Damköhler number is accompanied by error bars.

In Figure 3.2, we plot (3.37) (labeled A) and (3.38) (labeled B) as a function of Da for various Pe and Δt. At $Pe = 0$, both equations are in good agreement in the limits of low and high Da for all Δt. From (3.38), it is clear that for positive reaction probability ($P_s > 0$), which must always be the case, Pe cannot be greater than Da. (This restriction is physical and it is demonstrated theoretically in Section 3.5.2.) Thus, the reaction probability resulting from (3.37) is only valid when $Da \geq Pe$. Note that for intermediate values of Da the reaction probability (3.37) is greater than the simple constructed formula (3.38). By using the proposed formula (3.38) some accuracy in Da (specifically at intermediate Da) is sacrificed in order to make progress; however, it surprisingly shows in the results to work

very well for the values considered in the simulations (see BD simulation results in the next section).

3.5   Results

We proceed to examine the microstructural deformation caused by the surface reaction for both osmotic motor scenarios (fixed and free), adopting an axisymmetric spherical polar coordinate system with origin at the center of the osmotic motor (Figure 3.1). After analyzing the microstructure relative to the motor, a solution for the osmotic force can be obtained. For the fixed motor case, the problem can be solved for all stochiometric/diffusivity factor $(1 - sD_R/D_P)$. But for the free case only the case of $sD_R/D_P \rightarrow 0$ is considered. The effect of nonzero sD_R/D_P (apart from the scale factor in force (3.16)) will be quantitative, not qualitative.

Theoretical results shall be compared to Brownian dynamics simulations. Because we are interested in measuring the time-averaged osmotic force and thus the motor velocity, and we only have one motor per simulation, long and multiple runs are required to obtain accurate results. All simulation results are accompanied by error bars. Although the particles do not interact hydrodynamically, a free motor can affect itself due to the periodicity of the simulation cell through a long-range deformation of the surrounding microstructure. The motor can leave a "trail" that is almost free of particles whose length increases with faster speeds. This was also observed in the microrheology problem discussed by Carpen and Brady (2005). It is important to be aware of this effect to size the simulation cell accordingly.

3.5.1 Fixed motor

As described in Section 3.3, the disturbed microstructure for the fixed motor is governed by the Laplace's equation subject to no disturbance ($g \sim 1$) far away from the motor and at contact the bath particle flux $\boldsymbol{j}$ balances the nonuniform reaction. It is well know that the solution of the diffusion equation obtained via separation of variables is

$$f(r,\mu) = \sum_{m=0}^{\infty} A_m r^{-(m+1)} P_m(\mu), \tag{3.39}$$

where $P_m(\mu)$ is the Legendre polynomial of order m and argument $\mu = \cos\theta$ and A_m are unknown constants to be determined from the boundary condition at contact (Abramowitz and Stegun 1965). All A_m are only functions of Da. Although the microstructural deformation function (3.39) can be fully specified analytically for all Da by calculating the coefficients A_m, it is instructive to first examine the microstructural deformations that arise in the low- and high-Da regimes for the fixed osmotic motor. The nondimensional function $\mathcal{F}(Da)$ is computed from the pair-distribution function at contact and then the osmotic force. Both asymptotic limits are computed from (3.39) and their corresponding boundary conditions.

3.5.1.1 Limiting cases

At small Damköhler numbers when the ratio of the speed of reaction to the diffusive velocity is much less than unity, the suspension is only slightly disturbed from its equilibrium state, enabling the calculation of the pair-distribution function via a perturbation series expansion in Da, based on the general non-uniformity criterion proposed by van Dyke (1975). At $Da = 0$, the only valid solution for g is simply 1, corresponding to an undisturbed mi-

crostructure. The perturbation to g is illustrated by the density plot in Figure 3.3, where the microstructure is nearly isotropic. Bath particles are consumed on the reactive side decreasing their local concentration near the motor. Thus, there are more collisions with bath particles on the passive side of the motor, resulting in an imbalanced osmotic pressure and a force on the motor in the direction of the decreasing bath particle concentration. In this limit, it is simple to show that the first term of $O(Da)$ for the nondimensional function $\mathcal{F}(Da)$ is given by

$$\mathcal{F}(Da \ll 1) = \frac{3}{8}Da. \tag{3.40}$$

The resulting osmotic force is linear in Da: $F^{osm} \sim n_R kT(a+b)^2(1-sD_R/D_P)Da = n_R(a+b)^3(1-sD_R/D_P)6\pi\eta b\kappa$, where we have used the Stokes-Einstein-Sutherland expression for the bath particle diffusivity $D_b = kT/6\pi\eta b$. This has a simple physical interpretation: Each bath particle reacting with the motor strikes at speed κ and thus hydrodynamic force $6\pi\eta b\kappa$ and there are $n_R(a+b)^3$ colliding bath particles. The stoichiometric/diffusivity factor, $(1 - sD_R/D_P)$, then gives the net osmotic force.

In the limit as $Da \to \infty$ (very fast reaction), the diffusion of bath particles towards the reactive surface is slow in comparison to the speed of reaction. In this limit, one finds that the concentration of bath particles on the reactive half is zero; the microstructure experiences total deformation ($g = 0$). On the passive half the impenetrability condition continues to hold ($\partial g/\partial r = 0$). As shown in (3.39), an exact analytical description of the microstructure is only obtained in the limit as $m \to \infty$ (all A_m coefficients are needed). To overcome this analytical limitation, we approximate g by truncating the series at $m = m_{max}$ such that its contact value for all μ at m_{max} and at m_{max+1} is within an accepted error of 0.1 percent. Having considered this criteria, we found that at $m_{max} = 150$ so that $A_m = 0 \; \forall$
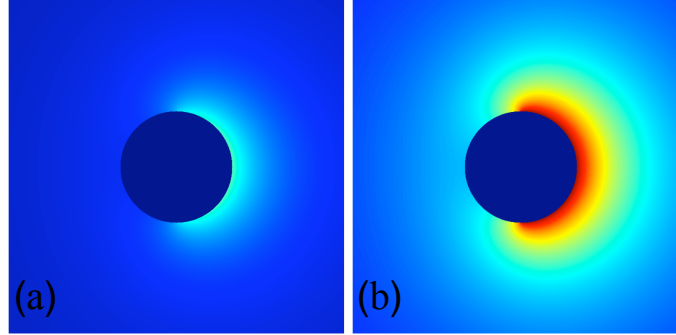
Figure 3.3: Low- and high-Da microstructural deformation in the plane of symmetry of the fixed osmotic motor. Red is low bath particle probability density and blue is the uniform level far from the motor. (a) Diffusion dominates at low Da, giving $F^{osm} \sim n_R kT(a+b)^2(1 - sD_R/D_P)Da$. (b) High Da, giving $F^{osm} \sim n_R kT(a+b)^2(1 - sD_R/D_P)$. The right half of the motor is reactive and its net osmotic force is from left to right.

$m > m_{max}$ and the microstructure is accurately represented in this limit. Figure 3.3 shows the density plot in the high Da limit, where no bath particles can be found near the reactive surface. Therefore, the value of $\mathcal{F}(Da)$ in the $Da \to \infty$ limit was found to be ~ 0.4515. In this regime of fast reaction, the osmotic force saturates and simply scales as the jump in bath particle concentration from the passive ($g \sim O(1)$) to reactive ($g = 0$) side times the area: $F^{osm} \sim n_R kT(a+b)^2(1 - sD_R/D_P)$.

3.5.1.2 Arbitrary Da

Having studied the two limiting cases for the fixed motor, we proceed to obtain the microstructure for arbitrary values of Da, and from there we move on to the osmotic force. Figure 3.4 shows the pair-distribution function at contact for various Damköhler numbers. As expected, the pair-distribution function at the reactive surface goes to zero as Da is increased. The concentration of bath particles jumps to higher values near $\pi/2$ ($\mu = 0$), clearly showing the two distinctive surfaces. Note that at the passive suface, $g(\boldsymbol{r})$ also decreases as Da is increased, suggesting that bath particles migrate from this region to the reactive surface. This is occurring because the reactive half is a sink for bath particles. In
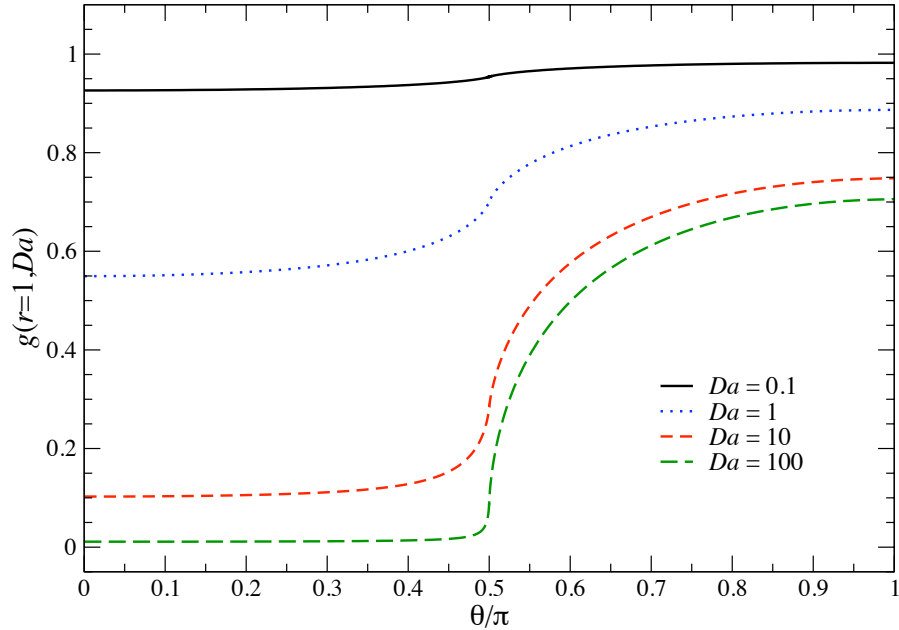
Figure 3.4: Pair-distribution function at contact for the fixed motor as a function of θ for various Da. The reactive and passive surfaces are located from 0 to $\pi/2$ and $\pi/2$ to π, respectively.

the limit as $Da \to \infty$, the pair-distribution function at contact in the passive side scales as $O(1)$, which is independent of the speed of reaction.

The major limitation of the general solution (3.39) is that as Da is increased, a considerable number of coefficients A_m in the expansion (3.39) are necessary to accurately represent the perturbed microstructure, making its implementation less practical. Even though we found that 150 terms in the series was good enough to properly represent the microstructure at high Da numbers, it is not entirely computationally feasible to calculate $\mathcal{F}(Da)$ for all Da using a symbolic mathematics program. It did work quickly and accurately in the limit as $Da \to \infty$ because its corresponding boundary conditions are simple and independent of Da, which allows us to compute many coefficients A_m in a reasonable amount of time. Therefore, we compute the pair-distribution function with fewer terms (or coefficients) in the series (24 to be exact) and its value at contact to calculate $\mathcal{F}(Da)$. At first, the solution

of $\mathcal{F}(Da)$ agrees with the low-Da limit, but diverges at high Da numbers as expected. A more accurate solution for $\mathcal{F}(Da)$ is obtained by a (9-9) Padé approximant used to extrapolate $\mathcal{F}(Da)$ to higher Da numbers. A (9-9) Padé approximant, plotted in Figure 3.5, shows that $\mathcal{F}(Da \to \infty) = 0.4485$, quite close to the expected value of 0.4515 from the asymptotics. We expect Figure 3.5 to represent a universal curve for the fixed osmotic force which has been made nondimensional by $kT/(a+b)$, the fraction of bath particles in the motor volume, $\phi = n_b(a+b)^3\, 4\pi/3$, and the stoichiometric/diffusivity factor $(1 - sD_R/D_P)$. The open symbols in the figure are the results of Brownian dynamics simulations for various conditions. We have used the proposed formula for P_s in order to find Da and construct this figure; it shows the formula works fine for the studied values. Clearly, the scaled osmotic force does not depend on the bath particle volume fraction ϕ_b, size ratio a/b, and from the time step Δt used in the simulations. The transition from reaction- to diffusion-controlled regimes occurs approximately at a Damköhler number of unity.

It is instructive to ask now what would be the magnitude of the force that must be exerted on the motor to keep it fixed? And what would happen to the local microstructure and the osmotic force if the motor were allowed to move? As described earlier, the maximum force occurs in the limit as $Da \to \infty$ for large motors $(a \gg b)$, $F^{osm} \sim n_b k_B T a^2$, where the force saturates. (For the benefit of this illustration, we have assumed $s = 0$.) Consider a motor of $a = 1\,\mu$m with a 0.1 M bath particle concentration. The resulting osmotic force is of order $0.2\,\mu$N, a respectable and easily measured force. In fact, it is rather large, as optical tweezers typically exert nano-Newton forces (Faucheux et al. 1995) and biological motors exert pico-Newton forces (Montemagno and Bachand 1999). Similar disagreement holds when compared to depletion forces that lead to depletion flocculation (Jenkins and Snowden 1996). Indeed, if the motor was released, it would start to move at a speed of
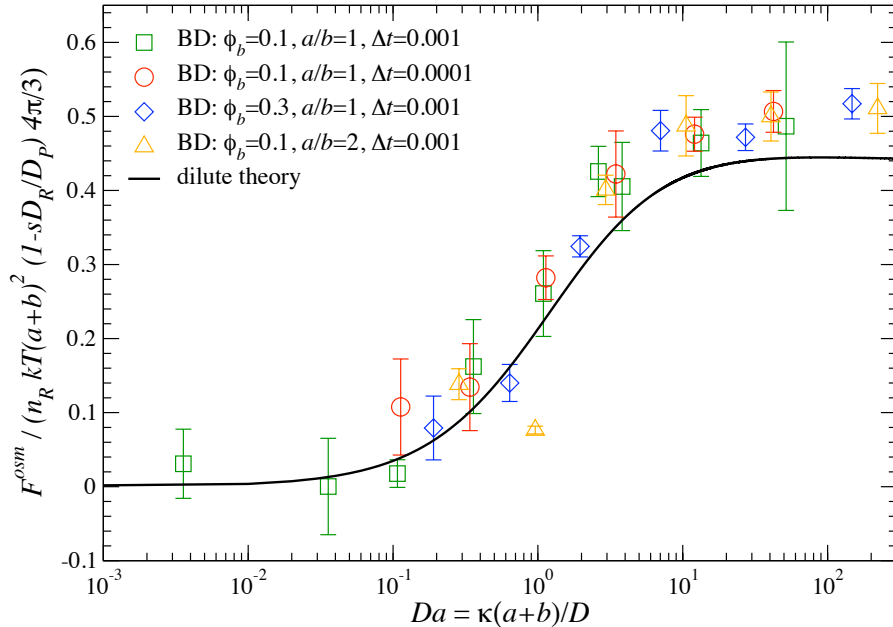
Figure 3.5: The osmotic force F^{osm} scaled $n_R kT(a+b)^2(1-sD_R/D_P)4\pi/3$ plotted against Da for various bath particle volume fractions, ϕ_b, size ratios a/b, and simulation time steps Δt. The theoretical prediction (curve) is compared with Brownian dynamics (BD) simulations (symbols).

order $10\,\mathrm{m/s}$. This surprising and aphysical result is resolved by noting that the motor cannot travel any faster than the bath particles can diffuse — that is, no faster than their diffusive velocity $U_{bath} \sim D/(a+b)$. If the motor were to move faster than this velocity, bath particles would accumulate in front of the motor on the reactive side and a deficit would appear behind the motor, as the bath particles could not keep up. The motor would thus loose the propulsive force that caused it to move in the first place or even reverse the direction of motion. The resolution of this paradox is to recognize that in a frame of reference traveling with the free motor, there will be an advective flux of bath particles towards the motor that will alter the bath particle probability distribution about the motor and consequently, the propulsive osmotic force. In what follows, we shall see a detailed picture of the microstructure as the osmotic motor moves freely (and with directionality) and how that compares to the fixed motor problem. We also show that the velocity of the

free motor for any Damköhler number is limited by the parameter β — the number of bath particles within a bath particle radius of the motor surface.

3.5.2 Free motor

When the osmotic motor moves, bath particles may accumulate on the reactive side and some could react. As the motor travels forward eliminating the bath particle concentration deficit, another one would appear on the passive side. As mentioned earlier, here we only consider the limiting case of $sD_R/D_P \to 0$ for which the product distribution drops out and the total pair-distribution function is the same as that of the reactants. The pair-distribution function $g = 1 + f$ is governed by the advection-diffusion Eq. (3.18) with associated boundary conditions (3.13) and (3.19). The pair-distribution function must be solved simultaneously with the implicit formula for the Péclet number, $Pe = \beta\mathcal{F}(Da, Pe)$, that also depends on the pair-distribution function via the nondimensional function $\mathcal{F}(Da, Pe)$. It is clear from Eq. (3.19) that the advective flux of bath particles towards the motor limits the concentration gradient created at the reactive surface. In addition to the Damköhler number, the other parameter in the free motor problem is the product β acting together to establish the non-equilibrium microstructure relative to the osmotic motor, and consequently, the motor velocity. After solving for Pe, we shall obtain an expression for the motor velocity U as a function of Da and β. First, we proceed to study the microstructure for small Da numbers, which can be computed analytically via separation of variables, and from here, $\mathcal{F}(Da, Pe)$. Although the problem could be solved analytically for small departures from equilibrium, it becomes challenging for increasing Da (and also β) when you have an implicit equation for Pe that must be solved conjointly with the advection-diffusion equation. Therefore, a numerical method is employed to solve for the pair-distribution function

g, the nondimensional function $\mathcal{F}(Da, Pe)$, and thus the motor velocity for all Damköhler numbers, including the limit as $Da \to \infty$, and all values of β. The Péclet number — the ratio of osmotic velocity to diffusion $D/(a+b)$ — that arises in the small and large β regimes is also examined.

3.5.2.1 Small departures from equilibrium (slow reaction)

At $Pe = 0$ the free motor simply reduces to the fixed motor problem discussed in Section 3.5.1 with osmotic force shown in Figure 3.5. Here we examine the microstructural deformation for the free motor at small Damköhler numbers, where diffusion dominates over the speed of reaction, in order to obtain a solution of the osmotic velocity under these conditions. This slight deviation from equilibrium enables us to calculate the pair-distribution function via a perturbation series expansion in Da, similar to the one employed for the microstructure in the fixed motor problem. The $O(Da)$ perturbation turns the advection-diffusion Eq. (4.10) into Laplace's equation and its general solution is given by (3.39). Like in the fixed motor problem, to fully represent the microstructure, the coefficients A_m must be determined from the corresponding boundary conditions. Now all the coefficients are functions of Da and Pe. For small departures from equilibrium ($Da \ll 1$), it is easy to show that the first term of $O(Da)$ for the nondimensional function $\mathcal{F}$ is given by

$$\mathcal{F}(Da \ll 1, Pe) = \frac{3}{8}Da - \frac{1}{3}Pe. \qquad (3.41)$$

Note that the first term in the right-hand side of (3.41) is identical to $\mathcal{F}(Da \ll 1)$ obtained in the fixed motor problem ($Pe = 0$ case). This quantity is reduced by a dimensionless concentration gradient of $O(Pe)$ created by the advective flux of bath particles toward the

motor. Clearly, Eq. (3.41) proves that the resulting osmotic force required for propulsion is less than the one created by the fixed motor, an observation expected for all Da. Substituting Eq. (3.41) into the implicit formula for Pe (3.23), we obtain

$$Pe = \frac{\frac{3}{8}\beta Da}{\frac{1}{2}\beta + 1}. \tag{3.42}$$

This shows that for small β, the Péclet number scales as $Pe \sim \beta Da$. Near equilibrium, the osmotic velocity is linear in Da: $U \sim n_b D_a (a+b)^2 Da = n_b b(a+b)^2 \kappa$. In the limit as $\beta \to \infty$ (large motors), Eq. (3.42) reduces to $Pe = \frac{3}{4} Da$, giving the motor velocity $U = \frac{3}{4}\kappa$, which is independent of bath particle concentration and particle size.

3.5.2.2 Scaling behavior in the limit as $Da \to \infty$ (fast reaction)

In the opposite (high Da) limit, the concentration of bath particles on the reactive surface is zero ($g = 0$). On the passive half of the motor the boundary condition becomes

$$\frac{\partial g}{\partial r} + Pe\mu g = 0. \tag{3.43}$$

The influence of β in the free motor behavior is the following. In the case of $\beta \ll 1$, we found that the dimensionless function $\mathcal{F}(Da \to \infty, Pe)$ is independent of β. This suggests that Pe is linear in β at low β and high Da. Thus, the motor velocity becomes $U \sim n_b D_a (a+b)^2$.

We proceed to examine the case of the dual limits: $Da \to \infty$ and $\beta \to \infty$. These limits represent the theoretical case where the motor moves the fastest (high Pe). Indeed, we mentioned earlier that the motor cannot move faster than the diffusive velocity of the bath particles $D/(a+b)$. Surprisingly, this is not the case in the dual limits: the motor moves faster and faster as β is increased. This apparent conflict is resolved by investigating the

microstructural deformation surrounding the motor and the scaling arguments present in these two limits (high Da and β). Bath particles can not accumulate in front of the motor because they are rapidly consumed by a thin region of zero bath particle concentration created by the diffusion-limited reaction. The fast moving motor leaves behind a long depleted wake into which bath particles diffuse from the sides. Although finding bath particles near and at the passive surface is improbable, there still is a region downstream of $\mu = 0$ where $g > 0$. Most importantly it is the disappearance of this region or jump in concentration that occurs near $\mu = 0$ that controls the velocity of the motor.

On the reactive portion, there is radial boundary layer of thickness $\delta \sim O(Pe^{-1}(a+b))$. In this region the boundary layer looks locally planar, and gradients along the boundary layer are small compared with those across it. Radial diffusion balances the perpendicular component of advection, giving an approximate equation

$$\frac{\partial^2 g}{\partial Y^2} = -\mu \frac{\partial g}{\partial Y}, \tag{3.44}$$

where $Y = Pe(r-1)$ is a coordinate perpendicular to the surface of the motor. This has solution $g = 1 - \exp(-\mu Y)$, only valid in the region $0 < \mu \leq 1$.

The boundary-layer solution breaks down when $\mu Pe \leq O(1)$ because there are rapid variations in μ. We have also studied the behavior near $\mu = 0$ and there are two regions: $\mu Pe \sim O(1)$ and $Pe(r-1) \sim O(1)$. Here we have diffusion in both radial and μ directions with advection only in the μ direction, giving an approximate equation

$$\frac{\partial^2 g}{\partial Y^2} + \frac{\partial^2 g}{\partial s^2} = -\frac{\partial g}{\partial s}, \tag{3.45}$$

where $s = \mu Pe$ is a coordinate parallel to the surface of the motor. The solution of Eq.

(3.45) must match $g \sim 1 - \exp(-sY/Pe)$ as $s \to \infty$ and $g \sim 1$ as $s \to -\infty$. Since

this is only over a region of $O(Pe^{-1})$ about $\mu = 0$, this gives a contribution to the integral

$\int g\mu d\mu \sim O(Pe^{-2})$. Similar scaling arguments at high Pe are observed in the microrheology

problem discussed by Squires and Brady (2005) and Khair and Brady (2006).

But there appears to be a larger region downstream of $\mu = 0$ where $\mu Pe^{\alpha} \sim O(1)$ and

$Pe^{\delta}(r - 1) \sim O(1)$ in which there is diffusion in the radial direction and advection in both

radial and μ directions. In this region it seems that g will be $O(1)$ at contact and since

this is over the region $\mu d\mu \sim O(Pe^{-2\alpha})$, it dominates over the region above. At first, it is

unclear how this region scales with Pe (the values of α and δ, specifically). One may predict

the exponents α and δ by a boundary-layer analysis of the Smoluchowski equation in the

limit $Pe \to \infty$. We propose a new set of spatial coordinates for this region: $t = \mu Pe^{\alpha}$ and

$z = Pe^{\delta}(r - 1)$. These are then substituted into the boundary condition at contact (3.43),

giving

$$Pe^{\delta}\frac{\partial g}{\partial z} + Pe^{1-\alpha}tg = 0. \tag{3.46}$$

Clearly, this equation states that $\delta = 1 - \alpha$ in order to balance radial diffusion with radial

advection at contact. A second and final condition can be obtained by substituting the

angular and radial transformations into Eq. (3.18), and finding the right balance among

the dominant contributions:

$$Pe^{2\delta}\frac{\partial^2 g}{\partial z^2} = -\left(Pe^{1-\alpha+\delta}t\frac{\partial g}{\partial z} + Pe^{1+\alpha}\frac{\partial g}{\partial t}\right). \tag{3.47}$$

Thus, the second condition is $2\delta = 1 + \alpha$. After solving these two equations with two

unknowns, the theoretical values for the two exponents are given by $\alpha = 1/3$ and $\delta = 2/3$.
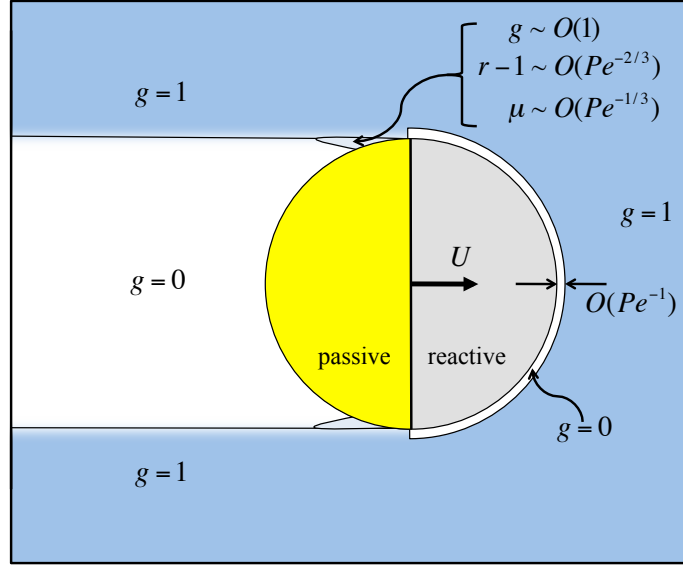
Figure 3.6: High-Pe microstructural deformations. An advection-diffusion boundary layer of width $\sim (a+b)Pe^{-1}$ forms at high Pe near the reactive surface, within which the deformation is $g = 0$. The upstream microstructure is unchanged ($g = 1$) outside of the boundary layer, and a wake with no bath particles ($g = 0$) trails the motor. There is also a small region downstream of $\mu = 0$, where $Pe^{1/3}\mu \sim O(1)$ and $Pe^{2/3}(r-1) \sim O(1)$. In this region, $g \sim O(1)$.

The governing Eq. (3.47) reduces to

$$\frac{\partial^2 g}{\partial z^2} = -\left(t\frac{\partial g}{\partial z} + \frac{\partial g}{\partial t}\right). \tag{3.48}$$

The general solution of (3.48) must match $g \sim 1 - \exp(-tz)$ as $t \to \infty$ and also be bounded by (3.46) in the zone $-\infty < t < 0$ at $z = 0$. The region $\mu d\mu$ is then $O(Pe^{-2/3})$. Since we know that $\beta \approx -Pe/\int g\mu d\mu$, we now know that $\int g\mu d\mu$ goes like $Pe^{-2/3}$. Thus, the product $\beta \approx -Pe^{5/3}/\int_{-\infty}^{0} g(0,t)t dt$, resulting in $Pe \sim \beta^{3/5}$ as $\beta \to \infty$. A picture of the various regions formed at high Pe near the osmotic motor is shown in Figure 3.6.
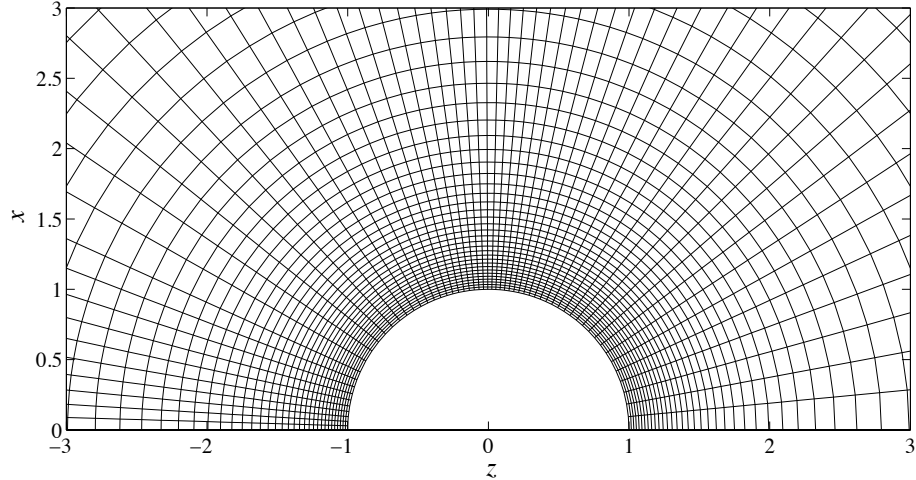
Figure 3.7: Sample finite difference grid in (transformed) spherical coordinates r, μ. Here, there are 60×60 grid points. The computational domain is the entire Cartesian $[x > 0, z]$ half space.

3.5.2.3 Arbitrary Da

The perturbation analysis presented in section 3.5.2.1 provides information on the microstructural deformation in the case of small departures from equilibrium. Attempting to continue the expansion to higher orders in Da to find the right scaling conditions in this limit is unwise. Numerically, solving the advection-diffusion equation accurately at high Da and β is a demanding task as well. The main challenge is to capture the pair-distribution function at and near contact whilst maintaining sufficient resolution in the far-field to represent the growing wake region behind the free motor. A finite difference scheme is used which accurately captures the action near the reactive surface, near $\mu = 0$, and near the passive surface. This is accomplished by implementing a grid spacing that decreases in a geometric progression towards areas of large bath particle concentration gradients. The numerical method distributes on a two-dimensional grid a dense collection of nodes close to $\mu = 0$, where the transition between reactive to passive surfaces gives large gradients in bath particle concentration. As Pe increases, one requires a greater number of grid points

82
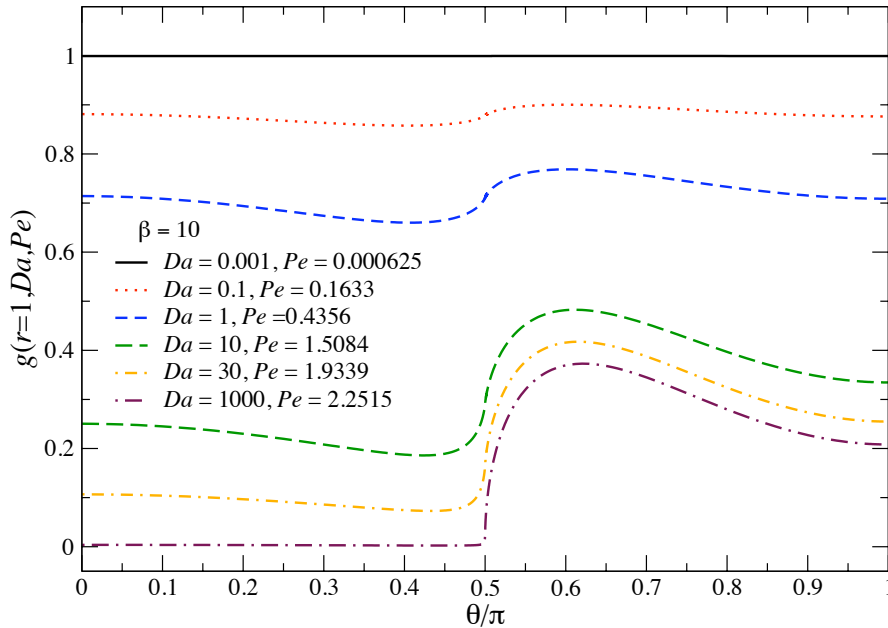
Figure 3.8: Pair-distribution function at contact for the free motor as a function of θ at $\beta = 10$ for various Da. The resulting Péclet number is included for each curve. The reactive and passive sides are located from 0 to $\pi/2$ and $\pi/2$ to π, respectively.

closely packed near contact ($r = 1$) and distributed sparsely far from the motor for the method to represent the properties of the suspension correctly. A typical grid discretization is shown in Figure 3.7.

In the limit as $Pe \to \infty$ (a consequence of fast reactions and high β), the pair-distribution function at contact is zero, except in a small region downstream of $\mu = 0$, where there is a slight jump in bath particle concentration mainly caused by the diffusion of bath particles perpendicular to the direction of motion, resulting in $\mathcal{F}(Da, Pe) \to 0$. For this case, we have assured in this region a numerical resolution (grid spacing) in the μ and r direction such that $Pe^{1/3}\Delta\mu < 1$ and $Pe^{2/3}\Delta r < 1$, respectively. Note that this criteria is based on the scaling arguments presented in Section 3.5.2.2 for the limit at high Da and β. Further details of finite difference methods can be found in LeVeque (2007).

In Figure 3.8 we plot the contact value for the pair-distribution function as a function
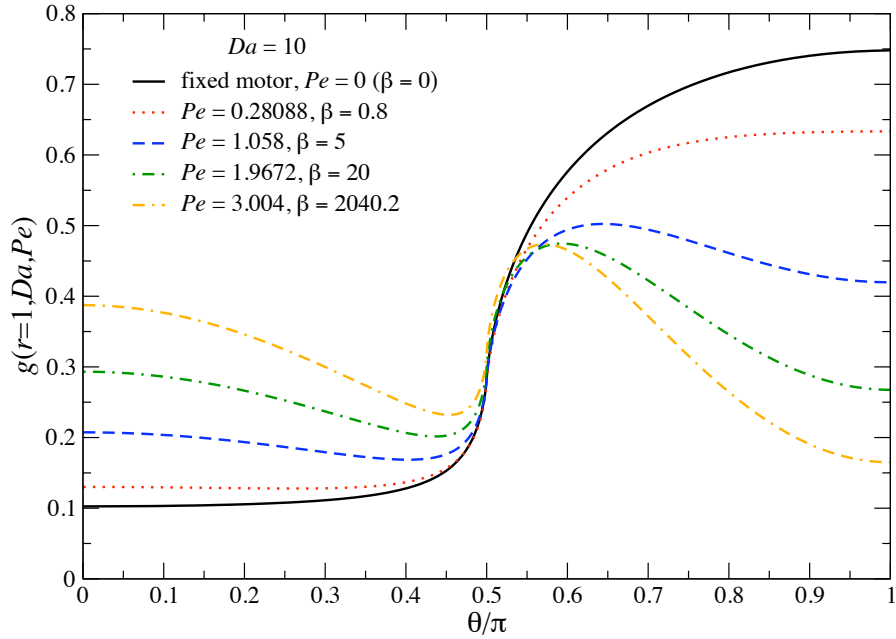
Figure 3.9: Pair-distribution function at contact for the free motor as a function of θ at $Da = 10$ for various β. The resulting Péclet number is included for each curve. The reactive and passive surfaces are located from 0 to $\pi/2$ and $\pi/2$ to π, respectively.

of the polar angle θ (scaled by π) for $\beta = 10$ and several Da resulting from the numerical solution. As expected, the pair-distribution function near the reactive surface $(0 < \theta < \pi/2)$ decreases for increasing Da. On the passive side $(\pi/2 < \theta < \pi)$, the pair-distribution function also decreases due to the motion of the motor, which leaves behind bath particles. In Figure 3.9 we show the pair-distribution function at contact as a function of the polar angle θ (scaled by π) for $Da = 10$ plotted for various β. Keeping Da constant and increasing β results in an increased concentration of bath particles on the reactive side, and a decreased concentration of bath particle on the passive side. For comparison, the pair-distribution function at contact that resulted for the fixed motor is included in the Figure 3.9. Also shown on the plots are the resulting Péclet numbers corresponding to the motor velocities. Physically, on the reactive side there is an inward radial flux of bath particles from upstream towards the motor (in a frame moving with the motor) due to advection by the relative
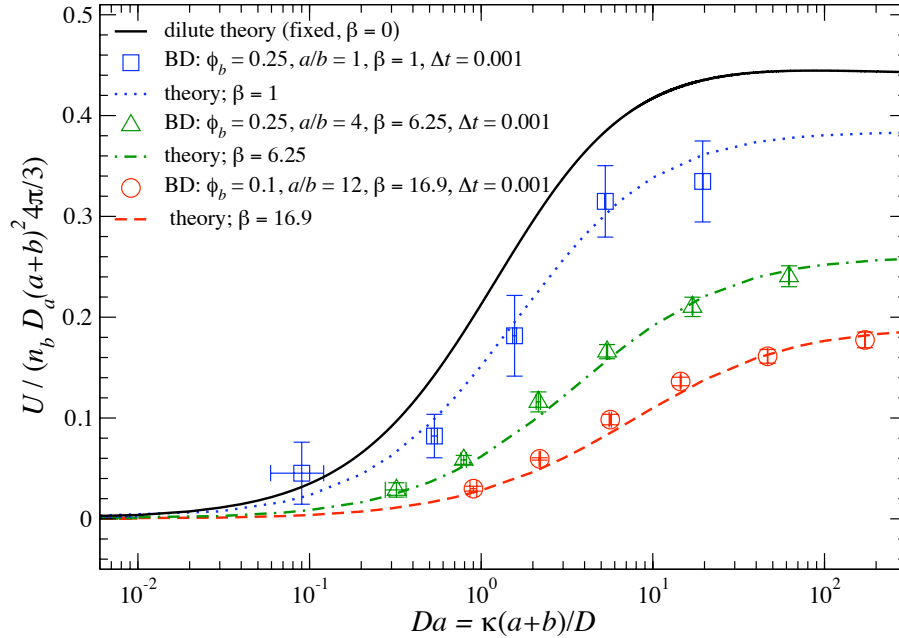
Figure 3.10: The motor velocity U scaled $n_b D_a (a+b)^2 4\pi/3$ plotted against Da for various values of β. The theoretical predictions (curves) are compared with Brownian dynamics (BD) simulations (symbols).

velocity. At finite Da, this flux of particles is hindered (or neutralized/partially consumed) by the surface reaction, resulting in an increased probability of finding a bath particle in close proximity to the motor as β is increased. On the other hand, in the passive side, the action of the relative velocity is to advect bath particles away from the motor, resulting in a decrease in the probability of finding a bath particle in this region. The resulting pair-distribution function at contact enables us to compute $\mathcal{F}(Da, Pe)$, thus simultaneously determining the Péclet number.

Figure 3.10 shows the results for the motor velocity U as a function of Da from the numerical method. The curves in Figure 3.10 correspond to increasing β. Simulation results are also included in the figure for same values of β. We show also, for comparison, the hypothetical (and nonphysical) osmotic velocity obtained by balancing the fixed motor force with Stokes drag force. The motor velocity has been made nondimensional by the
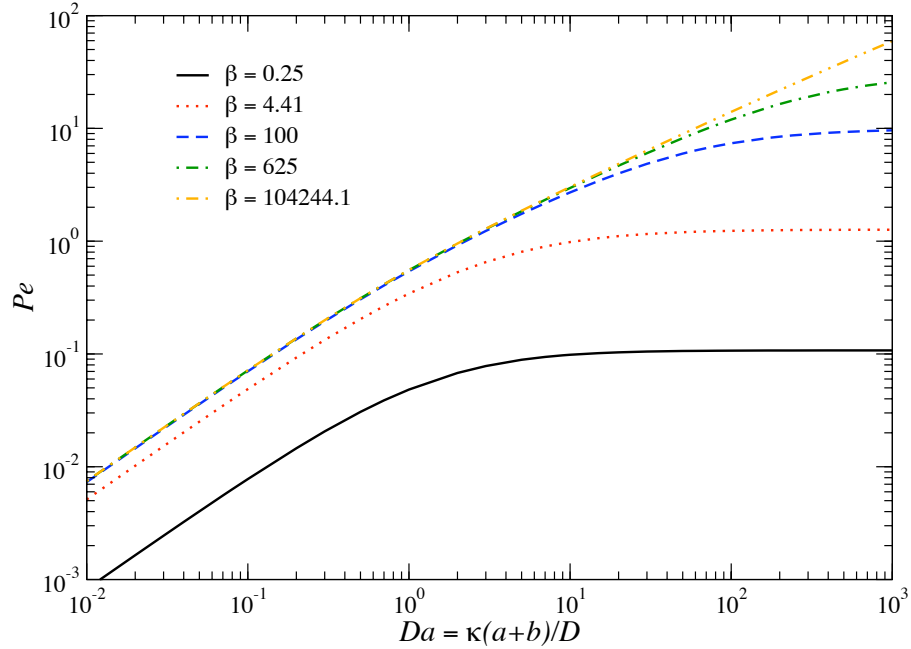
Figure 3.11: The resulting Péclet number Pe as a function of Da for various values of β

relative diffusive velocity of the bath particles, $U_{bath} = D/(a + b)$, and the fraction of bath

particles in the motor volume, $\phi = n_b(a + b)^3 \, 4\pi/3$. In contrast to the fixed motor, the

scaled motor velocity now depends on the size ratio a/b and on the bath particle volume

fraction ϕ_b, but it continues to be independent of the chosen time step Δt in the simulations.

The scaled motor velocity decreases with increasing β, showing that the advection of bath

particles indeed disturbs the bath particle concentration gradient needed for propulsion. At

small Da, the motor velocity curves are linear in Da agreeing with the analytical solution

obtained for all β in Section 3.5.2.1. In the limit of high Da and intermediate values of β,

the figure shows that all curves approach asymptotic values independent of Da, thus the

motor velocity saturates and simply scales as $U \sim n_b D_a(a + b)^2$.

The Péclet number Pe as a function of Da for various β is plotted in Figure 3.11. It

shows again for $Da \ll 1$, that $Pe \sim O(Da)$, while in the limit as $Da \to \infty$ and finite β, the

motor velocity saturates, implying that $Pe \to Pe_{max} \sim O(1)$, where Pe_{max} is a maximum
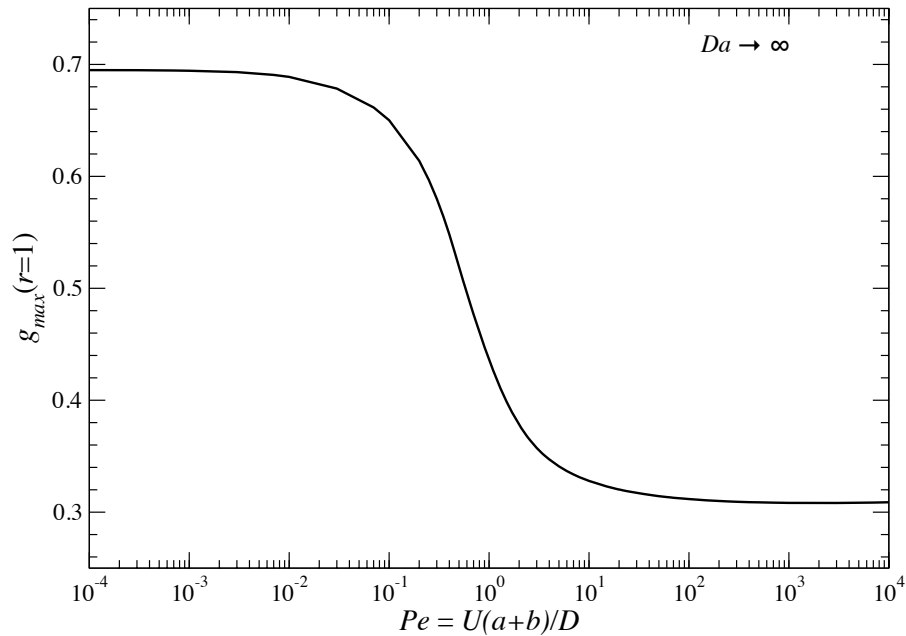
Figure 3.12: The maximum contact value of the pair-distribution function, g_{max}, as a function of Pe in the limit $Da \to \infty$

Péclet number independent of the speed of reaction. Thus the motor velocity scales as

$U \sim D/(a + b)$. However, for extremely high β the Péclet number scales as $Pe \sim Da^{3/5}$,

showing that the motor velocity scales as $U \sim D/(a + b)(\kappa(a + b)/D)^{3/5} = (D_a/b)^{5/2}\kappa^{3/5}$.

Thus, the Péclet number diverges as $Da \to \infty$. Initially we suggested in the limit $Pe \to \infty$,

$g \sim O(1)$ in the small region downstream of $\mu = 0$. To resolve this question, we plot in

Figure 3.12 the maximum contact value of the pair-distribution function, g_{max}, as a function

of Pe in the limit as $Da \to \infty$. The plot shows that g is in fact $O(1)$ in the limits of small

and large Pe, corresponding to slow and fast motor velocities, respectively.

In Figure 3.13 we examine the influence of β on Pe for various Damköhler numbers

(complementary behavior of Figure 3.11). In the limit of large motors, $\beta \to \infty$, there also

exists a maximum Péclet number, Pe_{max}, independent of bath particle concentration and

particle size for any finite Da. Each asymptotic value represents the saturation between

the motor velocity and the diffusive speed of bath particles, $U \sim D/(a + b)$. At saturation,
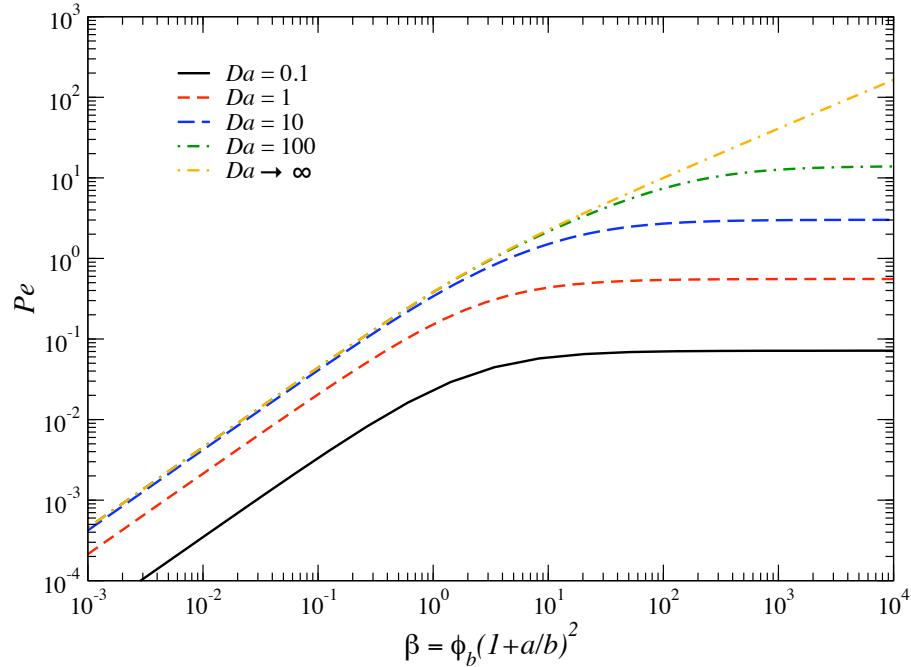
Figure 3.13: The resulting Péclet number Pe as a function of β for various values of Da

no matter how many additional bath particles are added to the suspension, the number of collisions between each side of the motor remains unchanged. We now investigate the influence of the product β on the Péclet number in the limit as $Da \to \infty$ also plotted in Figure 3.13. Although in the high-Da limit all bath particles colliding with the reactive surface are consumed (total microstructural deformation, $f = -1$), the self-created bath particle concentration gradient is limited by the advective flux of bath particles toward the reactive side and away from the passive side. This plot shows that the proposed scalings for Pe in the limit as $Da \to \infty$ are correct: the scaling condition for the Péclet number at small β is $Pe \sim \beta$ and in the limit as $\beta \to \infty$ it is $Pe \sim \beta^{3/5}$. When $\beta \ll 1$, the advective flux of bath particle is weak, thus the motor velocity scales linearly with β: $U \sim n_b b(a+b)^2 D/(a+b)$. On the other hand, in the limit as $\beta \to \infty$, the motor velocity becomes $U \sim n_b^{3/5}(a+b)^{6/5} D/(a+b)$. The transition from weak to strong advection (observed at the change in slope) in the limit as $Da \to \infty$ is near $\beta \approx 1$ and $Pe \approx 1$.
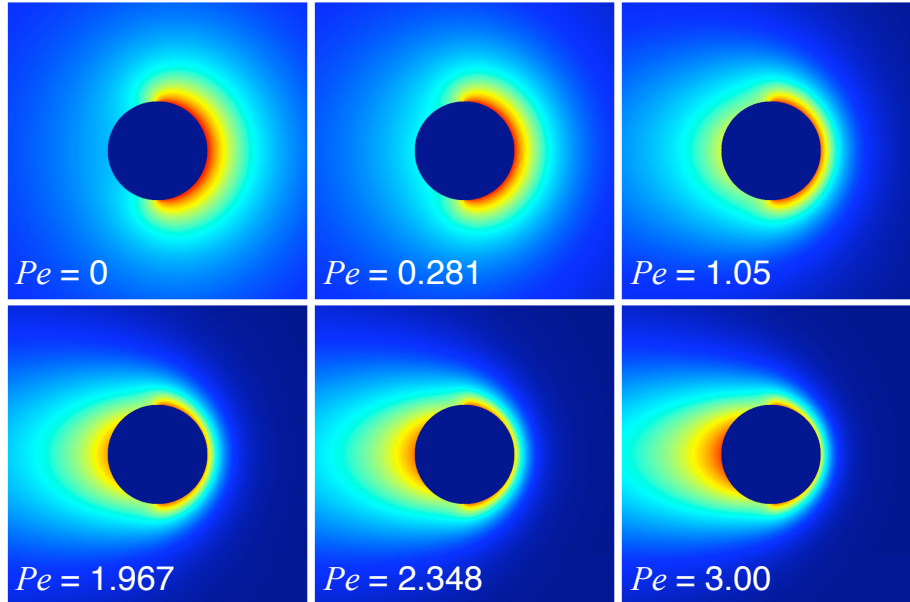
Figure 3.14: Density profiles in the symmetry plane of the osmotic motor at $Da = 10$. From left to right: Top row: $Pe = 0$ ($\beta = 0$), $Pe = 0.281$ ($\beta = 0.8$), $Pe = 1.058$ ($\beta = 5$); second row: $Pe = 1.967$ ($\beta = 20$), $Pe = 2.348$ ($\beta = 39.2$), $Pe = 3.00$ ($\beta = 2040.2$). Red is low bath particle probability density and blue is the uniform level far from the motor. The right half of the motor is reactive and its motion is from left to right.

In conclusion, the combined scaling condition for the Péclet number at high Da and β is

$$Pe \sim (\beta Da)^{3/5}.$$

Figure 3.14 shows density plots of the pair-distribution function about the motor at the same Damköhler number, $Da = 10$, but for different values of β. Also shown on the plots are the resulting Péclet numbers corresponding to the motor velocities. As the Péclet number increases, the advection of the bath particles past the motor distorts the bath particle concentration, shrinking the bath-particle-depleted region in front of the motor and leaving a trailing "wake" of reduced bath particle concentration. At even modest motor velocities (modest Pe), most of the rear of the motor has a very low bath particle concentration, which reduces the osmotic force and thus limits the speed of the motor. As shown above, this self-regulation results in a maximum motor velocity not greater than the diffusion velocity of the bath particles $U_{max} \sim U_{bath}$, unless the motor is subject to the dual limits as $\beta \to \infty$

and $Da \to \infty$ where Pe diverges and the motor moves infinitely fast.

In the next sections, we have assumed, for simplicity, that $sD_R/D_P = 0$ (e.g., consumption of reactant particles, fast diffusion of product particles). However, for the fixed motor problem, the osmotic force can be scaled by $(1 - sD_R/D_P)$ to account for other reaction stoichiometries and reactant/product diffusivities.

3.6 Scale-up to higher bath particle concentrations: relaxing ideal gas assumption

Another important aspect to consider is the excluded volume interactions among the bath particles — that is, relaxing the ideal gas assumption. This is a challenge for analytical modeling, but can easily be incorporated in BD simulations. It is not immediately obvious whether this effect will enhance or decrease the osmotic force. Although we have considered the ideal case of a suspension of hard-spheres, previous work in microrheology (Squires and Brady 2005; Carpen and Brady 2005) has shown that the results for such a model can be scaled up to predict the behavior of concentrated dispersions. It is desirable to obtain an universal curve that is independent of ϕ_b (if possible), as this would eliminate the necessity of making measurements at different bath particle volume fractions. In this section, we follow the reasoning proposed in microrheology to offer suggestions as to how our results may be extended to higher bath particle concentrations.

At small Pe, Brady (1994) showed that the microviscosity is inversely proportional to the long-time self-diffusivity D_∞^s. Further, Brady (1994) proposed a simple model for D_∞^s:

$$D_\infty^s \simeq D_0^s[1 + 2\phi_b g^{eq}(1; \phi_b)]^{-1}, \qquad (3.49)$$

where D_0^s is the short-time self-diffusivity, which in the absence of hydrodynamic interactions is just the isolated particle Stokes-Einstein-Sutherland diffusivity D, and $g^{eq}(1; \phi_b)$ is the equilibrium value of the pair-distribution function at particle-particle contact, which can be found from the Carnahan-Starling equation of state for hard-spheres (Carnahan and Starling 1969):

$$g^{eq}(1, \phi_b) = \frac{1 - \frac{1}{2}\phi_b}{(1 - \phi_b)^3}, \tag{3.50}$$

and it is only valid for $\phi_b \leq 0.50$. At high ϕ_b, the long-time self-diffusivity behaves as $D_\infty^s/D_0^s \sim [\phi_b g^{eq}(1; \phi_b)]^{-1}$. This expression is valid when the motor and bath particles are comparable in size.

The inclusion of the excluded volume interactions among the bath particles increases the number of collisions between the motor and bath particles. Physically, the term $\phi_b g^{eq}(1; \phi_b)$ that appears in (3.49) gives the number of particles contacting the motor. We shall use this as our scaling for the osmotic force, suggesting $F^{osm} \sim kT n_b g^{eq}(1; \phi_b)(a + b)^2 \mathcal{F}(Da)$. The motor velocity is just the force times the mobility of the motor, so the same scaling is applicable. In addition to scaling the force and the velocity for the fixed and free motor, respectively, we must also consider scaling the Damköhler number, which was defined based on the speed of reaction κ and Brownian speed $D/(a+b)$, and may therefore also be affected by the volume fraction. The time scale for the microstructural response is inversely proportional to the concentration-dependent long-time self-diffusivity $\tau \sim (a + b)^2/D_\infty^s$. From our previous discussion, the Brownian speed scales as $D_\infty^r(\phi_b)/(a + b)$, thus the appropriate Damköhler number is $Da = \kappa(a + b)/D_\infty^r$, where D_∞^r is the relative diffusivity at long times. (For the fixed motor case, D_∞^r is simply the long-time self-diffusivity of the bath particles). We define the scaled Damköhler number by $Da^* \sim Da[1 + 2\phi_b g^{eq}(1; \phi_b)]$. Now,
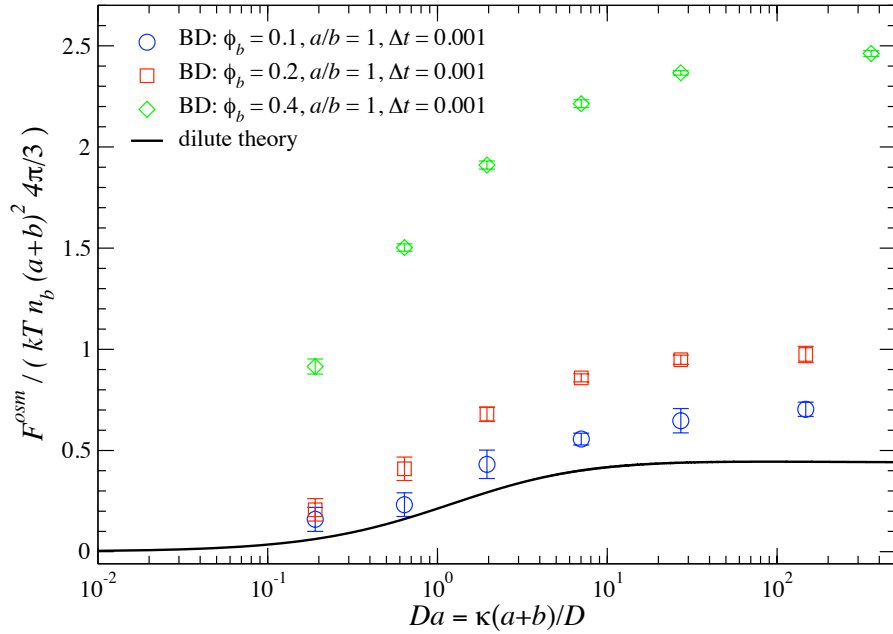
Figure 3.15: The osmotic force scaled by $kTn_b(a+b)^2 4\pi/3$ as a function of Da. The dilute theory (solid line) is compared to Brownian dynamics (BD) simulations (symbols) relaxing the ideal gas assumption for various ϕ_b. All particles in the suspension have same size and the simulation time step is $\Delta t = 0.001$.

the nondimensional function $\mathcal{F}(Da^*)$ depends on Da^*.

We also examine the resulting scaling for Pe, which now is based on the motor velocity U and relative Brownian speed $D^r_\infty/(a+b)$. The proposed "scaled" motor velocity is given by $U \sim D^r_\infty/(a+b)\beta g^{eq}(1;\phi_b)\mathcal{F}(Da^*, Pe^*)$, where the scaled Péclet number becomes $Pe^* \sim \beta g^{eq}(1;\phi_b)\mathcal{F}(Pe^*, Da^*)$. Note that Pe^* and Da^* in the function $\mathcal{F}(Pe^*, Da^*)$ are their scaled representations to account for higher bath particle concentrations. At low Pe, the dimensionless function $\mathcal{F}(Pe^*, Da^*)$ is independent of Pe, thus $Pe^* \sim Peg^{eq}(1;\phi_b)$. At high Pe, where the motor moves very fast, since the action is in the boundary layer there should be no scaling for the diffusivity. Thus, the Péclet number is independent of ϕ_b at high Pe (and $Pe^* \sim Pe$). Additional details and suggestions to scale-up the dilute theory to higher bath particle concentrations can be found in Squires and Brady (2005).
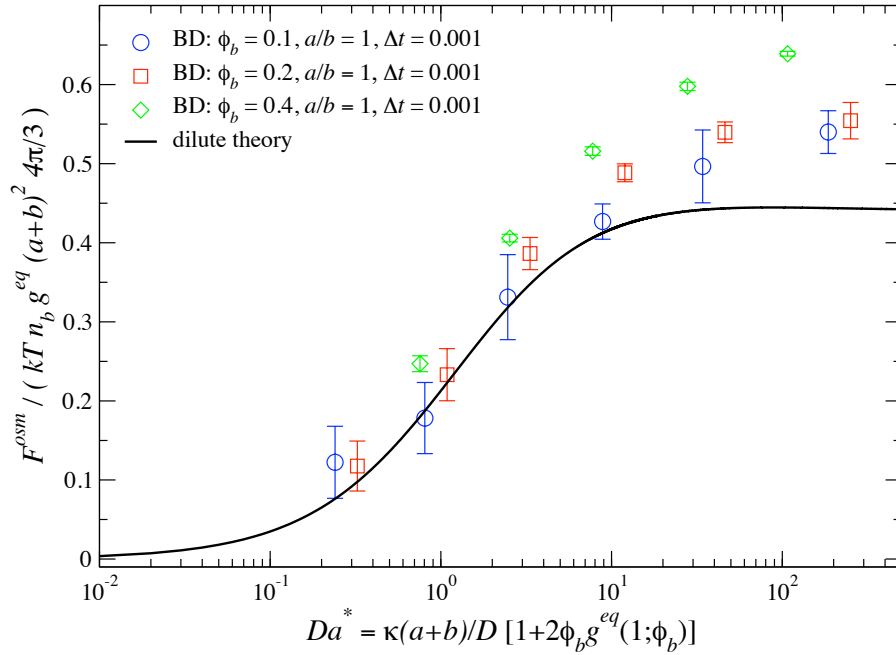
Figure 3.16: The osmotic force scaled by $kTn_bg^{eq}(1;\phi_b)(a+b)^24\pi/3$ as a function of the scaled Damköhler number $Da^* = Da[1 + 2\phi_bg^{eq}(1;\phi_b)]$. The dilute theory (solid line) is compared to scaled Brownian dynamics (BD) simulations (symbols) relaxing the ideal gas assumption for various ϕ_b. All particles in the suspension have same size and the simulation time step is $\Delta t = 0.001$.

BD simulations relaxing the ideal gas assumption were performed. Figure 3.15 shows the osmotic force resulting from BD simulations made nondimensional by $kT/(a+b)\phi$ for various bath particle volume fractions compared to the dilute theory as a function of the Damköhler number, Da. The symbols in the figure are independent of the simulation time step Δt. At low ϕ_b, the simulation results are in good agreement with the dilute theory as expected. But as ϕ_b is increased, the simulation results deviate away from the theory. The scaled results based on the proposed ideas are shown in Figure 3.16, where now the osmotic force is scaled by $kT/(a+b)\phi g^{eq}(1;\phi_b)$ and plotted against the scaled Damköhler number, Da^*. The plot shows that the ideas proposed to scale up the theory to higher bath particle concentrations are in close agreement with the simulation results. Indeed, the BD results do not perfectly overlap with the theory at high Da as observed for the "dilute limit" results

in Figure 3.5; however, the results are of the same order.

The above arguments apply equally well for the motor velocity, however, it is based on ideas that may only be valid when the motor and bath particles are comparable in size; outside this range other estimates may apply and (3.49) should be used with caution for large size ratios (or high β). The present scale-up conditions are only intended to be suggestions based on reasonable assumptions and previous works in microrheology (Squires and Brady 2005) rather than exact analytical modeling, which could be done for future investigations.

3.7 Fluctuations

When the osmotic motor is much larger than the typical length scale of the surrounding medium, the force fluctuations induced by the surrounding suspension may not be noticeable. However, if the motor size is comparable to the medium length scale, such fluctuations are important and can be considered as a type of noncontinuum effect. The work described above was intended to measure the *steady* (or mean) motion of the motor. The "steady" force it can exert may be much less then the peak fluctuating force, and the peak force may be all that is necessary to cause some desired action. Since the osmotic force arises from random collisions between the motor and bath particles, the motor experiences a fluctuating force and, in some cases, these fluctuations may provide a more important role than the averages, as in the case for living cells, heterogeneous colloidal systems, and nanotechnological applications. Surface reactions on colloidal particles not only provide an alternative for propulsion, but also could contribute by inducing/reducing and controlling these fluctuations for desirable purposes. Here we investigate the force and velocity fluctuations for the fixed and free motor, respectively, and their dependence on the Damköhler number Da

and β. The osmotic force fluctuates both in the direction of net force and in the transverse directions. Similar fluctuations are expected for the velocity of the moving motor.

With the N-particle distribution function P_N any statistical quantity may be calculated. Here, we examine the fluctuations about the mean. The force increment for a particular microstructural configuration is given by

$$\Delta \boldsymbol{F} = -kT\nabla \ln P_N. \tag{3.51}$$

As calculated in previous sections, an average gives the ensemble-averaged relative force increment. The difference between the force increment due to a particular microstructure and the average increment is given by

$$\Delta \boldsymbol{F}' = \Delta \boldsymbol{F} - \langle \Delta \boldsymbol{F} \rangle, \tag{3.52}$$

and fluctuations follow from the mean-square force variation,

$$\langle \Delta \boldsymbol{F}' \Delta \boldsymbol{F}' \rangle = \langle \Delta \boldsymbol{F}^2 \rangle - \langle \Delta \boldsymbol{F} \rangle^2. \tag{3.53}$$

For dilute systems, the term $\langle \Delta \boldsymbol{F} \rangle^2$ from the right-hand side can be neglected because it is of $O(\phi_b^2)$. Nondimensionalizing, we obtain

$$\langle \Delta \boldsymbol{F}' \Delta \boldsymbol{F}' \rangle = -\left(\frac{kT}{b}\right)^2 \phi_b \left(1 + \frac{a}{b}\right) \frac{3}{2} \int_{r=1}^{\infty} \int_{-1}^{1} \frac{\nabla g \nabla g}{g} r^2 dr \mu d\mu. \tag{3.54}$$

Before determining the fluctuations, we discuss briefly their scaling. For small Da numbers, $g \sim O(1)$ and $\nabla g \sim O(Da)$, giving an $O(Da^2)$ integral: the force fluctuations

scales as $\langle \Delta \boldsymbol{F}' \Delta \boldsymbol{F}' \rangle \sim (kT)^2 n_b(a+b)Da^2 = n_b(a+b)^3(6\pi\eta b\kappa)^2$. In the large-$Da$ limit, $g = 0$ on the reactive surface and $g \sim O(1)$ elsewhere. Thus, $\nabla g \sim O(1)$, giving an $O(1)$ integral and $\langle \Delta \boldsymbol{F}' \Delta \boldsymbol{F}' \rangle \sim (kT)^2 n_b(a+b)$.

For the free motor case, we compute the velocity fluctuations by transforming the force into velocity via Stokes drag. Thus, the nondimensional velocity fluctuations are given by

$$\langle \Delta \boldsymbol{U}' \Delta \boldsymbol{U}' \rangle = -\left(\frac{kT}{6\pi\eta a}\right)^2 \frac{1}{b^2}\phi_b \left(1 + \frac{a}{b}\right) \frac{3}{2} \int_{r=1}^{\infty} \int_{-1}^{1} \frac{\nabla g \nabla g}{g} r^2 dr \mu d\mu. \qquad (3.55)$$

For finite β the integral in (3.55) scales similar to the force fluctuations: at small Da, $\nabla g \sim O(Da)$ and $g \sim O(1)$, giving an $O(Da^2)$ integral; and in the limit as $Da \to \infty$, $\nabla g \sim O(1)$ and $g \sim O(1)$, resulting in an $O(1)$ integral. Thus, for slow reaction $\langle \Delta \boldsymbol{U}' \Delta \boldsymbol{U}' \rangle \sim D_a^2 n_b(a+b)Da^2 = (D_a/D)^2 n_b(a+b)^3\kappa^2$, while as $Da \to \infty$ the velocity fluctuations scales as $\langle \Delta \boldsymbol{U}' \Delta \boldsymbol{U}' \rangle \sim D_a^2 n_b(a+b)$. Now, for finite Da the integral in (3.55) is $O(1)$ in both low and high β limits, thus $\langle \Delta \boldsymbol{U}' \Delta \boldsymbol{U}' \rangle \sim D_a^2 n_b(a+b)$. In this case the motor experiences diffusion, and D is the relative (motor and bath) diffusivity, while for the fixed motor, D is simply the bath particles diffusivity.

In the absence of external forcing and non-uniform reaction at the motor surface, the theory predicts $\langle \Delta \boldsymbol{F}' \Delta \boldsymbol{F}' \rangle = 0$ as expected. It is important to comment that as $n_b \to 0$, when collisions are infrequent due to the high separation between particles, the fluctuations tend to zero. In contrast, the fluctuations increase in the same way the motor becomes larger by the fact that more bath particles can collide with the surface of the motor.

From Eq. (3.54) and (3.55), the parallel and perpendicular components of the force and velocity fluctuations are calculated, respectively. The nondimensional force fluctuations as a function of Da are shown in Figure 3.17. Here, $\langle \Delta F_{||} \Delta F_{||} \rangle$ is the fluctuation in the
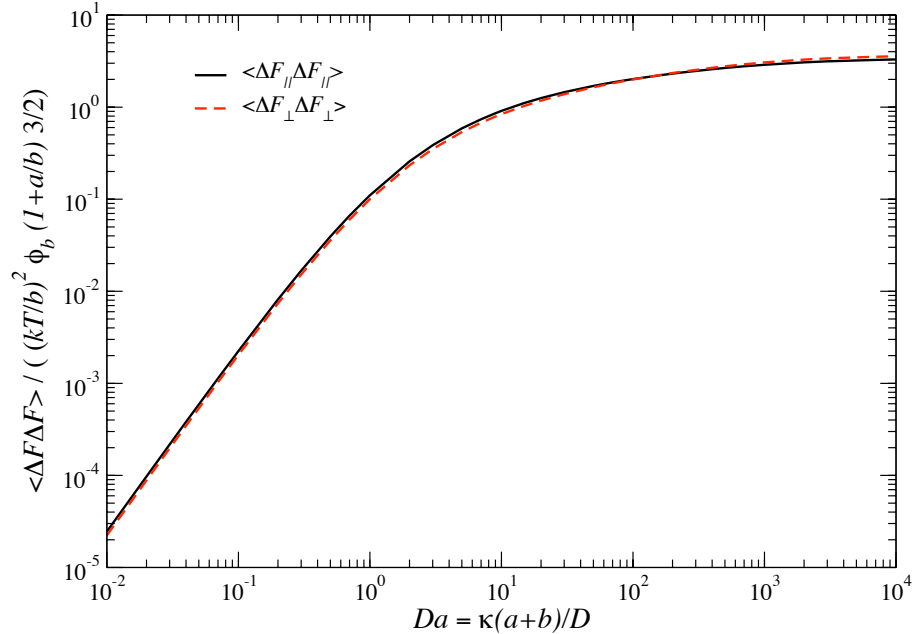
Figure 3.17: The osmotic force fluctuations on the fixed motor scaled by $3/2(kT/b)^2\phi_b(1 + a/b)$ plotted against Da: $\langle\Delta F_{||}\Delta F_{||}\rangle$ is the fluctuation in the force component parallel to the net force; $\langle\Delta F_\perp\Delta F_\perp\rangle$ is the fluctuation in the force component transverse to the net force.

force component parallel to the direction of the osmotic force, given by $\langle\Delta F_z\Delta F_z\rangle$, and $\langle\Delta F_\perp\Delta F_\perp\rangle$ is the fluctuation in the force component transverse to the direction of the osmotic force. In the case of the transverse fluctuations, there is an additional average over the two identical transverse directions, i.e., $\langle\Delta F_\perp\Delta F_\perp\rangle = (\langle\Delta F_y\Delta F_y\rangle + \langle\Delta F_x\Delta F_x\rangle)/2$. The increasing anisotropy with increasing Da is clear in Figure 3.18, which shows the ratio of parallel to perpendicular force fluctuations, $\langle\Delta F_{||}\Delta F_{||}\rangle/\langle\Delta F_\perp\Delta F_\perp\rangle$ as a function of Da. Both low and high Da give the force fluctuations ratio independent of Da. At high Da, there is a decreased probability of collisions on the reactive surface on the front of the motor. Although these will contribute to the parallel fluctuations, they will mainly contribute to perpendicular fluctuations — reaching an $O(1)$ asymptote in the limit as $Da \to \infty$.

Naturally, for the free motor we expect the same behavior for the velocity fluctuations plotted against Da at $\beta = 0$ ($Pe = 0$). In this case, $\langle\Delta U_{||}\Delta U_{||}\rangle$ is the fluctuation in
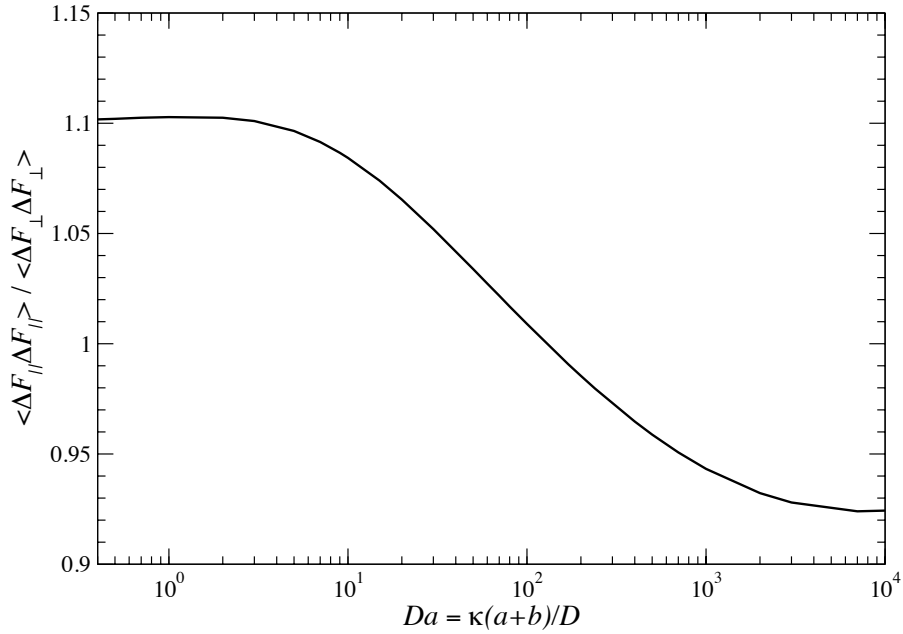
Figure 3.18: The ratio of parallel to perpendicular force fluctuations $\langle\Delta F_{||}\Delta F_{||}\rangle/\langle\Delta F_{\perp}\Delta F_{\perp}\rangle$ for the fixed motor plotted against Da

the velocity component parallel to the direction of motion and $\langle\Delta U_{\perp}\Delta U_{\perp}\rangle$ is the fluctuation in the velocity component transverse to the direction of motion, which is given by $\langle\Delta U_{\perp}\Delta U_{\perp}\rangle = (\langle\Delta U_y\Delta U_y\rangle + \langle\Delta U_x\Delta U_x\rangle)/2$. The nondimensional parallel and perpendicular components of the velocity fluctuations as a function of Da for various β are shown in Figures 3.19 and 3.20. For small Da, the nondimensional velocity fluctuations are $O(Da^2)$ independently of β. At high Da, the fluctuations are independent of Da as predicted. The ratio $\langle\Delta U_{||}\Delta U_{||}\rangle/\langle\Delta U_{\perp}\Delta U_{\perp}\rangle$ is plotted in Figure 3.21 as a function of Da for the same values of β. In contrast with the solution at $\beta = 0$ (included in the figure for comparison), the ratio at small Da decreases as β is increased due to the increment in advective forces (increasing directed motion). At high Da, the ratio increases for increasing β. The velocity fluctuations are more prominent in the parallel component because no bath particles are found at the surface at high Pe except in the region near $\mu = 0$ described earlier where $g \sim O(1)$.
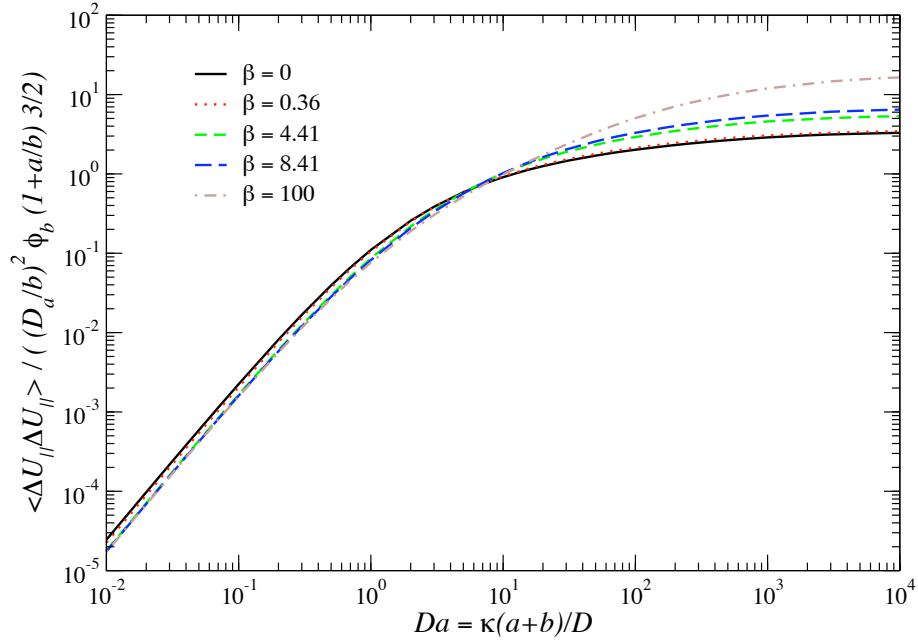
Figure 3.19: The free motor velocity fluctuation in the velocity component parallel to the net motion $\langle \Delta U_{||} \Delta U_{||} \rangle$ scaled by $3/2(D_a/b)^2 \phi_b(1+a/b)$ plotted against Da for various values of β

The nondimensional parallel and perpendicular velocity fluctuations as a function of β for low and high Da are investigated in Figure 3.22. The plot shows that both the nondimensional parallel and perpendicular velocity fluctuations are $O(1)$ at small and high β, independently of Da. Figure 3.23 shows the ratio $\langle \Delta U_{||} \Delta U_{||} \rangle / \langle \Delta U_\perp \Delta U_\perp \rangle$ as a function of β for various Da. For the values considered in this figure, note that at high β the ratio decreases as Da is increased. This information combined with Figure 3.21 suggests a more complete picture: for increasing Da the velocity fluctuations ratio increases, which is a consequence of having zero bath particle concentration at contact that exists at high Pe except in a region downstream of $\mu = 0$ that contributes with bath particle collisions perpendicular to motion. It is clear from the figures that the ratio is independent of β in the limit of low and high (but finite) Da.
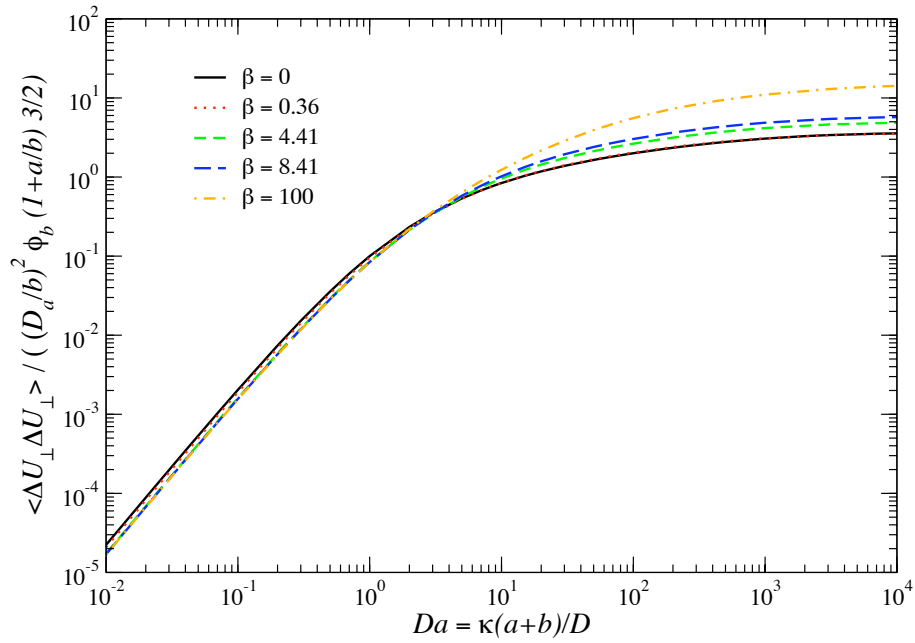
Figure 3.20: The free motor velocity fluctuation in the velocity component perpendicular to the net motion $\langle \Delta U_\perp \Delta U_\perp \rangle$ scaled by $3/2(D_a/b)^2 \phi_b(1+a/b)$ plotted against Da for various values of β
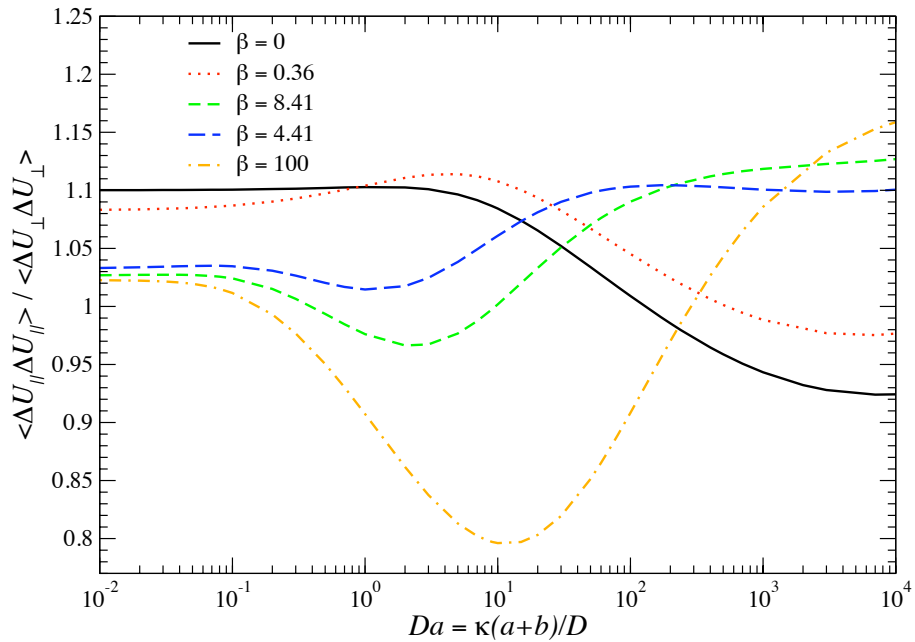
Figure 3.21: The ratio of parallel to perpendicular velocity fluctuations $\langle \Delta U_{||} \Delta U_{||} \rangle / \langle \Delta U_\perp \Delta U_\perp \rangle$ for the free motor plotted against Da for various values of β
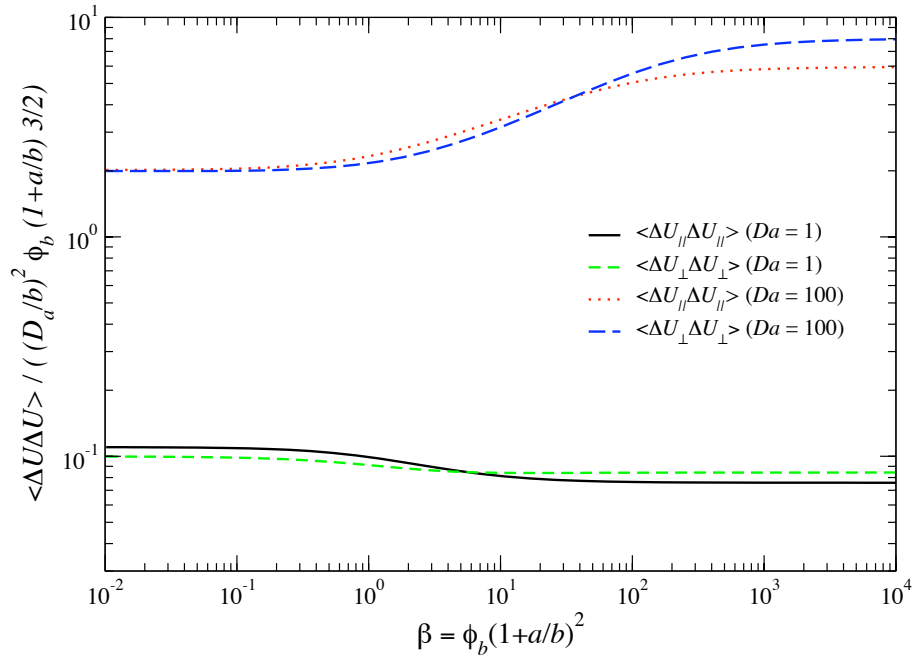
Figure 3.22: The motor velocity fluctuations scaled by $3/2(D_a/b)^2\phi_b(1+a/b)$ plotted against β for various Da: $\langle \Delta U_{\parallel}\Delta U_{\parallel}\rangle$ is the fluctuation in the velocity component parallel to the net motion; $\langle \Delta U_{\perp}\Delta U_{\perp}\rangle$ is the fluctuation in the velocity component transverse to the net motion.
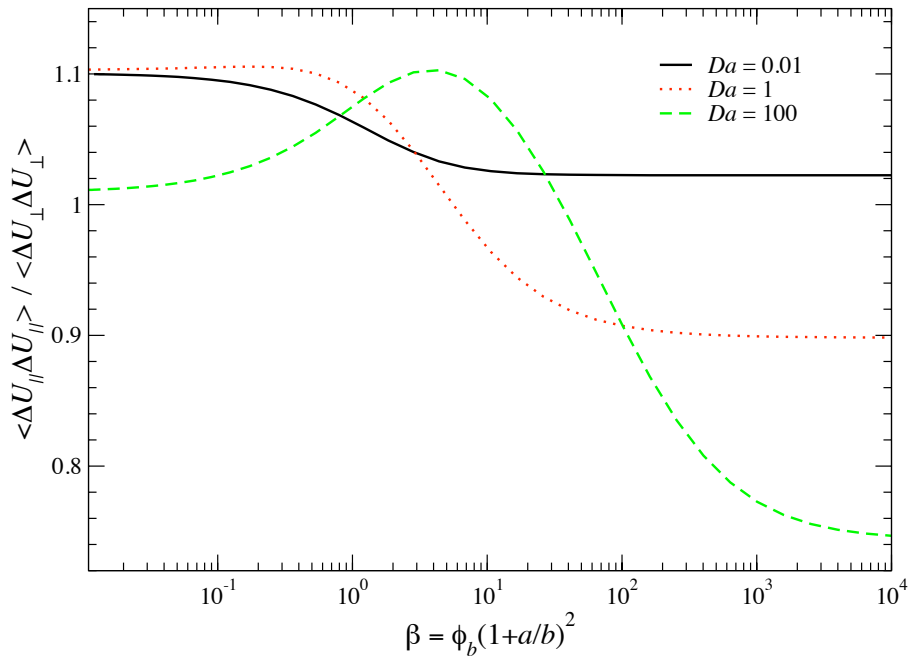
Figure 3.23: The ratio of parallel to perpendicular velocity fluctuations $\langle \Delta U_{\parallel}\Delta U_{\parallel}\rangle/\langle \Delta U_{\perp}\Delta U_{\perp}\rangle$ for the free motor plotted against β for various values of Da

3.8 Efficiency

It is relevant to ask how efficient the osmotic motor is. Energy conversion efficiency is the ratio between the useful output (mechanical work) of an energy conversion machine and the input, in energy terms. Energy conversion efficiency is not defined uniquely, but instead depends on the usefulness of the output. We suggest below an interpretation for the efficiency of conversion of chemical energy (free energy in this case) into motion via the dissipation of mechanical energy.

For ideal gas particles the amount of free energy of the suspension that changes if an additional particle were introduced is just the chemical potential given by

$$\mu = \mu_0 + kT \ln g, \tag{3.56}$$

where μ_0 is a reference value. Thus, the change in chemical potential of a reactant relative to its equilibrium probability density is $\Delta\mu = kT \ln g$. In particular, at the motor surface the change in chemical potential is $\Delta\mu = kT \ln g(r = 1)$. The rate at which the reactants supply free energy is therefore $(\boldsymbol{n} \cdot \boldsymbol{j})\Delta\mu$. The total rate of free energy supplied is

$$
\begin{aligned}
\dot{A} &= \oint_{r=a+b} \boldsymbol{n} \cdot \boldsymbol{j}\Delta\mu dS = -\int_{r=a+b} \nabla \cdot (\boldsymbol{j}\Delta\mu)dV + \oint_{r=a+b} \boldsymbol{n} \cdot \boldsymbol{j}\Delta\mu dS \\
&= -\oint \boldsymbol{n} \cdot \boldsymbol{j}\Delta\mu dS,
\end{aligned} \tag{3.57}
$$

since $\nabla \cdot \boldsymbol{j} = 0$ at steady state. At the motor surface we have the flux boundary condition $\boldsymbol{n} \cdot \boldsymbol{j} = -\mathcal{R}_R$, so that (3.57) becomes

$$\dot{A} = \oint_{r=a+b} \mathcal{R}_R \Delta\mu dS. \tag{3.58}$$

This is the entropy production, which is appropriate for an ideal gas. And there will be a similar expression for the products if created. For a first-order reaction rate, $\mathcal{R}_R = \kappa n_b g$, the free energy production is defined as

$$\dot{A} = kTn_b\,(a+b)^2\,2\pi\kappa\int_{-1}^{1} g(\boldsymbol{r})\ln g(\boldsymbol{r})h(\mu)\mu d\mu, \tag{3.59}$$

where the radial coordinate was nondimensionalized by the contact distant $a+b$.

Now, the motor has a net osmotic force exerted on it by the reactants given by $\boldsymbol{F}^{osm} = -kTn_b\oint \boldsymbol{n}g(\boldsymbol{r})dS$. From this force, the motor will have a Stokes velocity $\boldsymbol{U} = \boldsymbol{F}^{osm}/(6\pi\eta a)$. Thus, the rate of energy dissipation Φ is defined as

$$\Phi = \boldsymbol{U}\cdot\boldsymbol{F}^{osm} = \frac{1}{6\pi\eta a}\left(F^{osm}\right)^2 = \frac{kT}{6\pi\eta a}\left(2\pi n_b\,(a+b)^2\right)^2\left[\int_{-1}^{1} g(\boldsymbol{r})\mu d\mu\right]^2. \tag{3.60}$$

We define an efficiency of conversion of free energy into mechanical motion via the dissipation of mechanical energy by

$$\xi = \frac{\Phi}{\dot{A}} = \frac{\beta}{Da}\frac{3}{2}\frac{\left(\int_{-1}^{1} g(\boldsymbol{r})\mu d\mu\right)^2}{\int_{-1}^{1} g(\boldsymbol{r})\ln g(\boldsymbol{r})h(\mu)\mu d\mu}. \tag{3.61}$$

In Figure 3.24 we plot the efficiency of the fixed motor scaled by β as a function of Da (solid line). Earlier, we described that at small Damköhker numbers, where Brownian diffusion dominates over reaction, the microstructure deviates slightly from its equilibrium state proportional to Da enabling us to represent the pair-distribution function into a series expansion up to $O(Da)$, given by $g = 1 + Daf$. Substituting this two-term expansion into the efficiency formula (3.61), it is easy to show that the integral in the numerator is $O(Da^2)$ and the integral in the denominator is $O(Da)$. Thus, the efficiency is linear in β and independent
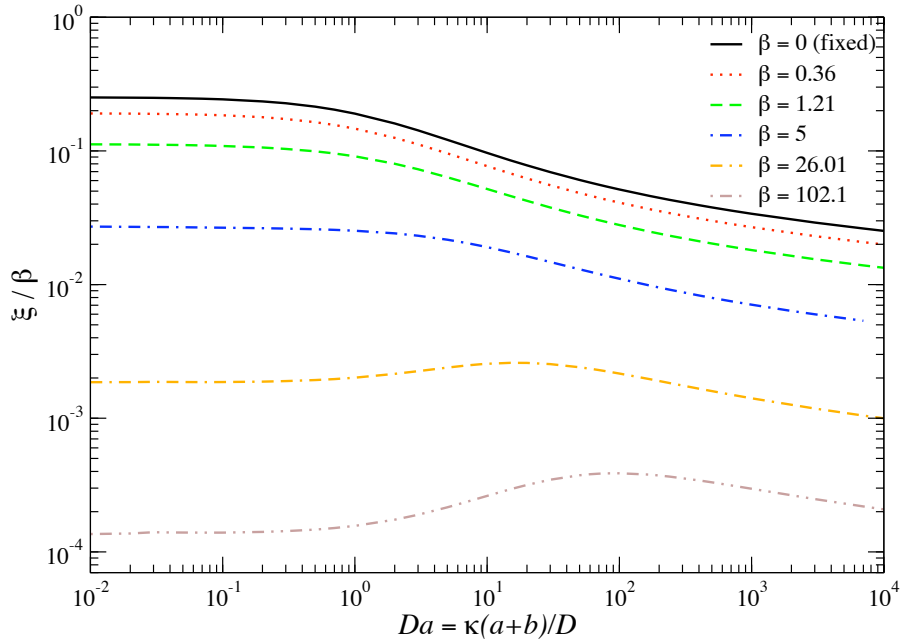
Figure 3.24: The motor efficiency scaled by β as a function of Da for various intermediate values of β

of Da in the limit as $Da \to 0$: $\xi \sim \beta$, as observed in Figure 3.24. In the opposite limit of high Da, the pair-distribution function scales as $g(1) \sim 1/Da$; therefore, the integral in the numerator is $O(1)$ and that in the denominator is $O(Da^{-1} \ln Da)$. Consequently, the efficiency of the fixed motor is $\xi \sim \beta/(\ln Da)$, which decays to zero as $Da \to \infty$. It is evident from these scaling arguments that the most efficient fixed motor (under the proposed energy conversion) is one that operates with slow reactions and that the most inefficient fixed motor is in the limit as $Da \to \infty$.

Also in Figure 3.24, we plot the efficiency of the free motor scaled by β as a function of Da for various β. The plot shows that the scaled motor efficiency decreases as β is increased, which is caused by the increment in advection (increasing Pe). Figure 3.25 is a plot of the free motor efficiency scaled by β as a function of β for various Da. For small Da, the efficiency behaves similar to the fixed case that is $\xi \sim \beta$, which is independent of the speed of reaction. But this is only reached if $\beta Da \ll 1$ so that $Pe \ll 1$. We have shown that
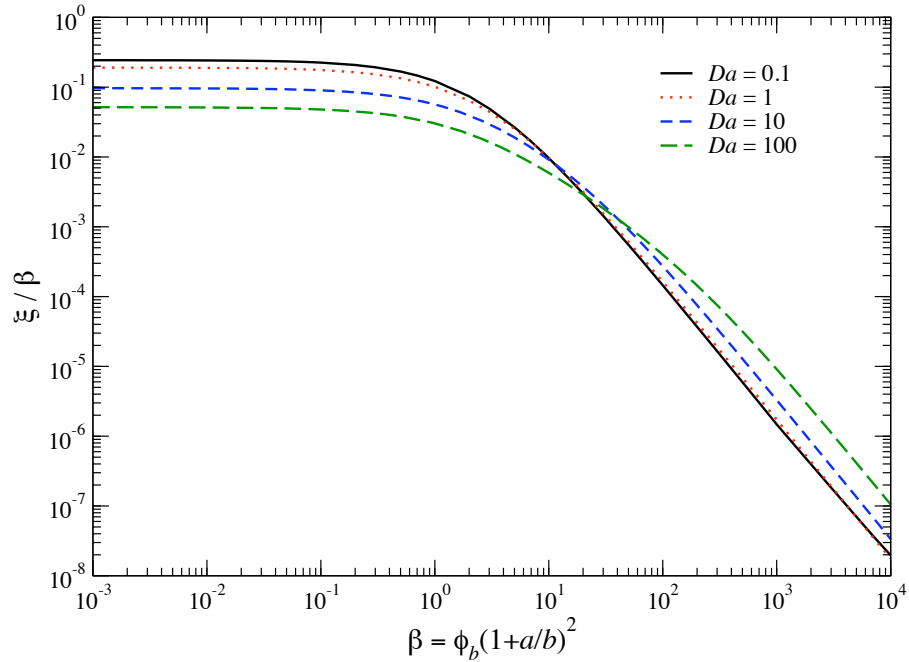
Figure 3.25: The motor efficiency scaled by β as a function of β for various Da

for any finite Da, no matter how large, there is a Pe_{max} observed in the limit as $\beta \to \infty$. This means that $\int g\mu d\mu$ must go as $1/\beta$. The denominator in (3.61) has $g(1) \sim 1/Da$ where the reaction occurs and $h(\mu)$ is zero elsewhere. Thus the integral in the denominator goes as $1/(Da \ln Da)$. Combining this together we have $\xi \sim 1/(\beta \ln Da)$ for $\beta \gg 1$ and $Da \gg 1$. The efficiency goes to zero as $Da \to \infty$, which is true for all β. The maximum efficiency for the free motor is observed at small Da and β, $\xi \sim \beta$.

Implications of this efficiency formula for other mechanisms involving chemically induced motion is unclear and further studies are needed, although this provides an exploitable and interesting perspective on how the motor could take advantage of its reaction speed and the surrounding microstructure properties to maximize the energy conversion.

3.9   Conclusions and discussion

The work presented in previous sections attempts to offer a theoretical framework for the osmotic motor. The core of our approach involves determining the reaction-induced perturbation to the suspension microstructure in order to calculate the driving force on the motor, from which the motor velocity is determined via application of Stokes drag law. We have derived an equation for the microstructure and solved it in the simplest limiting case of hard-sphere interactions in the absence of hydrodynamic interactions and rotational motion. The model was restricted to the limit where bath particles do not interact with each other and therefore behave as an ideal gas. Whilst being sufficiently simplistic to allow analytical and numerical analysis, the model nevertheless exhibits significant non-trivial properties. In addition to the theory, we developed a Brownian dynamics (BD) simulation that provided a means of verifying our theoretical results and also suggested ideas to scale up the dilute theory to higher bath particle concentrations. We examined two scenarios for the osmotic motor: one, in which the motor is held fixed by an external force $\boldsymbol{F}^{ext}$, and another where it is free to move.

Once the microstructural perturbation is known, relevant statistical quantities can be computed. We have calculated the fixed motor force for all values of Damköhler number, Da, bath particle volume fraction, ϕ_b, motor/bath size ratios, a/b, and stoichiometry/diffusivity factors, $(1 - sD_R/D_P)$. This results in a universal curve, onto which we expect a wide range of measurements will collapse. We showed that BD simulations agree with the theoretical predictions proving that the proposed simple formula for the reaction probability, P_s, is appropriate for the values considered in this work. For small perturbations to the microstructure, we found the osmotic force is linear in the Damköhler number Da. In the limit of

high Da, the force saturates and simply scales as $F^{osm} \sim n_R k_B T (a+b)^2 (1 - s D_R / D_P)$. We found this force to be large compared to typical colloidal forces indicating that this mechanism could be useful for self-propulsion (or for pumping fluids). It was shown that when the motor is set free, it moves rapidly toward the self-created low bath particle concentration region ($g \ll 1$) located near the reactive surface. Eventually (almost instantaneously) the motor catches up with bath particles reducing the gradient in bath particle concentration. Thus, the osmotic force is balanced by the viscous force acting on the moving motor.

For the free motor case, we assumed that the stoichiometry value s is zero, which simplifies greatly the governing equations. This assumption is unnecessary in the limit of small Péclet numbers, i.e., the fixed motor, and in the limit of large Péclet numbers where the effects of advection are the same for the reactants and products. The effect of nonzero $s D_R / D_P$ apart from being a scalar factor in the motor velocity will be quantitative, not qualitative. Thus, the osmotic velocity was calculated as a function of Da for various $\beta = \phi_b (1 + a/b)^2$. Also we demonstrated again that BD simulations are in agreement with the theoretical results. In general, we showed that the physical properties of the microstructure, a/b and ϕ_b (or the product β), directly contribute to the speed of the motor, an observation not shared by the fixed motor problem. For small Damköhler numbers, we showed the osmotic velocity scales as $U \sim \kappa$. In the limit of high Da, the free motor velocity saturates and scales as $U \sim n_b D_a (a + b)^2$. The advective flux of bath particles toward the motor alters the bath particle probability distribution relative to the motor and consequently, the propulsive force.

We also examined the influence of the product β on the osmotic velocity. The results in Figure 3.10 showed that the fixed motor is the limit as $\beta \to 0$ ($Pe = 0$) of the free motor; the fixed motor corresponds to an infinitely dilute suspension of bath particles. This is,

as it should be, because whether the motor is fixed or free it is just a change of reference frame. For a fixed motor there will be an advective flux at infinity to supply reactive bath particles to the motor. This also implies that the motor will induce a fluid flow to supply the bath particles and can be used as a pump — a novel microfluidic pump (and mixer). In the limit as $\beta \to \infty$ (very large motors) and for finite Da, the Péclet number also scales as $Pe \sim O(1)$, giving the motor velocity $U \sim D/(a + b)$. But at high Da and β, we found that the Péclet number goes to infinity as $Pe \sim (\beta Da)^{3/5}$. In general, we observed that at $\beta Da \ll 1$ the Péclet number is small (slow propulsion). In the limit of $\beta Da \gg 1$, advection dominates over diffusion in the local microstructure, thus Pe is large (fast propulsion). The reader should not be confused that these results are specific to the assumed reaction rate (heterogenous irreversible first-order reaction) and the size of the reactive area (half-reactive motor). Other scaling conditions and interesting features could arise for motors with different distributions of reactive area.

For a 1-μm-sized half-reactive motor and nanometer-sized bath particles (large β) the motor velocity $U \sim D/(a + b)$ is now of order 20 μm/s, a much more reasonable velocity, and one that is in fair agreement with the motivating experiments of Paxton et al. (2004). Although the mechanism suggested for the catalytic nanomotor is different from that for osmotic propulsion (Paxton et al. 2006), this result shows the significance of the speed magnitudes created by the osmotic motor for processes at nanoscale that require directed motion.

We have proposed methods to modify this theory to account for less dilute systems. Comparisons with measurements and (more) simulations will be necessary to determine whether these ideas are applicable. This could be helpful to understand the disagreement between the simulation results and the dilute theory at high Da and to extend this ideas to

cases when the osmotic motor and bath particles are different in size. Also, we computed the fluctuations resulting from the collisions between the motor and bath particles as a function of the Damköhler number and the product β. It was found that the scaled fluctuations are $O(Da^2)$ at small Da, and are independent of Da in the limit as $Da \to \infty$. For small and high β, we found that the scaled velocity fluctuations are independent of β. In addition, we calculated the ratio of parallel to perpendicular fluctuations for various Da and β, giving a better picture of how the fluctuations relate to the microstructural deformation relative to the motor.

We have derived an expression for the efficiency of conversion of free energy into mechanical energy, which measures the ability of the motor in harnessing its environment to create useful work. For an irreversible first-order reaction rate (consumption of bath particles), the motor efficiency ξ goes to zero as $Da \to \infty$. We found the efficiency of the fixed motor to be independent of Da for $Da \ll 1$. For fast reactions, the fixed motor efficiency scales as $\xi \sim \beta/(\ln Da)$. On the other hand, the efficiency of the free motor also scales as $\xi \sim \beta$ for slow reactions, but scales as $\xi \sim 1/(\beta \ln Da)$ for high Da and β. Many questions arise from investigating the motor efficiency. Can we define other types of efficiency? How does the motor efficiency compare to other reaction-driven transport mechanisms? Is it possible to design an osmotic motor as efficient as biological machines? There are many variables that could be manipulated to improve the efficiency that require further analysis, such as different portions of reactive surface on the motor and other types of reaction rate.

This work opens up many questions and future extensions for the theory and the simulations. Clearly, neither the motor nor the bath particles need to be spherical. A variety of behaviors are possible depending on the nature of the chemical reaction at the motor surface. We have considered only the simplest of chemical reactions, the irreversible first-

order reaction of product particles. And simplified to consumption of reactant particles for analytical application. How is the osmotic force modified for other chemistries? A reversible reaction? Production of bath particles rather than consumption at the free motor surface? What if there are enthalpic effects — specific interactions between the motor and the reactive species — in addition to entropic? One obvious question to ask is what is the optimal distribution of the reactive site on the motor surface? We considered one half of the motor surface to be reactive. Is this the best? Or is there an optimum for a different fraction? How does that optimum vary with the Damköhler number and the nature of the chemical reaction? What fraction of the limiting bath particle diffusion velocity can be obtained by a motor? Just how fast can it move?

In the analysis we have ignored the fact that a small motor will also be subject to its own Brownian motion, and in particular its rotary Brownian motion. As the motor rotates in response to Brownian torques the reactive side will no longer be in the same direction and this may limit the extent of its directed motion. The time scale for the establishment of the concentration profile about the motor is the diffusive time of the bath particles $\tau_b \sim a^2/D$. The time scale for rotary Brownian motion of the motor is its rotary diffusivity $D_r = kT/8\pi\eta a^3$. Thus, rotary motion of the motor will not be important as long as $\tau_b D_r \sim b/a \ll 1$, which is the case when the motor is much larger than the bath particles. Thus, the work described above is restricted to this limit. If this restriction is relaxed a large motor could travel at its osmotic velocity U for a time $1/D_r$ after which it could establish a new bath particle concentration profile and travel again at U but in a new (random) direction. Thus, for long times compared to $1/D_r$ the motor will undergo a random walk with a step length U/D_r.

In addition, we neglected hydrodynamic interactions between particles which would

affect the motor speed. Hydrodynamics would be expected to slow the motor's motion, but to what extent? At the pair level (one motor, one bath particle) hydrodynamics can be included analytically (following the work on microrheology, Khair and Brady (2006)), while for more concentrated systems, Stokesian dynamics (Brady and Bossis 1988; Banchio and Brady 2003) can be adapted to simulate reacting bath and motor particles.

The analysis can be generalized to have more than one solute (bath particle) species, and more than one motor. How will two or more motors act when they compete for the same reactant? Will a group of motors swarm together? Can this have relevance for the swarming of biological organisms?

Our investigation has demonstrated that autonomous motion can be generated quite simply by exploiting the ever-present thermal fluctuations via a chemical reaction at the motor surface. Osmotic propulsion provides a simple means to convert chemical energy into mechanical motion and work, and can impact the design and operation of nanodevices, with applications in directed self-assembly of materials, thermal management of micro- and nanoprocessors, and the operation of chemical and biological sensors. This opens up many possibilities for exploiting autonomous motion to ether propel particles and/or pump fluid, some of which are outlined in this work. Studies of autonomous motors may also help to understand chemomechanical transduction observed in biological systems (Theriot 2000) and to create novel artificial motors that mimic living organisms and which can be harnessed to perform desired tasks.

3.10   Bibliography

M. Abramowitz and I. A. Stegun. *Handbook of Mathematical Functions: with Formulas, Graphs, and Mathematical Tables.* Dover Publications, 1965.

M. P. Allen and D. J. Tildesley. *Computer Simulation of Liquids.* Oxford University Press, USA, 1989.

S. A. Allison, J. A. McCammon, and J. J. Sines. Brownian dynamics simulation of diffusion-influenced reactions — inclusion of intrinsic reactivity and gating. *J. Phys. Chem.*, 94 (18):7133–7136, 1990.

J. L. Anderson. Colloid transport by interfacial forces. *Annu. Rev. Fluid Mech.*, 21:61–99, 1989.

S. Asakura and F. Oosawa. On interaction between two bodies immersed in a solution of macromolecules. *J. Chem. Phys.*, 22(7):1255–1256, 1954.

A. J. Banchio and J. F. Brady. Accelerated Stokesian dynamics: Brownian motion. *J. Chem. Phys.*, 118(22):10323–10332, 2003.

G. K. Batchelor. Diffusion in a dilute polydisperse system of interaction spheres. *J. Fluid Mech.*, 131:155–175, 1983.

J. F. Brady. The long-time self-diffusivity in concentrated colloidal dispersions. *J. Fluid Mech.*, 272:109–133, 1994.

J. F. Brady and G. Bossis. Stokesian dynamics. *Annu. Rev. Fluid Mech.*, 20:111–157, 1988.

N. F. Carnahan and K. E. Starling. Equation of state for nonattracting rigid spheres. *J. Chem. Phys.*, 51(2):635, 1969.

I. C. Carpen and J. F. Brady. Microrheology of colloidal dispersions by Brownian dynamics simulations. *J. Rheol.*, 49(6):1483–1502, 2005.

R. Erban and S. J. Chapman. Reactive boundary conditions for stochastic simulations of reaction-diffusion processes. *Phys. Biol.*, 4(1):16–28, 2007.

D. L. Ermak and J. A. McCammon. Brownian dynamics with hydrodynamic interactions. *J. Chem. Phys.*, 69(4):1352–1360, 1978.

M. Fasolo and P. Sollich. Equilibrium phase behavior of polydisperse hard spheres. *Phys. Rev. Lett.*, 91(6), 2003.

L. P. Faucheux, G. Stolovitzky, and A. Libchaber. Periodic forcing of a Brownian particle. *Phys. Rev. E*, 51(6, Part A):5239–5250, 1995.

M. Fixman. Simulation of polymer dynamics. 1. General theory. *J. Chem. Phys.*, 69(4): 1527–1537, 1978. ISSN 0021-9606.

D. R. Foss and J. F. Brady. Brownian Dynamics simulation of hard-sphere colloidal dispersions. *J. Rheol.*, 44(3):629–651, 2000.

D. M. Heyes and J. R. Melrose. Brownian dynamics simulations of model hard-sphere suspensions. *J. Non-Newtonian Fluid Mech*, 46(1):1–28, 1993.

R. F. Ismagilov, A. Schwartz, N. Bowden, and G. M. Whitesides. Autonomous movement and self-assembly. *Angew. Chem. Int. Ed.*, 41(4):652, 2002.

P. Jenkins and M. Snowden. Depletion flocculation in colloidal dispersions. *Adv. Colloid Interface Sci.*, 68:57–96, 1996.

A. S. Khair and J. F. Brady. Single particle motion in colloidal dispersions: a simple model for active and nonlinear microrheology. *J. Fluid Mech.*, 557:73–117, 2006.

T. R. Kline, W. F. Paxton, T. E. Mallouk, and A. Sen. Catalytic nanomotors: Remote-controlled autonomous movement of striped metallic nanorods. *Angew. Chem. Int. Ed*, 44(5):744–746, 2005.

G. Lamm. Extended brownian dynamics .3. 3-Dimensional diffusion. *J. Chem. Phys.*, 80 (6):2845–2855, 1984.

G. Lamm and K. Schulten. Extended Brownian dynamics .2. Reactive, non-linear diffusion. *J. Chem. Phys.*, 78(5):2713–2734, 1983.

R. J. LeVeque. *Finite Difference Methods for Ordinary and Partial Differential Equations: Steady-State and Time-Dependent Problems.* Society for Industrial and Applied Mathematics, 2007.

R. V. Magan, R. Sureshkumar, and B. Lin. Influence of surface reaction rate on the size dispersion of interfacial nanostructures. *J. Phys. Chem. B.*, 107(38):10513–10520, 2003.

N. Mano and A. Heller. Bioelectrochemical propulsion. *J. Am. Chem. Soc.*, 127(33):11574–11575, 2005.

C. Montemagno and G. Bachand. Constructing nanomechanical devices powered by biomolecular motors. *Nanotechnology*, 10(3):225–231, 1999.

J. F. Morin, Y. Shirai, and J. M. Tour. En route to a motorized nanocar. *Org. Lett*, 8(8): 1713–1716, 2006.

S. Nakata, Y. Doi, and Y. Hayashima. Intermittent motion of a camphene disk at the center of a cell. *J. Phys. Chem. B.*, 106(44):11681–11684, 2002.

J Nardi, R Bruinsma, and E Sackman. Vesicles as osmotic motors. *Phys. Rev. Lett.*, 82 (25):5168–5171, 1999.

S. H. Northrup, S. A. Allison, and J. A. McCammon. Brownian dynamics simulation of diffusion-influenced bimolecular reactions. *J. Chem. Phys.*, 80(4):1517–1526, 1984.

S. H. Northrup, M. S. Curvin, S. A. Allison, and J. A. McCammon. Optimization of Brownian dynamics methods for diffusion-influenced rate-constant calculations. *J. Chem. Phys.*, 84(4):2196–2203, 1986.

G. A. Ozin, I. Manners, S. Fournier-Bidoz, and A. Arsenault. Dream nanomachines. *Adv. Mater.*, 17(24):3011–3018, 2005.

W. F. Paxton, S. Sundararajan, T. E. Mallouk, and A. Sen. Chemical locomotion. *Angew. Chem. Int. Ed.*, 45(33):5420–5429, 2006.

W. F. Paxton, K. C. Kistler, C. C. Olmeda, A. Sen, S. K. St. Angelo, Y. Y. Cao, T. E. Mallouk, P. E. Lammert, and V. H. Crespi. Catalytic nanomotors: Autonomous movement of striped nanorods. *J. Am. Chem. Soc.*, 126(41):13424–13431, 2004.

W. B. Russel, D. A. Saville, and W. R. Schowalter. *Colloidal Dispersions*. Cambridge University Press, 1989.

A. K. Schmid, N. C. Bartelt, and R. Q. Hwang. Alloying at surfaces by the migration of reactive two-dimensional islands. *Science*, 290(5496):1561–1564, 2000.

R. K. Soong, G. D. Bachand, H. P. Neves, A. G. Olkhovets, H. G. Craighead, and C. D. Montemagno. Powering an inorganic nanodevice with a biomolecular motor. *Science*, 290(5496):1555–1558, 2000.

T. M. Squires and J. F. Brady. A simple paradigm for active and nonlinear microrheology. *Phys. Fluids*, 17(7), 2005.

J. A. Theriot. The polymerization motor. *Traffic*, 1(1):19–28, 2000.

M. van Dyke. *Perturbation Methods in Fluid Mechanics*. Stanford: Parabolic Press, 1975.

K Yoshikawa and H Noguchi. A working hypothesis on the mechanism of molecular machinery. *Chem. Phys. Lett.*, 303(1–2):10–14, 1999.

Chapter 4

Osmotic propulsion: optimal reaction distribution

4.1 Introduction

An important task that nanotechnology faces today is the design and synthesis of nanomachines that can work in a controlled and desired manner in environments dominated by viscous forces, especially, if the device can operate without external forcing or signaling. Recently, the idea that anisotropic forces can be created on the body of a small object by an on-board chemical motor that recognizes the use of thermal fluctuations and changes in chemical equilibrium increases the possibility of discovering whole new classes of entirely synthetic nanomachines. These devices can be pre-programmed by synthesis and designed through surface chemistry to perform specific tasks. In practice, a variety of external fields have been used for colloidal transport in fluids such as electrophoresis, thermophoresis, and diffusiophoresis (Anderson 1989). While external fields have been used to sort and separate particles based on their response (i.e., DNA separation), this type of transport does not afford the flexibility of moving objects independently.

Autonomous motion at nanoscale requires the generation of a localized potential gradient. However, this proves rather challenging to achieve with macroscopic methods, especially when the location of interest is internal in a large object. Living organisms constantly generate localized gradients to achieve motion utilizing biochemical reactions. Most forms of movement in the living world are powered by protein machines known as biomolecular motors, which convert chemical energy to affect stepwise linear or rotary motion, and are essential in controlling and performing a wide variety of biological functions including intracellular transport, signal transduction, and muscle contraction (Soong et al. 2000; Yokokawa et al. 2004). These motors transport a wide variety of cargo, power cell locomotion, drive cell division and, when combined in large ensembles, allow organisms to move. Although bi-

ological motors are capable of complex and intricate functions, a main disadvantage is their inherent instability and constraints in the environmental conditions they work in, which makes it difficult to control their operation, specifically their directionality. Another example found in nature is membrane translocation proteins (e.g. flagella motor) that enables bacterial movement (Berg 2000). Understanding and harnessing such biological systems provides a strong motivation to design active nanostructures that can operate as molecular machines.

A catalytic reaction can be introduced to an inorganic nanosystem to achieve desirable motions. In principle, catalytic motors can be constructed from nanoscale building blocks having a myriad of compositions, sizes, and shapes with different surface structures and functionalities, and are powered by a diversity of environmentally friendly on-board fuels (Schliwa and Woehlke 2003). Paxton et al. (2004) observed that rod-shaped nanoparticles prepared with equal-length gold and platinum segments move autonomously in aqueous hydrogen peroxide solutions by catalyzing the formation of oxygen at the platinum surface. Directed motion at nanoscale objects is the first step to achieve integrated nanomachinery systems that can enable breakthrough applications in nanoelectronics, photonics, bioengineering, drug delivery, and disease treatment. Fournier-Bidoz et al. (2005) observed several kinds of rotational behavior with constant speed for the self-propelled nanorotors based on silicon wafer-tethered barcoded bimetal nanorods. Preliminary studies indicate that by varying the concentration of hydrogen peroxide as well as the length of the nickel segment, it is possible to control the angular velocity of the rotating nanorods. Paxton et al. (2006) demonstrated that controlled, continuous, and directed rotational motion of microscale objects can be achieved by using spatially defined catalytic regions. There have been attempts to synthesize nanostructures for catalytic applications or to examine the dependence of cat-

alytic properties on the size and shape of nanosize materials. Paxton and co-workers have discussed other variations and potential applications for the catalytic nanomotor. They also demonstrated the ideas of micropumps, microgears, and controlled motion of nanomotors using magnetic layers. One can imagine extending these ideas to include the sliding of one surface over another. However, to resemble many complicated motions that occur in biological motors in a controlled fashion, such as rotation, rolling, shuttling, delivery, etc., requires one to design the nanomotor to perform different motions or to design components that have the ability to achieve those motions once they are integrated together. The design should maximize the device's performance by considering its geometry and surrounding environment.

It is of interest to explore and understand how to optimize nanodevices driven by chemical reactions. Many remarkable and important questions are raised when designing catalytic motors. Most importantly, What is the optimal distribution of the reactive side on the motor surface? Some studies have considered one half of the motor to be reactive (Paxton et al. 2004). Is this the best? Or, is there an optimum for a different fraction? How does that optimum vary with the speed of reaction? Just how fast can it move? What information is learned about the surrounding medium? How can it be exploited for more complex operations or motions? Recently Golestanian et al. (2007) studied self-phoretic motion, where the "swimmer" generates gradients of a quantity (i.e., concentration, electric potential, temperature) through its surface activity, which induces motion through classical interfacial phoretic processes. In addition, they proposed ideas for optimizing the design of swimmers based on shape and patterns of surface properties.

In our previous work, we proposed osmotic propulsion as a simple mechanism for autonomous motion (Córdova-Figueroa and Brady 2008). Colloidal particles in solution move

freely and randomly, but, if the microstructure in the vicinity is disturbed by a surface chemical reaction, a resulting imbalance in osmotic pressure will induce autonomous motion — an osmotic motor. A simple theoretical model was constructed based on a formal statistical mechanical derivation starting from the N-particle probability density for finding bath particles surrounding the motor (see details in Chapter 3). It was applied for motors with a first-order reaction on half its surface. Other questions were discussed, such as, how large a force can be generated and how fast a half-reactive motor can move.

In this work, we extend and examine our theoretical framework for propulsion of the osmotic motor immersed in a dispersion of bath particles to other distributions of reactive sites. Our main goal is to provide a guide for optimizing the design of osmotic motors, which could be broadened to other types of mechanisms. We consider the size of the reactive site at the motor's surface to be determined by the polar angle θ_s — the angle that locates the transition from reactive to passive surface and measures from the front of the motor. In this analysis, we neglect hydrodynamic interactions between particles and rotary Brownian diffusion. Also, we assume that bath particles only interact with the motor thus behaving as an ideal gas. These assumptions enable us to have a simple model system to allow a clear analysis towards the understanding of many features unique to osmotic motors with different distributions of reactive sites. This also permits an easy introduction for optimizing self-propulsion.

The probability of finding bath particles relative to the osmotic motor is employed to calculate the driving force on the motor, from which the self-induced velocity is determined via application of Stokes drag law. The parameter that governs the motor behavior is the ratio of the speed of reaction to that of diffusion — the so-called Damköhler number Da. Increasing Da drives the suspension away from equilibrium, and thus generates a gradient

in bath particle concentration, which is utilized by the motor. Two possible scenarios for the motor are studied: one consisting of a motor held fixed and another one where the motor is free to move. We discuss the theory of osmotic propulsion in Section 4.2. In Section 4.3, we investigate the net osmotic force created by the fixed motor and its dependence on the angle θ_s. We compute the optimal angle θ_s necessary to obtain maximum osmotic force as a function of the Damköhler number. For the free motor scenario, the velocity of the motor for various θ_s and its implications for different bath particle concentrations and motor sizes are discussed. The behavior of the free motor is maximized by finding the optimal angle θ_s needed to create maximum velocity according to the Damköhler number and the properties of the suspension. Theoretical results are compared to Brownian dynamics simulations (Foss and Brady 2000; Carpen and Brady 2005) modified to consider surface reactions. We offer some concluding remarks in Section 4.4.

4.2 Theory

We consider a colloidal particle of radius a — the osmotic motor — surrounded by a sea of "bath" particles of radii b. The particles are modeled as hard-spheres immersed in an incompressible and continuum solvent of viscosity η and density ρ. For colloidal particles, inertia is negligible (small Reynolds number), thus enabling the use of the Stokes equations in describing the fluid flow. We neglect hydrodynamic interactions and rotary Brownian motion for all particles. Although this may seem to be a drastic approximation, it allows a simple and transparent analysis that captures and illustrates many of the significant physics observed in self-propulsion. The suspension of bath particles generates an osmotic pressure in the system given by $\Pi = n_b kT$, where kT is the thermal energy and n_b is the number density of bath particles. The structure and properties of this system are completely

determined by the forces of interaction among the particles; the solvent or fluid only enters in the form of a thermal bath providing kT of energy for each degree of freedom of the particles — the well-known fluctuation-dissipation theorem. A portion of the motor surface is reactive such that the bath particles undergo an irreversible first-order reaction with speed κ. For simplicity, we assume bath particles that undergo reaction are consumed[1]. Figure 4.1 shows a definition sketch of the osmotic motor-bath particles configuration. Note that in the figure we have chosen the reactive site to be axisymmetric with the z-axis. The interface between reactive and passive surfaces is defined by the polar angle θ_s, which takes values from 0 (completely inert) to π (completely reactive), and becomes the only variable that determines the distribution of reaction on the motor. Bath particles that collide on the passive surface, or do not react at all, are reflected by a hard-sphere potential, so that the particles do not interact until their hard-sphere radii touch, whereupon a force is exerted to prevent the hard-sphere radii a and b of the motor and bath particles, respectively, from overlapping.

Consumption of bath particles at the reactive portion of the motor's surface creates a low bath particle concentration region (depletion zone) that drives the microstructure away from equilibrium. This creates local bath particle concentration gradients that the motor can potentially use for propulsion (or for pumping fluid). Physically, the motor experiences fewer collisions on the reactive surface than on the passive (inert) surface, thus generating an imbalance in osmotic pressure about the motor, and consequently, a net "osmotic" force. Because rotational diffusion of particles is not included in this model (torque-free particles), the reactive site always points in the direction of this self-created net osmotic force, here

---

[1]This simple reaction could be interpreted as if reactant particles are instantaneously transformed into solvent molecules or into products that diffuse very fast away from the motor. Thus, mass is conserved and there is no need to resupply particles to the suspension. This issue was addressed in our previous work, Córdova-Figueroa and Brady (2008), and in Chapter 3. A simple scaling argument was derived to account for other reaction stoichiometries.
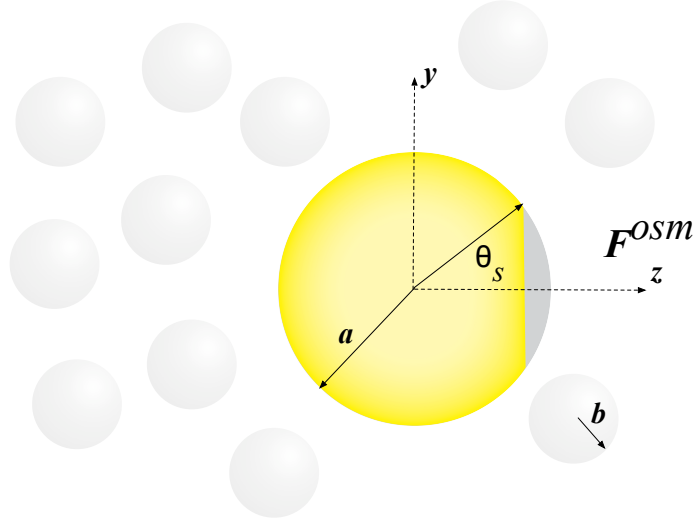
Figure 4.1: Definition sketch for the suspension: An osmotic motor of radius a with a first-order reaction on a portion of its surface determined by the polar angle θ_s (located in the z-axis) surrounded by bath particles of radii b induces an osmotic force $\boldsymbol{F}^{osm}$ that points towards low bath particle concentration regions. Particles are modeled as hard-spheres. The angle θ_s is measured from the front and takes values from 0 (completely inert) to π (completely reactive).

taken to be the z-coordinate (see Figure 4.1). To understand the resulting behavior of the osmotic motor, it is necessary to compute the local microstructural deformations caused by the nonuniform reaction, specifically, the pair-distribution function $g(\boldsymbol{r})$ thus determining the probability of finding a bath particle at a vector separation $\boldsymbol{r}$ from the motor.

Local deformations to the microstructure are of central importance to the driving force of the motor, therefore, we must solve for the distribution of bath particles surrounding the motor. The stochastic nature of Brownian motion requires such distribution to be found statistically. We denote the probability density of finding the motor and bath particles in a given configuration at time t, $P_N(\boldsymbol{x}_1, \boldsymbol{x}_2, ..., \boldsymbol{x}_N, t)$, where the label 1 denotes the motor and $2 \rightarrow N$ the bath particles, and $\boldsymbol{x}_i$ denotes the position of particle i. The non-equilibrium microstructure of colloidal dispersions can be directly calculated from a

Smoluchowski equation (Batchelor 1977, Felderhof 1988):

$$\frac{\partial P_N}{\partial t} + \sum_{i=1}^{N} \boldsymbol{\nabla}_i \cdot \boldsymbol{j}_i = 0 \tag{4.1}$$

where $\boldsymbol{j}_i$ is the probability flux carried by particle i. In the absence of hydrodynamic interactions and rotational motion, the balance of instantaneous forces acting on the motor exerted by particle j is given by

$$\boldsymbol{F}_1^H = \sum_{j=1}^{N} \left(\boldsymbol{F}^{ext} + \boldsymbol{F}_j^P - kT\boldsymbol{\nabla}_j \ln P_N \right), \tag{4.2}$$

where $\boldsymbol{F}^H$ is the hydrodynamic force that at low Reynolds number is linear in the velocity $\boldsymbol{U}$; $\boldsymbol{F}^{ext}$ is an external force (e.g., to hold particle, to pull particle through material) acting on the motor; $\boldsymbol{F}^P$ is the interparticle force, which we have assumed is central and corresponding to a hard-sphere potential; and $-kT\boldsymbol{\nabla} \ln P_N$ is the entropic, or Brownian, force on the motor due to random thermal fluctuations of the solvent molecules (Batchelor 1976). Bath particles in the suspension (labels $2 \rightarrow N$) move under the action of hydrodynamic forces and entropic forces, given by a force balance similar to (4.2) but with zero external forces, $\boldsymbol{F}^{ext} = 0$.

A closed equation for the pair-distribution function $g(\boldsymbol{r})$ is obtained by integrating the N-particle Smoluchowski equation (4.1) over the configurational degrees of freedom of $N-2$ bath particles, neglecting interactions between bath particles. The neglect of such high-order couplings restricts the theory to low bath particle volume fractions, $\phi_b = 4\pi b^3 n_b/3 \ll 1$; only one bath particle interacts with the motor, therefore, behaving as an ideal gas. For a detailed derivation of the pair-level Smoluchowski equation see Squires and Brady (2005) in their work on single particle motion in colloidal dispersions and microrheology in the

absence of hydrodynamic interactions.

The average force of the osmotic motor is obtained from (4.2) by averaging over the positions of the $N-1$ bath particles. The N-particle probability distribution can be written as $P_N(\boldsymbol{x}_1, \boldsymbol{x}_2, ..., \boldsymbol{x}_N, t) = P_{N-1/1}(\boldsymbol{r}_2, \boldsymbol{r}_3, ..., \boldsymbol{r}_N, t|\boldsymbol{x}_1, t)P_1(\boldsymbol{x}_1, t)$, where $P_{N-1/1}$ is the conditional probability for finding the $N-1$ bath particles in configuration $\boldsymbol{r}_{N-1}$ given that the motor is at location $\boldsymbol{x}_1$. Owing the statistical homogeneity of the suspension, $P_{N-1/1}$ does not depend on the position of the motor. Thus, the average force of the motor is defined

$$\langle \boldsymbol{F}_1^H \rangle_1 = \int \boldsymbol{F}_1^H P_{N-1/1}(\boldsymbol{r}_2, \boldsymbol{r}_3, ..., \boldsymbol{r}_N, t) d\boldsymbol{r}_2 ... d\boldsymbol{r}_N, \qquad (4.3)$$

where the subscript 1 on $\langle \ \rangle_1$ indicates to the conditional average relative to the motor at $\boldsymbol{x}_1$. A procedure to solve (4.3) assuming diluteness and hard-sphere interparticle forces is discussed in Squires and Brady (2005) for averaging stochastic quantities, so we shall proceed quickly. At the two-body level, the averaged forces acting on the osmotic motor becomes

$$\boldsymbol{F}^H = \boldsymbol{F}^{ext} - n_b kT \oint_{r=a+b} \boldsymbol{n} g(\boldsymbol{r}) dS, \qquad (4.4)$$

where the integral is over the surface of contact between the motor and bath particles, $r = a+b$, with normal $\boldsymbol{n}$ directed radially out from the motor. We have dropped the brackets and label 1 denoting the motor for clarity. The hydrodynamic Stokes drag force, defined as $\boldsymbol{F}^H = -6\pi\eta a\boldsymbol{U}$ (where $\boldsymbol{U}$ is the motor velocity), is balanced by a constant external force $\boldsymbol{F}^{ext}$ and the average entropic or osmotic force, $\boldsymbol{F}^{osm} = -n_b kT \oint_{r=a+b} \boldsymbol{n} g(\boldsymbol{r}) dS$, exerted on the motor by collisions with bath particles. From Eq. (4.4) we see clearly that the thermal motion of the bath particles acts to resist the motion of the motor or, if present, the external force. In the absence of surface reaction on the motor (inert colloids), the pair-distribution

function $g(\boldsymbol{r})$ is isotropic and the integral in (4.4) is zero. Indeed, if the particle is fully reactive over its surface $g(\boldsymbol{r})$ is also isotropic. This implies that for the motor to create an anisotropic environment, or regions of low bath particle concentration necessary to drive the suspension away from equilibrium, the reaction must be on a portion of the motor to break the symmetry.

To compute the net osmotic force acting on the motor, we need to determine the pair-distribution function $g(\boldsymbol{r})$ about the motor. In addition to studing the behavior of the osmotic motor subject to different distributions of reactive sites, we are interested in optimizing the resulting osmotic force and providing ideas on how to design better osmotic motors in terms of the properties considered here for the simple model motor. In a particle-level description, the osmotic force increases if the motor maximizes the number of hard-sphere collisions with bath particles in the vicinity on its left hemisphere (negative z-axis in Figure 4.1). We demonstrate that this can be easily done by selecting the right distribution of reaction on the spherical motor for a given Damköhler number, and also by taking into consideration the number of bath particles in the vicinity that collide with the motor. We shall see that half reactive or fast reaction is not necessarily the right design choice for spheres if maximum osmotic force is desired. Osmotic motors could take advantage of their geometry and the flux of bath particles toward the motor to minimize the reactive portion on the surface, an option often needed for designing and constructing 'efficient' nanodevices.

Two scenarios for the osmotic motor are considered: one in which the motor is held fixed and another one where the motor is free to translate with velocity $\boldsymbol{U}$. A spherical coordinate system (r, θ) is adopted to model the particles.

4.2.1 Fixed motor

In the fixed motor scenario, the osmotic motor experiences no motion. The net osmotic force created autonomously by the surface reaction balances the external force that keeps the motor fixed ($\boldsymbol{F}^{ext} = \boldsymbol{F}^{osm}$). Therefore, only bath particle positions evolve by Brownian motion. The osmotic force along the z-axis is given by

$$F^{osm} = -n_b k_B T (a + b)^2 \oint n_z g(r = 1; Da, \theta_s) \, d\Omega, \qquad (4.5)$$

where $d\Omega = dS/(a + b)^2$ is the solid angle of integration and n_z is a unit vector along the z-axis. We have made length dimensionless by the contact distance $a + b$. The probability density flux is simply the diffusion of bath particles $\boldsymbol{j} = -D\nabla g$. Conservation of bath particles about the fixed motor satisfies the steady-state diffusion equation,

$$\nabla^2 g = 0, \qquad (4.6)$$

subject to the undisturbed microstructure condition far from the motor,

$$g \sim 1 \text{ as } r \to \infty, \qquad (4.7)$$

and at contact, the flux to the motor is balanced by the nonuniform reaction:

$$\boldsymbol{n} \cdot \nabla g = Da \, h(\boldsymbol{n}) \, g. \qquad (4.8)$$

The parameter that governs the motor behavior is the ratio of the speed of reaction to that of diffusion — the so-called Damköhler number $Da = \kappa(a + b)/D$, where the characteristic

length is the sum of the motor and bath particle radii and D is the relative diffusivity. Here, the relative diffusivity D is simply the diffusivity of bath particles D_b. The distribution of reaction on the surface is determined by the dimensionless function $h(\boldsymbol{n})$, which we take to be 1 on the reactive surface $(0 < \theta < \theta_s)$ and 0 on the passive surface $(\theta_s < \theta < \pi)$ (see Figure 4.1). We must compute the pair-distribution function at contact, and thus determine the net osmotic force. For simplicity, we shall refer to the integral of the pair-distribution over the surface of contact in (4.5) as $\mathcal{F}(Da, \theta_s) = -\frac{3}{4\pi} \oint_{r=1} n_z g(\boldsymbol{r}) d\Omega$, a nondimensional function of the Damköhler number and the angle θ_s that represents the asymmetric bath particle distribution created by the nonuniform reaction on the motor. The osmotic force can be maximized by finding the best distribution for reactive sites for each Damköhler number. These values are obtained from the derivative of the nondimensional function $\mathcal{F}(Da, \theta_s)$ with respect of Da and keeping the angle θ_s constant, which at maximum, the derivative must equal zero.

4.2.2   Free motor

The second scenario corresponds to a motor that is free to translate at velocity $\boldsymbol{U}$ due to the reaction-driven osmotic force. No external forces, $\boldsymbol{F}^{ext} = 0$, or imposed particle gradients act on the motor. By contrast, the osmotic motor migrates autonomously through the suspension. The resulting net osmotic force balances the hydrodynamic Stokes drag force $\boldsymbol{F}^H$, giving the motor velocity along the z-axis

$$U = -n_b D_a (a + b)^2 \oint n_z g(r = 1; Da, Pe, \theta_s) \ d\Omega, \tag{4.9}$$

where $D_a = kT/6\pi\eta a$ is the Stokes-Einstein-Sutherlad diffusivity of the osmotic motor. In a reference frame moving with the motor, which translates at velocity $\boldsymbol{U}$, each bath particle is advected with velocity $-\boldsymbol{U}$ and moves diffusively. Therefore, the probability density flux is given by $\boldsymbol{j} = -D\nabla g - \boldsymbol{U}g$. Continuity of bath particles requires that $\nabla \cdot \boldsymbol{j} = 0$, so that, at steady-state, the pair-distribution function $g(\boldsymbol{r})$ for the free motor satisfies the advection-diffusion equation

$$\nabla^2 g = -Pe\frac{\partial g}{\partial z}, \tag{4.10}$$

and has taken the motion to be along the z-axis. The associated boundary conditions are

$$g \sim 1 \text{ as } r \to \infty, \tag{4.11}$$

$$\frac{\partial g}{\partial r} = (Da\ h(\boldsymbol{n}) - Pe\mu)\,g \text{ at } r = 1, \tag{4.12}$$

so that $\boldsymbol{n} \cdot (\boldsymbol{U}/U) = \cos\theta = \mu$. We made all lengths dimensionless by scaling it with the contact distance $a + b$, and velocity with the yet unknown osmotic velocity U. The expression at contact (4.12) shows the competition between self-propulsion of the motor in driving the environment away from equilibrium and Brownian motion attempting to restore the disturbed microstructure. The Péclet number Pe is the ratio of the "self-induced" osmotic velocity U to the relative Brownian velocity $D/(a + b)$. The free motor undergoes Brownian motion; therefore, the relative diffusivity D is now the sum of the motor and bath particle diffusivity: $D = D_a + D_b$. From (4.9) the implicit equation for the Péclet number is

$$Pe = \frac{U(a + b)}{D} = \beta\mathcal{F}(Da, Pe, \theta_s), \tag{4.13}$$

where $\beta = \phi_b(1+a/b)^2$ and $\mathcal{F}(Da, Pe, \theta_s)$ is now a nondimensional function of the Damköhler number, the Péclet number, and the angle θ_s; $\mathcal{F}(Da, Pe, \theta_s)$ must be solved simultaneously with the governing equations to get a solution for the motor velocity U. The Péclet number is not an independent parameter, but rather is regulated by Da and β. In fact, the resulting Pe could behave differently depending on the portion of the reactive surface. The product β corresponds to the number of bath particles within a bath particle radius of the motor surface: $\beta \sim n_b(a + b)^2 b$.

Consumption of bath particles near the reactive surface, which is controlled by Da, creates a low bath particle concentration region in which the motor prefers to move. As it moves forward, the osmotic motion acts as a source/sink of bath particles on the motor particle surface. On the reactive surface, the osmotic motion is a source of bath particles, which eventually reduces the motor's driving force and therefore its speed by restoring the depleted region. On the rear surface, the motor creates a wake of low bath particle concentration, again reducing the motor velocity. This has the physical effect of limiting the osmotic pressure imbalance resulting from the surface reaction. Note that at $Pe = 0$ the free motor problem reduces to the scenario in which the motor is held fixed, giving similar microstructural deformation for active surface reaction. Here, osmotic propulsion is maximized by finding a set of values (θ_s, Da) where the derivative of $\mathcal{F}(Da, Pe, \theta_s)$ with respect to Da results in zero. The calculations are repeated for different values of β.

4.3   Results

Our aim in this work is to extend the dilute theory applied to half-reactive osmotic motors presented in Chapter 3 to different distributions of reactive sites (various θ_s). This analysis also allows for the exploration of optimal reactive surface distributions to generate maximum

driving force in multiple scenarios. The microstructural deformation relative to the motor is determined by adopting a spherical coordinate system. We compute the osmotic force balanced by the external force to keep the motor fixed. And in the case that the motor is free to move, the motor velocity is calculated. In addition to the dilute theory, we employ Brownian dynamics (BD) simulations that allow us to test our theoretical analysis. It also provides an insightful physical interpretation of the surface reaction and a particle-level description of osmotic propulsion. We perform simple hard-sphere BD simulations (Foss and Brady 2000; Carpen and Brady 2005) where if a bath particle collides with the motor on the reactive surface, it has a probability to undergo reaction. If no reaction occurs, then the bath particle collides with the motor just as it does on the nonreactive surface. The BD simulations should correspond to the analytical model, and the force imparted to the motor comes directly from the hard-sphere collisions with the bath particles not from any integration of the pair-distribution function over the surface as in (4.5). Additional details of the simulation method considered in this work can be found in Chapter 3, which is modified to account for different distributions of reactive sites.

4.3.1 Fixed motor

Here, we solve the fixed motor problem with different reactive site distributions. The general solution of the diffusion equation (4.6) satisfying the boundary condition (4.7) is obtained by separation of variables, giving

$$g(r, \mu) = 1 + \sum_{n=1}^{\infty} A_n r^{-(n+1)} P_n(\mu), \qquad (4.14)$$

where $P_n(\mu)$ are the Legendre polynomials with argument $\mu = \cos\theta$ and A_n are unknown constants to be determined from the boundary condition (4.8).

It is instructive to first examine the osmotic force that arises at small and high Da numbers to see how it scales with the angle θ_s. For small Da, the problem can be solved analytically, but its implementation diverges for increasing Da, reflecting the singular nature of the diffusion equation (diffusion-limited problem). Therefore, for intermediate and large Damköhler numbers, we employ a finite difference method that solves for the pair-distribution function depending on the angle θ_s in a procedure that converges very rapidly. Before presenting our results, we comment briefly on the numerical method. The Smoluchowski equation and its corresponding boundary conditions are discretised by approximating the radial and angular derivatives by central differences. As Da is increased, the demand for grid points increases to capture accurately the low bath particle concentration regions and the large gradients that may be present. Thus, the computational cost of the finite difference scheme also increases with Da (and increasing Pe for the free motor problem discussed in Section 4.3.2). Typically, 900×900 grid points were used, and accuracy was tested by comparing the resulting pair-distribution function at contact to that computed using a 1000×1000 grid. We proceed below to compute the osmotic force for arbitrary Da and various θ_s from which the framework of maximum force is studied. Our numerical method follows suggestions presented in the appendix of Khair and Brady (2006) in solving the Smoluchoswki equation for the active microrheology problem. For the interested reader, additional details on finite differences method are found in LeVeque (2007).

4.3.1.1 Low Da limit

At small Da, when diffusion dominates over reaction, the pair-distribution function can be transformed into a regular perturbation expansion in Da. The microstructure is described by Eq. (4.14), however, finding A_n from the boundary condition becomes simple in this limit. This allows us to easily get a solution for the pair-distribution function at contact, and thus the osmotic force at small perturbations from equilibrium for any angle θ_s is calculated. In the limit of $Da \ll 1$, the dimensionless function $\mathcal{F}(Da, \theta_s)$ is given by

$$\mathcal{F}(Da \ll 1, \theta_s) = \frac{3}{8} \sin^2 \theta_s Da. \tag{4.15}$$

Eq. (4.15) reduces to 0 for inert ($\theta_s = 0$) and fully reactive ($\theta_s = \pi$) motors. These results are expected for isotropic microstructures around the osmotic motor; the pair-distribution function at contact is a constant. In the case of a half-reactive motor ($\theta_s = \pi/2$), $\mathcal{F}(Da)$ gives $\frac{3}{8}Da$, as reported in Chapter 3. The resulting osmotic force at small Damköhler numbers is linear in Da: $F^{osm} \sim n_b kT(a+b)^2 Da \sin^2 \theta_s = n_b(a+b)^3 6\pi\eta b\kappa \sin^2 \theta_s$, where we have used the Stokes-Einstein-Sutherland expression for the bath particle diffusivity $D_b = kT/6\pi\eta b$. Physically, this force is interpreted as if each bath particle reacting with the motor strikes the motor with speed κ and thus hydrodynamic force $6\pi\eta b\kappa$, and there are $n_b(a+b)^3$ colliding bath particles. The geometric factor $\sin^2 \theta_s$ adjusts the force according to the reaction distribution. We find that for a small reactive site ($\theta_s \to 0$) the osmotic force scales as $F^{osm} \sim n_b(a+b)^3 6\pi\eta b\kappa\theta_s^2$. And in the case of a small passive surface ($\theta_s \to \pi$), the osmotic force is $F^{osm} \sim n_b(a+b)^3 6\pi\eta b\kappa(\theta_s - \pi)^2$. Note both limits of the osmotic force are $O(Da\theta_s^2)$. Eq. (4.15) predicts that for the motor to maximize the osmotic force at $Da \ll 1$, which is given by $F^{osm}_{max} = \frac{1}{2}\pi kT n_b(a+b)^2 Da$, the angle θ_s must be $\pi/2$, meaning
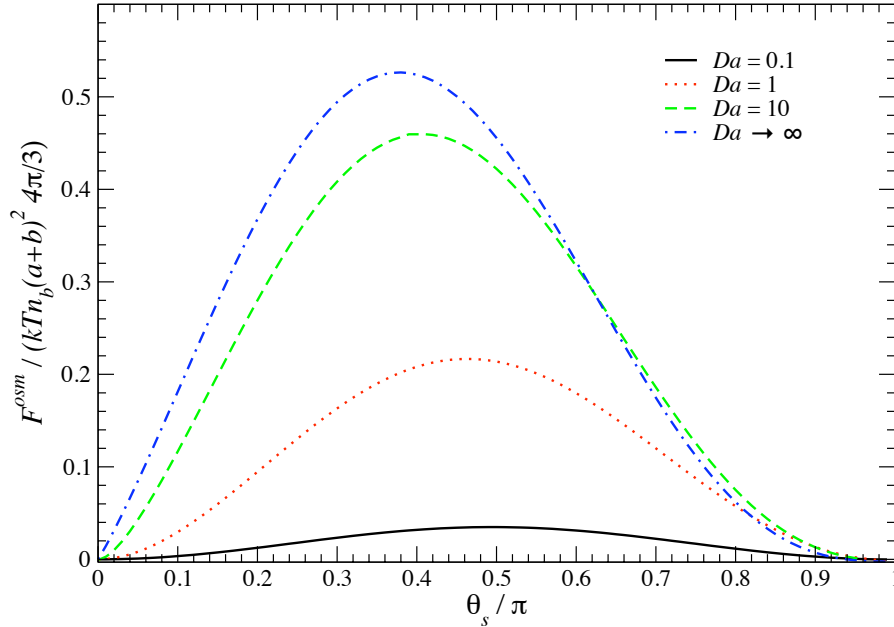
Figure 4.2: The osmotic force F^{osm} scaled by $kTn_b(a+b)^2 4\pi/3$ as a function of the angle θ_s scaled by π for various Da

equal distribution of the reactive and passive surface on the motor.

4.3.1.2 High Da limit

For fast reaction (high Da), the process is limited by the diffusion of bath particles. In this limit, the pair-distribution function on the reactive surface is zero ($g = 0$), all colliding bath particles are consumed. On the passive surface, the impenetrability condition $\partial g/\partial r = 0$ holds. The governing equations become independent of Da, therefore A_n is only a function of θ_s. One needs to find an accurate solution of A_n which makes analytical symbolic methods arduous and time-consuming. Instead of expanding the pair-distribution function for higher-order terms in Da, the corresponding set of equations for this limit is simply solved numerically based on the method briefly mentioned above. The relevant quantity to calculate is the nondimensional function $\mathcal{F}(Da, \theta_s)$ in the limit as $Da \to \infty$ aiming to examine how the osmotic force behaves for different values of θ_s. Figure 4.2 shows the
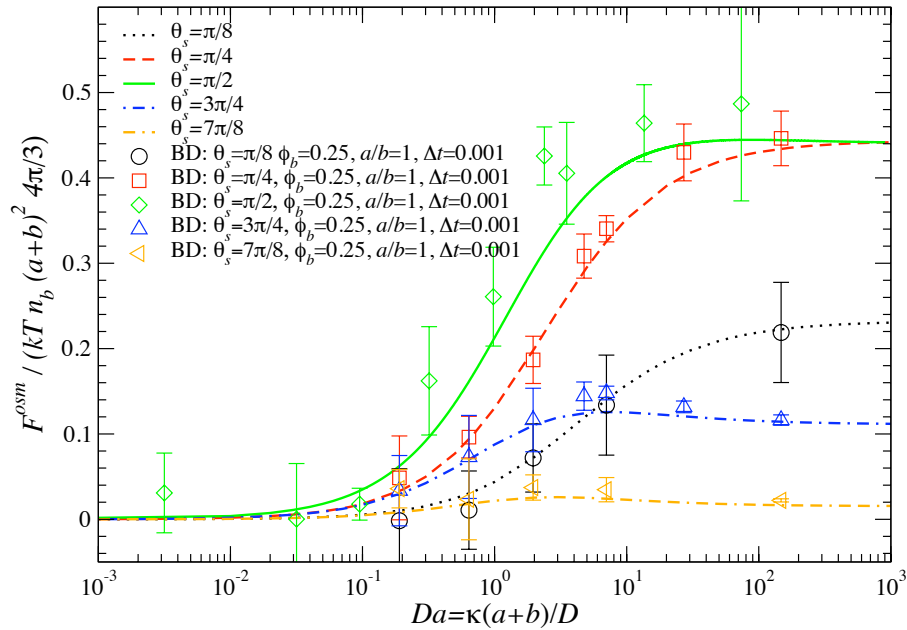
Figure 4.3: The osmotic force F^{osm} scaled by $kTn_b(a+b)^2 4\pi/3$ as a function of Da for various angles θ_s. The theoretical predictions (curves) are compared with Brownian dynamics (BD) simulations (symbols).

numerical results of the osmotic force F^{osm} scaled by $kT/(a+b)\phi$ ($\phi = 4\pi/3n_b(a+b)^3$ is the fraction of bath particles in the motor volume) in the limit as $Da \to \infty$ as a function of the angle θ_s. It was determined that for motors with an irreversible first-order reaction on half motor, the osmotic force in the limit as $Da \to \infty$ saturates and is independent of Da, an observation that clearly continues to hold for motors with other distributions of reactive site. The pair-distribution on the passive surface is $O(1)$. The resulting osmotic force in this limit scales as $F^{osm} \sim n_b kT(a+b)^2 f(\theta_s)$. For small and large reactive sites, we found that the function $f(\theta_s)$ is $O(1)$. The maximum value of $\mathcal{F}(Da)$ is simply the scaled maximum osmotic force, F^{osm}_{max}. This value in the curve for $\mathcal{F}(Da \to \infty)$ shown in Figure 4.2 is approximately 0.5271, and corresponds to an angle $\theta_s \approx 0.3776\pi$ ($= 67.97^o$), representing the optimal angle θ_s^{op} for reactive surface for fast reactions. Indeed, this distribution represents a 37.76% reactive motor.

4.3.1.3 Arbitrary Da

Having solved the dispersion microstructure and the osmotic force in the limiting cases for

the Damköhler number (slow and fast reactions), we continue to study the osmotic force for

arbitrary Da. Figure 4.3 plots the scaled osmotic force, $F^{osm}/kT\phi/(a+b) = \mathcal{F}(Da, \theta_s)$, as

a function of Da for various θ_s. The plot agrees with Eq. (4.15) as expected for small Da

numbers and the results obtained in the limit as $Da \to \infty$. In fact, at small Da, all curves

collapse into a single one when scaling the osmotic force with the geometric factor $\sin^2\theta_s$

found analytically. The open symbols in the figure are the result of Brownian dynamics

simulations modified to allow surface reaction in different distributions. As the theory

predicted, the scaled osmotic force is independent of size ratio a/b, bath particle volume

fraction ϕ_b, and from the time step Δt used in the simulations. Note in the figure that the

maximum value in each curve is not necessarily found in the high-Da limit, but at some

arbitrary Da.

This observation is seen in Figure 4.2 where we have plotted $F^{osm}/kT\phi/(a + b) =$

$\mathcal{F}(Da, \theta_s)$ as a function of the angle θ_s for arbitrary values of Da. This plot clearly shows

that the maximum osmotic force F^{osm}_{max} (where the derivative of $\mathcal{F}(Da, \theta_s)$ with respect of

θ_s is zero) changes as the Damköhler number is varied, thus giving an optimal distribution

of reactive site θ_s^{op} for each Da. We proceed to find the scaled maximum osmotic force

F^{osm}_{max} for various Da and its corresponding optimal angle θ_s^{op}. Figure 4.4 plots the resulting

optimal angle, θ_s^{op}, and scaled maximum force as a function of Da. Clearly, when Brownian

motion dominates over reaction ($Da \ll 1$) the optimal angle that results in maximum force

is $\theta_s^{op} = \pi/2$. The maximum force scales as $F^{osm}_{max} \sim kTn_b(a + b)^2 Da$. Near $Da \approx 1$ the

curves slowly decay to a new value. Note that in the limit as $Da \to \infty$, the optimal angle

approaches an asymptotic value of 0.3776π, as mentioned in Section 4.3.1.2. In this limit,
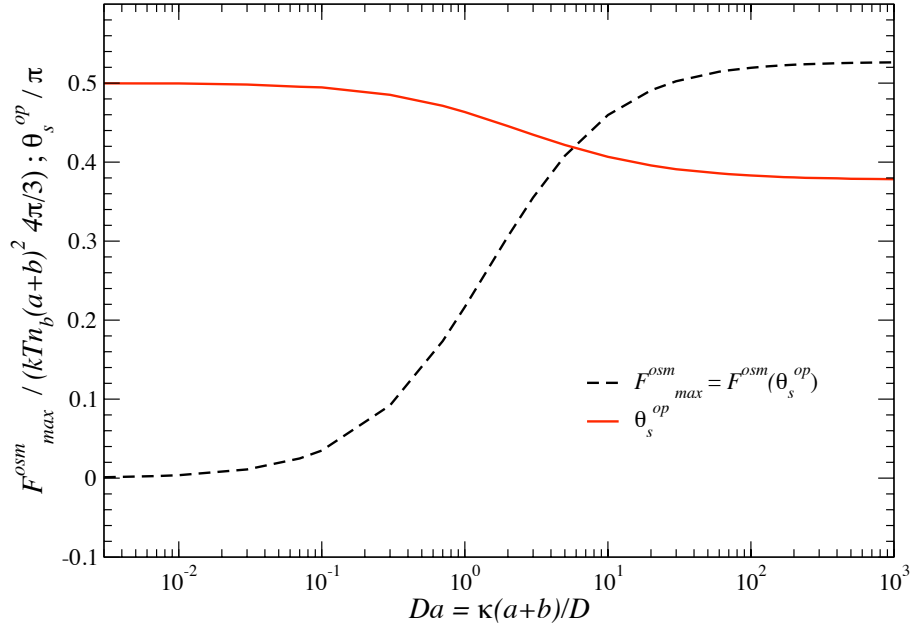
Figure 4.4: The maximum osmotic force F_{max}^{osm} scaled by $kTn_b(a+b)^2 4\pi/3$ and its corresponding optimal angle θ_s^{op} scaled by π as a function of Da

the maximum osmotic force saturates and becomes independent of the speed of reaction, thus $F_{max}^{osm} \sim kTn_b(a+b)^2$.

In order to interpret in physical terms the maximum osmotic force, we examine the microstructure evolution of bath particles about the fixed osmotic motor for increasing Damköhler number and varying angle θ_s. In Figure 4.5 we show density plots of the microstructure surrounding the motor at small and high Da for $\theta_s = \pi/4$ and $3\pi/4$. For $Da \ll 1$ (slow reaction), the microstructural deformation is proportional to Da and slightly disturbed near the reactive surface. Moving to $Da \approx 1$ or greater, the reaction now comes into play, and the deformation near the reactive surface clearly exhibits a low bath particle concentration region. Bath particles diffuse at a characteristic time $\tau_D \sim (a+b)^2/D$ much slower than the characteristic time taken by the reaction to create the depleted (no bath particles) region near the reactive surface, $\tau \sim (a+b)/\kappa$. Thus, the microstructure reaches saturation and remains unchanged at high Da, which is appropriate for first-order surface
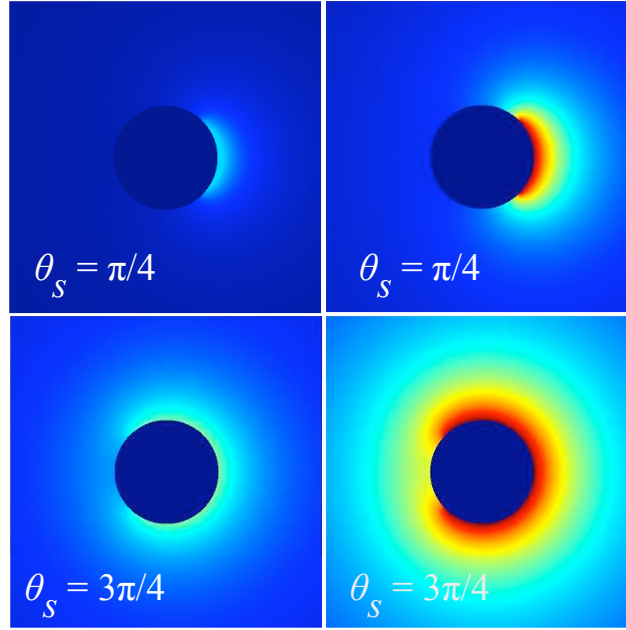
Figure 4.5: Density profiles in the symmetry plate of the fixed osmotic motor at low and high Da for different distributions of reactive site. Regions of low bath particle concentration are in red and the undisturbed regions in blue. The top row is a motor with an angle $\theta_s = \pi/4$ and the second row is a motor with an angle $\theta_s = 3\pi/4$. At small Da (left column), the microstructure near the reactive surface is slightly disturbed, thus the osmotic force is proportional to Da. In the limit of high Da (right column), the microstructure is fully disturbed on the reactive surface causing a region of low bath particle concentration. The osmotic force saturates and becomes independent of Da.

reactions.

Consider the equilibrium microstructure (no reaction) about the fixed motor as our state of reference. Bath particle collisions with the fixed motor occurring anywhere in the surface area from $\pi/2$ to π (left hemisphere of the motor) result, in average, in a force in the z-direction that scales as $F_z^{osm} \sim n_b kT(a+b)^2$. Otherwise, if collisions occur on the surface area from 0 to $\pi/2$ (right hemisphere of the motor), the resulting force points in the negative z-direction, which scales as $F_{-z}^{osm} \sim -n_b kT(a+b)^2$. In equilibrium, the sum of both equal in magnitude but opposite in sign forces is zero: $F^{osm} \sim F_z^{osm} + F_{-z}^{osm} = 0$. However, if the reaction is active on a portion of the surface of the motor, it creates a nonuniform bath particle concentration that drives the osmotic force away from its equilibrium value.

We have shown that the magnitude of this "driving" force also depends on the size of the reactive surface, because, in general, the distribution of bath particles about the motor varies accordingly. The motor could increase the self-created net osmotic force if condition $F_z^{osm} \gg F_{-z}^{osm}$ is exploited, and is achievable if the concentration of bath particles is increased on the left hemisphere. This is done here by choosing correctly the distribution of reaction depending on the Damköhler number — the nondimensional speed of reaction. Previously, it was shown from the solution of the pair-distribution function at contact for various Da for half-reactive fixed motors that the self-created osmotic pressure imbalance could drive bath particles located in the proximity of the passive surface to the reactive surface. Therefore, the equilibrium concentration on the passive surface ($g = 1$) is reduced. This bath particle (diffusion) migration depends on the speed and the type of reaction. And also on the geometry of the motor. These facts play an important role for the motor's ability to harness its environment and to maximize its driving force.

For slow reactions, we found that the concentration of bath particles is slightly disturbed at the reactive surface (see density plots in Figure 4.5). The net osmotic force is small for slow reactions fundamentally because local gradients in bath particle concentration are also small, and as calculated earlier, the osmotic force responds linearly in Da. If you decrease the distribution of the reactive site to angle θ_s less than $\pi/2$ (reaction on front), bath particle collisions occurring on the motor surface area within θ_s to $\pi/2$, in principle, provide "kicks" in the negative direction, F_{-z}^{osm} and reduce the net osmotic force in the desired direction. Resultantly, in the linear-response regime, the scaled osmotic force plotted in Figure 4.2 predicts a maximum force at $\theta_s = \pi/2$. This theoretical prediction is also observed in Figure 4.4. In fact, the angle $\theta_s = \pi/2$ (half-reactive motor), represents the largest portion of reactive surface necessary to design fixed osmotic motors, but only those optimal for slow

reactions. As Da is increased, the depletion zone near the reactive surface acts as a sink of bath particles and consequently, causes the bath particle concentration to decrease near the passive surface if compared to slower reactions. All this implies that one can properly reduce the reactive surface area (or increase the passive surface) if desired, as long as the motor continues generating maximum force, by increasing the Damköhler number in a fashion that keeps low motor/bath collisions ($g \ll 1$) occurring within $\theta_s < \theta < \pi/2$. Consequently, this reduces bath particle "kicks" in the opposite direction, which are not harnessed at small Da, and keeps $F_z^{osm} \gg F_{-z}^{osm}$ maximized. As observed in Figure 4.4, the minimum optimal angle θ_s^{op} permitting the motor to generate maximum force is 0.3776π. Figure 4.6 shows density plots of the structure surrounding the fixed motor at $Da = 100$ (fast reaction) for various θ_s. Note that decreasing θ_s from $\pi/2$ (optimal reaction distribution at low Da) to its limiting optimal reaction distribution at high Da, the bath particle distribution on the rear of the motor increases, causing an increment in the net osmotic motor in the desired direction. For reactive surfaces greater than the passive (reaction on rear), independently of the speed of reaction, there is less surface available for bath particles to collide without reacting, which is necessary to create F^{osm}. We have demonstrated that maximum force for fixed "spherical" osmotic motors is always achieved for angles θ_s^{op} less than $\pi/2$: motors with half or more passive surfaces.

So far, we have assumed the motor is fixed. If the motor is released, there will be an advective flux of bath particles towards the motor that will alter the concentration distribution of bath particles surrounding the motor and consequently reduce the propulsive force. All the explanations presented to describe the maximized osmotic force should also apply for the free motor. Advection flux carries more bath particles toward the front of the motor but it leaves behind bath particles located near the rear portion. We expect this additional
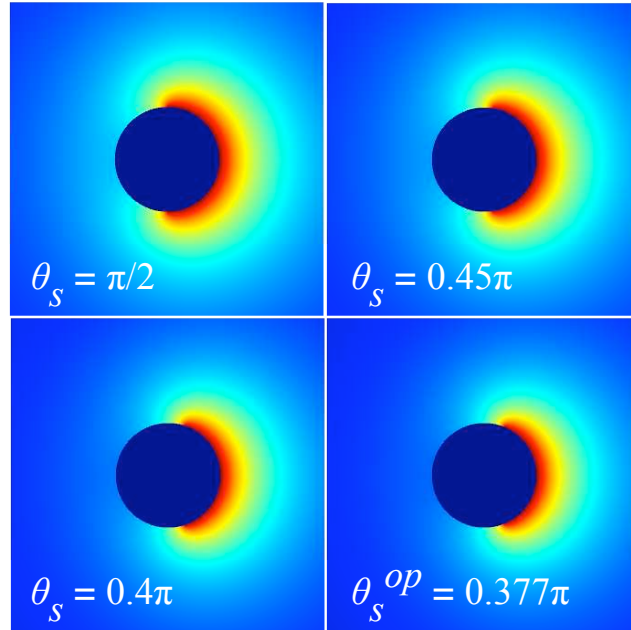
Figure 4.6: Density profiles in the symmetry plane of the fixed osmotic motor at $Da = 100$ for different reaction distributions ($\theta_s = \pi/2, 0.45\pi, 0.4\pi, 0.377\pi$). Regions of low bath particle concentration are in red and the undisturbed regions in blue. The bath particle distribution on the rear of the motor increases as θ_s is decreased (lighter blue turning into darker blue) to its optimal reaction distribution $\theta_s^{op} = 0.377\pi$, and thus maximizes F^{osm}.

force acting on the motor to change the values of the optimal angles considerably in the presence of strong advective forces (high Pe). We proceed to examine the microstructural deformation about the free motor. Specifically, we compute the nondimensional function $\mathcal{F}(Da, Pe, \theta_s)$ and thus, the velocity of the motor for different distributions of reactive site, Damköhler numbers, and product β. Also, the behavior of the optimal angles for maximum velocity U_{max} (expressed as Pe) is examined as a function of Da for various β.

4.3.2 Free motor

Solving for the pair-distribution function $g(\boldsymbol{r})$ about the free motor is analytically challenging when an implicit equation for Pe must be solved simultaneously with the advection-diffusion equation. In fact, the problem becomes more complex with the addition of the variable θ_s in the set of equations that describe the microstructure surrounding the free

142

motor. Aside from these limitations, it is simple to solve this problem analytically in the limit of small Da. For arbitrary Da we solve for the pair-distribution function numerically, which allows us to study behaviors at small and high β for any angle θ_s, and its relation to the motor velocity. The numerical (finite difference) method employed is similar to the method used for the fixed motor problem at intermediate and high Da (Section 4.3), where additional grid points are located where they are needed (e.g., large gradients in g near θ_s). The numerical method properly captures the low bath particle concentration region near the reactive surface as Da is increased and, as we shall illustrate below, in the rear of the motor for increasing Pe.

4.3.2.1   Low Da limit

For slow reactions, the microstructure is slightly perturbed near the reactive surface causing small gradients in bath particle concentration. One can easily transform the pair-distribution function $g(\boldsymbol{r})$ into a regular perturbation expansion in Da allowing us to compute analytically the first term $O(Da)$ of the dimensionless function $\mathcal{F}(Da, Pe)$. In the limit of $Da \ll 1$, the dimensionless function $\mathcal{F}(Da, Pe)$ is given by

$$\mathcal{F}(Da \ll 1, Pe) = \frac{3}{8} \sin^2 \theta_s Da - \frac{1}{3} Pe. \tag{4.16}$$

Again, the geometric factor describing the reactive surface distribution is $\sin^2 \theta_s$. For isotropic environments, as in the case of $\theta_s = 0$ and $\theta_s = \pi$, the microstructure around the motor is symmetric, giving constant pair-distribution function at contact and $\mathcal{F}(Da, Pe) = 0$, independently of the speed of reaction. As reported in Chapter 3, Eq. (4.16) reduces to $\mathcal{F}(Da \ll 1, Pe) = \frac{3}{8} Da - \frac{1}{3} Pe$ for half reactive motor ($\theta_s = \pi/2$). From (4.16) the resulting

Pe is simply

$$Pe = \left(\frac{\frac{3}{8}\beta \sin^2 \theta_s}{\frac{1}{2}\beta + 1} \right) Da. \qquad (4.17)$$

In the limit of small β, the Peclet number scales as $Pe \sim \beta \sin^2 \theta_s Da$. The osmotic velocity is limited by the speed of reaction and scales linearly with Da: $U \sim n_b D_a (a+b)^2 Da \sin^2 \theta_s = n_b b(a+b)^2 \kappa \sin^2 \theta_s$. The motor behavior for the limiting cases of θ_s at small Da numbers is examined. In the limit as $\theta_s \to 0$, the velocity of the motor is $U \sim n_b b(a+b)^2 \kappa \theta_s^2$. In the opposite limit $(\theta_s \to \pi)$, the velocity behaves as $U \sim n_b b(a+b)^2 \kappa (\theta_s - \pi)^2$. Indeed, for small β both limits are $O(\beta Da\theta_s^2)$. In the case when particles are very far from each other, bath particles are unlikely to collide or be consumed on the reactive surface for the motor to create local concentration gradients; thus the motor moves diffusively but does not experience propulsion. In the limit as $\beta \to \infty$, the Peclet number is $O(\sin^2 \theta_s Da)$. Therefore, the velocity of the motor becomes

$$U = \frac{3}{4}\kappa \sin^2 \theta_s, \qquad (4.18)$$

which is independent of the concentration of bath particles and particle sizes. From (4.17) we found that for slow reactions, the maximum velocity is

$$U_{max} = \left(\frac{\frac{3}{8}\beta}{\frac{1}{2}\beta + 1} \right) \kappa, \qquad (4.19)$$

and it is obtained at $\theta_s^{op} = \pi/2$. At this same optimal angle a maximum force was accomplished by the fixed motor at small Da.

4.3.2.2 High Da limit

It is helpful to investigate the microstructure at high Damköhler numbers for surface reactions on the front portion $(0 < \theta_s < \pi/2)$ and on the rear portion $(\pi > \theta_s > \pi/2)$ of the motor separately, considering both circumstances exhibit different behaviors. Fast reactions on the reactive surface create a sink of bath particles, which is limited by the diffusion of the bath particles. In the limit as $Da \to \infty$, all bath particles colliding with the reactive surface are consumed, therefore, the pair-distribution function at contact is zero on this portion $(g = 0)$. The boundary condition (4.12) at the passive surface becomes

$$\frac{\partial g}{\partial r} = -Pe\mu g. \tag{4.20}$$

In the limit of small Pe, a regular perturbation expansion in Pe turns the microstructural evolution Eq. (4.10) into Laplace's equation $\nabla^2 g = 0$ with a general solution given by (4.14). The boundary condition at the passive surface becomes $\partial g/\partial r = -\mu$. Note that the Péclet number is nowhere in the governing equations, therefore, $g \sim O(1)$ and the nondimensional function $\mathcal{F}(Da \to \infty, Pe \ll 1) \approx \int g\mu d\mu \sim O(1)$. Thus, for slow propulsion at high Da, the Péclet number scales as $Pe \sim \beta$. This scaling is true for all distributions of reactive surfaces.

In our previous work, we have found that for half-reactive motors the Péclet number scales as $Pe \sim (\beta Da)^{3/5}$ in the limit of high Da and β (see details in Chapter 3). We demonstrate below that this scaling is unique for half-reactive motors. A fast moving motor (high Pe) develops a wake of zero bath particles on the rear of the motor that grows as Pe is increased, a similar feature observed in inert probe particles used for active microrheology measurements (Squires and Brady 2005; Khair and Brady 2006).

First we examine fast reaction on the front portion of the motor. The reactive region is located within $\mu_s < \mu < 1$, where $\mu_s = \cos\theta_s$. In the high Da and Pe limit, diffusion is only important in a thin region of $O(Pe^{-1}(a+b))$ adjacent to the motor, outside of which advection dominates and $g = 1$. This region is governed by a balance between radial diffusion and radial advection, giving an approximate equation

$$\frac{\partial^2 g}{\partial Y^2} + \mu \frac{\partial g}{\partial Y} = 0, \tag{4.21}$$

where $Y = Pe(r=1)$ is a coordinate perpendicular to the reactive surface. This equation has a solution of

$$g = 1 - e^{-\mu Y}. \tag{4.22}$$

There will be a region of rapid angular variation near μ_s that scales as $1/Pe$. The angular coordinate is then transformed into $s = Pe(\mu - \mu_s)$ to represent this region, where radial and angular diffusion balances radial and angular advection. These scalings for the perpendicular and parallel coordinates are substituted into the governing equation (4.10), giving

$$\frac{\partial^2 g}{\partial Y^2} + (1-\mu_s^2)\frac{\partial^2 g}{\partial s^2} = -\left(\mu_s \frac{\partial g}{\partial Y} - (1-\mu_s^2)\frac{\partial g}{\partial s}\right), \tag{4.23}$$

subject to the undisturbed probability density far from this region, $g \sim 1$ as $Y \to \infty$, and at $Y = 0$ the boundary condition becomes

$$\frac{\partial g}{\partial Y} + \mu_s g = 0. \tag{4.24}$$

The general solution of g in this region must match the solution (4.22) as $s \to -\infty$. A strong advection (high Pe) increases the bath particle concentration in the region within

$\mu_s < \mu < 0$ and reverses the gradient in concentration necessary for propulsion. The pair-distribution function is order Pe in this region. On the rear (passive) portion of the motor, the pair-distribution function is $O(1)$. Integrating g over the surface of contact will give a negative $\mathcal{F}(Da, Pe)$ and one that is finite as $Pe \to \infty$. But the motor never achieves this limit. In fact, there is a limiting Pe that is $O(1)$ and independent of concentration and particle size as $\beta \to \infty$. This means that the nondimensional function $\mathcal{F}(Da, Pe) \approx \int g\mu d\mu$ decays as $1/\beta$ at high β to saturate the motion of the motor with the relative diffusive flux. Thus, the resulting motor velocity in this limit for fast reaction on the front portion is simply $U \sim D/(a+b)$ — the relative diffusive speed of the particles.

We now proceed to examine fast reaction on the rear portion of the motor. On the reactive region within $0 < \mu < 1$, there is also a thin region of $O(Pe^{-1})$ near contact where the pair-distribution function is satisfied by Eq. (4.22), which is caused by the advective flux of bath particles toward the moving motor. The pair-distribution function is unity outside of this thin region. The reactive surface on the rear portion within $\mu_s < \mu < 1$ acts as a sink of bath particles and drives a free-shear layer-like evolution of bath particle concentration from unity above (outside of the wake) to zero below (reactive surface: $g = 0$). It is possible here that the value of g at the passive surface is very small for large Pe. The pair-distribution function at the passive surface satisfies Eq. (4.20), showing that g is exponentially small such as $g \sim e^{-Pe}$. Recalling that $\beta \approx Pe/\int g\mu d\mu$, we then obtain the scaling $\beta \sim Pe\, e^{Pe}$ as $Pe \to \infty$, which can also be read $\ln \beta \sim Pe + \ln Pe$. Resultantly, the Péclet number behaves as $Pe \sim \ln \beta$ in the limit of high β. This strong dependence in Pe would then appear as if there was a finite Pe as $\beta \to \infty$, much like the case for front half reactive. The proposed scaling arguments are investigated numerically in the next section.
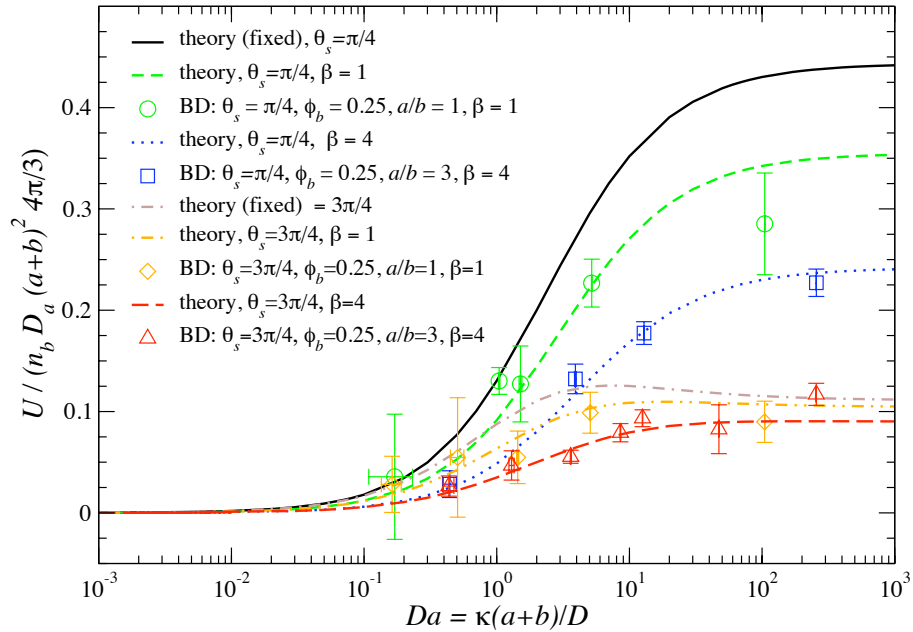
Figure 4.7: The motor velocity scaled by $D_a n_b(a+b)^2 4\pi/3$ as a function of Da for various angles θ_s and β. The theoretical predictions (curves) are compared with Brownian dynamics (BD) simulations (symbols). A time step $\Delta t = 0.001$ was chosen for the BD simulations.

4.3.2.3 Arbitrary Da

After considering the boundary conditions at contact and far from the motor, the pair-distribution function $g(\boldsymbol{r})$ is solved numerically for various distributions of reactive sites and simultaneously with the implicit formula of the Péclet number for arbitrary Damköhler numbers. This enables us to compute the nondimensional function $\mathcal{F}(Da, Pe, \theta_s)$ for a variety of physical conditions expressed in the product β and Da, and propose explanations for the results obtained. Figure 4.7 plots the scaled velocity of the motor, $U/(D_a\phi/(a+b)) = \mathcal{F}(Da, Pe, \theta_s)$, as a function of Da for various angles θ_s and values of β. The open symbols in the figure are the result of Brownian dynamics simulations. The time step of the simulation is 0.001. The results in the figure show that the fixed motor is the limit as $\beta \to 0$ ($Pe = 0$) of the free motor; the fixed motor corresponds to an infinitely dilute suspension of bath particles. This is true for any distribution of the reactive site. The plot agrees with Eq.
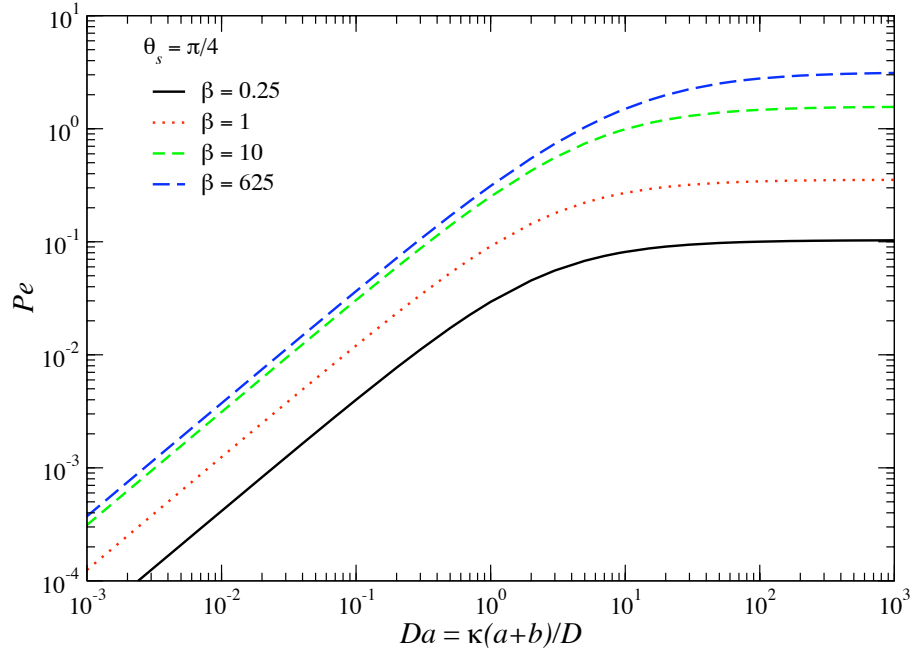
Figure 4.8: The Péclet number Pe as a function of Da at $\theta_s = \pi/4$ and various β

(4.16) as expected for small Da numbers. In the limit as $Da \to \infty$, the velocity of the motor

saturates and becomes independent of Da. As the theory predicted, the scaled velocity of

the motor depends on the size ratio a/b, the concentration of bath particles expressed as

their volume fraction, ϕ_b (combined in $\beta = \phi_b(1 + a/b)^2$), but not on the time step Δt used

in the simulations. The decreasing nondimensional function $\mathcal{F}(Da, Pe, \theta_s)$ for a given θ_s as

β is increased reflects the fact that the gradient in bath particle concentration at contact

is affected by the Péclet number. For the physical values considered in this figure, Pe is

small.

In Figure 4.8, the behavior of Pe for a motor with reaction only on the front portion

is investigated as a function of Da for arbitrary values of β. We have chosen the angle

$\theta_s = \pi/4$ to represent the physics encountered on all the reaction distributions that are

less than half motor. The figure shows that in the limit of small Da, the Péclet number is

$O(Da)$, independently of the value of β. A different behavior is expected at high Da, when
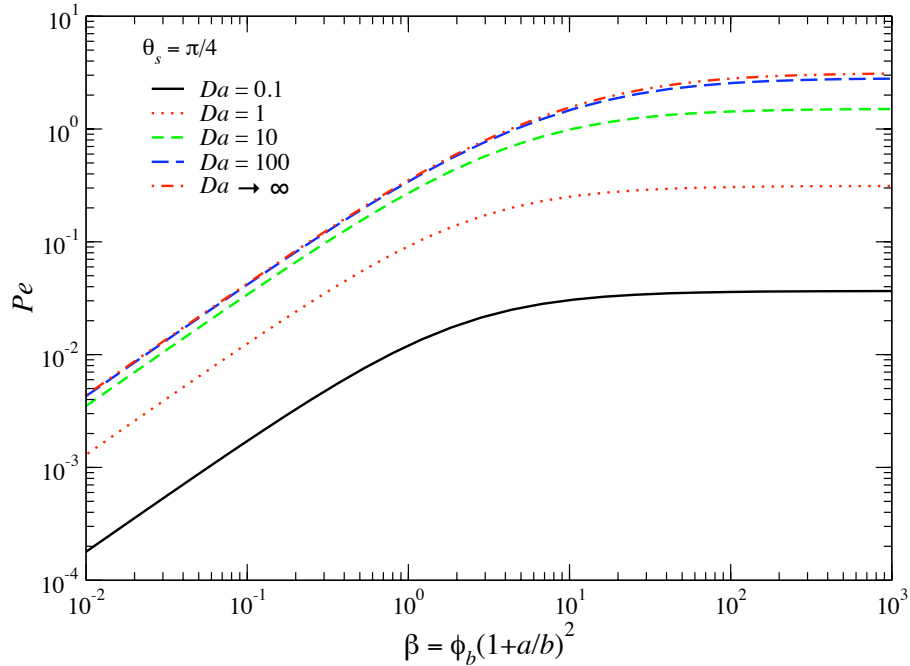
Figure 4.9: The Péclet number Pe as a function of β at $\theta_s = \pi/4$ and various Da

reaction dominates the microstructural deformation over diffusion. For all β, it is observed

that the Péclet number is independent of the speed of reaction just as $Da \to \infty$. Thus,

the motor velocity saturates and becomes uncontrolled by Da. The dependence of β on the

Péclet number is shown in Figure 4.9 for various Da and assuming $\theta_s = \pi/4$. Firstly, the

Péclet number is linear in β for small β. Therefore, the right scaling for small Da and β

is $Pe \sim \beta Da$; the motor velocity behaves as $U \sim n_b b(a+b)^2 \kappa$. At high β, we found that

$Pe \sim O(1)$, which shows that the motor velocity is simply $U \sim D/(a+b)$ — the relative

diffusive speed of the particles. At saturation, adding more bath particles to collide with

the motor does not change the probability distribution of bath particles around the motor

nor, consequently, its behavior. We have also plotted in Figure 4.9 the Péclet number in

the limit as $Da \to \infty$, where we found that at small β, it is linear in β, and at high β, it

becomes independent of β. The autonomous behavior of the motor with reaction on the

front portion is controlled by the self-induced advective flux of bath particles toward the
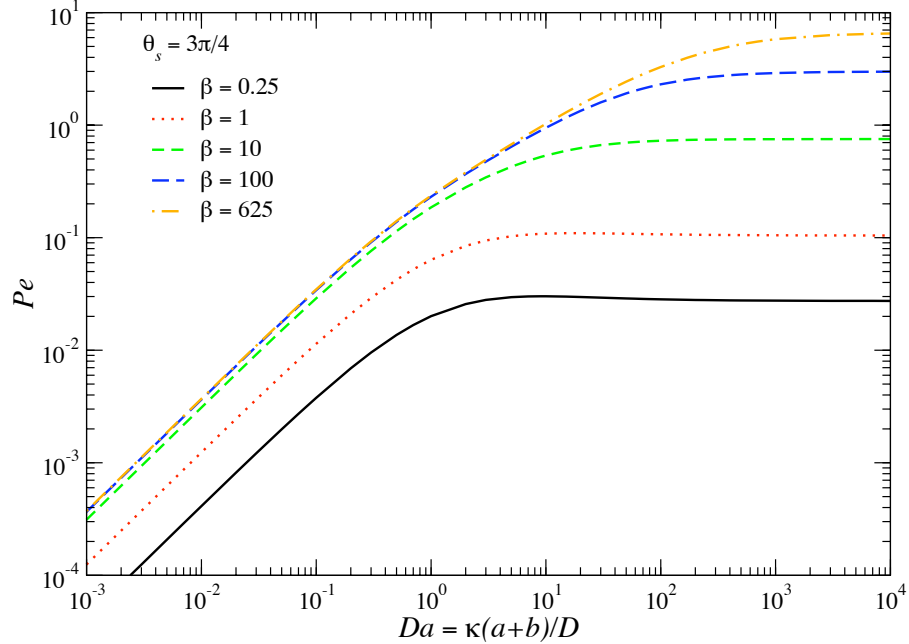
Figure 4.10: The Péclet number Pe as a function of Da at $\theta_s = 3\pi/4$ and various β

front and away from the motor, however, it saturates in the limit of high Da and β before
it reaches microrheology build up that could change the sign of the bath particle gradient
and reverse the process. Evidently, the motor regulates itself to avoid such behavior.

This observation is not the case for half-reactive motors ($\theta_s = \pi/2$), where the Péclet
number was found to diverge as $Pe \sim (\beta Da)^{3/5}$ in the limit of high β and Da, proving
the singularity that is present at such reaction distribution. It was determined that the
nondimensional function $\mathcal{F}(Da, Pe, \theta_s = \pi/2)$ goes to zero as $Pe^{-2/3}$, thus preventing any
microrheology build up that could stop or reverse the motion. The reader can find a detailed
description of half-reactive motors in Chapter 3. We proceed to investigate the resulting
Pe for a motor with reaction on the rear portion. We have plotted in Figure 4.10 the Péclet
number as a function of Da for arbitrary values of β. The angle $\theta_s = 3\pi/4$ is considered to
illustrate the physics involved for all reaction distributions that are greater than half motor.
It is found that for small Da, the Peclet number is linear in Da. This is consistent with
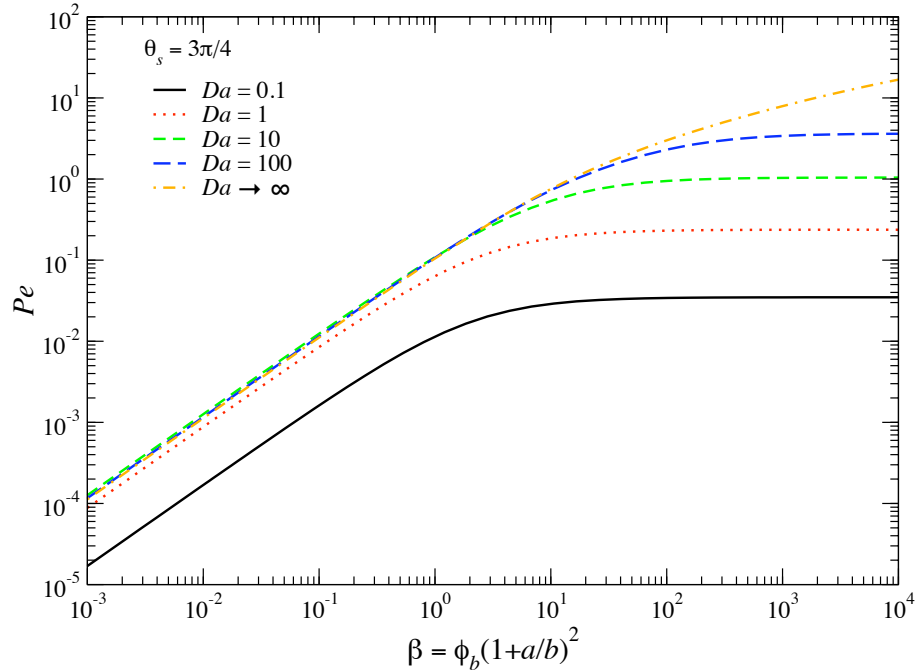
Figure 4.11: The Péclet number Pe as a function of β at $\theta_s = 3\pi/4$ and various Da

what was found analytically for all distributions of the reactive site. As Da is increased, the Péclet number reaches a limiting value ($Pe \sim O(1)$) for small and intermediate β. This is not the case in the high β limit, where the Péclet number seems to approach an asymptote, but, in fact, it scales as $Pe \sim \ln(Da)$ in the limit as $Da \to \infty$. The resulting Péclet number against the product β at the angle $\theta_s = 3\pi/4$ and multiple values of Da is shown in Figure 4.11. It is found that for small β, the Péclet number scales as $Pe \sim \beta$, which is true for all values of θ_s. Thus, it becomes clear that for all distributions of slow reactions the Péclet number scales as $Pe \sim \beta Da$, giving a motor velocity of $U \sim n_b b(a + b)^2 \kappa$ as found analytically in Section 4.3.2.1. In the limit as $\beta \to \infty$, the figure shows that for arbitrary but finite Da, Pe is $O(1)$ (saturation limit), thus the osmotic motor scales as $U \sim D/(a+b)$, which is a similar result obtained for reactions on the front portion. The figure reiterates that at both high β and Da, the Péclet number appears to approach a plateau. In fact, it was found that Pe increments are exponentially small. This behavior is examined in Figure
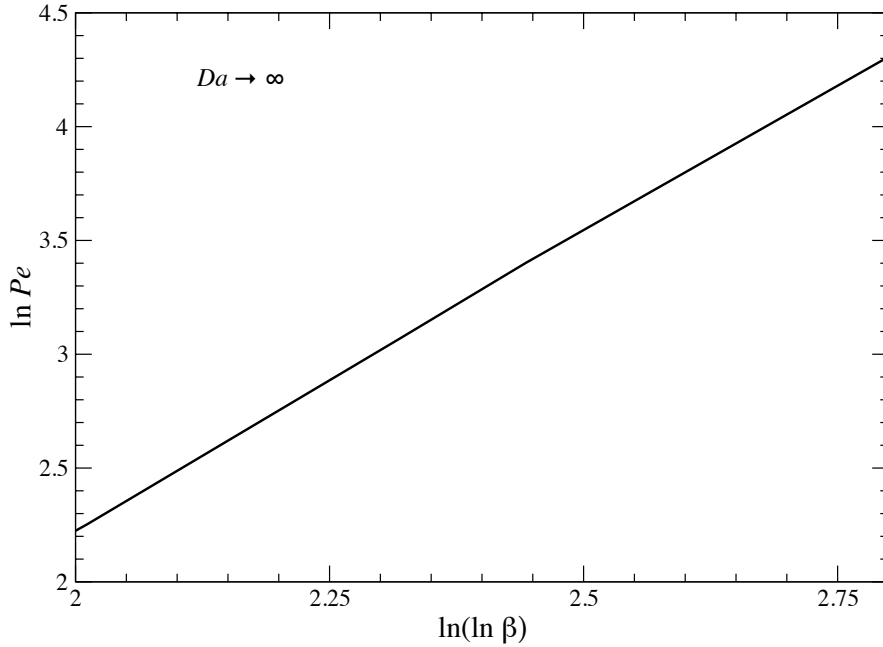
Figure 4.12: The natural logarithm of the Péclet number, $\ln Pe$, as a function of $\ln(\ln \beta)$ at $\theta_s = 3\pi/4$ in the limit as $Da \to \infty$

4.12 (complementary to Figure 4.11), where the natural logarithm of the Péclet number, $\ln Pe$, is plotted as a function of $\ln(\ln \beta)$ at $\theta_s = 3\pi/4$ in the limit as $Da \to \infty$. The figure clearly shows a linear dependence, giving $Pe \sim \ln \beta$ in the process of $\beta \to \infty$, which was predicted in Section 4.3.2.2 using scaling arguments. This same scaling is also expected in this limit for other angles within $\pi/2 < \theta_s < \pi$. Resultantly, the Péclet number scales as $Pe \sim \ln(\beta Da)$ at high β and Da for reaction distributions on the rear of the motor. Thus, the motor velocity scales as $U \sim D/(a + b) \ln(n_b b(a + b)^3 \kappa/D)$. A motor with reaction on the rear portion does not experience microrheology build-up at high Pe because all bath particles colliding in the front side are consumed $(g = 0)$.

Independently of the distribution of reactions over the surface, a fast moving motor develops behind a wake of low bath particle concentration $(g \approx 0)$ that grows as Pe. Indeed, for small reactive sites and small passive sites, Pe is also small, thus the wake is not
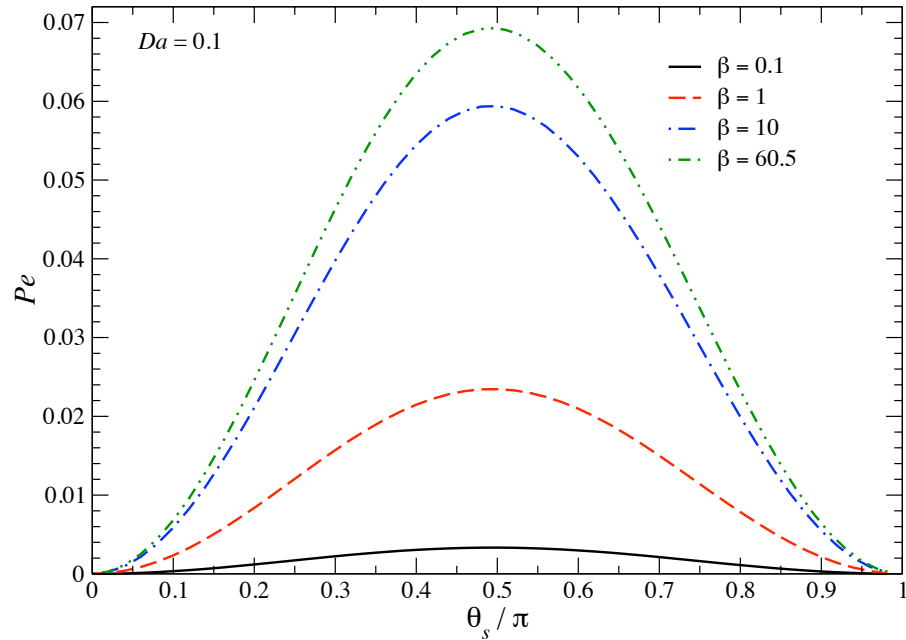
Figure 4.13: The Péclet number Pe as a function of the angle θ_s scaled by π at $Da = 0.1$ for various β

as fully developed as we expect at high Pe for intermediate reaction distributions. Outside of the wake, the pair-distribution function is $g \sim 1$. Bath particles from this region that migrate in the wake are rapidly advected away from the motor. If the distribution of the reactive site on the motor is greater than $\pi/2$, the motor velocity does not saturate (this is contrary to what is observed for motors with distributions within $0 < \theta_s < \pi/2$) because bath particles traveling on the boundaries of the low density wake that are close to the rear portion of the motor could diffuse inside the wake and collide with the passive surface. It is this concentration contribution, which is small, that prevents saturation. This explains the scaling argument dependent on bath particle concentration found for Pe in the limit of high β and Da.

Having investigated the Péclet number as a function of Da and β, we now present the resulting Pe as a function of θ_s in Figures 4.13 and 4.14. Figure 4.13 shows the Péclet
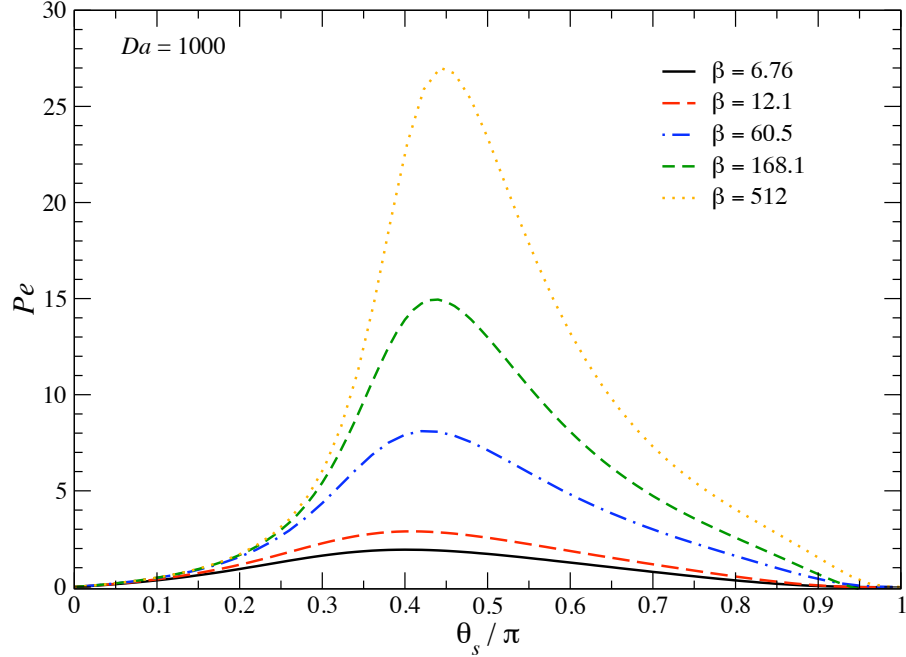
Figure 4.14: The Péclet number Pe as a function of the angle θ_s scaled by π at $Da = 1000$ for various β

number as a function of θ_s at $Da = 0.1$ and various β. Note that the curves are nearly symmetric with respect to $\theta_s = \pi/2$, showing that at small Da a maximum is located at $\pi/2$ independently of the value of β. As expected, the Péclet number increases as β is increased. Each curve approximates Eq. (4.17), which was obtained analytically and described in Section 4.3.2.1. In Figure 4.14, the Péclet number is plotted against θ_s at $Da = 1000$ and various β. In contrast to what is observed for small Da, the curves are asymmetric with respect to $\theta_s = \pi/2$. As β is increased, the Péclet number increases and the maximum value in each plot, which are all located on the front portion of the motor, shifts toward $\pi/2$ (the optimal angle θ_s^{op}). This result ($\theta_s^{op} = \pi/2$) differs from the optimal angle for maximum force obtained at high Da for the fixed motor: $\theta_s^{op} \approx 0.3776\pi$, which is also the result at $\beta = 0$. If the angle θ_s is less than $\pi/2$ (reaction on the front), the advective flux of bath particles arriving to the surface fraction from θ_s to $\pi/2$ increases the probability
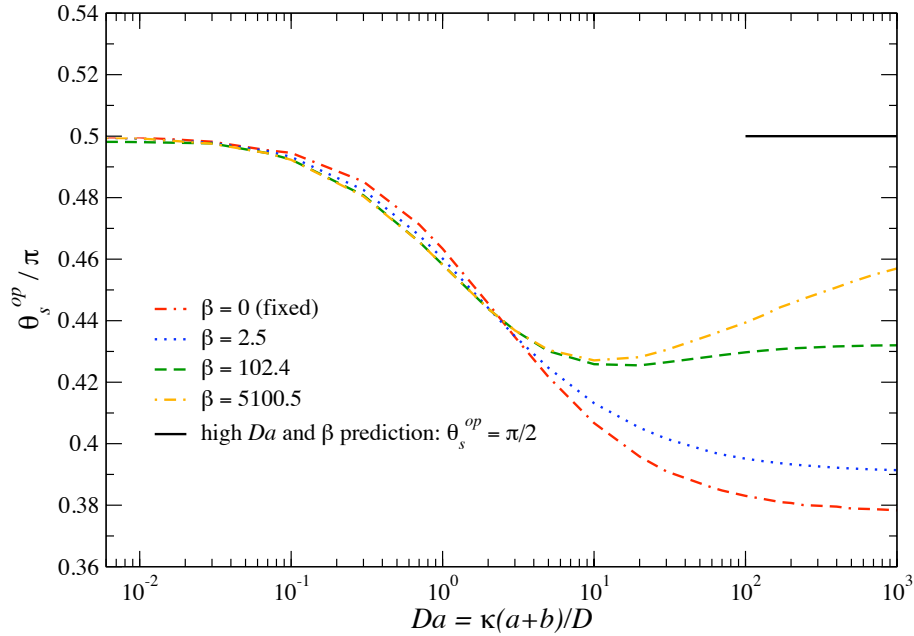
Figure 4.15: The optimal angle θ_s^{op} scaled by π as a function of Da for various β. The solid horizontal line is the predicted limit of θ_s^{op} at small Da; the dashed horizontal line is the predicted limit of θ_s^{op} at high Da.

of finding bath particles in that region, and consequently reduces the motor's speed by providing hard-sphere forces in the opposite desired direction of motion. Therefore, only half-reactive motors subject to fast reactions and high β are less affected by the strong advective flux of bath particles toward the front side of the motor. In the limit of high β, the Péclet number in the region within $0 < \theta_s < \pi/2$ was found to be limited by $D/(a+b)$ and the region within $\pi/2 < \theta_s < \pi$, scales as $Pe \sim \ln \beta$. Similar plots were constructed for other Damköhler numbers in order to obtain the optimal distribution of the reactive site that gives maximum velocity (Pe).

To study the behavior of the maximized motor velocity, we plot in Figure 4.15 the resulting optimal angles θ_s^{op} as a function of Da for various β. As shown above, for small Da the optimal angle is $\pi/2$ for all values of β, which is also observed in the figure (solid line). In the limit as $\beta \to 0$, the curve for the optimal angle as a function of Da corresponds to
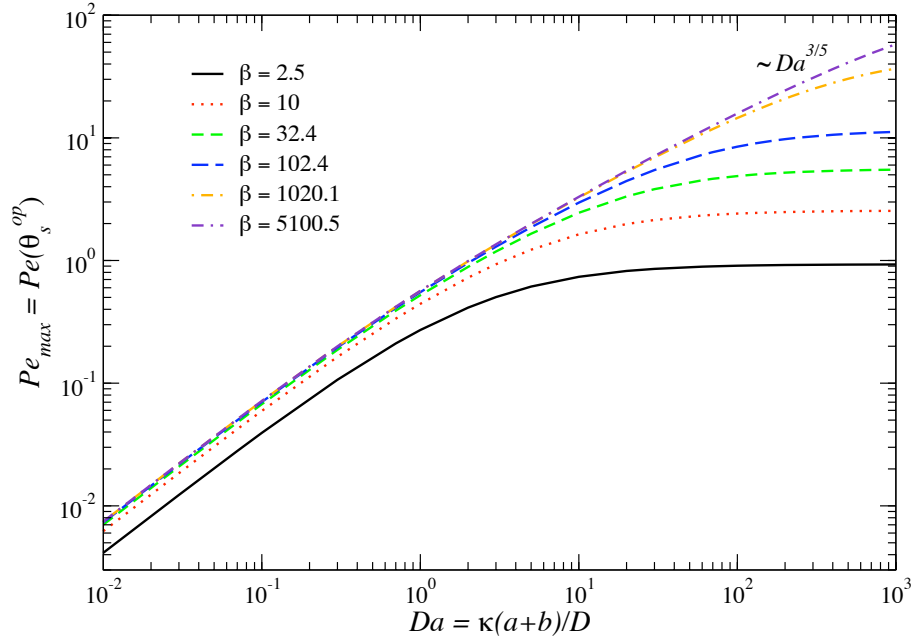
Figure 4.16: The maximum Péclet number $Pe_{max} = Pe(\theta_s^{op})$ as a function of Da for various β

the data plotted in Figure 4.4, which is included for comparison with curves for nonzero β. This $\beta = 0$ curve approaches the value of $\theta_s^{op} \approx 0.3776\pi$ in the case of a fast reaction. In the opposite limit (high Da), the optimal angle increases as the product β is increased, but we were unable to calculate numerically the resulting optimal angle and plot its behavior for very high Da and β values. At these extreme limits, the numerical method requires large grids with many nodes in the regions where most needed (regions of large bath particle gradients), making the process computationally unfeasible and a different approach is required. Note that for increasing β, the optimal angle θ_s^{op} shows a "bottom" with inflection point near $Da \approx 10$ and $\theta_s^{op} \approx 0.43\pi$. The physical meaning of this inflection point is unknown.

The maximum Péclet number Pe_{max}, which corresponds to the Péclet number evaluated at θ_s^{op} ($Pe_{max} = Pe(\theta_s^{op})$), is plotted in Figure 4.16 as a function of Da for arbitrary values of β. This plot shows that at small Da, $Pe_{max} \sim Da$ for all β. In limit of high Da, there is a limiting Pe_{max} for small and arbitrary values of β, and thus $U_{max} \sim D/(a+b)$. This is not

the case in the limit of high β, where the maximum Péclet number diverges (not limited by diffusion) and scales as $Pe_{max} \sim (\beta Da)^{3/5}$, thus $U_{max} \sim (D_a/b)^{5/2}\kappa^{3/5}$. In fact, this is the same scaling observed for the Péclet number at high Da and β for half-reactive motors (see details in Chapter 3). Based on this observation, we predict that the optimal angle goes to $\pi/2$ in the limit of high Pe, which results in the limits as $Da \to \infty$ and $\beta \to \infty$ (Figure 4.15). Note that as $\beta \to \infty$ the optimal angle is the same ($\theta_s^{op} = \pi/2$) in the limits of small Da and $Da \to \infty$. It is known that increasing the product β corresponds to increasing the number of bath particles colliding within a bath particle radius of the motor surface. In the limits of high Da and β, the advective flux of bath particles (given by Pe) toward the motor and parallel to the direction of motion is high. This has the net effect of building up bath particles near any passive surface area within $0 < \theta < \pi/2$ (right hemisphere), which limits self-propulsion for the motor by reducing the bath particle concentration gradient created by the motor. A moving motor under these conditions cannot obtain maximum velocity for optimal angles less than $\pi/2$ because the strong advective force ($Pe \gg 1$) restores any regions of low bath particle concentration that could be created near passive surface portions located within θ_s and $\pi/2$ as an indirect consequence of the fast reaction. The optimal angles for maximum propulsion of the free motor are less than or equal to $\pi/2$, similar to the fixed motor scenario.

To illustrate the effect of increasing Da to the microstructure, we show in Figures 4.17 and 4.18 density profiles of the suspension surrounding the osmotic motor with distribution of reaction given by the angles $\theta_s = \pi/4$ and $\theta_s = 3\pi/4$. The top row of both figures corresponds to the case of $\beta = 10$ and increasing Da; and the bottom row to $Da = 100$ and increasing β. It is observed for $\beta = 10$ that the region of low bath particle concentration near the reactive surface grows as Da until it saturates in the limit of high Da, where
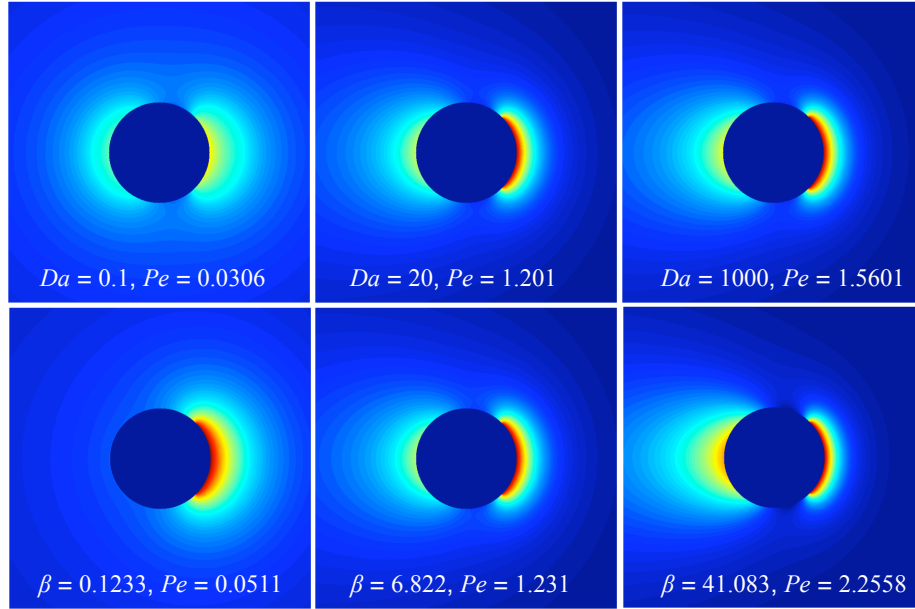
Figure 4.17: Density profiles in the symmetry plate of the fixed osmotic motor at a distributions of reaction $\theta_s = \pi/4$. Regions of low bath particle concentration are in red and the undisturbed regions in blue. The top row corresponds to $\beta = 10$ and increasing Da; the bottom row represents $Da = 100$ and increasing β. The motion is from left to right.

it becomes limited by the diffusion of bath particles. The behavior of the microstructure is different if Da is maintained constant, but the product β is varied. The density plots show that the depleted region near the reactive surface decreases for increasing β until an advection-diffusion boundary layer of width $\sim (a + b)/Pe$ is formed at high Pe on the front of the motor (right hemisphere). In the case of $\theta_s = \pi/4$, the boundary layer within $0 < \theta < \theta_s$ contains no bath particles ($g = 0$) and the deformation within $\theta_s < \theta < \pi/2$ has magnitude of order Pe. The microstructure is unchanged ($g = 1$) outside of the boundary layer. Simultaneously, the moving motor creates a wake with no bath particles ($g = 0$) in the rear of the motor (left hemisphere). In the case of $\theta_s = 3\pi/4$, the front side of the motor forms a boundary layer of zero concentration and $O(1/Pe)$. The remaining reactive surface reduces the bath particle concentration in the vicinity, however, at high Da the migration of bath particles from outside this region to the passive surface prevents saturation and a
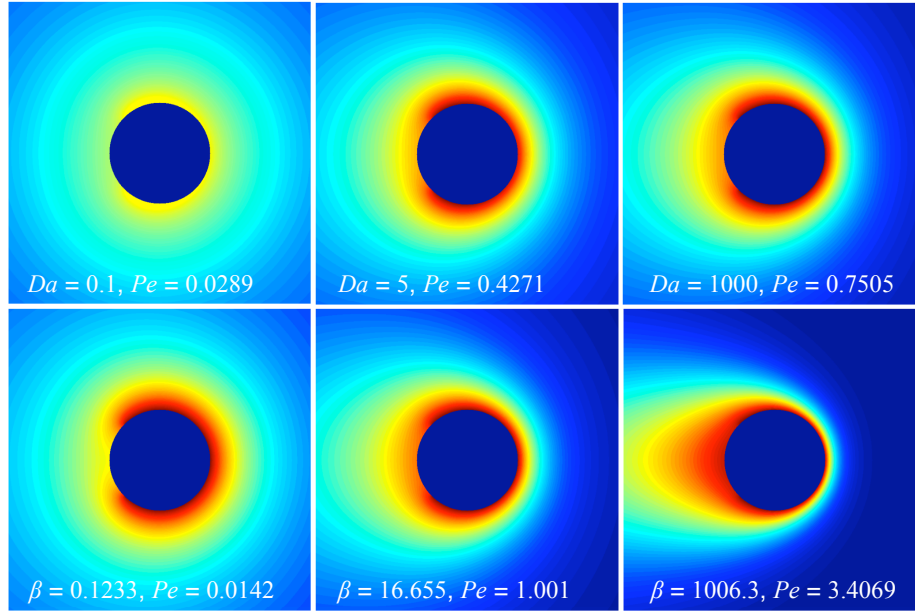
Figure 4.18: Density profiles in the symmetry plate of the fixed osmotic motor at a distributions of reaction $\theta_s = 3\pi/4$. Regions of low bath particle concentration are in red and the undisturbed regions in blue. The top row corresponds to $\beta = 10$ and increasing Da; the bottom row represents $Da = 100$ and increasing β. The motion is from left to right.

finite velocity for the motor. Also shown on the figures are the resulting Péclet numbers corresponding to the motor velocities.

4.4 Conclusions and discussion

The work presented offers a theoretical framework for the behavior of an osmotic motor subject to different distributions of reactive surfaces established by the angle θ_s. For simplicity, it was assumed that an irreversible first-order reaction consumes bath particles at a portion of the motor surface. The basis of our concept involves determining the reaction-induced perturbation to the suspension microstructure in order to calculate the driving force on the motor, from which the motor velocity is determined via application of the Stokes drag law. A theory for the microstructure evolution was provided and solved in the simplest limiting case of hard-spheres in the absence of hydrodynamic interactions and rotational diffusion.

The model was restricted to the limit where bath particles do behave as an ideal gas. In addition to the theory, we used a Brownian dynamics simulation that provided a means of verifying our theoretical results. We examined two scenarios for the osmotic motor: one in which the motor is held fixed by an external force $\boldsymbol{F}^{ext}$, and another where the motor is free to move.

Once the microstructural deformation caused by the surface reaction is known, relevant statistical quantities can be computed. We have calculated the fixed motor force for all values of Damköhler number, Da, bath particle volume fraction, ϕ_b, and motor/bath size ratios, a/b, for different values of the angle θ_s. For each angle θ_s, the results collapse into an universal curve after scaling the osmotic force by $kTn_b(a + b)^2 4\pi/3$. We have shown that BD simulations agree with the theoretical predictions. For small perturbations to the microstructure, we found the osmotic force is order Da times the geometric factor $\sin\theta_s^2$. In the limit of high Da, the force saturates and simply scales as $F^{osm} \sim n_b kT(a+b)^2 f(\theta_s)$, where the function $f(\theta_s)$ is independent of θ_s in the limits of small and large reactive sites.

When the motor is let free, it moves rapidly toward the self-created low bath particle concentration region ($g \ll 1$) located near the reactive surface. The resulting advective flux of bath particles toward the motor alters the bath particle probability distribution relative to the motor, and, consequently, the propulsive force. Eventually (almost instantaneously) the motor catches up with bath particles reducing the gradient in bath particle concentration. Independently of the amount of reactive surface, the motor cannot move faster than the rate in which the depleted region in front of the motor is created. If the contrary happens, the motor destroys the concentrated gradient needed for propulsion. Therefore, the osmotic force is balanced by the viscous force acting on the moving motor. The resulting motor velocity was calculated as a function of Da for various $\beta = \phi_b(1 + a/b)^2$ and angles θ_s. Also

we demonstrated again that BD simulations are in agreement with the theoretical results. In general, we have shown that the physical properties of the microstructure, the size ratio a/b and the bath particle volume fraction ϕ_b (the product β), directly contribute to the speed of the motor, an observation not found in the fixed motor problem.

At small Da numbers, we have shown that motor velocity is described simply by $U = \frac{3}{8}\beta\sin^2\theta_s\kappa/(\frac{1}{2}\beta+1)$. For small β, the motor velocity scales as $U \sim D_a n_b(a+b)^2 Da \sin\theta_s^2$, while in the limit as $\beta \to \infty$, it becomes $U = \frac{3}{4}\kappa\sin\theta_s^2$. To study the high-$Da$ limit, we divided the analysis to reaction on front and reaction on rear of the motor. When the reaction is on front, the Péclet number scales as $Pe \sim \beta$ at small β, resulting in the motor velocity $U \sim D_a n_b(a+b)^2$. We also found that for all values of β in the limit as $Da \to \infty$, the Péclet number is $O(1)$. Thus, the motor velocity saturates and becomes limited by the diffusive velocity of the bath particles, $U \sim D/(a+b)$, which is independent of bath particle concentration and particle size. For reaction on the rear, we found that the Péclet number scales as $Pe \sim \beta$ for small β, giving the motor velocity $U \sim D_a n_b(a+b)^2$. This limit is observed for all distributions of the reactive site. However, in the limit as $\beta \to \infty$, the Péclet number appears to slowly approach a limiting speed as $Pe \sim \ln\beta$, thus the motor velocity scales as $U \sim D/(a+b)\ln(n_b(a+b)^2)$ and does depend on the concentration of bath particles and particle size. In fact, only at $\theta_s = \pi/2$ (half reactive motor) we observed that in the limit as $Da \to \infty$ and $\beta \to \infty$ the Péclet number diverges as $Pe \sim (\beta Da)^{3/5}$, giving the motor velocity $U \sim D/(a+b)\ln(n_b b(a+b)^3\kappa/D)$.

The optimal angle for maximum propulsion was computed as a function of the Damköhler number and various β. For small Da we found that independently of the value of β, the optimal angle is $\theta_s^{op} = \pi/2$. At high Da, the optimal angle changes depending on the value of β. At $\beta = 0$ (no motion), the optimal angle θ_s^{op} converges to approximately 0.3776π. As

β is increased and the advective forces become stronger on the motor, the optimal angle increases as well. In the limit as $\beta \to \infty$, the optimal angle is again at $\theta_s^{op} = \pi/2$. This is the case because, for half-reactive motors, the Péclet number diverges for increasing β and Da, meaning that the gradient in bath particle concentration goes to zero.

In this study, we have neglected hydrodynamic interactions and rotation diffusion. Inclusion of hydrodynamic interactions does affect quantitatively (not qualitatively) the results for the osmotic force. It could also change the values of the optimal angles, but up to what extent is unknown. Adding rotational diffusion to the model may change the net osmotic force, however changing the distribution of the reactive surface could potentially be used to reduce the effect of rotational motion to the net force and even to regulate it in general. Indeed, rotational diffusion is negligible for large motors when compared to translational diffusion, $D_a^r/D_a \sim (1/a)^2$, where $D_a^r = kT/8\pi\eta a^3$ is the motor rotary diffusivity. Another important means to limit the rotation of the motor is to have a non-spherical motor with a relatively large aspect ratio and have reaction occurring on one end only, much like the catalytic nanorods used in the original experiments of Paxton et al. (2004).

In general, it should be interesting to expand and compare the proposed ideas for optimal angles to other transport mechanisms (e.g., diffusiophoresis). A similar argument for optimizing the design of swimmers based on patterns of surface properties was presented by Golestanian et al. (2007). We have demonstrated that more reactive surfaces do not translate to higher forces or velocities. As we have done for spheres, motors with other geometries (e.g., cylinders, spheroids) could be characterized by a length parameter describing the amount of the reactive surface, which is then optimized for better performance. Many important questions are raised when designing catalytic motors. How does the portion of reactive surfaces vary from shape to shape? What is the best shape? What happens if there

is more than one motor? Can motors be used to assist other motors to optimize propulsion?

The design and construction of osmotic motors can revolutionize applications in directed self-assembly of materials, thermal management of micro- and nanoprocessors, and the operation of chemical and biological sensors. One can potentially construct a system or array of motors with different distributions of reactive sites, where each motor produces different osmotic forces when supplying reactant bath particles to the medium. Another interesting possibility is the design of intelligent motors that regulate distribution of reactive sites autonomously or via external inputs (e.g., UV light, magnets) to control speed and manage different tasks.

4.5 Bibliography

J. L. Anderson. Colloid transport by interfacial forces. *Annu. Rev. Fluid Mech.*, 21:61–99, 1989.

G. K. Batchelor. Brownian diffusion of particles with hydrodynamic interaction. *J. Fluid Mech.*, 74:1–29, 1976.

H. C. Berg. Motile behavior of bacteria. *Phys. Today*, 53(1):24–29, 2000.

I. C. Carpen and J. F. Brady. Microrheology of colloidal dispersions by Brownian dynamics simulations. *J. Rheol.*, 49(6):1483–1502, 2005.

U. M. Córdova-Figueroa and J. F. Brady. Osmotic Propulsion: The Osmotic Motor. *Phys. Rev. Lett.*, 100(15):158303–158307, 2008.

D. R. Foss and J. F. Brady. Brownian Dynamics simulation of hard-sphere colloidal dispersions. *J. Rheol.*, 44(3):629–651, 2000.

S. Fournier-Bidoz, A. C. Arsenault, I. Manners, and G. A. Ozin. Synthetic self-propelled nanorotors. *Chem. Commun.*, (4):441–443, 2005.

R. Golestanian, T. B. Liverpool, and A. Ajdari. Designing phoretic micro- and nano-swimmers. *New J. Phys.*, 9, 2007.

A. S. Khair and J. F. Brady. Single particle motion in colloidal dispersions: a simple model for active and nonlinear microrheology. *J. Fluid Mech.*, 557:73–117, 2006.

R. J. LeVeque. *Finite Difference Methods for Ordinary and Partial Differential Equations: Steady-State and Time-Dependent Problems*. Society for Industrial and Applied Mathematics, 2007.

W. F. Paxton, S. Sundararajan, T. E. Mallouk, and A. Sen. Chemical locomotion. *Angew. Chem. Int. Ed.*, 45(33):5420–5429, 2006.

W. F. Paxton, K. C. Kistler, C. C. Olmeda, A. Sen, S. K. St. Angelo, Y. Y. Cao, T. E. Mallouk, P. E. Lammert, and V. H. Crespi. Catalytic nanomotors: Autonomous movement of striped nanorods. *J. Am. Chem. Soc.*, 126(41):13424–13431, 2004.

M. Schliwa and G. Woehlke. Molecular motors. *Nature*, 422(6933):759–765, 2003.

R. K. Soong, G. D. Bachand, H. P. Neves, A. G. Olkhovets, H. G. Craighead, and C. D. Montemagno. Powering an inorganic nanodevice with a biomolecular motor. *Science*, 290(5496):1555–1558, 2000.

T. M. Squires and J. F. Brady. A simple paradigm for active and nonlinear microrheology. *Phys. Fluids*, 17(7), 2005.

R. Yokokawa, S. Takeuchi, T. Kon, M. Nishiura, R. Ohkura, K. Sutoh, and H. Fujita. Hybrid nanotransport system by biomolecular linear motors. *J. Microelectromech. S.*, 13 (4):612–619, 2004.

Chapter 5

Osmotic propulsion by surface flux

5.1 Introduction

Self-propulsion at nano-scales through a fluid medium is one of the most difficult challenges facing nanoscience today. The goal is to synthesize and exploit motors made from a myriad of nanoscale building blocks that obtain on-board or off-board power from chemical reactions. The created work allows these devices to propel themselves through a fluid phase while, simultaneously or sequentially, performing a task or series of tasks. Such nanomachines, whether individual, or assembled into designed architectures, might someday transport medicine in the human body, conduct operations in cells, move cargo around microfluidic chips, manage light beams, agitate liquids close to electrode surfaces, and search for and destroy toxic organic molecules in polluted water streams (Ozin et al. 2005). Recent developments suggest that chemically powered nanomachines will become a resounding possibility to overcome the endless limitations and restrictions found at low Reynolds numbers (Purcell 1977). The mechanics of propulsion in this regime have been studied extensively, however, this study has been focused on explaining the motions of microorganisms in fluid medium and their applications to man-made devices (Steer and Viswanathan 1992). As an example, the flagellated bacteria *Serratia marcescens* have been employed as fluidic actuators to propel custom designed microstructures through the use of a swarm blotting technique. The flow deposition of bacteria is used to create a motile bacterial carpet that can generate local fluid motion inside a microfabricated system (Kim and Breuer 2007, 2008).

Researchers have investigated a variety of external fields for colloidal transport in fluids, such as electrophoresis for directing charged particles (Obrien and White 1978), thermo- and diffusio-phoresis migration due to temperature and concentration gradients (Goldhirsch

and Ronis 1983; Anderson and Prieve 1984), and optical tweezers to manipulate particles using light gradients (Applegate et al. 2004), which are applicable for nanodevice motion. Phoretic motion has been extensively studied for its utility in microfluidics devices or even adapted to consider surface reactions (Howse et al. 2007). Recent experiments have shown that phoretic motion of particles can not only be induced externally, but also by on-board processes (e.g., chemical reactions) that changes the properties of its environment and thus create local gradients. Paxton et al. (2006) explored the role of electrokinetics in the spontaneous motion of platinum-gold nanorods suspended in hydrogen peroxide (H_2O_2) solutions that may rise from the bimetallic electrochemical decomposition of H_2O_2. Self-diffusiophoresis was suggested as the mechanism propelling polystyrene microspheres half coated with platinum immersed in a hydrogen peroxide solution (Howse et al. 2007). In both experiments, the decomposition of hydrogen peroxide on the platinum surface into oxygen and water harnesses the chemical free energy of the medium, which is then converted into motion.

Some biological cells propel themselves using chemical surface reactions. Polymerizing networks of actin filaments generate force for a variety of movements in living cells, intra- and intercellular motility of certain bacterial and viral pathogens, and motility of endocytic vesicles and other membrane-bound organelles. During actin-based motility, coexisting populations of actin filaments exert both pushing and retarding forces on the moving cargo (Giardini et al. 2003). Moving intracellular bacteria display phase-dense "comet tails" made of actin filaments, the formation of which is required for motility. For intracellular *Listeria monocytogenes*, it was found that the actin filaments remain stationary in the cytoplasm as the bacterium moves forward, and that length of the comet tails is linearly proportional to the rate of movement (Theriot et al. 1992). It was shown by Smith et al.

(1995) that polarized localization (asymmetric distribution) of the protein is required for efficient unidirectional movement. The fact that actin polymerization alone is capable of providing sufficient force to push out a lipid bilayer has been tested in polystyrene beads coated with purified ActA protein, causing them to undergo directional movement in an actin-rich cytoplasmic extract (Cameron et al. 1999). Numerous models have been proposed to describe the physics controlling the behavior of the actin polymerization motor (Mogilner 2006; Leshansky 2006), however, many biophysical questions remain about the mechanism and control of actin network growth and about how network architecture of actin filaments influences behavior.

It is well known that when two fluid volumes are separated by a semipermeable membrane, fluid will flow from the volume of low particle concentration, to the volume of high particle concentration. (This process is important in biological systems, in which it provides the primary means of transporting water into and out of cells.) The fluid flow may be stopped, or even reversed by applying pressure on the volume of higher concentration. If there are particles only in one volume of the system, then the pressure on it that stops the flow is called the osmotic pressure. The particle motion is wholly determined by the fluctuations of thermal collisions with nearby solvent molecules. Whenever a particle motion is blocked by the membrane, it will transfer momentum to it and, therefore, generate pressure on it. For dilute concentrations, the osmotic pressure Π is given by van't Hoff formula (van't Hoff 1888), which is identical to the pressure formula for an ideal gas: $\Pi = n_b kT$, where n_b is the solute concentration and kT is the thermal energy. If we now stop holding the membrane, the osmotic pressure difference between the two sides of the system will push the membrane until thermodynamic equilibrium is reached. A simple mechanism of cell and organelle motility based on osmotic pressure differences, as in the classic example de-

scribed above, was presented by Williams and De Gennes (1993) and Leonetti (1995). This well-known principle was shown experimentally for lipid vesicles by the action of pumping solvent across the semipermeable cellular membrane in an applied solute concentration gradient (Nardi et al. 1999).

However, one could illustrate this principle without a semipermeable membrane. Consider a colloidal particle — the osmotic motor— immersed in an uniform bath particle concentration. A bath particle located near the motor interacts and delivers momentum to it in some specific direction. Therefore, the motor must deliver a nonzero momentum to its neighbor fluid molecules in other directions. The overall average momentum, delivered by the fluid molecule to both the motor and neighbor fluid molecules, must be zero (Brownian motion). If the bath particle concentration in the vicinity of the motor is disturbed, for example as a result of a chemical surface reaction, more bath particle interactions on a portion of the motor create a net osmotic force that could be used by the motor for directed motion — such motion is called osmotic propulsion.

Our own recent work (Córdova-Figueroa and Brady 2008) has focused on developing theoretical frameworks for osmotic propulsion by studying, possibly, the simplest scenario: a spherical osmotic motor particle with a first-order reaction on a portion of its surface that converts reactants into products in the suspension. The motor has the ability to break any microstructural symmetry of the total bath particle concentration (the sum of reactant and product concentrations) depending on the reaction stoichiometry and the diffusion of reactants and products. Thus, it creates a net osmotic force useful for propulsion or to pump fluid. As the motor moves forward, eliminating low concentration regions, it pushes the microstructure of the colloidal particles out of equilibrium. In turn, the progress of the motor is retarded by the presence of bath particles, which, through Brownian diffusion,

act to restore equilibrium. The force resisting the self-induced motor's motion depends on the concentration of bath particles and particle sizes. The relative magnitude of the speed of reaction to the thermal motion of the bath particles sets the degree of microstructural deformation and is known as the Damköhker number, Da.

Recently, Golestanian et al. (2005) used the thin-interfacial-limit expressions for phoretic motion as the basis for their chemically induced mechanism. However, our osmotic mechanism is not restricted to this limit; indeed, our motor particle could actually be smaller than the reactant/product particles. The "osmotic force" approach produces precisely the result for the flux of one species (the motor) due to a concentration gradient of another species (the bath particles) as derived by Batchelor (1983) when hydrodynamic interactions are neglected. It is well known that when small Brownian particles are excluded from the region between two nearly touching (larger) colloidal particles, this results in more collisions of the small particles on the "outer" surfaces of the large particles, which in turn results in a net osmotic force on each large particle causing them to attract (Jenkins and Snowden 1996). This is exactly the mechanism at work in our osmotic motor.

In the present work, we examine the self-propulsion of an osmotic motor creating a constant flux of product particles, j_0, on a hemisphere (Section 5.2) surrounded by a dispersion of "bath" particles. As an analogy to the semipermeable membrane example, we consider two possible scenarios for the motor: fixed by an external force, or free but the self-created osmotic force balanced by Stokes drag force due to viscous forces (Section 5.2.1). In Section 5.3, we develop a Brownian dynamics (BD) simulation based on the algorithms presented by Foss and Brady (2000) for sheared colloidal dispersions and by Carpen and Brady (2005) for active particle-tracking microrheology. A relationship between the particle-level interpretation of the flux that BD provides and the macroscopic quantity that is the Damköhler
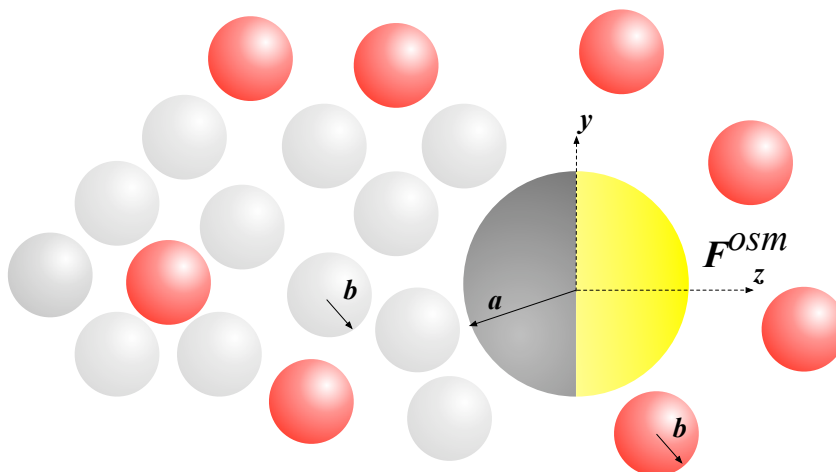
Figure 5.1: Schematic description of the osmotic motor of radius a and bath particles of radii b (in gray). The left side of the motor produces a constant flux of particles of radii b (in red). A net osmotic force $\boldsymbol{F}^{osm}$ is created toward lower bath particle concentration regions.

number was derived, enabling us to compare the simulation results with the theory. The net driving force is investigated in the limits of slow and fast flux in relation to diffusion for different bath particle concentrations and motor to bath particle size ratios (Section 5.4).

In Section 5.5 we also propose ideas for a problem that consists of a reversible reaction on a portion of the motor. This type of reaction unifies the recent work done considering a first-order surface reaction (see details in Chapters 2 and 3) and the constant flux problem addressed in this work. Lastly, some concluding remarks and a comparison to the polymerization motor are present in Section 5.6.

5.2 The osmotic force

Consider the behavior of a colloidal particle of radius a — the osmotic motor — immersed in a dispersion of bath particles of radii b. Both motor and bath particle sizes are large compared to the solvent molecules (filling voids between particles) so that their behavior can be described by the familiar equations of colloidal physics (Russel et al. 1989). Figure

5.1 shows a schematic description of the osmotic motor and bath particles. Different types of interparticle forces can exist between the motor and bath particles, but we model these interactions in the simplest way by adopting a hard-sphere potential so that the particles do not interact until their radii touch. In the present work, we neglect hydrodynamic interactions and rotary diffusive motion. Although this may seem to be a severe approximation, it allows a clear analysis that illustrates many of the significant physics of colloidal particles. The hard-sphere suspension generates an osmotic pressure Π proportional to the thermal energy kT of the medium times the total bath particle concentration n_b. For simplicity, it is assumed that the bath particles are dilute and therefore behave as an ideal gas. The average collisions of bath particles on the motor exert an osmotic force given by

$$\boldsymbol{F}^{osm} = -kT \int \boldsymbol{n} n_b dS, \tag{5.1}$$

where $\boldsymbol{n}$ is a unit vector normal to the excluded volume located at $(a+b)$ and the integral of the osmotic pressure is over the available surface for bath particle collisions with the motor.

In the absence of any external forces or gradients, the bath particle concentration about the motor remains in equilibrium. Thus, the osmotic force is zero. We have proposed a model to describe, possibly, the simplest mechanism in which a motor can propel itself autonomously without external inputs or "assistances" (Córdova-Figueroa and Brady 2008). The motor works by changing the local concentration of bath particles via a surface reaction. If the reaction is properly located on the surface, it can break the symmetric structure of bath particles about the motor, and therefore it can create a net osmotic force useful for propulsion. This osmotic force must be balanced by an externally imposed force $\boldsymbol{F}^{ext}$ to hold the motor fixed, or by the hydrodynamic Stokes drag force $\boldsymbol{F}^{hyd} = -6\pi\eta a\boldsymbol{U}$, where η

is the viscosity of the solvent and U is the motor velocity.

The above description of the basic physics governing the osmotic motor, while simple, is nevertheless completely accurate. A formal statistical mechanical derivation starting from the $N-$particle probability density for finding reactive bath particles surrounding the motor and the entropic origin of the osmotic force is possible and follows the work on single particle motion in colloidal dispersions and microrheology (Squires and Brady 2005; Khair and Brady 2006). That derivation also shows that there is no restriction on the size of the motor relative to the bath particles.

It is assumed that the reaction takes place on half of the surface of the motor, while the other half is passive (Figure 5.1). The bath particle concentration near the motor does depend on the type of reaction rate that governs the chemical reaction and also on the distribution of reactive surfaces (see details in Chapter 4). The behavior of an osmotic motor subject to a first-order irreversible reaction on a portion of its surface was discussed in Córdova-Figueroa and Brady (2008). In that problem, the osmotic force was found to be proportional to the speed of reaction for slow reactions (reaction limited), and independent of it for fast reactions (diffusion limited). But these limits are not necessarily the case for other types of reactions. The reaction rate is balanced by the flux of bath particles at the motor surface. It is in this balance that the reaction rate establishes the resulting nonequilibrium bath particle concentration near the surface, which could then be used by the motor to propel itself through the suspension. There are, in fact, a myriad of reaction rate models that we can test theoretically for the osmotic motor to see their behavior for arbitrary reaction speeds. Here, we proceed to examine the motor's behavior subject to a constant flux of product particles, which can also be seen as a zeroth-order reaction. We discuss qualitatively the governing equations in the case of a reversible reaction $R \leftrightarrow sP$

on a portion of the motor surface, where R and P are reactant and product particles, respectively, and "s" is the stoichiometry number.

5.2.1 Surface flux

Suppose a constant flux of particles of radii b are produced on the half surface of the osmotic motor (Figure 5.1). The product particles are assumed to be identical to the bath particles in the suspension. The flux of product particles at the reactive surface is given by j_0 — the number of product particles per time per surface area. Similar to what we have presented in past works, two possible scenarios for the motor are investigated: one, in which the motor is held fixed, and a second one where it moves freely. Whether the motor is fixed or free is just a change of reference frame. For a fixed motor there will be an advective flux at infinity that removes bath particles from the suspension at the same rate of the product particle formation flux.

To compute the osmotic force, we must solve for the product particle concentration n_P around the motor. We made n_P nondimensional by the undisturbed bath particle concentration far away from the motor, n_b^∞. Therefore, the scaled product particle concentration is governed by the diffusion equation:

$$\nabla^2 \tilde{n}_P = 0. \tag{5.2}$$

Eq. (5.2) is accompanied by boundary conditions:

$$\tilde{n}_P \sim 1 \text{ as } r \to \infty \tag{5.3}$$

and

$$\frac{\partial \tilde{n}_P}{\partial r} = Dah(\boldsymbol{n}) \text{ at } r = 1, \tag{5.4}$$

where we define the Damköhler number

$$Da = \frac{j_0(a+b)}{Dn_b^{\infty}} \tag{5.5}$$

that measures the ratio of the formation speed of product particles, j_0/n_b^{∞}, to the diffusion speed, $D/(a+b)$. The fixed motor does not undergo diffusion; thus, for this case the diffusion coefficient is just that of the bath particles: $D = D_b$. All lengths were nondimensionalized by the contact distance $a + b$. The distribution of reaction on the surface is determined by the dimensionless function $h(\boldsymbol{n})$, which we take to be -1 on the reactive half and 0 on the passive half. Increasing Da, drives the suspension away from equilibrium. Thus, the fixed motor creates an osmotic force

$$\boldsymbol{F}^{osm} = -kTn_b^{\infty}(a+b)^2 \oint \boldsymbol{n}\tilde{n}_P d\Omega, \tag{5.6}$$

where $d\Omega = dS/(a+b)^2$ is the solid angle. Bath particles will accumulate on the reactive (rear) side and push the motor with osmotic force (5.6). Solving the diffusion equation for the scaled product particle concentration $\tilde{n}_P$ about the fixed motor is easily obtained analytically via separation of variables.

Letting the motor propel freely through the suspension (no external force holding it) develops an advective flux of bath particles towards the motor that balances diffusion. This changes the bath particle concentration distribution about the motor and consequently, the osmotic force (5.6). The scaled product particle concentration distribution now satisfies the

advection-diffusion equation given by

$$\nabla^2 \tilde{n}_P = -Pe \frac{\partial \tilde{n}_P}{\partial z}, \tag{5.7}$$

where the direction of motion is taken to be along the z-axis (Figure 5.1). Far way from the motor, the concentration simply satisfies (5.3). At contact, the boundary condition becomes

$$\frac{\partial \tilde{n}_P}{\partial r} = Dah(\boldsymbol{n}) - Pe\mu\tilde{n}_P, \tag{5.8}$$

where $\mu = \cos\theta$. The ratio of advective flux to the diffusive motion is given by the Péclet number $Pe = U(a+b)/D$. The velocity is found from balancing the Stokes drag on the motor with the osmotic force, giving

$$\boldsymbol{U} = -\frac{kT}{6\pi\eta a} n_b^\infty (a+b)^2 \oint \boldsymbol{n}\tilde{n}_P(\boldsymbol{n}; Da, Pe) d\Omega, \tag{5.9}$$

where the bath particle concentration now depends on the Damköhler and Péclet numbers. The unknown motor velocity and the Péclet number must be found self-consistently, along with the scaled product particle concentration $\tilde{n}_P$. The free motor also undergoes Brownian motion; therefore the diffusion coefficient is now the sum of the motor and bath particle diffusivities: $D = D_a + D_b$. From (5.9), the implicit equation for the Péclet number is

$$Pe = -\frac{D_a}{D} n_b^\infty (a+b)^3 \oint n_z \tilde{n}_P(\boldsymbol{n}; Da, Pe) d\Omega = \phi_b \left(1 + \frac{a}{b}\right)^2 \mathcal{F}(Da, Pe), \tag{5.10}$$

where we have used the Stokes-Einstein-Sutherland expression for the motor diffusivity $D_a = kT/6\pi\eta a$; $\phi_b = 4\pi b^3 n_b^\infty/3$ is the bath particle volume fraction and $\mathcal{F}(Da, Pe) = -\frac{3}{4\pi} \int_{r=1} n_z \tilde{n}_P d\Omega$ represents the nondimensional bath particle concentration distribution at

contact as a function of the Damköhler and Péclet numbers. We denote for future references the product $\phi_b (1 + a/b)^2$ as β, which corresponds to the number of bath particles within a bath particle radius of the motor surface.

At $Pe = 0$ ($\beta = 0$), the problem reduces to the fixed motor case and the nondimensional function $\mathcal{F}$ is a function of Da only, $\mathcal{F}(Da)$. Note that the advective flux in (5.8) exerts both pushing and retarding forces on the motor. Bath particles will accumulate on the passive (front) side in a similar fashion as observed in the active microrheology problem (Squires and Brady 2005; Khair and Brady 2006). We expect that the motor velocity increases as Da is increased, forming a tail-like region of dense product particle concentration on the rear of the motor that grows as Pe. If the motor were to move faster than the constant flux of product particles it would leave behind the particles needed to push it forward. However, the motor regulates its speed to prevent this issue to occur and thus sustains propulsion. Solving the advection-diffusion equation simultaneously with Pe for all values of Da and β, which is needed to obtain the motor velocity (5.9), is demanding analytically. For this matter, a finite difference method is employed. In addition, the theory is compared to Brownian dynamics simulations. This allows us to study the problem in a particle level description and also interpret the osmotic force in terms of hard-sphere collisions rather than an integral of $\tilde{n}_P$ over the surface of contact (5.6).

5.3   Brownian dynamics simulations

The Brownian dynamics (BD) method is well-established and has been investigated and expanded by various researchers. In the BD method the components of the system are allowed to respond to the instantaneous forces present in a given configuration, which causes the system to adopt a new configuration. Even in the absence of external forces (e.g.,

magnetic, gravitational, etc.) between the components, the system will still evolve from one configuration to the next due to thermal fluctuations. Our approach is similar to that used by Foss and Brady (2000) for sheared colloidal dispersions and by Carpen and Brady (2005) for active particle-tracking microrheology. BD has also been used to investigate reactive suspensions subject to different reaction rates (Andrews and Bray 2004). A further description of BD is given in Allen and Tildesley (1989), so we shall proceed quickly.

The motion of the individual particles at small Reynolds number is governed by the steady-state Langevin equation — a balance between the forces that may be present in the suspension:

$$\boldsymbol{F}^H + \boldsymbol{F}^B + \boldsymbol{F}^{HS} + \boldsymbol{F}^{ext} = 0, \tag{5.11}$$

where in the absence of hydrodynamic interactions $\boldsymbol{F}^H$ is the Stokes drag force $\boldsymbol{F}^{hyd}$; $\boldsymbol{F}^{HS}$ represents hard-sphere forces; $\boldsymbol{F}^{ext}$ represents the external force only applied to hold the motor fixed; and $\boldsymbol{F}^B$ are the Brownian forces given by

$$\overline{\boldsymbol{F}^B} = 0 \tag{5.12}$$

and

$$\overline{\boldsymbol{F}^B(0)\boldsymbol{F}^B(t)} = 2kT\boldsymbol{R}\delta(t), \tag{5.13}$$

where $\boldsymbol{R}$ is the resistance matrix in the absence of hydrodynamic interactions. The overbars denote an ensemble average over the thermal fluctuations in the fluid, with the amplitude of the Brownian force being given by the fluctuation-dissipation theorem. The sum of all the forces acting on the suspension is zero. Rotational diffusion of the particles does not matter for spherical particles in the absence of hydrodynamic interactions (torque-free particles).

In the absence of external forces, Eq. (5.11) is integrated over the simulation time step Δt to give the nondimensional particle evolution equation for this system:

$$\Delta \boldsymbol{x} = \Delta \boldsymbol{x}^B + \Delta \boldsymbol{x}^{HS} \tag{5.14}$$

with

$$\overline{\Delta \boldsymbol{x}^B} = 0. \tag{5.15}$$

For bath particles,

$$\overline{\Delta \boldsymbol{x}^B \Delta \boldsymbol{x}^B} = 2\Delta t \boldsymbol{I}, \tag{5.16}$$

and for the motor,

$$\overline{\Delta \boldsymbol{x}^B \Delta \boldsymbol{x}^B} = 2 \left(\frac{b}{a} \right) \Delta t \boldsymbol{I}, \tag{5.17}$$

where $\boldsymbol{I}$ is the isotropic tensor. We have made length nondimensional by the bath particle radius, b, and time by the characteristic bath particle diffusive time, $\tau_b = b^2/D_b$. The random Brownian step, $\Delta \boldsymbol{x}^B$, has zero mean (denoted by the overbar) and variance equal to the single-particle Stokes-Einstein-Sutherland diffusivity in the absence of hydrodynamic interactions. Clearly, Eq. (5.17) shows that the Brownian step of the motor decreases as the motor size is increased.

The simulation method searches for particle pairs that have overlapped during the time step Δt and updates the positions of the particles by first Brownian forces, and second by an iterative method which corrects collisions by applying the hard-sphere force/displacement $\Delta \boldsymbol{x}^{HS}$. This hard-sphere collision scheme is based on the algorithm of Heyes and Melrose (1993) in which the simulation checks for particle overlaps and displaces the overlapping particles along their lines of centers back to contact in response to a hard-sphere-like in-

terparticle force. Because bath particles are considered to behave as an ideal gas, only hard-sphere collisions between the motor and bath particles are allowed. This "potential-free" algorithm implements the hard-sphere potential considered in the theory.

The above approach was used to examine the motor in two cases: fixed or free. In order to keep the motor fixed at a given configuration, an external force $\boldsymbol{F}^{ext}$ equal in magnitude to the self-created osmotic force is exerted on the motor. Thus, the motor does not move at all and only the bath particle configurations evolve by diffusion. In this case, the hard-sphere collision scheme needs to take into account the fact that since the motor is fixed, the bath particles need to displace the entire amount back to contact position. On average, more particles in the suspension collide with the reactive surface than on the passive surface, causing a nonuniform distribution of collisions. The average osmotic force $\boldsymbol{F}^{osm}$ is simply the hard-sphere force of the bath particles exerted on the fixed motor

$$\boldsymbol{F}^{osm} = -\frac{kT}{b} \frac{\langle \Delta \boldsymbol{X}^{HS} \rangle}{\Delta t}, \qquad (5.18)$$

where the average $\langle \cdot \rangle$ is defined as the average over a time period. Indeed, in the absence of reaction (the constant flux of product particles) the average hard-sphere force is zero.

Releasing the external force acting on the fixed motor causes it to move forward eliminating regions of low bath particle concentration. Thus, the hard-sphere force must balance the hydrodynamic force $\boldsymbol{F}^{hyd}$. The average motor velocity is given by the sum of the average Brownian and hard-sphere velocity contributions:

$$\boldsymbol{U} = \frac{D_b}{b} \frac{\langle \Delta \boldsymbol{X} \rangle}{\Delta t} = \frac{D_b}{b} \left(\frac{\langle \Delta \boldsymbol{X}^B \rangle}{\Delta t} + \frac{\langle \Delta \boldsymbol{X}^{HS} \rangle}{\Delta t} \right). \qquad (5.19)$$

Observing that the time-averaged Brownian displacement is zero, $\langle \Delta \boldsymbol{X}^B \rangle = 0$, one obtains

$$\boldsymbol{U} = \frac{D_b}{b} \frac{\langle \Delta \boldsymbol{X}^{HS} \rangle}{\Delta t}. \tag{5.20}$$

The motion of the motor only has non-zero contribution along the z-axis, where we define the average velocity in this direction as $U = n_z \cdot \boldsymbol{U}$. The Péclet number $Pe = U(a+b)/D$ is given by

$$Pe = \frac{a}{b} \frac{\langle \Delta \boldsymbol{X}^{HS} \rangle}{\Delta t}. \tag{5.21}$$

As stated in the theory, there is a constant production of bath particles, Q_P (units of product particles per time), coming out from one hemisphere of the motor particle that must be emulated in BD. We define the time-averaged product particles created during each time step $\langle N_P \rangle = Q_P \tau_b \Delta t$. All product particles appear at a distance $a+b$ from the center of the motor (Figure 5.1). However, $\langle N_P \rangle$ has some stochastic variations, which could be represented with a Poisson distribution (Andrews and Bray 2004). The Poisson distribution is a discrete probability distribution that expresses the probability of a number of events occurring in a fixed period of time, but only if these events occur with a known average rate and independently of the time since the last event. Similar characteristics are present in this problem; N_P product particles are created at each time step with time average given by $\langle N_P \rangle$. During a time step, the probability at which N_P bath particles are produced is given by a Poisson distribution

$$P(N_P) = \frac{(\langle N_P \rangle)^{N_P}}{N_P!} \exp(-\langle N_P \rangle). \tag{5.22}$$

Note that Eq. (5.22) decays slowly to zero as $N_P \rightarrow \infty$. To save computational time,

the Poisson distribution $P(N_P)$ is truncated at $N_{P,max}$, the maximum number of product particles allowed to be formed at each time step.

In order to emulate the constant flux of product particles on the reactive surface, an "accept-reject" algorithm is considered. The algorithm consists of generating sampling values from the Poisson probability distribution function $P(N_P)$ by using an assisting distribution $f(N_P)$, under the only restriction that $P(N_P) < Mf(N_P)$ where $M > 1$ is an appropriate bound on $P(N_P)/f(N_P)$. Rejection sampling is usually used in cases where the form of $P(N_P)$ makes sampling difficult, as in this case. Instead of sampling directly from the distribution $P(N_P)$, we use an envelope distribution $Mf(N_P)$ where sampling is easier. These samples from $Mf(N_P)$ are probabilistically accepted or rejected. This method relates to the general field of Monte Carlo techniques, including Markov chain Monte Carlo algorithms that also use a proxy distribution to achieve simulation from the target distribution $P(N_P)$. It forms the basis for algorithms such as the Metropolis algorithm (Robert and Casella 1999). The validation of this method is the envelope principle: when simulating the pair $(N_P, v = u * Mf(N_P))$, where u is a sample from (0,1), one produces a uniform simulation over the subgraph of $Mf(N_P)$. Accepting only pairs such that $u < P(N_P)/Mf(N_P)$ then produces pairs (N_P, v) uniformly distributed over the subgraph of $P(N_P)$ and thus, marginally, a simulation from $P(N_P)$ (von Neumann 1951).

Our implementation of the above algorithm in BD comprises of the next key steps. At each time step Δt a random number c is generated from a Gaussian distribution with zero mean and standard deviation of 1. A deviation from the average number of produced bath particles at each time step, $\langle N_P \rangle$, is calculated with this random number: $N_P = \sigma c + \langle N_P \rangle$, where $\sigma = \sqrt{N_{P,max}/2}$. The parameter N_P is rounded off to the closest integer and compared to $N_{P,max}$. If N_P is greater than zero and less than $N_{P,max}$, the value is accepted.

Otherwise, the value is rejected and another c is generated until the condition is satisfied. Then, the values of $P(N_P)$ and $P_{max} = P(\langle N_P \rangle)$ are calculated. An assisting function slightly greater than $P(N_P)$, that overlaps with the domain is proposed. The function is given by $f(N_P) = P_{max} \exp(-(N_P - \langle N_P \rangle)^2/N_{P,max})$. Once $f(N_P)$ is calculated, it is multiplied by a random number u that ranges uniformly from 0 to 1. If $u < P(N_P)/Mf(N_P)$, the value N_P is accepted, which becomes the number of bath particles created in that specific time step. Otherwise, the value N_P is rejected and another u must be generated starting the whole iterative process again. We have chosen arbitrarily $M = 1.1$ to guarantee that the envelope of the assisting function is greater than P_{max}. Now that the total number of product particles that the motor creates at each Δt is known, the same number, N_P, of bath particles are uniformly taken out of the simulation box. This maintains a constant total number of bath particles N during the simulation run. This action of removing bath particles as new ones are formed, on average, does not produce any significative changes to the results. To prevent errors in the above algorithm and in the results, one must impose the condition $N_{P,max} \gg \langle N_P \rangle$ at all times. In the simulations, we have truncated the Poisson distribution at no less than $N_{P,max} = 10$ and no greater than $\langle N_P \rangle/N_{P,max} = 0.1$, giving an adequate representation of the Poisson distribution. For the values of Q_P and Δt considered in the simulations, variations to the results should not be appreciable for higher values of $N_{P,max}$.

A relation between Q_P and the Damköhler number can be easily obtained using the definition of Da, giving

$$Q_P = j_0 A_{rxn} = Da \left(\frac{D\, n_b^\infty}{a+b} \right) A_{rxn}, \tag{5.23}$$

where $A_{rxn} = 2\pi(a+b)^2$ is the "contact" reactive surface area. Therefore, the time-averaged number of product particles created at each time step, $\langle N_P \rangle$, is simply

$$\langle N_P \rangle = \frac{3}{2}Da\left(\frac{D}{D_b}\right)\left(1 + \frac{a}{b}\right)\phi_b\Delta t, \tag{5.24}$$

which shows its direct dependence on Da, the bath particle volume fraction ϕ_b, and the size ratio a/b. Simulation results are compared to the theory using Eq. (5.24). For fixed motors, $D/D_b \equiv 1$ and Eq. (5.24) becomes $\langle N_P \rangle = \frac{3}{2}Da(1 + a/b)\phi_b\Delta t$. For free motors, $D/D_b \equiv (1 + b/a)$, thus $\langle N_P \rangle = \frac{3}{2}Da(1 + a/b)(1 + b/a)\phi_b\Delta t$.

Factors such as bath particle volume fraction and the number of bath particles in the simulation cell, can lead to a wide variation in computational time. Because we are interested in measuring the motor's average force (or velocity if it is free), and we only have one motor per simulation, long and/or multiple runs are required to obtain good accuracy. The averaging is done over a period of T time steps where we have T forces/velocities (for the motor). The resulting averages for each simulation run are then averaged together to obtain the final average, as well as the deviation from the average. In general, runs are for 1000 simulation time units ($T\Delta t$). The number of bath particles was chosen according to the value of Q_P, but it was not less than 600 particles. If the motor creates too many product particles (high Q_P), a tail-like region of high product particle density is created on the reactive surface that could cross the periodic boundary enclosing the particles. Before starting the simulations, we ensure that there are enough bath particles in the suspension and that the simulation box is large enough to avoid this issue.

5.4 Results

The nonequilibrium bath particle concentration caused by the constant flux is examined for the fixed and free motors, adopting an axisymmetric spherical polar coordinate system with origin at the center of the osmotic motor. This enables us to compute the propulsive force for different Damköhler numbers and values of the product β. Theoretical results will be compared to Brownian dynamics simulations based on the method described in Section 5.3. The simulation method can be implemented for all size ratios, but it becomes computationally intensive for large motors. Therefore, we were able to obtain simulation results for all Da but we restricted the values of β within $0 \leq \beta \leq 10$.

5.4.1 Fixed motor

We first solve the governing equations of the bath particle concentration about the *fixed* motor, and thus the osmotic force. The scaled concentration of bath particles is transformed into $\tilde{n}_P = 1 + Da f_P$, where it becomes clear that the governing equations are independent of Da. The diffusion equation for f_P is solved via separation of variables, giving

$$\tilde{n}_P(r, \mu) = \sum_{m=1}^{\infty} A_m r^{-(m+1)} P_m(\mu), \tag{5.25}$$

where $P_m(\mu)$ is the Legendre polynomial of order m and argument $\mu = \cos\theta$ and A_m are the coefficients (Abramowitz and Stegun 1965). We have kept only the solutions that decay at infinity. The boundary condition at $r = 1$ is satisfied when

$$\sum_{m=1}^{\infty} -(m+1)A_m P_m(\mu) = h(\boldsymbol{n}), \tag{5.26}$$

where the coefficients A_m are given by

$$A_m = -\frac{2m+1}{m+1}\int_{-1}^{1} P_m(\mu)h(\boldsymbol{n})d\mu. \tag{5.27}$$

The general solution for f_P is substituted into Eq. (5.6). The nondimensional function $\mathcal{F}(Da) = -\frac{3}{4\pi}Da\int_{r=1} n_z f_P d\Omega$, representing the particle concentration distribution at contact, results in

$$\mathcal{F}(Da) = \frac{3}{8}Da. \tag{5.28}$$

Thus, the resulting osmotic force for the fixed motor is simply

$$F^{osm} = \frac{kT}{a+b}\phi\left(\frac{3}{8}Da\right), \tag{5.29}$$

where $\phi = 4/3\pi n_b^{\infty}(a+b)^3$ is the fraction of bath particles in the motor volume. The osmotic force scales linearly with Da: $F^{osm} \sim n_b^{\infty}(a+b)^3(6\pi\eta b j_0/n_b^{\infty})$. This has a simple physical finding: each product particle strikes the motor with speed κ and thus hydrodynamic force $6\pi\eta b j_0/n_b^{\infty}$, and there are $n_b^{\infty}(a+b)^3$ colliding bath particles. We plot in Figure 5.2 the scaled osmotic force as a function of Da. The symbols are the result of BD simulations for different bath particle concentrations and particle size. Note that the simulation results collapse into a single universal curve independent of ϕ_b and a/b, and the simulation time step Δt considered in the simulations. The formula to obtain Da from a particle-level point of view has been demonstrated to work for the values shown here; however, the simulation results are off by a scale factor $\sim 3/4$ and the reason for this discrepancy is unclear[1]. The

[1]There is a possibility that in order to compare Q_P and Da properly one needs to integrate the continuous equation over a time step and then take the limit as $\Delta t \to 0$. Since these time-dependent diffusion problems have "power" behaviors, there is a chance to obtain the exponent in such an integration procedure. Further studies are necessary to examine such a discrepancy.
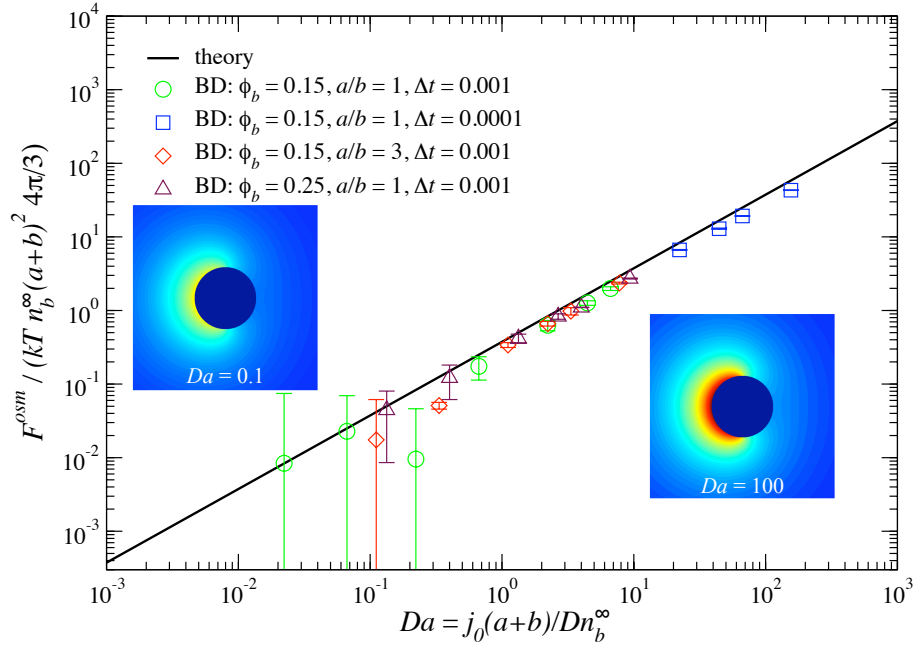
Figure 5.2: The osmotic force F^{osm} scaled by $kTn_b^\infty(a+b)^2 4\pi/3$ as a function of Da for different values of β. The theoretical prediction (line) is compared to Brownian dynamics (BD) simulations (symbols) for various bath particle volume fractions, ϕ_b, size ratios, a/b, and simulation time step Δt. There is a discrepancy between the theory and the simulation results of $\sim 3/4$. The inserts are density profiles in the symmetry plane of the osmotic motor at $Da = 0.1$ and 100. Color red represents higher concentration regions of bath particles; and color blue represents undisturbed or lower concentration regions.

concentration of bath particles is illustrated in the inserts of Figure 5.2 showing density plots of the fixed motor at $Da = 0.1$ and $Da = 100$. As expected, the denser zone (red color) is located near the reactive surface (left side of the motor) with product particle concentration going as $\hat{n}_P \sim Da$ for all values of Da (all reaction speeds). The product bath particles will diffuse away from the motor toward regions less concentrated. Note that the force is not saturated nor limited by diffusion.

5.4.2 Free motor

We now consider the *free* motor problem, which basically addresses the fact that the osmotic (driving) force must be balanced by the hydrodynamic force $\boldsymbol{F}^{hyd}$. Firstly, we point out

that the motor cannot move faster than the speed in which product particles are formed. This is its only driving mechanism. If the contrary occurs, the motor leaves behind the dense area of particles that pushes the motor forward. Thus, the motor velocity is bounded by $D_a/(a+b) \leq U < j_o/n_b^\infty$, where $D_a/(a+b)$ is the diffusive velocity of the motor without reaction.

We start our analysis by transforming the concentration of bath particles into: $\hat{n}_P = 1 + Da f_P$. This expression is substituted in equation (5.7), giving

$$\nabla^2 f_P = -\alpha Da \frac{\partial f_P}{\partial z}, \tag{5.30}$$

and boundary conditions

$$f_P \sim 0 \text{ as } r \to \infty \tag{5.31}$$

and

$$\frac{\partial f_P}{\partial r} = h(\boldsymbol{n}) - \alpha\mu(1 + Da f_P) \text{ at } r = 1, \tag{5.32}$$

where $\alpha = Pe/Da$.

We proceed to first examine the product particle concentration and the motor velocity that arise in the low and high Da regimes, which enables us to obtain the limiting behaviors for low and high β.

5.4.2.1 Slow propulsion

In the limit of small Da, where Brownian motion dominates over the constant flux, the concentration of bath particles is only slightly perturbed from its equilibrium state (no constant flux). Here, the Péclet number is also small ($Pe < Da$). Therefore, a regular perturbation expansion in Da ($f_P = f_{P,0} + Da f_{P,1} + O(Da^2)$) is substituted in the above

governing equations, resulting in the following $O(1)$ equations:

$$\nabla^2 f_{P,0} = 0, \tag{5.33}$$

subject to zero concentration far from the motor, $f_{P,0} \sim 0$, and, at contact ($r = 1$), the boundary condition becomes

$$\frac{\partial f_{P,0}}{\partial r} = h(\boldsymbol{n}) - \alpha\mu f_{P,0}. \tag{5.34}$$

Eq. (5.33) can be easily solved via separation of variables with solution given by equation (5.25). The nondimensional function $\mathcal{F}(Da, Pe)$ becomes

$$\mathcal{F}(Da, Pe) = \frac{3}{8}Da - \frac{1}{3}Pe, \tag{5.35}$$

same as in the first-order reaction problem discussed in Chapter 3. Clearly, Eq. (5.35) is reduced to the results for the fixed motor at $Pe = 0$. This shows that the advective flux does reduce the bath particle concentration gradient created by the motor. And at small Da that first negative contribution is $O(Pe)$. Substituting Eq. (5.35) into the implicit formula for the Péclet number (5.10), we obtain

$$Pe = \frac{\frac{3}{8}\beta Da}{\frac{1}{2}\beta + 1}. \tag{5.36}$$

In the limit of small β, the Péclet number scales as $Pe \sim \beta Da$. Note that the motor velocity scales as $U \sim D_a n_b^{\infty}(a + b)^2 Da \sim D_a/D(a + b)^3 j_0$ for small β. In the limit as $\beta \to \infty$, the motor velocity becomes

$$U = \frac{3}{4}\frac{j_0}{n_b^{\infty}}, \tag{5.37}$$

which is independent of bath particle concentration and the size of the particles, and it is identical to the motor velocity obtained from the first-order reaction problem in Chapter 3.

5.4.2.2 Fast propulsion

In the limit of high Da, when the constant product particle flux is faster than the diffusive speed of bath particles, and high Pe, the fast moving motor experiences different behaviors around its surface. In the front of the motor, diffusion is important only in a thin boundary layer of thickness $\delta \sim O((a+b)/Pe)$ adjacent to the motor, outside of which advection dominates (Squires and Brady 2005). On the rear, a wake of high product particle concentration diffusing away from the motor is created with length measured from the surface order Pe. Outside of the wake, the concentration is in equilibrium, and $\hat{n}_P = 1$ there. There is a small region past $\mu = 0$ where the bath particle concentration at contact grows as $\hat{n}_P(1) \sim Da$. All the propulsion gradient must occur near this region (passive to reactive transition).

At high Da, the bath particle concentration is perturbed again by substituting $f_P = \hat{f}_{P,0} + \frac{1}{Da}\hat{f}_{P,1} + O(Da^{-2})$ into the advection-diffusion Eq. (5.33) and boundary conditions (5.31) and (5.32), resulting

$$\nabla^2 \hat{f}_{P,0} = -Pe\frac{\partial \hat{f}_{P,0}}{\partial z}, \tag{5.38}$$

and boundary conditions

$$\hat{f}_{P,0} \sim 0 \text{ as } r \to \infty \tag{5.39}$$

and

$$\frac{\partial \hat{f}_{P,0}}{\partial r} = h(\boldsymbol{n}) - Pe\mu\hat{f}_{P,0} \text{ at } r = 1, \tag{5.40}$$

where we have taken the limit as $Da \to \infty$. Note that the above equations are independent

of Da. The nondimensional function $\mathcal{F}$ becomes

$$\mathcal{F}(Da, Pe) = -\frac{3}{4\pi}Da \int_{r=1} n_z \hat{f}_{P,0} d\Omega. \tag{5.41}$$

From the boundary condition at contact (5.40), the function of $\hat{f}_{P,0}$ at contact scales as $1/Pe$. Thus, the Péclet number becomes

$$Pe = \beta\mathcal{F}(Da, Pe) \sim \beta\frac{Da}{Pe}, \tag{5.42}$$

which scales as $Pe \sim (\beta Da)^{1/2}$ in the limit of high Da. Therefore, the motor velocity scales as $U \sim D/(a+b)(\beta Da)^{1/2} \sim (a^2 j_0 D_a)^{1/2}$. This scaling condition is obtained by noting that at high Pe there is a balance of surface flux and advection, $j_0 \sim U n_P$, giving the scaling for the bath particle concentration $n_P \sim j_0/U$. The osmotic force $F^{osm} = -kT \oint \boldsymbol{n} n_P dS \sim kT a^2 j_0/U$ must balance the hydrodynamic force $F^{hyd} = 6\pi\eta a U$ retarding the propulsion of the motor. Finding the velocity that results in this balance gives $U \sim (a^2 j_0 D_a)^{1/2}$. This means that the motor could sustain and increase its propulsion as far as it continues creating more product particles to prevent being stopped by the build-up of bath particles in front of the motor.

5.4.2.3   Arbitrary Da

Having examined the two limiting cases for the free motor, we now proceed to treat the case of general Da and product β. It is challenging for higher orders of Da and all values of β to solve analytically the advection-diffusion equation and its corresponding boundary conditions simultaneously with the implicit formula for Pe. Therefore, we employ a (fast) finite different method that accurately captures (with additional grid points) the regions of
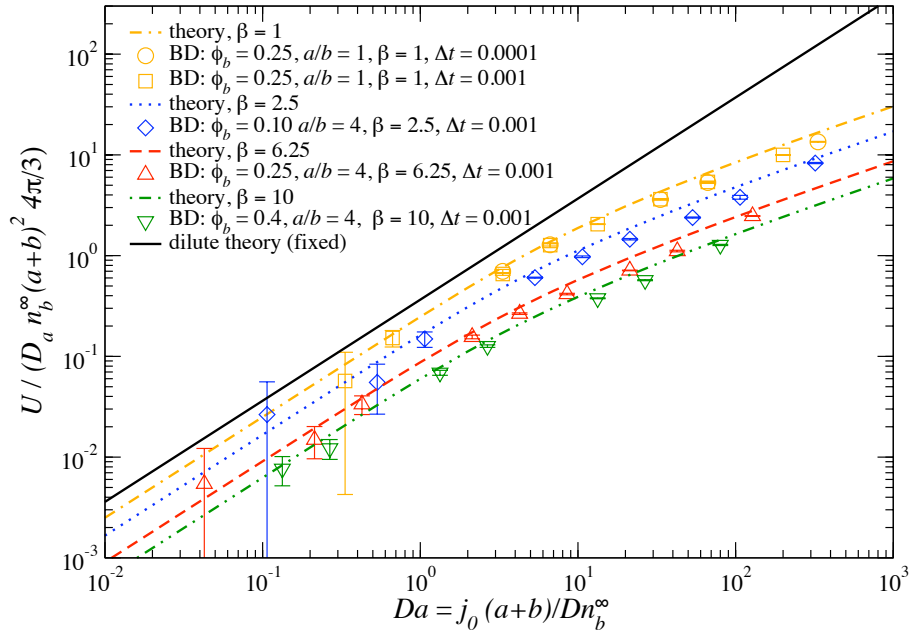
Figure 5.3: The osmotic velocity U scaled by $D_a n_b^\infty (a+b)^2 4\pi/3$ as a function of Da for various values of β. The theoretical predictions (lines) are compared to Brownian dynamics simulations (symbols) for same β and various Δt. There is a discrepancy between the theory and the simulation results of $\sim 3/4$.

large bath particle gradients without compromising the condition far from the motor. The resolution of the method is tuned to accommodate the order $1/Pe$ region in front of the motor, the long concentrated wake behind the motor that appears at high Da and β, and near $\theta = \pi/2$ — the transition from passive to reactive surface.

In Figure 5.3 we plot the predictions for the motor velocity U as a function of the Damköhler number resulting from the numerical method. The motor velocity has been made nondimensional by the diffusive velocity of the motor $D_a/(a+b)$, and the fraction of bath particles in the motor volume, ϕ. Thus, the figure represent the nondimensional function $\mathcal{F}(Da, Pe)$. The curves in the figure correspond to various values of β and the symbols to simulation results for same β and time step Δt. We have included, for comparison, the nondimensional osmotic force (expressed as a Stokes velocity) for the fixed motor. Again, the formula derived to compute Da from the simulations shows to be in close agreement
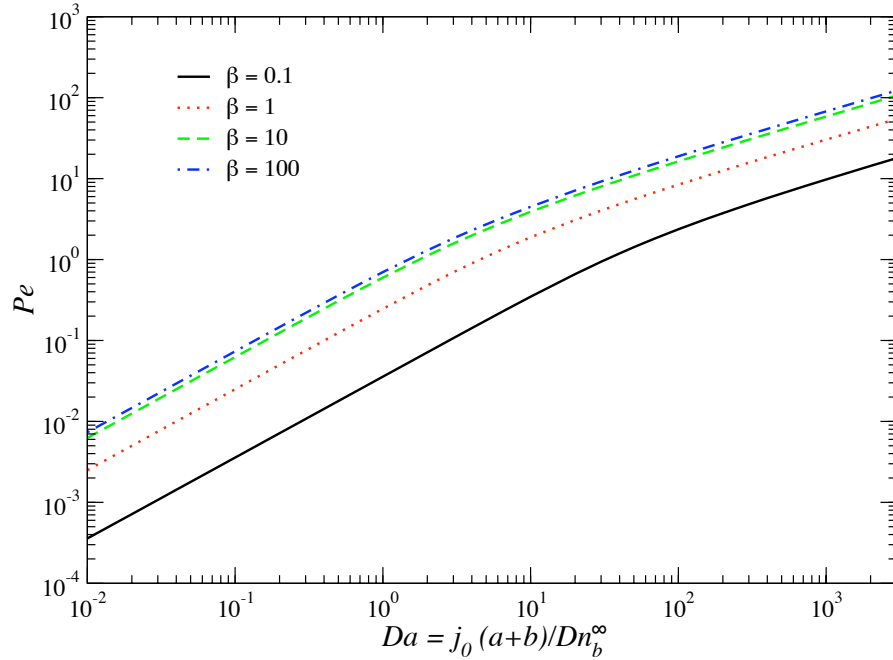
Figure 5.4: The Péclet number Pe as a function of the Damköhler number $Da = j_0(a + b)/Dn_b^\infty$ for various β

with the theory based on the values here presented. However, the same discrepancy (a scale factor $\sim 3/4$) that was observed in the fixed motor problem continues here, suggesting that such a discrepancy comes from the formula to connect Q_P and Da and not from the properties of the suspension. The plot agrees with the limits of low and high Da. At small Da, the motor velocity is linear in Da. In the opposite limit, the motor velocity behaves as $Da^{1/2}$. It is apparent that the curves decrease as β is increased, which demonstrates the direct dependence of β in increasing the Péclet number. As Pe is increased the bath particle distribution at contact decreases.

The Péclet number as a function of Da for various β is plotted in Figure 5.4. This plot is an extension to Figure 5.3, where we now investigate the behavior for arbitrary β against Da. Firstly, at small Da, the Péclet number is order Da for all β, showing that $\mathcal{F}(Da, Pe) \sim Da$ as expected. In the limit as $Da \to \infty$, the curves scale as $Pe \sim Da^{1/2}$.
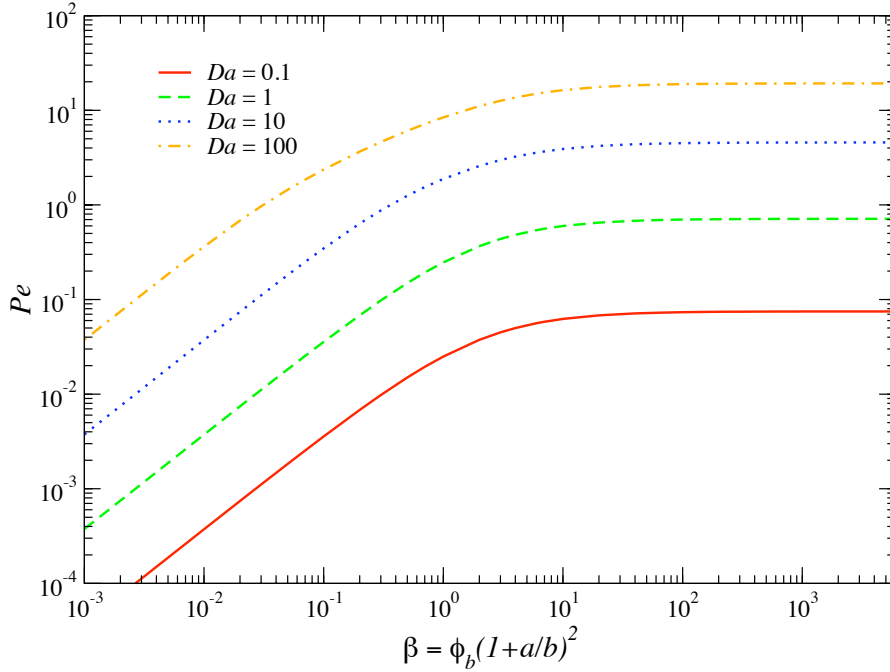
Figure 5.5: The Péclet number Pe as a function of the product β for various $Da = j_0(a + b)/Dn_b^\infty$

Note that the curves in Figure 5.4 increase as β is increased, reflecting the effect of having more bath particles near the motor. Usually, the transition from low to high Da regimes occur near $Da = 1$. This is not the case in this problem. This transition appears to happen at a later Damköhler number, but as β is increased it comes closer to 1.

In Figure 5.5 we plot the Péclet number as a function of β for arbitrary values of Da. The plot shows that for small Da, Pe is linear in β. Therefore, for small Da and β, $Pe \sim \beta Da$. For finite Da, the motor velocity saturates as $\beta \to \infty$, giving $Pe \sim O(1)$. The motor moves at a diffusive velocity $U \sim D/(a + b)$, which is independent of the concentration of bath particles and particle size. It is expected from the scaling argument discussed in Section 5.4.2.2 that in the limits as $Da \to \infty$ and high β, the Péclet number diverges as $Pe \sim \beta^{1/2}$. Thus, the nondimensional function $\mathcal{F}(Da, Pe)$ scales as $\alpha^{-1} = Da/Pe$ at high Pe. Clearly, this behavior is not shown in Figure 5.5. The Péclet number also
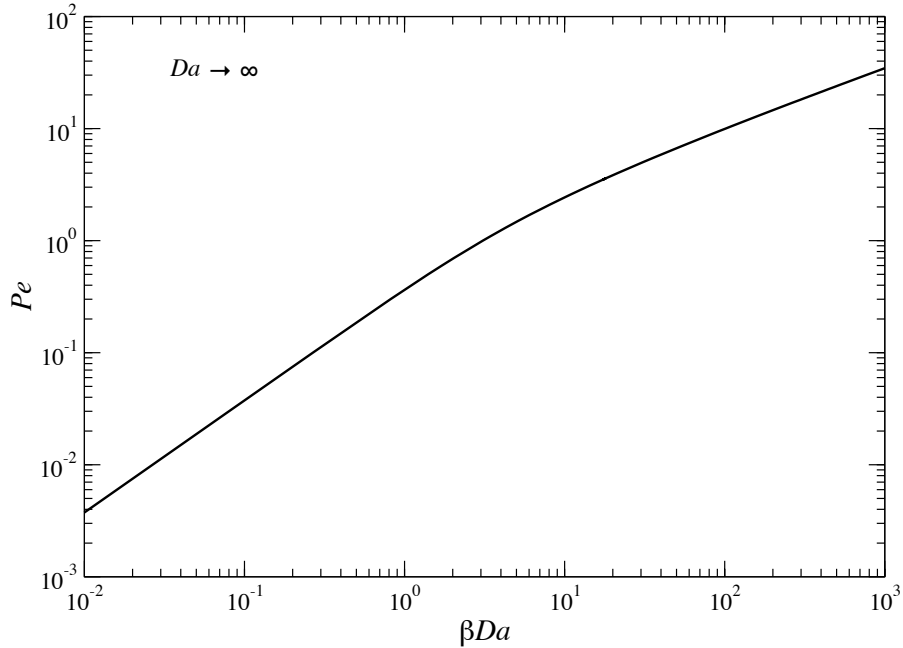
Figure 5.6: The Péclet number Pe as a function of the product βDa in the limit as $Da \to \infty$

saturates for the high Da values considered in the plot, suggesting that a different condition

must be satisfied. The Péclet number as a function of the parameter βDa, which appears

naturally from scaling the governing equations in the limit as $Da \to \infty$, is plotted in Figure

5.6. At low βDa, the Péclet number scales linearly as $Pe \sim \beta Da$. This plot shows that

it is the combined condition $\beta Da \gg 1$, not simply $\beta \gg 1$, that shows the square-root

behavior at high Da and β: $Pe \sim (\beta Da)^{1/2}$, which was also predicted using a simple

force balance. This limiting behavior means that the characteristic time of propulsion

$\tau_U \sim a/U$ is given by the geometric mean $\tau_U \sim (\tau_{j_0} \tau_a)^{1/2}$, where $\tau_{j_0} \sim 1/a^2 j_0$ is the

characteristic time of the constant flux and $\tau_a \sim a^2/D_a$ is the characteristic diffusive time

of the motor. The product βDa is independent of the uniform concentration of bath particles

n_b^∞: $\phi_b(1 + a/b)^2 Da \sim b(a + b)^3 j_0/D$. Note that the curves in Figure 5.5 increase as the

Damköhler number is increased, showing the effect of having more product particles being

formed at the motor provide additional collisions for directed motion. The transition from
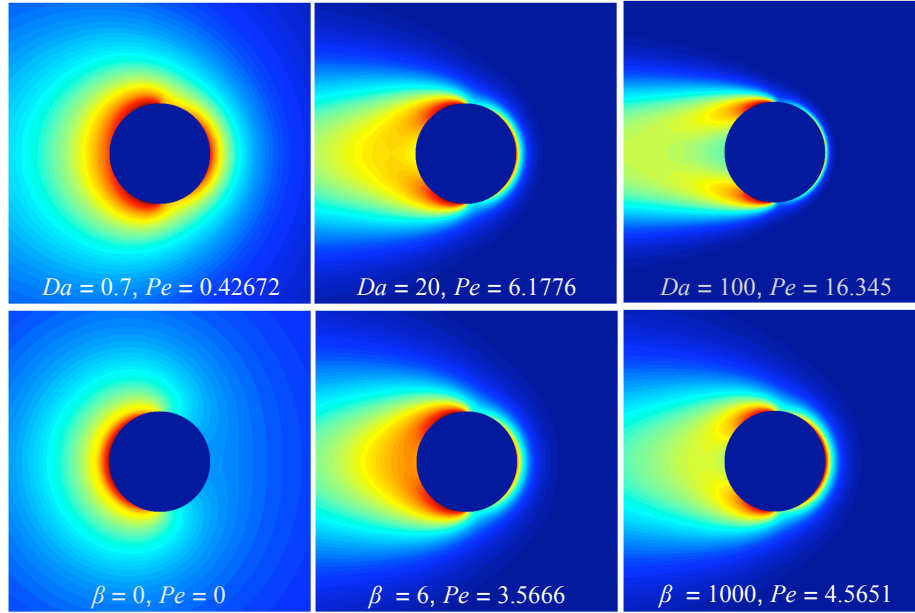
Figure 5.7: Bath particle density profiles in the symmetry plane of the osmotic motor at at $\beta = 10$ for different Da (top row) and at $Da = 10$ for different values of β (bottom row). Color red implies regions of accumulation or high concentration of bath particles; and color blue represents undisturbed or lower bath particle concentration regions. The left half of the motor is reactive and its motion is from left to right. As Pe increases, bath particles accumulate in the front side of the motor and a high bath particle concentration wake is developed in the rear.

low to high β regimes occurs near $\beta = 1$. And in Figure 5.6 such transition from low to high Pe in the limit as $Da \to \infty$ occurs near $\beta Da = 1$.

Figure 5.7 shows density plots around a motor at $\beta = 10$ for different Da (top row) and also at $Da = 10$ for different values of β (bottom row). Also shown on the plots are the resulting Péclet numbers corresponding to the motor velocities. At small Da, Brownian motion is dominant enough to minimize the effect of the reaction, and the density is almost symmetric (as it would be at equilibrium). This symmetry breaking is clearly seen for high Da, with the development of a high bath particle density layer on the front of the motor and a high-density comet-like wave behind the motor. This wake grows longer as the Péclet number is increased, reflecting the decreasing ability of thermal/Brownian motion to heal the disturbed suspension. It is observed in the density plots that by increasing

β and keeping Da fixed, the concentration of bath particles is reduced near the reactive surface as it increases near the passive. As described in Squires and Brady (2005), in the high Pe limit, the effect of a moving particle on the suspension is strongly localized to a thin advection-dffusion boundary layer of thickness $O((a+b)/Pe)$ on the front side of the motor. In this limit (high Pe), the bath particle concentration goes to zero as $1/Pe$ on the reactive surface (rear side) except in a thin region downstream of $\mu = 0$ that controls the mechanism for propulsion.

5.5   Reverse reaction

We have addressed the behavior of an osmotic motor subject to a constant (stream) flux of product particles formed at one hemisphere. Here, we describe the governing equations for a motor subject to a reversible reaction. The bath particles are divided into reactants labeled R, and products P. We consider a portion of the surface to be reactive such that the reactant bath particles undergo a reversible first-order reaction of products according to: $R \leftrightarrow sP$, where for each reactant particle "s" product particles are produced and the stoichiometry value s can be greater than or equal to zero. At the reactive surface, there is an equilibrium reactant concentration given by n_R^{eq}. As we shall see below, this rate of reaction enables us to unify the results for the nonequilibrium concentration of particles about the motor in the cases of an irreversible first-order reaction (presented in Chapter 3) and a constant flux on the surface of the motor described in the previous sections.

We first consider a fixed motor. Since the reaction only takes place at the motor surface, the reactants and products diffuse in the surrounding fluid with translational diffusivities D_R and D_P, respectively, and their concentrations satisfy Laplace's equation. For the reactant: $\nabla^2 n_R = 0$, subject to the imposed concentration far from the motor, n_R^∞; and the flux to

the motor is balanced by the reaction on the motor surface: $\boldsymbol{n} \cdot \nabla n_R = r_R(a+b_R)/D_R$. All lengths have been nondimensionalized by the sum of the motor and reactant radii: $a+b_R$. The products satisfy a similar equation with the subscript R replaced by P. However, the osmotic force is proportional to the *total* concentration of bath particles $n_b = n_R + n_P$, which satisfies $\nabla^2 n_b = 0$, subject to $n_b^\infty = n_R^\infty + n_P^\infty$, and at the motor surface $\boldsymbol{n} \cdot \nabla n_b = r_R(a+b_R)/D_R \times (1 - sD_R/D_P)$. Here we consider a first-order reversible reaction with rate constant κ (units of velocity), i.e., $r_R = \kappa(n_R - n_R^{eq})$. Defining the scaled concentration differences $\tilde{n}_R = (n_R - n_R^\infty)/(n_R^\infty - n_R^{eq})$ and $\tilde{n}_b = (n_b - n_b^\infty)/[(n_R^\infty - n_R^{eq})(1 - sD_R/D_P)]$ it is easy to see that $\tilde{n}_R$ and $\tilde{n}_b$ satisfy the same Laplace equation and boundary conditions. Thus, only the reactant concentration profile is needed to completely solve the problem.

The reactant concentration profile is governed by the ratio of the speed of reaction to that of diffusion — the Damköhler number $Da = \kappa(a+b)/D$. We have dropped the subscript R for the reactant and will simply refer to the reactant as a bath particle. The boundary condition at the motor surface now becomes: $\boldsymbol{n} \cdot \nabla \tilde{n} = Da(\tilde{n}+1)h(\boldsymbol{n})$. Thus, the governing equations are the same for a fixed motor with a first-order irreversible reaction on a portion of its surface. The osmotic force (5.1) becomes

$$\boldsymbol{F}^{osm} = -kTn_R^\infty \left(1 - \frac{n_R^{eq}}{n_R^\infty}\right)\left(1 - s\frac{D_R}{D_P}\right)(a+b)^2 \oint_{r=1} \boldsymbol{n}\tilde{n}\, d\Omega \qquad (5.43)$$

where $d\Omega = dS/(a+b_R)^2$ is the solid angle[2]. In Figure 5.8, we plot the osmotic force exerted on a half-reactive fixed motor as a function of Da. The stoichiometry/diffusivity factor, $(1 - sD_R/D_P)$, tells how many products are produced per reactant, s, and how fast the products diffuse relative to the reactants, D_R/D_P. And it is this combination

---

[2]Technically, for spherical reactants and products of different radii, the integral in (5.43) should be over the "contact" surfaces at $a+b_R$ and at $a+b_P$. This introduces a negligible error, especially in the large motor limit $a \gg b_{R,P}$.
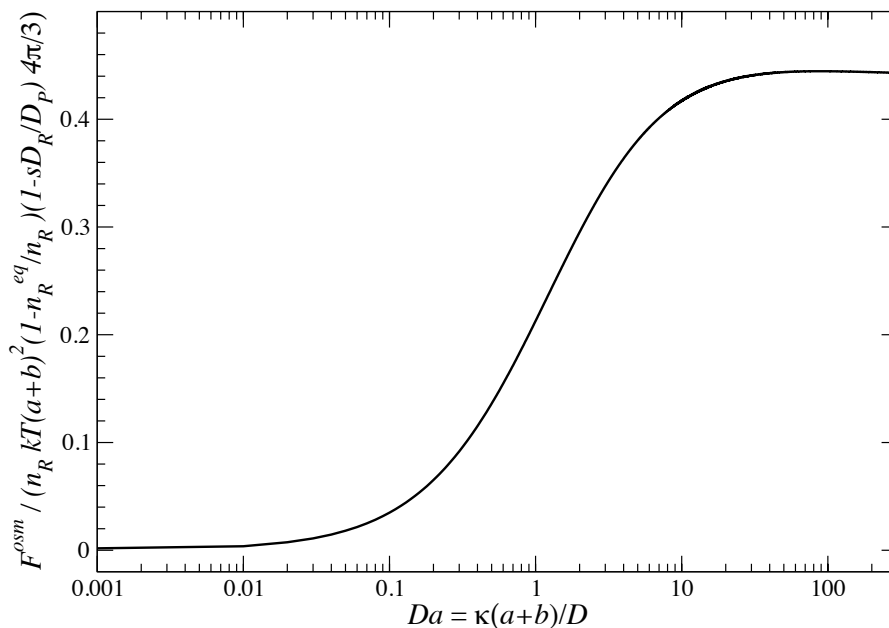
Figure 5.8: The osmotic force F^{osm} scaled by $n_R^\infty kT(a+b)^2(1-n_R^{eq}/n_R^\infty)(1-sD_R/D_P)4\pi/3$ as a function of the Damköhler number $Da = \kappa(a+b)/D$. The motor is considered to be half reactive. For small Da, the scaled osmotic force is linear in Da. In the limit of high Da, the scaled osmotic force saturates and becomes independent of Da.

that governs the behavior. The reversibility factor, $(1 - n_R^{eq}/n_R^\infty)$, determines how many products are transformed back into reactants in comparison to the equilibrium concentration of reactants. The *sign* of the force will depend on which particle diffuses faster and on the ratio of n_R^{eq}/n_R^∞. It is expected that for slow reactions, the osmotic force is proportional to Da, giving $F^{osm} \sim n_R^\infty \left(1 - n_R^{eq}/n_R^\infty\right)(1 - sD_R/D_P)(a+b)^3(6\pi\eta b\kappa)$. However, the force saturates for fast reactions and becomes independent of the speed of reaction: $F^{osm} \sim kTn_R^\infty \left(1 - n_R^{eq}/n_R^\infty\right)(1 - sD_R/D_P)(a+b)^2$.

Now, we consider the scenario if the motor was released and was able to move freely. In a frame of reference traveling with the free motor, there will be an advective flux towards the motor. The scaled reactant concentration satisfies the advection-diffusion equation: $\nabla^2\tilde{n}_R = -Pe_R\partial\tilde{n}_R/\partial z$, where the direction of motion is taken to be the z-direction. The products also satisfy the same equation with R replaced by P. The scaled

total concentration does not satisfy the same equation as the reactants. It is governed by

$\nabla^2 \tilde{n}_b = -(Pe_R - Pe_P)/(1 - sD_R/D_P)\partial \tilde{n}_R/\partial z - Pe_P \partial \tilde{n}_b/\partial z$, subject to $\tilde{n}_b \sim 0$ far away,

and at the motor surface

$$\frac{\partial \tilde{n}_b}{\partial r} + Pe_P \mu \left(\tilde{n}_b + \frac{1}{\left(1 - s\frac{D_R}{D_P}\right)\left(1 - \frac{n_R^{eq}}{n_R^\infty}\right)} \right) =$$

$$Da(\tilde{n}_R + 1)h(\boldsymbol{n}) - \mu \left(\frac{Pe_R - Pe_P}{1 - s\frac{D_R}{D_P}} \right) \left(\tilde{n}_R + \frac{1}{\frac{n_R^\infty}{n_R^{eq}} - 1} \right), \qquad (5.44)$$

where $\mu = \cos \theta$. In the small and large Péclet number limits, the scaled total concentration

$\tilde{n}_b$ does satisfy the same equation as the reactants. This is also true when $Pe_R = Pe_P$. In

the limit as $n_R^{eq}/n_R^\infty \to 0$, the condition at contact (5.44) reduces to the condition expected

for an irreversible reaction. In the opposite limit, $n_R^{eq}/n_R^\infty \to \infty$, the boundary condition

at contact becomes that of a constant flux of bath particles created on the reactive surface

balancing the flux of particles. In fact, the osmotic force (5.43) changes sign and points

away from the constant flux (as in Figure 5.1). The solution for $\tilde{n}_b$ diverges in the cases

$sD_R/D_P = 1$ and $n_R^{eq}/n_R^\infty = 1$, however, for these two situations the osmotic force (5.43)

is zero. This equation reduces in the limits as $sD_R/D_P \to 0$ and $n^{eq}/n^\infty \to 0$ into the

simplest irreversible reaction: $R \to 0$. The motor velocity is clearly Eq. (5.43) expressed

as a Stokes velocity. We can get the proper limits for large β and Da from Eq. 5.44, which

enables us to examine how the behavior of the motor velocity changes as the reaction is

modified from surface flux to first-order.

5.6   Conclusions and discussion

Studies of reaction-driven propulsion mechanisms present great opportunities in the control and motion of nanodevices and the understanding of many biological systems. We have proposed a simple model of propulsion for particles harnessing their environment via a surface reaction. Our proposed model consists of a colloidal particle — the osmotic motor — immersed in a dispersion of "bath" particles, that propels itself by creating a constant flux of particles on one hemisphere. For simplicity, we neglected hydrodynamics interactions and rotational diffusion, and considered the product particles to be the same size as the bath particles. This nonuniform production of particles disturbs the equilibrium concentration and thus the osmotic pressure acting on the motor. The integration of the osmotic pressure over the surface of contact for collisions between the motor and surrounding particles gives the osmotic force, which relates to the particle gradient generated by the motor. Our work has demonstrated, analytically and by simulation, that autonomous motion can be generated quite simply by exploiting the ever-present random thermal motion via a chemical reaction at the motor surface. We have solved for the bath particle concentration around a motor, subject to a constant flux of product particles on the half surface. This enabled us to compute the osmotic force for all Damköhler numbers — the ratio of the speed of the product particle flux j_0/n_b^∞ to the diffusive velocity $D/(a + b)$. The employed Brownian dynamics simulations show excellent agreement with the theory.

We have considered two possible scenarios for the motor: *fixed* and *free*. The osmotic force resulting for the fixed motor was found to be linear in Da for all Damköhler numbers: $F^{osm} \sim n_b^\infty (a + b)^3 (6\pi\eta b j_0/n_b^\infty)$. Product particles are concentrated near the reactive surface and diffuse away from the fixed motor. In the free motor case, the osmotic force is

balanced by the Stokes drag force $\boldsymbol{F}^{hyd}$, giving an expression for the velocity of the motor. As the motor propels though the suspension, bath particles start to accumulate on the front side of the motor (passive surface). At small Da, it was found that the motor velocity is $U = \frac{3}{8}\beta j_0/n_b^\infty/(\frac{1}{2}\beta + 1)$. In the limit as $\beta \to \infty$ (large motors), the motor velocity is simply $U = \frac{3}{4}j_0/n_b^\infty$, independent of β. For intermediate and finite Da, there is a limiting speed in the limit as $\beta \to \infty$ that scales as the diffusive velocity of the bath particles: $U \sim D/(a + b)$. This saturation limit observed at high β suggests that no matter how many bath particles are added to the suspension it would not change the steady-state total particle concentration around the motor. At high Da and β, diffusion of bath particles is slower than the constant flux. On the front side of the motor a boundary layer of order Pe is formed where radial diffusion is balanced by radial advection. Here, the Péclet number scales as $Pe \sim (\beta Da)^{1/2}$. Thus, the motor velocity scales as $U \sim (a^2 j_0 D_a)^{1/2}$.

We have addressed the governing equations for an osmotic motor subject to a reversible reaction. Our goal was to illustrate the limiting behaviors of sD_R/D_P and n_R^{eq}/n_R^∞ and their connection to the results obtained for the bath particle concentration assuming an irreversible first-order and a zeroth-order (constant flux) reaction at the motor surface. What is the behavior of the motor for arbitrary values of sD_R/D_P and n_R^{eq}/n_R^∞? What role do other types of reactions play? How do other distributions of reaction (e.g., constant particle formation on strategically located sites) affect the behavior of the motor? How will a motor consuming bath particles on one side and formation on the other side act for different speeds of reactions, shapes, and suspension properties? Can this have relevance for the osmotic propulsion of lipid vesicles (Nardi et al. 1999)? We leave these questions open for the interested reader.

Although we have assumed that only a single species is formed by the motor, this model

can be extended to polydisperse suspensions of hard-spheres and multiple reactant/product species. If reactant or product particles are of same size as the inert species already present in the dispersion (the bath particles), this changes the total particle concentration. Otherwise, the inert species do not affect the reactant or product particle concentration. The *total* osmotic force is based on the sum of all the individual osmotic forces created by each species. Another drastic simplification is assuming that j_0 (or κ) remains constant. In reality, there are many factors that could influence the rate of reaction, such as concentration, temperature (endothermic and isothermic reactions), type of solvent, and pressure. And potentially this alters the driving mechanism for propulsion presented in this work.

The results of our model resembles superficially the polymerization motor, which also operates by asymmetric distribution of concentration around the motor and forms a comet-like tail of polymers as it is propelled forward. It was observed by Cameron et al. (1999) and Bernheim-Groswasser et al. (2002) that the actin-based motility of polystyrene beads decreases as the size of the beads are increased. For high β, the motor velocity in our model scales as $U \sim D/(a + b) \sim D_b/a$, which goes to zero as $1/a$ for very large motors. Also, the tail length formed by bacterium *Listeria monocytogenes* (Theriot et al. 1992) is linearly proportional to the rate of movement. We have shown that for slow reactions $(Da \ll 1)$, the motor velocity is linear in the rate of formation of product particles and scales as $U \sim b(a + b)^2 j_0$. The moving osmotic motor exhibits a wake that grows as Pe is increased. The Péclet number is also linear in the rate of product particle formation: $Pe \sim j_0(a + b)/Dn_b^{\infty}$. Indeed, these behaviors could also be observed in other reaction-driven motility mechanisms. We are not suggesting that the polymerization motor operates exactly as the osmotic motor, but this similarities clearly show that our mechanism could be a good alternative for explaining motility of microorganisms and organelles and exploiting

for man-made settings.

5.7   Bibliography

M. Abramowitz and I. A. Stegun. *Handbook of Mathematical Functions: with Formulas, Graphs, and Mathematical Tables.* Dover Publications, 1965.

M. P. Allen and D. J. Tildesley. *Computer Simulation of Liquids.* Oxford University Press, USA, 1989.

J. L. Anderson and D. C. Prieve. Diffusiophoresis — Migration of colloidal particles in gradients of solute concentration. *Sep. Purif. Methods*, 13(1):67–103, 1984.

S. S. Andrews and D. Bray. Stochastic simulation of chemical reactions with spatial resolution and single molecule detail. *Phys. Biol.*, 1(3):137–151, 2004.

R. W. Applegate, J. Squier, T. Vestad, J. Oakey, and D. W. M. Marr. Optical trapping, manipulation, and sorting of cells and colloids in microfluidic systems with diode laser bars. *Opt. Express*, 12(19):4390–4398, 2004.

G. K. Batchelor. Diffusion in a dilute polydisperse system of interaction spheres. *J. Fluid Mech.*, 131:155–175, 1983.

A. Bernheim-Groswasser, S. Wiesner, R. M. Golsteyn, M. F. Carlier, and C. Sykes. The dynamics of actin-based motility depend on surface parameters. *Nature*, 417(6886):308–311, 2002.

L. A. Cameron, M. J. Footer, A. van Oudenaarden, and J. A. Theriot. Motility of ActA protein-coated microspheres driven by actin polymerization. *Proc. Nat'l. Acad. Sci. U. S. A.*, 96(9):4908–4913, 1999.

I. C. Carpen and J. F. Brady. Microrheology of colloidal dispersions by Brownian dynamics simulations. *J. Rheol.*, 49(6):1483–1502, 2005.

U. M. Córdova-Figueroa and J. F. Brady. Osmotic Propulsion: The Osmotic Motor. *Phys. Rev. Lett.*, 100(15):158303–158307, 2008.

D. R. Foss and J. F. Brady. Brownian Dynamics simulation of hard-sphere colloidal dispersions. *J. Rheol.*, 44(3):629–651, 2000.

P. A. Giardini, D. A. Fletcher, and J. A. Theriot. Compression forces generated by actin comet tails on lipid vesicles. *Proc. Nat'l. Acad. Sci. U. S. A.*, 100(11):6493–6498, 2003.

I. Goldhirsch and D. Ronis. Theory of thermophoresis .1. General considerations and mode coupling analysis. *Phys. Rev. A*, 27(3):1616–1634, 1983.

R. Golestanian, T. B. Liverpool, and A. Ajdari. Propulsion of a molecular machine by asymmetric distribution of reaction products. *Phys. Rev. Lett.*, 94(22), 2005.

D. M. Heyes and J. R. Melrose. Brownian dynamics simulations of model hard-sphere suspensions. *J. Non-Newtonian Fluid Mech*, 46(1):1–28, 1993.

J. R. Howse, R. A. L. Jones, A. J. Ryan, T. Gough, R. Vafabakhsh, and R. Golestanian. Self-motile colloidal particles: From directed propulsion to random walk. *Phys. Rev. Lett.*, 99(4), 2007.

P. Jenkins and M. Snowden. Depletion flocculation in colloidal dispersions. *Adv. Colloid Interface Sci.*, 68:57–96, 1996.

A. S. Khair and J. F. Brady. Single particle motion in colloidal dispersions: a simple model for active and nonlinear microrheology. *J. Fluid Mech.*, 557:73–117, 2006.

M. J. Kim and K. S. Breuer. Microfluidic pump powered by setf-organizing bacteria. *Small*, 4(1):111–118, 2008.

M. J. Kim and K. S. Breuer. Use of bacterial carpets to enhance mixing in microfluidic systems. *J. Fluid Eng-T. ASME*, 129(3):319–324, 2007.

M. Leonetti. Cell-movement by osmotic current. *Europhys. Lett.*, 32(7):561–565, 1995.

A. M. Leshansky. Actin-based propulsion of a microswimmer. *Phys. Rev. E*, 74(1):012901, 2006.

A. Mogilner. On the edge: modeling protrusion. *Curr. Opin. Cell Biol.*, 18:32–39, 2006.

J Nardi, R Bruinsma, and E Sackman. Vesicles as osmotic motors. *Phys. Rev. Lett.*, 82 (25):5168–5171, 1999.

R. W. Obrien and L. R. White. Electrophoretic mobility of a spherical colloidal particle. *J. Chem. Soc. Farad. T. 2*, 74:1607–1626, 1978.

G. A. Ozin, I. Manners, S. Fournier-Bidoz, and A. Arsenault. Dream nanomachines. *Adv. Mater.*, 17(24):3011–3018, 2005.

W. F. Paxton, S. Sundararajan, T. E. Mallouk, and A. Sen. Chemical locomotion. *Angew. Chem. Int. Ed.*, 45(33):5420–5429, 2006.

E. M. Purcell. Life at low Reynolds number. *Am. J. Phys.*, 45(1):3–11, 1977.

C. P. Robert and G. Casella. *Monte Carlo Statistical Methods*. Springer-Verlag, 1999.

W. B. Russel, D. A. Saville, and W. R. Schowalter. *Colloidal Dispersions*. Cambridge University Press, 1989.

G. A. Smith, D. A. Portnoy, and J. A. Theriot. Asymmetric distribution of the Listeria-monocytogenes acta protein is required and sufficient to direct actin-based motility. *Mol. Microbiol.*, 17(5):945–951, 1995.

T. M. Squires and J. F. Brady. A simple paradigm for active and nonlinear microrheology. *Phys. Fluids*, 17(7), 2005.

B. Steer and H. Viswanathan. Propulsion Mechanisms For Micro-mobile Robots That Operate In A Fluid Environment. *OCEANS '92. 'Mastering the Oceans Through Technology'. Proceedings.*, 2:825–830, 1992.

J. A. Theriot, T. J. Mitchison, L. G. Tilney, and D. A. Portnoy. The rate of actin-based motility of intracellular Listeria-monocytogenes equals the rate of actin polymerization. *Nature*, 357(6375):257–260, 1992.

J. H. van't Hoff. The function of osmotic pressure in the analogy between solutions and gases. *Philos. Mag.*, 26(159):81–205, 1888.

J von Neumann. Various techniques used in connection with random digits. monte carlo methods. *National Bureau of Standards AMS*, 12:36–38, 1951.

D. R. M. Williams and P. G. De Gennes. Cell motility by nonlinear osmotic swimming. *Europhys. Lett.*, 24(4):311–316, 1993.

Chapter 6

Conclusions

6.1 Conclusions and future directions

Recently, reaction-driven propulsion has emerged as a possible mechanism to move objects at the micro- and nanoscale. From biological motors to catalytic nanomotors, experimental methods have continued to progress and propose new ideas that could be tested or explained, fundamentally, in theoretical developments. To address these discoveries, we have proposed a simple model for propulsion: a colloidal particle — the osmotic motor — immersed in a hard-sphere dispersion of colloidal "bath" particles subject to a nonuniform surface reaction creating an imbalance in osmotic pressure. The hard-sphere colloidal dispersions are perhaps the "simplest" particle system; nevertheless, as shown in the previous chapters, its properties are nontrivial and require careful analysis.

In Chapter 2, we presented perhaps a simplistic interpretation of a reaction-driven motor. Our motor derives its propulsive motion from the free energy present in the concentration gradient of the reactant bath particles. This gradient in free energy (or chemical potential) exerts a force on the motor and that force is balanced by the drag of the solvent — the Stokes drag. The motion is not force-free. If one sums the force on the motor and on all of the reactant bath particles, then the total force is indeed zero, as it must be. Since we have neglected any hydrodynamic interactions between the motor and bath particles, there is no velocity disturbance. The motor is propelled or entrained by the flux of reactant particles down the concentration gradient established by the heterogeneous chemical reaction occurring on the motor surface, just as a gradient in concentration of one chemical species can drive the flux of another (Batchelor 1983). As showed in an earlier paper by Squires and Brady (2005), one can express this free energy driving force as the integral of the concentration of the reactant — the osmotic pressure — over the motor surface. In

the absence of any external forces or particle gradients acting on the motor, the concentration of bath particles about the motor is uniform and thus the osmotic force is zero. To illustrate the interesting physics involved in this problem, we assumed that on half of the surface there is a first-order reaction in control of creating a net osmotic force. On the reactive portion of the motor surface for each reactant particle "s" product particles are produced. The departure from equilibrium or the uniform concentration of bath particles is controlled by the Damköhler number Da: the ratio of the speed of reaction κ and the Brownian motion of particles $D/(a+b)$. This osmotic force was found to be proportional to the thermal energy kT, the stoichiometry/diffusivity factor, $(1 - sD_R/D_P)$, the available area for collisions $(a+b)^2$, and the gradient in bath particle concentration at contact. The stoichiometry/diffusivity factor, $(1 - sD_R/D_P)$, tells how many products are produced per reactant, s, and how fast the products diffuse relative to the reactants, D_R/D_P.

We found that the osmotic force created by a fixed motor is proportional to Da for slow reactions, however, for fast reactions the force saturates and it becomes independent of Da. If the (fixed) motor is released, it cannot travel any faster than the bath particles can diffuse. If the motor were to move faster than this velocity, the bath particles would not keep up, and the motor would loose the propulsive force that caused it to move in the first place. The resolution of this paradox is to recognize that in a frame of reference traveling with the free motor there will be an advective flux of bath particles towards the motor that will alter the concentration distribution about the motor and, consequently, the propulsive force. The strength of the advective flux compared to the diffusive motion is given by a Péclet number $Pe = U(a+b)/D$, where U is the free motor velocity. It was found that Pe is a function of Da and the product $\phi_b(1 + a/b)^2$, which combines the bath particle volume fraction, ϕ_b, and the size ratio of motor to bath particle, a/b, into a single parameter and

corresponds to the number of bath particles within a bath particle radius of the motor surface. The results showed that the fixed motor is the limit as $\phi_b(1 + a/b)^2 \to 0$ $(Pe = 0)$ of the free motor, corresponding to an infinitely dilute suspension of bath particles as we expected, and whether the motor is fixed or free, it is just a change of reference frame. For a fixed motor there will be an advective flux at infinity to supply reactive bath particles to the motor. This also implies that the motor will induce a fluid flow to supply the bath particles and can be used as a pump — a novel microfluidic pump (and mixer). For small Damköhler numbers, the motor velocity is proportional to κ; however, we found that for finite $\phi_b(1 + a/b)^2$ the motor velocity saturates and scales as $U \sim D/(a + b)$ — the diffusive speed of the particles.

In Chapter 3, a formal statistical mechanical derivation of the microstructural deformation of the dispersion and the osmotic force was presented, which follows the work on single particle motion in colloidal dispersions and microrheology (Squires and Brady 2005; Khair and Brady 2006). For simplicity, it was assumed that the surrounding particles behave as an ideal gas enabling us to make analytical progress. All calculations were performed for a half-reactive motor with a first-order reaction. We calculated the fixed motor force for all values of Damköhler number, Da, bath particle volume fraction, ϕ_b, motor/bath size ratios, a/b, and stoichiometry/diffusivity factors, $(1 - sD_R/D_P)$. This resulted in a universal curve, onto which a wide range of measurements collapsed, and also agreed with Brownian dynamics simulations. For small perturbations to the microstructure, we found that the osmotic force is linear in the Damköhler number Da. In the limit of high Da, the force saturates and becomes independent of Da. We found this force to be large compared to typical colloidal forces, indicating that this mechanism could be useful for self-propulsion (or for pumping fluids). It was shown that when the motor is let free, it moves rapidly

toward lower bath particle concentration regions located near the reactive surface. Almost instantaneously the motor catches up with the bath particles reducing the gradient in bath particle concentration. Therefore, the osmotic force is balanced by the viscous force acting on the moving motor. For the free motor case, we assumed that the stoichiometry value "s" is zero, which greatly simplifies the governing equations. This assumption is unnecessary in the limit of small Péclet numbers, i.e., the fixed motor, and in the limit of large Péclet numbers where the effects of advection are the same for the reactants and products. The effect of nonzero sD_R/D_P apart from being a scalar factor in the motor velocity will be quantitative, not qualitative. Thus, the osmotic velocity was calculated as a function of Da for various $\beta = \phi_b(1 + a/b)^2$. Also, we demonstrated again that BD simulations are in agreement with the theoretical results. In general, we showed that the physical properties of the microstructure, a/b and ϕ_b (or the product β), directly contribute to the speed of the motor, an observation not shared by the fixed motor problem. For small Da numbers, we showed the osmotic velocity is simply $U = \frac{3}{8}\beta\kappa/\left(\frac{1}{2}\beta + 1\right)$. In the limit as $\beta \to \infty$, the motor velocity becomes $U = 3\kappa/4$, which is independent of the bath particle concentration and the particle size. For finite Da and high β, the motor velocity reaches saturation and scales as $U \sim D/(a+b)$. But at high Da and β, we found that the Péclet number diverges as $Pe \sim (\beta Da)^{3/5}$, giving a motor velocity that scales as $U \sim (D_a/b)^{5/2}\kappa^{3/5}$. In general, we observed that at $\beta Da \ll 1$ the Péclet number is small (slow propulsion). In the limit of $\beta Da \gg 1$, advection dominates over diffusion in the local microstructure, thus Pe is large (fast propulsion).

We have proposed ideas to modify the dilute theory to account for concentrated systems. Comparisons with measurements and Brownian dynamics simulations will be necessary to determine whether these ideas are applicable. In this work, we modeled the particle

interactions adopting a hard-sphere potential, so that the bath particles do not interact with the motor until their hard-sphere radii touch, whereupon a force is exerted to prevent overlapping. The problem can be extended to other forces existing between the motor and bath particles, including electric forces between charged double layers, van der Waals forces, and steric repulsions, by simply using the "excluded annulus" model, in which a single parameter λ based on the ratio of the hydrodynamic radii and and the hard-sphere radii tunes hydrodynamic interactions (Brady and Morris 1997). Hydrodynamics would be expected to slow the motor's motion, the question here is to what extent. At the pair level (one motor, one bath particle) hydrodynamics can be included analytically (following the work on microrheology, Khair and Brady (2008)), while for more concentrated systems, Stokesian dynamics (Banchio and Brady 2003) can be adapted to simulate reacting bath and motor particles. Many interesting applications can be considered with the addition of hydrodynamic interactions.

Recently, Ruckner and Kapral (2007) examined the motion of a single, chemically powered nanodimer comprised of two linked spheres, one of which has equal interactions with the solvents and the reactants but catalyzes reactants into solvents. The other sphere is inert but interacts differently with the solvent molecules produced in the reaction. The uneven interactions on the nanodimer generates a nonequilibrium concentration gradient at the catalytic end that in conjunction with the force difference at the noncatalytic end leads to directed motion.

Inclusion of hydrodynamics is also needed to examine the inverse question of how much fluid it can pump, rather than how fast the motor can move. If we place a motor in a microchannel, what kind of flow velocity can it generate in the channel? Will the flux of reactive bath particles be limited by the walls? How will this change the scaling with Da?

What kind of flows are created if one portion of the channel walls is a sink for bath particles and another a source? Can this be used to promote mixing in micro- and nanofluidic devices? Can the motion of a motor be directed to one region of a channel by the supply of reactants? Can a motor be tailored to be a sensor for a specific chemical or biological compound? Questions are plentiful just by modeling osmotic propulsion with other particle interactions.

The "steady" force that a motor can exert may be much less than the peak fluctuating force, and the peak force may be all that is necessary to cause some desired action. Since the osmotic force arises from random collisions between the motor and bath particles, the motor experiences a fluctuating force and, in some cases, these fluctuations may provide a more important role than the averages, as in the case for living cells and heterogeneous colloidal systems, that could be useful for nanotechnological applications. We computed theoretically the time-averaged fluctuations resulting from the collisions between the motor and bath particles as a function of the Damköhler number and the product β. It was found that the time-averaged force fluctuations are $O(Da^2)$ at small Da, and are independent of Da in the limit as $Da \rightarrow \infty$. Also, for small and large β, the time-averaged force fluctuations become $\sim (kT)^2 n_b(a+b)$. We calculated the ratio of parallel to perpendicular fluctuations for various Da and β, giving a better picture of how the fluctuations relate to the microstructural deformation relative to the motor. In addition to the theory, simulations should also be considered in order to give us a better picture of the fluctuating force of the motor as time progresses. An interesting problem that can be studied in simulations consists of a motor fixed by an external force and subject to a fast reaction on half surface that is set free at a certain time. The motor exerts a large peak force driving the motor forward and thus, reduces the self-created bath particle depleted region until it saturates and reaches a

limiting speed which is less than the initial one that comes from the result of the balance between advection and diffusive forces. Again one can apply the external force to hold the motor, and consequently repeat the process. Thus, the initial bath particle concentration distribution about the fixed motor is recovered at a diffusive time scale b^2/D_b, as is the osmotic force. This cycle can be useful to produce large but short-in-duration osmotic forces that can be harder to obtain from moving motors. This principle can also be used to obtain information about the surrounding medium in response to the motion of the motor.

We have derived an expression for the efficiency of conversion of free energy into mechanical energy, which measures the ability of the motor in harnessing its environment to create useful work. For an irreversible first-order reaction rate (consumption of bath particles) on half motor's surface, the motor efficiency ξ goes to zero as $Da \to \infty$. We found the efficiency of the fixed motor to be independent of Da for $Da \ll 1$. For fast reactions, the fixed motor efficiency scales as $\xi \sim \beta/(\ln Da)$. On the other hand, the efficiency of the free motor also scales as $\xi \sim \beta$ for slow reactions, but scales as $\xi \sim 1/(\beta \ln Da)$ for high Da and β. Many questions arise by investigating the motor efficiency. Can we define other types of efficiency? How does the motor efficiency compare to other reaction-driven transport mechanisms? Is it possible to design an osmotic motor as efficient as biological machines (Purcell 1997; Chattopadhyay et al. 2006)? There are many variables that could be manipulated to improve the motor efficiency, such as the portion of the reactive surface on the motor and the expressions for the reaction rate.

In Chapter 4, we offer a theoretical framework for the behavior of a spherical osmotic motor subject to different distributions of reactive surface (described by the angle θ_s). For simplicity, it was assumed that an irreversible first-order reaction consumes bath particles at a portion of the motor surface ($s = 0$). The basis for our model involves determining the

reaction-induced perturbation to the suspension microstructure in order to calculate the driving force on the motor. The motor velocity is determined via application of the Stokes drag law. A theory for the microstructure evolution was provided and solved in the simplest limiting case of hard-spheres in the absence of hydrodynamic interactions and rotational diffusion. The model was restricted to the limit where bath particles behave as an ideal gas. In addition to the theory, we used a Brownian dynamics simulation that provided a means of verifying our theoretical results. We examined two scenarios for the osmotic motor subject to different distributions of reactive surface: one, in which the motor is held fixed by an external force, and another where the motor is free to move.

We calculated the osmotic force exerted by bath particles to a fixed motor for all values of Damköhler number, Da, bath particle volume fraction, ϕ_b, and motor/bath size ratios, a/b, for different values of the angle θ_s. For each angle θ_s, the results collapse into an universal curve after scaling the osmotic force by $kTn_b(a+b)^2 4\pi/3$. We have shown that BD simulations agree with the theoretical predictions. For small perturbations to the microstructure, we found the osmotic force is of order Da times the geometric factor $\sin\theta_s^2$. In the limit of high Da, the force saturates and simply scales as $F^{osm} \sim n_b kT(a+b)^2 f(\theta_s)$, where the function $f(\theta_s)$ is independent of θ_s in the limits of small and large reactive sites. The osmotic force exerted on a free motor is balanced by the viscous force acting on the moving motor. The resulting motor velocity was calculated as a function of Da for various $\beta = \phi_b(1 + a/b)^2$ and angles θ_s. Also we demonstrated again that BD simulations are in agreement with the theoretical results. In general, we have shown that the physical properties of the microstructure, the size ratio a/b and the bath particle volume fraction ϕ_b (the product β), directly contribute to the speed of the motor, an observation not found in the fixed motor problem. At small Da, we have shown that the motor veloc-

ity is $U = \frac{3}{8}\beta \sin \theta_s^2 \kappa / (\frac{1}{2}\beta + 1)$. This expression reduces to $U = \frac{3}{4}\kappa \sin \theta_s^2$ in the limit as $\beta \to \infty$. To study the high-Da limit, we divided the analysis to the reaction on front and the reaction on the rear of the motor. When the reaction is on front, the Péclet number scales as $Pe \sim \beta$ at small β, resulting in the motor velocity $U \sim D_a n_b (a + b)^2$. We also found that for all values of β in the limit as $Da \to \infty$, the Péclet number is $O(1)$. Thus, the motor velocity is limited by the dffusive velocity of the bath particles $U \sim D/(a+b)$, which is independent of bath particle concentration and particle size. For reaction on rear, the scaling arguments are different. For small β, we also found that the Péclet number scales as $Pe \sim \beta$, giving the motor velocity $U \sim D_a n_b (a + b)^2$. Therefore, this limit is reached independently of the distributions of the reactive site. However, in the limit as $\beta \to \infty$, the Péclet number slowly approaches a limiting speed as $Pe \sim \ln \beta$, thus the motor velocity scales as $U \sim D/(a + b) \ln(n_b (a + b)^2)$, as it depends on the concentration of bath particles and particle size. In fact, only at $\theta_s = \pi/2$ (half-reactive motor) we observed that in the limit as $Da \to \infty$ and $\beta \to \infty$ the Péclet number diverges as $Pe \sim (\beta Da)^{3/5}$.

The optimal angle for maximum propulsion was computed as a function of the Damköhler number and various β. For small Da we found that for all values of β, the optimal angle for maximum propulsion is $\theta_s^{op} = \pi/2$. At high Da, the optimal angle changes depending on the value of β. At $\beta = 0$ (no motion), the optimal angle θ_s^{op} converges to approximately 0.3776π. As β is increased and the advective forces become stronger on the motor (increasing Pe), the optimal angle increases as well. In the limit as $\beta \to \infty$, the optimal angle is again at $\theta_s^{op} = \pi/2$, because, exclusively for half-reactive motors, the Péclet number diverges for increasing β and Da, which means that the gradient in bath particle concentration goes to zero.

This work illustrates in simple terms that an osmotic motor with different distributions

of reaction exhibits different behaviors depending on the speed of reaction and the value of β — bath particle concentration and size of the particles. The understanding of such behaviors and their relation to the distribution of reaction could enable scientists to properly design reaction-driven nanodevices. These ideas could potentially open a new field that deals with the theory, development, and experimentation of smart reactive surfaces on nanodevices that modify themselves to achieve desired tasks or motions. We showed that there are optimal distributions of reaction for better propulsion. An interesting project can be the extension of these concepts of optimization based on reactive surface distributions to other transport mechanisms, such as diffusiophoresis and surface-tension gradients that also rely on the establishment of a gradient to provide the driving force for motion. Future directions should consider the role of hydrodynamic interactions, rotational motion, and other reaction rates.

In Chapter 5, we proposed a simple model that consists of a colloidal particle — the osmotic motor — immersed in a dispersion of bath particles that propels itself by creating a constant flux of particles on one hemisphere. The model enabled us to compute the osmotic force for all Damköhler numbers — the ratio of the speed of the product particle flux j_0/n_b^∞ to the diffusive velocity $D/(a+b)$. We have solved for the bath particle concentration around a motor in two possible scenarios: *fixed* and *free*. The osmotic force resulting from the fixed motor was found to be linear in Da for all Damköhler numbers: $F^{osm} \sim n_b^\infty(a+b)^3(6\pi\eta b j_0/n_b^\infty)$. Product particles are concentrated near the reactive surface and diffuse away from the fixed motor. In the free motor case, the osmotic force is balanced by the Stokes drag force $\boldsymbol{F}^{hyd}$, giving an expression for the velocity of the motor. As the motor propels though the suspension, bath particles start to accumulate on the front side of the motor (passive surface). At small Da, it was found that the motor velocity scales

as $U = \frac{3}{8}\beta(j_o/n_b^\infty)/(\frac{1}{2}\beta + 1)$. For large motors ($\beta \to \infty$), the motor velocity is simply

$U = \frac{3}{4}(j_o/n_b^\infty)$, which is independent of β. For any finite Da, there is a limiting speed in

the limit as $\beta \to \infty$ that scales as the diffusive velocity of the bath particles, $U \sim D/(a+b)$.

At high Da and β, diffusion of bath particles is slower than the constant flux. On the front

side of the motor a boundary layer of order Pe is formed where radial diffusion is balanced

by radial advection. Here, the Péclet number scales as $Pe \sim (\beta Da)^{1/2}$. Thus, the motor

velocity scales as $U \sim (a^2 j_0 D_a)^{1/2}$. We also considered Brownian dynamics simulations,

which showed excellent agreement with the theory.

In addition to a constant flux condition at the motor's surface, we addressed the govern-

ing equations for an osmotic motor subject to a nonuniform reversible surface reaction. We

showed the limiting behaviors of sD_R/D_P and n_R^{eq}/n_R^∞, and their connections to the results

obtained for the bath particle concentration assuming an irreversible first-order and a sur-

face flux reaction. It is instructive to ask, what is the behavior of the motor for arbitrary

values of sD_R/D_P and n_R^{eq}/n_R^∞? How is the osmotic force modified for other chemistries?

What if there are enthalpic effects — specific interactions between the motor and the reac-

tive species — in addition to entropic? What if the reaction is iso- or endothermic? How

efficient is the osmotic motor for other chemistries?

Although we have assumed that only a single species reacts with the motor, this model

can be extended to polydisperse suspensions of hard-spheres and multiple reactive species.

If reactant or product particles are of same size as the inert species already present in the

dispersion (the bath particles), this changes the total particle concentration. Otherwise, the

inert species do not affect the reactant or product particle concentration. The *total* osmotic

force is based on the sum of all the individual osmotic forces created by each species. Another

drastic simplification is assuming that j_0 (or κ) remains constant. In reality, there are many

factors that could influence the rate of reaction, such as concentration, temperature, type of solvent, and pressure. Potentially, this could alter the driving mechanism for propulsion.

In the analysis we have ignored the fact that a small motor will also be subject to its own Brownian motion, and in particular its rotary Brownian motion. As the motor rotates in response to Brownian torques, the reactive side will no longer be in the same direction, and this may limit the extent of its directed motion. The time scale for the establishment of the concentration profile about the motor is the diffusive time of the bath particles $\tau_b \sim a^2/D$. The time scale for rotary Brownian motion of the motor is its rotary diffusivity $D_r = kT/8\pi\eta a^3$. Rotary motion of the motor will not be important as long as $\tau_b D_r \sim b/a \ll 1$, which is the case when the motor is much larger than the bath particles. Thus, the work described in previous chapters is restricted to this limit. What happens when this restriction is relaxed? Even in this limit a large motor will travel at its osmotic velocity U for a time $1/D_r$ after which it will establish a new bath particle concentration profile and travel again at U but in a new (random) direction. Thus, for times long compared to $1/D_r$ the motor will undergo a random walk with a step length U/D_r and thus should have a mean-square displacement that grows linearly in time with a translational diffusivity that scales as U^2/D_r. Would this be true? How does the mean-squared displacement of the motor depend on the reaction rate, bath particle concentration, etc.?

Clearly, neither the motor nor the bath particles need to be spherical. We shall ask the question of how the shape of the motor affects the osmotic force exerted by bath particles in the suspension. What happens to the osmotic force if the motor, for example, is a cylinder (i.e., catalytic nanorod) or a spheroid (i.e., microorganisms)? What is the optimal reactive distribution for other motor geometries? One can start the investigation of these shape effects on self-propulsion following the work on Khair and Brady (2008), where it was

asked what role did the shape of the "probe" play on measuring microrheological properties. Rotational diffusion can also be relevant component in other particle geometries.

Rotary motion is also possible by having reactive patches strategically located about the motor surface. Paxton et al. (2006) has recently demonstrated such movement on a free platinum/gold gear suspended in a hydrogen peroxide solution. The individual teeth were coated with platinum on one face of each tooth. It was shown that the decomposition of hydrogen peroxide at platinum surface generates interfacial forces across each tooth. The gear rotates at $\sim 1s^{-1}$, corresponding to a linear velocity of ~ 300 μm/s at the platinum-coated gear tooth. It was found that this linear velocity is more than an order of magnitude faster than the nanorod movement (Paxton et al. 2004). The theoretical framework developed for single motors may be used to study other interesting problems. A natural extension is to consider two motors with separation $\boldsymbol{d}$ connected by an inertialess thin rod — the osmotic rotor — immersed in a colloidal dispersion of bath particles with reactive surfaces of each motor pointing toward opposite directions. Consequently, we expect the osmotic forces exerted on the motors to have components parallel and perpendicular to $\boldsymbol{d}$. In the case of fixed rotor, for large $|\boldsymbol{d}|$ the parallel components for each motor vanish, while the perpendicular components are, by symmetry, identical and equal to that for a single osmotic motor. We can make a swimmer from the osmotic rotor by having it create rotary motion, but then attaching it to a chiral object so that there is the rotational-translational coupling in Stokes flow. One can then ask how fast such a motor could go. The idea is not to do any hydrodynamics as far as the reaction problem is concerned, but to use the hydrodynamic resistance matrix to get the translational velocity. This resembles the dynamics of bacterial flagella made from a rotary motor and thin helical filament (Namba 1993; Berg 2003).

Once these motors or rotors move autonomously, what tasks can they do? Can we

attach them to other devices to create complex systems or movements? And how does the behavior compare to the one observed individually? How is the fuel (reactant) supplied to the medium? And by whom? One important aspect to be studied is multiple motors. Depletion flocculation could occur if small particles are excluded from a zone separating two nearly touching osmotic motors and the imbalance osmotic pressure of the small particles causes an entropic force leading to flocculation. In fact, reaction-induced bath particle depleted regions of two or more motors can collapse and hinder or stop their propulsion mechanism. A contrary behavior occurs if a passive surface of a motor collapses with the reactive surface of another motor. The two motors could move and collaborate together in this configuration. How does the net force increase for this two-motor configuration? Could they be separated randomly? Or, is it necessary to apply an external force to separate them? What happens if rotary Brownian motion is dominant? Will a group of motors swarm together? Can this have relevance for the swarming of biological organisms? How will two or more motors act when they compete for the same reactant? Osmotic motors could be designed to regulate their motion by chemotactic effects. Chemotaxis is a phenomenon observed in nature in which bodily cells, bacteria, and other single-cell or multicellular organisms direct their movements according to certain chemicals in their environment (Bray et al. 2007). This is important for bacteria to find food (e.g., glucose) by swimming towards the highest concentration of food molecules, or to flee from poisons (e.g., phenol). In multicellular organisms, chemotaxis is critical to early (e.g., movement of sperm towards the egg during fertilization) and subsequent phases of development (e.g., migration of neurons or lymphocytes) as well as in normal function. These biological features could also be mimicked by "intelligent" nanodevices if such operations are necessary, depending on the final goal. How can rules or information be included on-board the motor to self-regulate

itself? These questions are not unique for osmotic motors, but relevant as well for other propulsion mechanisms proposed by other authors.

At the theoretical and computational levels, we need to understand the enhanced diffusion expected for moving osmotic motors at arbitrary Damköhler numbers. In particular, we need to compute the effective self-diffusivity D^{eff}, which determines the capacity of the motor to depart far from its initial point. From scaling arguments, we can easily suggest the orders for slow and fast reactions. It is known that the effective motor diffusivity scales as $D^{eff} \sim l^2/\tau$, where l is the step size taken by the motor and τ is the diffusive time scale a^2/D_0. The short-time self-diffusivity, D_0, measures the average instantaneous motor mobility, which is simply the bare diffusivity of the motor in the absence of hydrodynamic interactions. For inactive motors ($Pe = 0$), the step size scales as the motor radius a and the effective diffusivity is proportional to D_0. At small Pe (slow propulsion), the length scale is now $l \sim Pe\, a$, giving the effective self-diffusivity $D^{eff} \sim Pe^2 D_0$. Our work has shown that the result of small Pe means the Damköhler number and the product β is also small, thus $Pe \sim \beta Da$. Therefore, the effective diffusivity scales as $D^{eff} \sim D_0(\beta Da)^2$. At high Pe, advective forces dominate over difusion. The length scale is $l \sim Pe\, a$, however, the time scale is now that of advection $\tau \sim Pe\, a^2/D_0$. This suggests that $D^{eff} \sim Pe D_0$. For the half-reactive motor discussed in Chapter 3, we have found that at high Da and β, the Péclet number scales as $Pe \sim (\beta Da)^{3/5}$, resulting in the effective self-diffusivity scaling as $D^{eff} \sim D_0(\beta Da)^{3/5}$. Further analysis is necessary to comprehend these scaling conditions and the diffusion for arbitrary Da, bath particle concentration, and particle sizes, and its qualitative behavior with the inclusion of hydrodynamics interactions, complex chemistries, multiple motors, etc.

Our research has demonstrated analytically and by simulation that autonomous motion

can be generated quite simply by exploiting the ever present random thermal motion via a chemical reaction at the motor surface. This model and future theoretical direction should be tested in lab experiments. A simple experimental set-up to prove the action of osmotic pressure gradients induced by chemical reactions should be the starting point. This opens up many possibilities for exploiting autonomous motion to either propel particles and/or pump fluid, some of which are outlined in this work. Osmotic propulsion provides a simple means to convert chemical energy into mechanical motion and work, and can impact the design and operation of nanodevices, with applications in directed self-assembly of materials, thermal management of micro- and nanoprocessors, and the operation of chemical and biological sensors. Studies of autonomous motors may also help us to understand chemomechanical transduction observed in biological systems and to create novel artificial motors that mimic living organisms, which can be harnessed to perform desired tasks.

6.2 Bibliography

A. J. Banchio and J. F. Brady. Accelerated Stokesian dynamics: Brownian motion. *J. Chem. Phys.*, 118(22):10323–10332, 2003.

G. K. Batchelor. Diffusion in a dilute polydisperse system of interaction spheres. *J. Fluid Mech.*, 131:155–175, 1983.

H. C. Berg. The rotary motor of bacterial flagella. *Annu. Rev. Biochem.*, 72:19–54, 2003.

J. F. Brady and J. F. Morris. Microstructure of strongly sheared suspensions and its impact on rheology and diffusion. *J. Fluid Mech.*, 348:103–139, 1997.

D. Bray, M. D. Levin, and K. Lipkow. The chemotactic behavior of computer-based surrogate bacteria. *Curr. Biol.*, 17:12–19, 2007.

S. Chattopadhyay, R. Moldovan, C. Yeung, and X. L. Wu. Swimming efficiency of bacterium Escherichia coli. *PNAS*, 103(37):13712–13717, 2006.

A. S. Khair and J. F. Brady. Single particle motion in colloidal dispersions: a simple model for active and nonlinear microrheology. *J. Fluid Mech.*, 557:73–117, 2006.

A. S. Khair and J. F. Brady. Microrheology of colloidal dispersions: Shape matters. *J. Rheol.*, 52(1):165–196, 2008.

K. Namba. A biological molecular machine — bacterial flagellar motor and filament. *Wear*, 168(1–2):189–193, 1993.

W. F. Paxton, S. Sundararajan, T. E. Mallouk, and A. Sen. Chemical locomotion. *Angew. Chem. Int. Ed.*, 45(33):5420–5429, 2006.

W. F. Paxton, K. C. Kistler, C. C. Olmeda, A. Sen, S. K. St. Angelo, Y. Y. Cao, T. E. Mallouk, P. E. Lammert, and V. H. Crespi. Catalytic nanomotors: Autonomous movement of striped nanorods. *J. Am. Chem. Soc.*, 126(41):13424–13431, 2004.

E. M. Purcell. The efficiency of propulsion by a rotating flagellum. *Proc. Natl. Acad. Sci. USA*, 94:11307–11311, 1997.

G. Ruckner and R. Kapral. Chemically powered nanodimers. *Phys. Rev. Lett.*, 98(15), 2007.

T. M. Squires and J. F. Brady. A simple paradigm for active and nonlinear microrheology. *Phys. Fluids*, 17(7), 2005.